



UNIVERSIDAD NACIONAL AUTÓNOMA DE MÉXICO

POSGRADO EN ASTROFÍSICA
ASTROFÍSICA TEÓRICA
INSTITUTO DE ASTRONOMÍA

ESTUDIOS NUMÉRICOS DE FENÓMENOS DE ACRECIÓN Y
EYECCIÓN EN ASTROFÍSICA

TESIS

QUE PARA OPTAR POR EL GRADO DE:
DOCTOR EN CIENCIAS (ASTROFÍSICA)

PRESENTA:

ALEJANDRO AGUAYO ORTIZ

TUTORES

DIEGO LÓPEZ CÁMARA RAMÍREZ
INSTITUTO DE ASTRONOMÍA, UNAM

EMILIO TEJEDA RODRÍGUEZ
INSTITUTO DE FÍSICA Y MATEMÁTICAS, UMSNH

MÉXICO, Cd. Mx., JUNIO 2022



Universidad Nacional
Autónoma de México



UNAM – Dirección General de Bibliotecas
Tesis Digitales
Restricciones de uso

DERECHOS RESERVADOS ©
PROHIBIDA SU REPRODUCCIÓN TOTAL O PARCIAL

Todo el material contenido en esta tesis esta protegido por la Ley Federal del Derecho de Autor (LFDA) de los Estados Unidos Mexicanos (México).

El uso de imágenes, fragmentos de videos, y demás material que sea objeto de protección de los derechos de autor, será exclusivamente para fines educativos e informativos y deberá citar la fuente donde la obtuvo mencionando el autor o autores. Cualquier uso distinto como el lucro, reproducción, edición o modificación, será perseguido y sancionado por el respectivo titular de los Derechos de Autor.

A Tachis, Clío y Mota

Agradecimientos

A la Universidad Nacional Autónoma de México por ser mi segunda casa durante 15 años y al Instituto de Astronomía por brindarme un espacio donde pude estudiar, trabajar y hacer investigación durante todo el posgrado.

Al Consejo Nacional de Ciencia y Tecnología (CONACyT) por brindarme la beca que me permitió dedicarme de tiempo completo al doctorado (CVU 788898). Al Programa de Apoyo a los Estudios de Posgrado (PAEP) por haberme permitido viajar a congresos y escuelas internacionales. A la Dirección General de Cómputo y de Tecnologías de Información y Comunicación (DGTIC) de la UNAM, por el soporte recibido para el uso de la supercomputadora Miztli (proyecto LANCAD-UNAM-DGTIC-406).

Al Posgrado en Astrofísica por haberme permitido realizar mi sueño de convertirme en astrónomo. A Bertha, Adriana, Heike y Laurent por siempre estar al pendiente de los estudiantes, ayudarnos con todos los trámites y, personalmente, por apoyarme en los momentos difíciles que tuve a mediados del doctorado.

A mis sinodales, Dr. Jorge Cantó, Dra. Verónica Lora, Dr. Héctor Olivares y Dr. Néstor Ortiz, por haber aceptado formar parte de mi sínodo, por tomarse el tiempo para leer mi trabajo y por todos sus comentarios.

A Dr. Fabio de Colle, Dr. Enrique Moreno y Dr. Alejandro Cruz-Osorio por haber formado parte de mi comité tutor y por brindarme su apoyo durante todo el doctorado.

Agradezco profundamente a Dr. Xavier Hernández por haber sido mi colaborador desde el inicio del doctorado y animarme a aplicar mi código en un problema sumamente interesante, el cual acabó por convertirse en parte fundamental de esta tesis.

Al Dr. Olivier Sarbach no solo por haber colaborado conmigo en varios proyectos y ser parte de mi sínodo, sino también por su amabilidad y paciencia, así como por ser siempre esa sonrisa amigable en la audiencia cuando me tocaba dar alguna charla.

A mi co-tutor, Dr. Emilio Tejada, por todo el apoyo que me has brindado desde que formaste parte de mi sínodo de licenciatura hace 6 años. Por haberme invitado a trabajar contigo y guiarme a lo largo de todo este trabajo. Gracias por haberme brindado no solo tu tutoría, sino también tu amistad. A mi también co-tutor, Dr.

Diego López-Cámara, por haberme aceptado como su estudiante casi a mediados del doctorado, a pesar de que ya estaba muy avanzado el proyecto. Por involucrarte de lleno en mi trabajo y siempre buscar la forma en la que pudiera hacer mejor las cosas. Gracias a los dos por tratarme no como un estudiante, sino como un colaborador, por valorar siempre mis ideas, por su tiempo, sus enseñanzas y por su enorme comprensión con la decisión que tome al final del doctorado. A ambos les estoy infinitamente agradecido.

A mis amigxs del posgrado Luis, Vero, Alexia, Eli, Fer, Mabel, René, Sheila, Aroche, Francisco, Andrés, Dan y Omar, por todos los buenos momentos que pasamos juntos, por los paseos en bici, por las tardes que nos quedábamos a hacer tarea, por las idas al Calacas y por siempre estar ahí cuando los necesité.

A Chimal por nunca dejar de insistir en que trabajáramos juntos y por darme la oportunidad de seguir haciendo ciencia de una forma mucho más enriquecedora. A todo AperVox por ser el mejor equipo de trabajo.

A todxs lxs integrantes de iuaniDivulgación y de Astrofísicos en Acción, por brindarme la oportunidad de hacer divulgación de la ciencia.

A Gaby y Arturo por no dejar que nuestra amistad se pierda con la distancia. A Yahel por todas esas pláticas sobre la vida y la buena música. A Ana Elisa, por tu alegría que se contagia. A Pablito siempre estar al pendiente y apoyarme en todo momento.

A mis hermanos Rodrigo y Estíbaliz, por haberme apoyado en todas las decisiones que he tomado, por estar presentes cuando más lo requería y por siempre velar por mis intereses. A mi padre, Benjamín, por todas las noches de guitarra, por todas las historias, por todas las veces que me hiciste la vida más sencilla mientras yo trabajaba en el doctorado y por todo el sacrificio que realizaste durante tantos años para que nunca nos faltara nada. A los tres les quiero agradecer por este gran equipo que formamos después de los últimos años que han sido verdaderamente complicados.

A mi madre, Estela, porque gracias a ti decidí dedicarme a la ciencia. Me duele que no puedas estar aquí conmigo para ver la culminación de este proceso, pero agradezco profundamente que estuvieras durante toda mi vida. Gracias por todo el amor que nos diste, por haberte entregado por completo a tu familia y por mantenernos siempre unidos. Te extraño.

Finalmente, quiero agradecerle a mi compañera de vida, Lucero. Esta tesis también va dedicada a ti. De no haber sido por ti, por tu apoyo y tu cariño, no me hubiera sido posible llegar hasta aquí. Gracias por darme fuerzas en todos los momentos difíciles, por tu comprensión y por siempre saber cómo sacarme una sonrisa. Gracias a ti y tu familia por recibirme como uno de los suyos, así como por brindarnos, a mi, mis hermanos y mi papá, toda su ayuda en los momentos más complicados. Gracias por darnos la oportunidad de volver a caminar juntos por esta vida. Gracias por ayudarme a entender que *dejarse llevar suena demasiado bien...*

Contents

1	Introduction	7
1.1	Gas accretion	8
1.1.1	Spherical accretion	8
1.1.2	Wind accretion	9
1.1.3	Accretion disks	10
1.1.4	Hot accretion flows	11
1.2	Astrophysical jets and outflows	12
1.2.1	Blandford-Znajek mechanism	13
1.2.2	Blandford-Payne mechanism	14
1.2.3	Alternative mechanisms	16
1.3	Choked accretion mechanism	17
2	AZTEKAS: a GRHD numerical code	19
2.1	AZTEKAS: numerical methods	20
2.1.1	Finite volume method	20
2.1.2	Approximate Riemann solver	21
2.1.3	Polynomial spatial reconstruction schemes	23
2.1.4	Time integration	24
2.1.5	Primitive variable recovery	25
2.1.6	Ghost cells	25
2.2	AZTEKAS-HD: non-relativistic hydrodynamics	26
2.2.1	Euler equations	26
2.2.2	HD in balanced form	28
2.3	AZTEKAS-HD: code validation	28
2.3.1	Shock tube	28
2.3.2	Double Mach reflection	32
2.3.3	Sedov-Taylor blast wave	34
2.3.4	Hydrodynamic instabilities	37
2.3.5	Astrophysical jet	40
2.3.6	Bondi spherical accretion	42

2.3.7	Wind accretion	44
2.4	AZTEKAS-GRHD: general relativistic hydrodynamics	46
2.4.1	3+1 formalism	46
2.4.2	General relativistic hydrodynamics	47
2.4.3	GRHD in balanced form	49
2.4.4	Primitive variable recovery	50
2.5	AZTEKAS-GRHD: code validation	51
2.5.1	Tests in Minkowski spacetime	51
2.5.2	Tests in black hole spacetimes	55
3	Spherical accretion: Bondi, Michel, and rotating black holes	63
4	Relativistic wind accretion on to a Schwarzschild black hole	79
5	Choked accretion: from radial infall to bipolar outflows by breaking spherical symmetry	93
6	Choked accretion onto a Schwarzschild black hole: a hydrodynamical jet-launching mechanism	105
7	Choked accretion onto a Kerr black hole	127
8	Conclusions	155
	Bibliography	159

Resumen

La acreción de gas hacia objetos masivos es un problema sumamente importante en astrofísica, debido a que se puede encontrar en una gran variedad de escenarios, desde el nacimiento de estrellas hasta eventos de altas energías. Diversos modelos matemáticos han sido desarrollados en las últimas décadas para poder explicar las cada vez más refinadas observaciones, así como el funcionamiento del mecanismo interno de estos fenómenos y su relación con los chorros de gas que estos expulsan.

En esta tesis exploramos y extendemos diferentes problemas de acreción hacia objetos masivos. Primero, realizamos un análisis detallado de las diferencias entre los modelos clásicos de acreción esférica, tanto en el caso relativista como en el no-relativista, y extendemos el modelo, usando simulaciones numéricas, al caso de acreción a un agujero negro en rotación. Posteriormente, estudiamos el problema de acreción de viento, extendiendo el modelo clásico al caso relativista, en donde el objeto central corresponde a un agujero negro sin rotación.

Asimismo, desarrollamos y exploramos distintos regímenes de un mecanismo de acreción-eyección al cual hemos llamado *choked accretion*, el cual constituye un modelo completamente hidrodinámico en donde obtenemos una solución de un gas acretado ecuatorialmente hacia un agujero negro, y un flujo eyectado por los polos. Este modelo, que fue estudiado utilizando tanto soluciones analíticas como simulaciones numéricas, fue estudiado en los regímenes de potencial gravitacional no-relativista y para los casos de agujero negro (con y sin rotación) en el caso relativista. El mecanismo *choked accretion* proporciona una relación directa entre el fenómeno de acreción y eyecciones bipolares.

Finalmente, en esta tesis presentamos la versión más reciente del código de hidrodinámica numérica AZTEKAS. Este código fue desarrollado a la par de todos los estudios mencionados previamente, y fue validado por medio de pruebas de comparación tanto con soluciones analíticas como con simulaciones numéricas reportadas comúnmente en la literatura.

Abstract

Gas accretion towards massive objects is an extremely important problem in astrophysics, since it can be found in a wide variety of scenarios, from the birth of stars to high-energy events. Various mathematical models have been developed over the past decades in order to explain the increasingly refined observations, as well as the operation of the internal mechanism of these phenomena and their relationship to the jets powered by them.

In this thesis, we explore and extend different gas accretion problems. First, we perform a detailed analysis of the differences between the classical spherical accretion models, both in the relativistic and non-relativistic cases, and we extend the model, using numerical simulations, to the case of accretion on to a rotating black hole. Subsequently, we study the wind accretion problem, extending the classical model to the relativistic case, where the central object corresponds to a non-rotating black hole.

Moreover, we develop and explore different regimes of an accretion-ejection mechanism which we have called *choked accretion*, which constitutes a completely hydrodynamic model in which we obtain a solution of a gas being accreted equatorially towards a black hole, and a flux ejected through the poles. This model, which is studied using both analytical solutions and numerical simulations, is analysed in the non-relativistic gravitational potential regimes and for the black hole cases (with and without rotation) in the relativistic case. The *choked accretion* mechanism provides a direct relationship between the phenomenon of accretion and bipolar ejections.

Finally, in this thesis we also present the current version of the numerical hydrodynamics code AZTEKAS. This code was developed alongside all the previously mentioned studies, and was validated through comparison tests with both analytical solutions and numerical simulations commonly reported in the literature.

Collaborations

The research presented in this thesis is the result of the author's own work, as well as the outcome of the scientific collaborations mentioned below, except where explicit reference is made to the results of others. The thesis is based on the following research papers:

- Tejada E., **Aguayo-Ortiz A.**, 2019, MNRAS, 487, 3607. [doi:10.1093/mnras/stz1513](https://doi.org/10.1093/mnras/stz1513)
- **Aguayo-Ortiz A.**, Tejada E., Hernandez X., 2019, MNRAS, 490, 5078. [doi:10.1093/mnras/stz2989](https://doi.org/10.1093/mnras/stz2989)
- Tejada E., **Aguayo-Ortiz A.**, Hernandez X., 2020, ApJ, 893, 81. [doi:10.3847/1538-4357/ab7ffe](https://doi.org/10.3847/1538-4357/ab7ffe)
- **Aguayo-Ortiz A.**, Sarbach O., Tejada E., 2021, PhRvD, 103, 023003. [doi:10.1103/PhysRevD.103.023003](https://doi.org/10.1103/PhysRevD.103.023003)
- **Aguayo-Ortiz A.**, Tejada E., Sarbach O., López-Cámara D., 2021, MNRAS, 504, 5039. [doi:10.1093/mnras/stab1127](https://doi.org/10.1093/mnras/stab1127)

Introduction

Gravity is the dominant force that rules the evolution of the Universe. From the movement of planets up to the filamentary structure in which the galaxy superclusters are found, gravity is the main responsible for the overall dynamics that is seen in astrophysical scenarios. However, much of the complexity behind said phenomena comes not just from the gravitational attraction, but from the matter and electromagnetic fields that forms or surrounds the astrophysical objects. At this level, it is gas and plasma, as well as their interaction with gravitational and electromagnetic fields, the responsible for many of the most energetic phenomena in the Universe. In particular, when there is gas around a massive object, like a star or a black hole, the gravitational field tends to attract all the matter to the central mass, producing a phenomenon known in astrophysics as *accretion*.

Gas accretion is one of the most efficient ways of extracting energy from matter. In fact, it is well known that accretion onto a black hole is the most efficient one (King, 2010), besides from matter-antimatter annihilation. For a rapidly rotating black hole, the conversion from rest mass into energy by accreting gas is around 30% (Thorne, 1974). This is why the most energetic and luminous phenomena in the Universe are often associated to the gas accretion onto a compact object.

Due to this efficiency of energy extraction, it is believed that gas accretion is intrinsically related with another important astrophysical phenomena, *ejection*, which can be found as relativistic and non-relativistic jets, winds and outflows (King, 2010).

The study of gas accretion-ejection scenarios in astrophysics is a big challenge. The physics behind them is extremely complex as it not only requires a macroscopic description of the behaviour of the gas dynamics¹, but also needs to take into account gravity fields or, in general, space-time curvature, electromagnetic fields,

¹In this thesis we are going to assume the hydrodynamic limit, where the characteristic scale of the system under study is much greater than the mean free path of the gas particles. Another limit worth mentioning here, the so-called Vlasov limit, arises when the typical length scale of the system is comparable to the mean free path between particle collisions, and is based on kinetic theory of gases to describe the plasma dynamics (see e.g. Sarbach & Zannias, 2013; Acuña-Cárdenas et al., 2022).

microphysics and any other external effect that could affect the behaviour of the gas. The first approaches that attempted to study the case of gas being accreted by a massive object, needed to simplify the problem by considering some kind of symmetry and ignoring external effects (like magnetic fields and so on). In recent years, by developing state-of-the-art numerical methods and numerical codes, the scientific community has been able to perform detailed simulations considering the most extreme scenarios (e.g. [Liska et al., 2021](#); [Mizuno, 2022](#)).

In this work, we address different accretion problems by means of analytic solutions and numerical simulations, extending well-known Newtonian models to their relativistic counterparts, as well as presenting the *choked accretion* mechanism, a purely hydrodynamic solution that connects the gas accretion phenomena with the production of massive bipolar outflows.

The thesis is divided as follows. In Chapter 1, we briefly review some of the best established accretion models and solutions, as well as some ejection mechanisms and their relation to astrophysical phenomena. In Chapter 2, we present AZTEKAS, a GRHD numerical code developed as a part of this work. In this chapter we show the numerical methods and algorithms used in the code, as well as a series of validation tests. In Chapters 3 and 4 we show the relativistic extensions of two classical accretion solutions: Bondi and BHL accretion models. Chapters 5, 6 and 7 correspond to the choked accretion papers in the non-relativistic, Schwarzschild black hole and Kerr black hole cases, respectively. Finally, in Chapter 8, we summarize the results obtained in this thesis and present the conclusions.

1.1 Gas accretion

In this section, we will review some of the most important models that have been developed for the gas accretion theory. The solutions presented here are especially important for the content of this thesis.

1.1.1 Spherical accretion

Spherical accretion, due to its symmetry, is one of the starting points for studying gas accretion phenomena. One of the pioneering works on this topic was presented by [Bondi \(1952\)](#), in which the author found a full-hydrodynamic, steady-state analytic solution of a spherically symmetric infinite gas cloud being accreted by a Newtonian mass potential. In this seminal work, Bondi provides a prescription for computing the rate at which mass is accreted in the vicinity of the central mass. This model, despite its simplicity, has been used to estimate the accretion and growth rate of the central supermassive black hole in the centre of galaxies and active galactic nuclei (AGNs, [Russell et al., 2015](#); [Moffat, 2020](#)), and even to study the growth of a mini-black hole inside a neutron star ([Richards et al., 2021](#)).

One of the first studies to extend this solution was presented by [Michel \(1972\)](#),

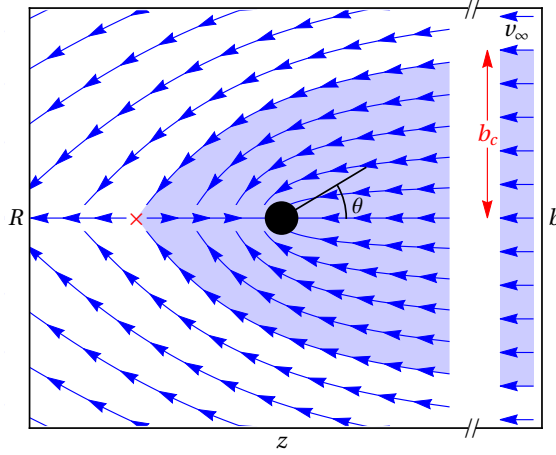


Figure 1.1: Schematic representation of the Bondi-Hoyle-Lyttleton wind accretion problem. Figure taken from [Tejeda & Aguayo-Ortiz \(2019\)](#).

where the author studies the general relativistic counterpart of Bondi’s problem, finding a steady-state, spherically symmetric gas accretion solution onto a Schwarzschild black hole. Since then, this model has been widely revisited and extended by considering different physical ingredients such as fluid’s angular momentum, magnetic fields and radiative transfer (e.g., [Proga & Begelman, 2003](#); [Igumenshchev & Narayan, 2002](#); [McKinney et al., 2014](#)), to name a few.

In this thesis, we revisit these classical solutions performing a detailed comparison between the non-relativistic and relativistic analytic models, and extending them into the case of a rotating Kerr black hole by means of full general relativistic hydrodynamic simulations. This paper is presented in Chapter 3.

1.1.2 Wind accretion

In general, it is fair to assume that every massive object will be in relative motion with respect to its surroundings. One example of this is the so-called wind accretion problem, in which a star or compact object moves through an infinitely large gas cloud with at a constant relative velocity. This phenomenon was first studied by [Hoyle & Lyttleton \(1939\)](#) and [Bondi & Hoyle \(1944\)](#) (BHL, hereafter), where the authors found an analytic solution for a supersonic wind accreting onto a massive object (see [Figure 1.1](#)). The complexity of the problem, unlike the Bondi spherical accretion problem, does not admit a full hydrodynamic analytic solution, so the authors use a ballistic approximation to describe the gas moving towards the massive object.

Extensions to this model have been performed by assuming different types of gasses or equations of state. In the seminal work by [Petrich et al. \(1988\)](#), the authors found an exact analytic solution of a black hole moving through a medium by considering an ultra-relativistic stiff equation of state. This solution is valid for both rotating and non-rotating black holes, and constitutes a fully three-dimensional flow

description.

The BHL model is often invoked to describe scenarios where a star or compact object moves inside a larger medium. For example, authors have adopted the BHL problem to study the motion of binary stars (Comerford et al., 2019) or star clusters through a uniform gas medium (Kaaz et al., 2019) to study the evolution of those systems. Other authors have studied the common envelope phase in the evolution of a binary system where a giant star has swallowed its companion. In this scenario, a compact object moves inside the massive star, accreting material in the way. This accretion has been described as a wind accretion problem by different authors (Moreno Méndez et al., 2017; López-Cámara et al., 2019; Cruz-Osorio & Rezzolla, 2020).

In this thesis, we extend the BHL problem to the general relativistic case, by solving the ballistic approximation problem around a Schwarzschild black hole, obtaining the mass accretion rate, density field and fluid streamlines, as in the Newtonian classic solution. This paper is presented in Chapter 4.

1.1.3 Accretion disks

A fundamental ingredient to take into account in the study of accretion is the angular momentum of the infalling gas, which adds an extra degree of complexity when solving the equations of hydrodynamics. The rotation of the gas inside a gravitational potential often results in, due to the conservation of angular momentum, the formation of an equatorial disk around the central massive object.

Different solutions have been proposed to the problem of gas rotating around a central massive object. Fishbone & Moncrief (1976) present a solution of the relativistic Euler equations for an ideal gas. This model consists of a general stationary solution for a rotating isentropic (constant entropy) fluid disk around a Kerr black hole. Similarly, Paczynski & Abramowicz (1982) introduce solutions for geometrically thick disks. In both cases, the authors provide stable solutions in which the disk counteracts the black hole attraction solely by centrifugal forces, nevertheless, no accretion whatsoever is achieved in these models. These two solutions are commonly used, even nowadays, as initial conditions for general relativistic magnetohydrodynamic (GRMHD) simulations of accretion disks (e.g., Dexter et al., 2021; Most et al., 2021; Yao et al., 2021). On the other hand, in the works of Mendoza et al. (2009) and Tejeda et al. (2012), the authors found an analytic solution to the finite rotating cloud accretion problem in the non-relativistic and relativistic case, respectively. These models assume a ballistic approximation for the fluid, similar to the one used in the BHL problem, and show the formation of a thin disk (due to the absence of pressure) along the equatorial plane.

The first accretion disk models were proposed separately by Prendergast & Burbridge (1968) and Shakura & Sunyaev (1973), the later model is often called the α thin disk model. This solution consists of a hydrodynamic mechanism, based on dimensional arguments, from which an effective viscosity in the disk is responsible for the angular momentum transfer to the outer parts of the disk, allowing the gas to

be accreted by the central object. This viscosity is parametrized by $0 < \alpha < 1$, and accounts for the unknown physics that may cause angular momentum transport in the disk (e.g., magnetic fields). In order to obtain this solution, the authors integrate the equations along the vertical component of the disk, in order to obtain a thin accretion disk description. The Shakura-Sunyaev α -disk model has been widely extended (e.g., Novikov & Thorne, 1973; Pariev et al., 2003; Penna et al., 2013) and implemented for the study of luminous AGNs (e.g., Li et al., 2021) and soft X-ray binary sources (e.g., Panotopoulos et al., 2021).

On the other hand, Balbus & Hawley (1991) have shown that, if a poloidal magnetic field is anchored to an accretion disk, the field lines are dragged by the rotation of the disk developing a magneto-rotational instability (MRI). This instability produces the turbulence necessary to produce an effective viscosity that transport the angular moment outwards, allowing the gas to be accreted by the central massive object. This accretion mechanism has been observed in GRMHD simulations (e.g., Siegel & Metzger, 2017; Porth et al., 2019), and it is considered as the most likely mechanism for transportation of angular momentum and dissipation of energy in hot accretion flows, which will be briefly discussed in the next subsection.

1.1.4 Hot accretion flows

Another important ingredient to be considered in accretion flows is the radiation emitted by the gas, which generates a radiative pressure that opposes the gravitational force that accretes the fluid. A limiting value in the luminosity emitted is achieved when both forces balance each other in a spherically symmetric setting, this is called the Eddington luminosity (Eddington, 1925):

$$L_{\text{Edd}} = \frac{4\pi GMc}{\kappa}, \quad (1.1)$$

where κ is the electron scattering opacity. This limit luminosity is assumed to be equal to a fraction of the energy rate accreted by the black hole $L_{\text{Edd}} = \eta \dot{M}_{\text{Edd}} c^2$, where η is the radiative efficiency of the accretion disk and \dot{M}_{Edd} is the corresponding mass accretion rate.

If the disk luminosity is below Eddington's, a cool geometrically thin disk model like the Shakura-Sunyaev α -model can be used to describe the dynamics of the fluid. In this case, the heat produced by viscous dissipation is efficiently radiated away from the disk. However, when the luminosity surpasses the Eddington limit, the radiative efficiency decreases, trapping the radiation and eventually advecting it inwards with the accreted gas, producing a slim optically thick disk. On the other hand, if the gas density is low, the black hole naturally accretes at sub-Eddington rates, hence the viscously dissipated energy is not radiated away and, instead, is used to increase the temperature, producing a hot, geometrically thick, optically thin and radiatively inefficient accretion disk.

These kinds of accretion flow are often referred to as hot accretion flows. In particular, in the cases mentioned above, in which the non-dissipated energy is advected with the accreted gas, are named advection-dominated accretion flows (ADAF, [Ichimaru, 1977](#); [Narayan & Yi, 1994, 1995](#); [Abramowicz et al., 1995](#)).

The ADAFs and, in general, the hot accretion flow solutions are of special interest for this thesis since, among their different interesting features (see the review by [Yuan & Narayan, 2014](#)), these models show that the Bernoulli parameter B_e can become positive in some regions of the flow, meaning that the fluid is unbounded to the central object, as well as unstable against convection, which implies that they are related to outflows, winds and jets. In fact, in the work by [Blandford & Begelman \(1999\)](#), the authors show that, together with the advected radiation, the presence of outflows and winds coming from the disk may help to reduce the radiative efficiency of the disk. This is known as the advected-dominated inflow-outflow solution (ADIOS). This association between astrophysical jets and hot accretion flows has been successfully used to model systems as low-luminosity AGNs (e.g., [Davelaar et al., 2019](#)) and hard or quiescent X-ray binaries (e.g., [Begelman et al., 2015](#)).

Although these models' features suggest a connection between hot accretion flows and jets/outflows, they do not explain the mechanism behind these ejections. In the following section, we will briefly discuss the nature of astrophysical jets and outflows, mentioning the astrophysical scenarios in which these phenomena are found, as well as two of the best established jet-launching mechanisms, and some alternatives that have been developed to explain them.

1.2 Astrophysical jets and outflows

Jets and outflows are natural processes in which matter and energy, as well as other physical quantities (e.g., magnetic flux), are expelled out into a medium surrounding a central massive body. They are a ubiquitous astrophysical phenomenon since they can be found in a wide variety of astrophysical scenarios. From stellar to extragalactic objects, ranging in velocities of around tenths of km s^{-1} to almost the speed of light, and with lengths that go from a few astronomical units to kiloparsecs, they are all believed to be related to some kind of accretion process. The difference between a jet and a simple outflow is that the first one refers to a fast, highly collimated ejection, whereas the latter is slower and not necessarily collimated.

Less collimated ejections, or outflows, are often found as stellar winds (cf. [Vink, 2011](#)), or ejections at the last stages of stellar evolution (luminous blue variables and planetary nebula, [Weis & Bomans, 2020](#); [Kwitter & Henry, 2021](#), respectively), however, they have been found in a wide variety of astrophysical scenarios. For example, as molecular outflows along with highly collimated jets in young stellar objects (YSOs, [Yen et al., 2019](#)); in the galactic scales, as massive molecular outflows that are thought to help to regulate the growth and evolution of galaxies ([Spilker et al., 2020](#)) or as mildly relativistic bipolar ejections in fast-rising blue optical tran-

sients (Coppejans et al., 2020). Another important type of less collimated outflows are the disk winds, which have been found in protostellar systems (Bjerkeli et al., 2016), as well as in accretion disks around black holes (Braitto et al., 2018), and which are usually found along with jets.

Meanwhile, highly collimated jets are found in more specific scenarios than the less collimated counterparts. In the non-relativistic regime, jets are mostly found in YSOs (Anglada et al., 2018), where the central massive object corresponds to a star in its early stage of evolution. On the other hand, in the relativistic regime, jets are powered by the accretion onto a compact object such as a neutron star or, more commonly, a black hole, either a stellar mass, like in X-ray binaries (Espinasse et al., 2020) or a supermassive one, like in AGNs (Blandford et al., 2019). Relativistic jets are also found in high energy phenomena like short gamma ray bursts (GRBs, Pavan et al., 2021), which corresponds to the collision of a binary neutron star system, and long GRBs (Shrestha et al., 2022), which form in the collapse of a rapidly rotating massive star in the final stages of its evolution.

Although the main ingredient in all the astrophysical scenarios where jets and outflows are found is the presence of a massive central object and a rotating gas accretion disk around it, a fundamental ingredient for these ejections seems to be a magnetic field and its interaction with the whole system. This allows the formation and stability of the disk, as well as the launching and collimation of the jet (Hawley et al., 2015). The most accepted processes for the launching of the jet are the magneto-centrifugal mechanisms proposed by Blandford & Znajek (1977) and Blandford & Payne (1982), which are briefly explained in the following sections, along with some pure hydrodynamic alternatives.

1.2.1 Blandford-Znajek mechanism

Blandford & Znajek (1977, BZ77) propose a mechanism by which rotational energy of a Kerr black hole is efficiently extracted. If a sufficiently large amount of charged particles are rotating around the black hole, along with a strong magnetic field (10^{15} G Lee et al., 2000), then, under the condition that the magnetic pressure is greater than the gas pressure², the field lines co-rotate along with the black hole, anchoring them to the event horizon, and forming a toroidal component of the field that travels along the axis of rotation (see Figure 1.2). The induced electric currents around it feel the presence of an external magnetic field, which produces the deceleration in the rotation of the black hole. The extracted energy from this deceleration is expelled following the motion of the toroidal field lines and creating a Poynting flux, i.e., a purely electromagnetic energy flux.

The maximum energy rate extracted from the black hole spin, known as the

²This is known as *force-free* condition. Blandford & Znajek (1977) shown that for strength magnetic fields, vacuum is unstable against the positron-electron pair creation, which feeds the induced currents.

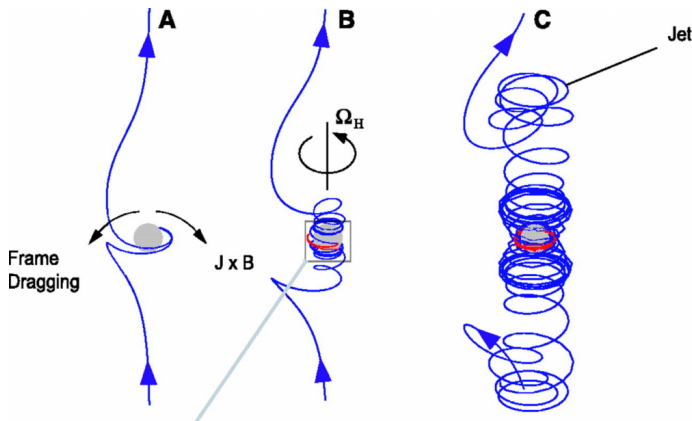


Figure 1.2: Snapshots of a simulation of a black hole-driven jet, showing the behaviour of the magnetic field around a rotating black hole in the [Blandford & Znajek \(1977\)](#) mechanism. The simulation shows the formation of a toroidal component of the magnetic field anchored to the rotating black hole, producing a collimated structure. Image taken from [Semenov et al. \(2004\)](#).

Blandford-Znajek luminosity, is

$$L_{\text{BZ}} \sim \left(\frac{B_p^2}{4\pi} \right) \pi R_h^2 \left(\frac{R_h \Omega_h}{c} \right)^2 c, \quad (1.2)$$

where B_p is the maximum value of the poloidal magnetic field component, R_h is the characteristic radius of the system (e.g., event horizon's size) and Ω_h is the black hole angular velocity. For the case of an AGN, $L_{\text{BZ}} \sim 10^{45} \text{ erg s}^{-1}$. The maximum theoretical energy that can be extracted from a $1 M_\odot$ black hole is 10^{54} erg ([Lee et al., 2000](#)).

The BZ77 model is believed to be the mechanism behind most of the high energy astrophysical scenarios in which the central engine is powered by a rotating black hole. However, since this model depends on the black hole spin, it does not provide an explanation for the jets that are observed in astrophysical systems in which the central accretor is not a black hole. In these cases it is assumed that the energy extraction comes from the accretion disk, which is addressed by the next jet-launching mechanism.

1.2.2 Blandford-Payne mechanism

The [Blandford & Payne \(1982, BP82\)](#) mechanism consists of a magneto-rotational process by which both energy and angular momentum are magnetically extracted from the accretion disk, due to the poloidal field lines anchored to the disk, and that extend out to great distances (see [Figure 1.3](#)). The collimated flux is obtained due to the presence of a toroidal component of the magnetic field, as in BZ77. In this work, the authors found an auto-similar magneto-hydrodynamic solution for the

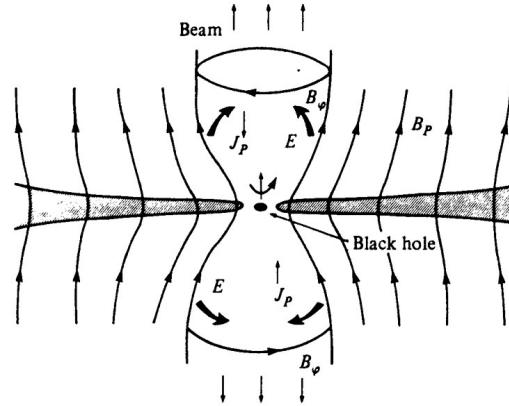


Figure 1.3: Schematic representation of the [Blandford & Payne \(1982\)](#) mechanism. A poloidal magnetic field is fixed into the accretion disk, co-rotating with it, extracting angular momentum from the disk and producing a collimated flux. Image taken from [Muxlow & Garrington \(1991\)](#), respectively.

axisymmetric flux. This process is invoked for systems where there exists a weak magnetic field and the magnetic pressure is lower than the gas pressure of the disk. The energy extraction rate is about 10^{43} erg s^{-1} for a magnetic field intensity of 10^3 G.

The advantage of the BP82 model, as mentioned before, is that it does not require a rotating black hole as the central mass of the system, which makes it applicable to a wide variety of astrophysical scenarios. Moreover, some works have shown that the BP82 model could be found along with the BZ77 mechanism, producing winds from the accretion disk, while the BZ77 launch a collimated jet (e.g. [Dihingia et al., 2021](#)).

The differences between BZ77 and BP82, even though they both require magnetic fields to extract energy and angular momentum, is that, for BP82, the magnetic field intensity is much less than the one needed by BZ77. Moreover, in BZ77 the magnetic field lines are fixed at the black hole's event horizon, whereas in the BP82 model, the lines are fixed to the accretion disk. On the other hand, in the BZ77 mechanism the flux is purely electromagnetic, in contrast to BP82, where there is also a matter flux.

Even though these mechanisms provide a good explanation on how energy is extracted from star/black hole-disk systems, it was until the last decade when clear observational evidence in their support started to appear (e.g. [Narayan & McClintock, 2012](#)). This motivated different authors to revisit these magneto-centrifugal mechanisms by means of numerical simulations (see [Mizuno, 2022](#), for a review on the recent advances on general relativistic magneto-hydrodynamic (GRMHD) numerical simulations). These simulations have extended our understanding of the jet launching process, coupling it with other much more complex physical ingredients and scenarios like neutrino-cooling (e.g. [Siegel & Metzger, 2018](#)), radiative trans-

fer (e.g. [Bronzwaer et al., 2018](#)) or tilted accretion disks (e.g. [Liska et al., 2021](#)), to name a few.

1.2.3 Alternative mechanisms

Despite the great success that magneto-centrifugal mechanisms have had in explaining the launch of astrophysical jets, there are still some open questions. For example, it remains unclear what the process of particle acceleration due to black hole spin looks like ([Tchekhovskoy, 2015](#)); lack of direct evidence of the magnetic field in jets coming from stars or accretion disks, nor that this is the main cause of their collimation ([Hawley et al., 2015](#)); the connection between the acceleration-collimation of the jet and the process of accretion by the disk remains to be understood ([Romero et al., 2017](#)), as well as its matter content in jets dominated by Poynting flow ([Hawley et al., 2015](#)).

This is why it has been considered that, probably, the presence of a large-scale magnetic field alone is not the only cause of collimation or the ejection of the jet itself. Magnetic mechanisms such as those mentioned above are likely to be only one part of a more complete and unified mechanism for the explanation of the origin and collimation of astrophysical jets ([Livio, 1997](#)). Some works have tried to explain the collimation of jets ejected from a Kerr black hole without the need for a magnetic field, invoking latitudinal anisotropies in the geometry of spacetime ([Bicak et al., 1993](#)), or studying geodesics of extracted particles due to the Penrose process ([Gariel et al., 2010](#)).

Another alternative mechanism is mediated by neutrino-antineutrino annihilation. In the context of long GRBs, with a typical mass accretion rate of the order of $0.1 - 1 M_{\odot} \text{ s}^{-1}$, the density and temperature are large enough ($\rho \sim 10^{10} \text{ g cm}^{-3}$ y $T \sim 10^{11} \text{ K}$) to emit neutrinos at the vicinity of the black hole. A fraction of these neutrinos annihilate in the polar regions of the black hole, creating positron-electron pairs and depositing energy in the polar region of the black hole, potentially launching a relativistic jet ([Leng & Giannios, 2014](#)).

However, while these studies help explain jet collimation, and in some cases matter extraction, they work for relativistic scenarios. In the case of YSOs, where there are not always direct and reliable measurements of the intensity and geometry of the magnetic field in the jet ([Hartigan, 2009](#)), the extraction of material can probably be obtained in another way, as studied by [Hernández et al. \(2014\)](#), from a completely hydrodynamic mechanism based on latitudinal anisotropies in the density of a spherical cloud. In this work, a perturbative analysis of the hydrodynamic equations is made very close to the accreting object. The equations are solved considering an isothermal gas cloud, with a higher density at the equator than at the poles. This opens the possibility of studying various accretion configurations around massive objects, both in relativistic and non-relativistic cases. In the next section, we briefly discuss a new mechanism that relates the accretion phenomena with the ejection of material.

1.3 Choked accretion mechanism

Motivated by the work presented by [Hernández et al. \(2014\)](#), the main goal of this thesis is to present the development of an inflow-outflow model that we have called *choked accretion*. This model corresponds to an extension of Bondi's spherical accretion solution in which an axisymmetric, large-scale, small-amplitude deviation in the density field is introduced. The deviation consists of the inclusion of an equatorial-to-polar density contrast, in which the accreted material is more concentrated on an equatorial belt than on the polar regions.

The choked accretion mechanism shows how, by the inclusion of even a slight density gradient, a bipolar outflow is generated from the accreted material. This outflow is produced due to incapability of the central massive object to accrete at rates larger than a certain threshold, hence the incoming material chokes at a gravitational bottleneck, redirecting the excess flux throughout the polar regions, representing a direct relation between the accretion and ejection fluxes.

We study the choked accretion model in the non-relativistic and relativistic regimes, considering both rotating and non-rotating black holes. We analyse the behaviour of this mechanism by using both analytic steady-state models and full-hydrodynamic numerical simulations performed with the numerical code AZTEKAS, which is also presented as part of this work. In this thesis we present the three articles where we published our results, as well as discuss the astrophysical applicability of the model.

AZTEKAS: a GRHD numerical code

The equations that describe the gas dynamics in an astrophysical scenario are the Euler equations. They constitute a system of not closed hyperbolic partial differential equations that, in most cases, have no exact solutions. Usually, analytic solutions to these equations can be found in highly idealized cases, either by assuming some kind of symmetry or a self-similar problem (e.g., [Taylor, 1950](#); [Bondi, 1952](#)). However, in the general case where more complex scenarios are taken into account, these equations have to be solved numerically.

Numerical hydrodynamics and, in general, the study of hyperbolic partial differential equations, constitutes a full branch of physics. Some relevant introductory literature to this topic are the books by [Laney \(1998\)](#), [LeVeque \(2002\)](#) and [Toro \(2009\)](#). The continuous search for new and better algorithms to solve these set of equations has led to the development of robust and more accurate computational codes. These have been used to test and further extend theoretical models that continuously enrich our understanding of the Universe.

In the special case of hydrodynamics, one of the first numerical codes to be extensively used for astrophysical hydrodynamics is the ZEUS code ([Stone & Norman, 1992](#)), which uses a finite difference scheme for the discretization of the differential equations. Even more, ZEUS has a GNU Public Licence (GPL) for its distribution which through the years has made it a starting point for many researchers. Nowadays more accurate and efficient numerical methods have been developed, reducing computational costs and leading to the development of a wide variety of hydrodynamic numerical codes. Some examples of hydrodynamic Eulerian¹ codes are the [Yguazú \(Raga et al., 2000\)](#) and [GUACHO \(Esquivel et al., 2009\)](#) for non-relativistic hydrodynamics, the [Mezcal \(De Colle et al., 2012\)](#), [PLUTO \(Mignone et al., 2007\)](#) and [FLASH \(Fryxell et al., 2000\)](#) for the non-relativistic and special-relativistic regimes, as well as [CAFE \(Lora-Clavijo et al., 2015\)](#) [Athena++ \(Stone et](#)

¹Another approach to solve the hydrodynamic equations are the Lagrangian algorithms used in the *smoothed particle hydrodynamics* codes (e.g. [Price et al., 2018](#)), which are not addressed in this work.

al., 2008, 2020) and **HARM** (Gammie et al., 2003) for the general relativistic regime.

In this chapter, we are not aiming at presenting a new and different, state-of-the-art code. Our intention is to present and validate our free software (open source, open access) **AZTEKAS**: a general relativistic hydrodynamic code written in C and parallelized using shared memory with OpenMP. Moreover, we present an overview of the most relevant methods and algorithms used in our code, as well as several standard benchmark tests for validation in both relativistic and non-relativistic regimes. This code was first used in the article Aguayo-Ortiz et al. (2018), and is the one used for all the numerical analysis performed for this thesis.

2.1 AZTEKAS: numerical methods

In this section, we are going to briefly discuss the methods and numerical algorithms used in AZTEKAS to solve the hydrodynamic equations, which constitute a system of hyperbolic partial differential equations. We show here the discretization schemes, interpolation methods and integration techniques implemented in our code.

2.1.1 Finite volume method

The system of partial differential equations in hydrodynamics, conforms a set of hyperbolic equations (see LeVeque, 2002). These equations can be written in a fully conservative (with no source terms) or balanced (with source terms) form as:

$$\frac{\partial \mathbf{q}(\mathbf{u})}{\partial t} + \frac{\partial \mathbf{f}^i(\mathbf{u})}{\partial x^i} = \mathbf{s}(\mathbf{u}), \quad (2.1)$$

where \mathbf{q} are the conservative variables, $\mathbf{f}^i = (\mathbf{f}^1, \mathbf{f}^2, \mathbf{f}^3)^2$ are the fluxes of the conservative variables along the three spatial dimensions and \mathbf{s} are the source terms related to external forces, energy sinks or geometrical effects. The vector \mathbf{u} represents the primitive variables of the problem. Each one of these variables is a set of m quantities, where m is the number of equations. Finding the solution to this system of equations means to find $\mathbf{u}(t, \bar{x})$. In order to numerically integrate equations (2.1), the finite volume method (FVM) discretization is obtained in the following way.

Let us begin by considering a three-dimensional domain described in Cartesian coordinates³. This domain is then divided into a grid of $N_x \times N_y \times N_z$ cells (or control volumes), centred at $\bar{x}_{i,j,k} = (x_i, y_j, z_k)$, where the subindices $0 \leq i < N_x$, $0 \leq j \leq N_y$ and $0 \leq k \leq N_z$, represent the i -th, j -th and k -th position on the grid along each direction. Every cell has a volume $\Delta V = \Delta x \times \Delta y \times \Delta z$, meaning that the cell interfaces along, for example, the x direction, are defined at $x_{i\pm 1/2} = x_i \pm \Delta x/2$. Note that by using this definition of ΔV , we are assuming an uniform discretization.

²Note that the super index i represent an implicit summation.

³The specific case in cylindrical and spherical coordinates is discussed in the following sections.

By integrating equation (2.1) over a control volume, we can obtain its semi-discrete form for the FVM (cf. [LeVeque, 2002](#); [Toro, 2009](#)):

$$\begin{aligned} \frac{d\mathbf{Q}_{i,j,k}}{dt} = & -\frac{1}{\Delta x} [\mathbf{F}_{i+1/2,j,k}^x - \mathbf{F}_{i-1/2,j,k}^x] - \frac{1}{\Delta y} [\mathbf{F}_{i,j+1/2,k}^y - \mathbf{F}_{i,j-1/2,k}^y] \\ & - \frac{1}{\Delta z} [\mathbf{F}_{i,j,k+1/2}^z - \mathbf{F}_{i,j,k-1/2}^z] + \mathbf{S}_{i,j,k}, \end{aligned} \quad (2.2)$$

where we have defined the cell average of \mathbf{q} and \mathbf{s} as

$$\mathbf{Q}_{i,j,k} := \frac{1}{\Delta V} \int_{x_{i-1/2}}^{x_{i+1/2}} \int_{y_{j-1/2}}^{y_{j+1/2}} \int_{z_{k-1/2}}^{z_{k+1/2}} \mathbf{q}(t, \bar{x}) dV, \quad (2.3)$$

$$\mathbf{S}_{i,j,k} := \frac{1}{\Delta V} \int_{x_{i-1/2}}^{x_{i+1/2}} \int_{y_{j-1/2}}^{y_{j+1/2}} \int_{z_{k-1/2}}^{z_{k+1/2}} \mathbf{s}(t, \bar{x}) dV, \quad (2.4)$$

and the average flux across the cell interfaces as:

$$\begin{aligned} \mathbf{F}_{i\pm 1/2,j,k}^x &:= \frac{1}{\Delta S_{i\pm 1/2}} \int_{y_{j-1/2}}^{y_{j+1/2}} \int_{z_{k-1/2}}^{z_{k+1/2}} \mathbf{f}^x(t, \bar{x}_{i\pm 1/2,j,k}) dS_{i\pm 1/2}, \\ \mathbf{F}_{i,j\pm 1/2,k}^y &:= \frac{1}{\Delta S_{j\pm 1/2}} \int_{x_{i-1/2}}^{x_{i+1/2}} \int_{z_{k-1/2}}^{z_{k+1/2}} \mathbf{f}^y(t, \bar{x}_{i,j\pm 1/2,k}) dS_{j\pm 1/2}, \\ \mathbf{F}_{i,j,k\pm 1/2}^z &:= \frac{1}{\Delta S_{k\pm 1/2}} \int_{x_{i-1/2}}^{x_{i+1/2}} \int_{y_{j-1/2}}^{y_{j+1/2}} \mathbf{f}^z(t, \bar{x}_{i,j,k\pm 1/2}) dS_{k\pm 1/2}, \end{aligned} \quad (2.5)$$

where $\Delta S_{\{i,j,k\}\pm 1/2}$ is the surface normal to $\mathbf{f}^{\{x,y,z\}}$ at $x_{i\pm 1/2}$, $y_{j\pm 1/2}$ and $z_{k\pm 1/2}$, respectively. In the particular case of Cartesian coordinates, $\Delta S_{i\pm 1/2} = \Delta y \times \Delta z$, for example.

The average quantities $\mathbf{Q}_{i,j,k}$ and $\mathbf{S}_{i,j,k}$ may be approximated in a simple way as the value of \mathbf{q} and \mathbf{s} at the centre of the cell ([LeVeque, 2002](#)). The numerical fluxes \mathbf{F}^i , on the other hand, are defined at the boundaries of each control volume, so their evaluation must depend on the values of \mathbf{Q} on each side of the interface in which they are defined.

2.1.2 Approximate Riemann solver

In order to compute the fluxes across the cell interfaces, it is common to use a Godunov-type method ([Godunov, 1959](#)), which approximates the fluxes by using the information of the conservative variables in a cell and its neighbours. These methods consist in solving a local Riemann problem at each cell interface.

The Riemann problem consists of an initial data of two constant states divided by an interface. For most hyperbolic systems, this problem can be solved exactly

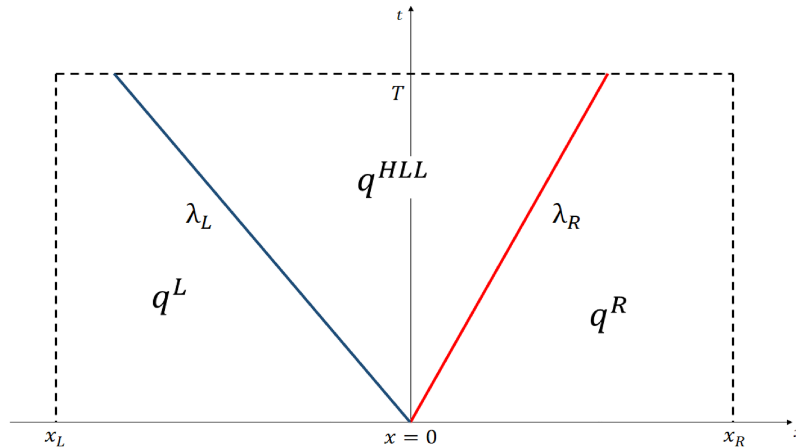


Figure 2.1: Schematic representation of the evolution at the interface of a 1D solution in an interface of a Riemann problem using the HLL scheme. Figure taken from [Aguayo-Ortiz et al. \(2018\)](#).

by analysing the evolution of the solution along the characteristics⁴ of the equation (see [Toro, 2009](#)). If we consider a Riemann problem on the boundary between the contiguous cells at a time t_n , it is possible to solve the problem in an exact or approximate form and, from this, obtain an expression for the numerical fluxes. This kind of algorithms are called *Riemann solvers*, and are one of the most commonly used techniques for the so-called *high resolution shock capturing* (HRSC) methods. Some of the most commonly used algorithms are the HLL ([Harten et al., 1983](#)) which gives a simple, two-characteristic velocity description of the evolution of the problem at the interface (see Figure 2.1); HLLE ([Einfeldt, 1988](#)) which extends the HLL method to the relativistic case and HLLC ([Toro et al., 1994](#)), which uses two extra characteristic velocities for the propagation of the solution.

In AZTEKAS, the main Riemann solver used, for both the non-relativistic and relativistic versions, is the HLLE formula ([Harten et al., 1983](#); [Einfeldt, 1988](#)):

$$\mathbf{F} = \begin{cases} \mathbf{f}^L & \text{if } \lambda_L \geq 0, \\ \frac{\lambda_R \mathbf{f}^L - \lambda_L \mathbf{f}^R + \lambda_L \lambda_R (\mathbf{q}^R - \mathbf{q}^L)}{\lambda_R - \lambda_L} & \text{if } \lambda_L < 0 < \lambda_R, \\ \mathbf{f}^R & \text{if } \lambda_R \leq 0, \end{cases} \quad (2.6)$$

where $\mathbf{f}^{\{L,R\}}$ and $\mathbf{q}^{\{L,R\}}$ are the fluxes and conservative variables of the left and right states in the Riemann problem set at the interface between two contiguous cells. This means that, for each control volume, there are two Riemann problems along each direction, one at each boundary.

The values λ_L and λ_R represent the characteristics with the larger velocity going to the left and to the right, respectively. These quantities are determined by obtaining

⁴The characteristics, or characteristic curves, are curves along which the equation simplifies in some particular manner ([LeVeque, 2002](#)). For example, in the case of a conservative equation (2.1), along these curves the conservative variables \mathbf{q} remain constant in time.

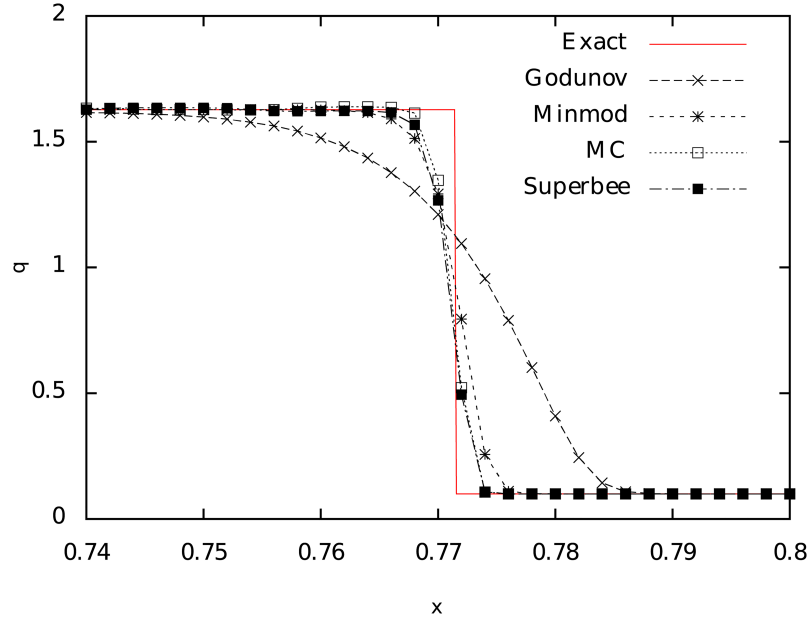


Figure 2.2: Comparison between the piecewise linear reconstructions (Minmod, MC and Superbee) against the piecewise constant one (Godunov). Figure taken from [Aguayo-Ortiz et al. \(2018\)](#).

the eigenvalues of the Jacobian matrix $\mathcal{B} = \partial \mathbf{f} / \partial \mathbf{q}$. This scheme turns out to be second order accurate over smooth solutions, but first-order near discontinuities like shock waves ([Toro, 2009](#)).

The advantage of the HLLE scheme is that, in order to obtain the fluxes, only the eigenvalues of the matrix \mathcal{B} are needed, unlike other methods like the Marquina ([Marquina, 1994](#)) or the Roe ([Roe, 1981](#)) approximate Riemann solvers, for which the eigenvectors are also needed. The disadvantage of the HLLE method is its dissipative nature, the reason why it does not properly resolve contact discontinuities. To solve this problem, another characteristic velocity based method named HLLC has been developed for both HD (see [Toro et al., 1994](#)) and RHD (see [Mignone & Bodo, 2005](#)). HLLC considers two additional characteristic velocities to solve the Riemann problem, and hence is less dissipative than HLLE and better resolves the contact discontinuities, when present. Both algorithms for the HD case are included in AZTEKAS.

2.1.3 Polynomial spatial reconstruction schemes

In a piecewise-constant representation of the primitive variables at the grid cells, as the one assumed in the approximate Riemann solver presented above, any information about the behaviour of the quantities inside the numerical cell is lost ([Rezzolla & Zanotti, 2013](#)). This can be solved by using spatial reconstruction techniques, which also improve the spatial accuracy of the numerical method. As [Del Zanna](#)

& Bucciantini (2002) pointed out, when discontinuous solutions are of main interest, second-order total variation diminishing (TVD) schemes, coupled with Riemann solvers, are probably the best choice for obtaining sharp resolution of discontinuities. In order to do this, we implement in AZTEKAS different types of spatial reconstruction schemes for the primitive variables. We use the Minmod (Roe, 1986), MC (van Leer, 1977) and Superbee (Roe, 1986) linear reconstructions, which are second-order methods. In Figure 2.2, we show a comparison of the capture of a shock wave using the linear reconstructors mentioned before, against the piecewise constant (Godunov) one. We can see how the discontinuity is better resolved by using any of the linear approximations rather than the zero-order reconstruction. We also implement a fifth-order weighted essentially non-oscillatory (WENO5) scheme (Titarev & Toro, 2004), which uses a different approach for the reconstruction that leads to a better capture of discontinuities and non-linear effects (see Lora-Clavijo et al., 2015).

It is not necessary to compute the spatial reconstruction of \mathbf{u} over all the cell. The only values required in order to compute the fluxes via a Riemann solver are the ones that rely on the interfaces between contiguous control volumes. For each boundary, there have to be estimated the *left* and *right* points that generate the states of the Riemann problem.

2.1.4 Time integration

For temporal integration, we can write the FVM semi-discrete equation (2.2) as:

$$\frac{d\mathbf{Q}_{i,j,k}}{dt} = \mathcal{R}(\mathbf{Q}), \quad (2.7)$$

where $\mathcal{R}(\mathbf{Q})$ is the right-hand side of equation (2.2). In this way, dividing the time interval into subintervals $[t_n, t_{n+1}]$, we can use an explicit time variation diminishing Runge-Kutta method (Shu & Osher, 1988), to integrate over time. In AZTEKAS, we have implemented the second order:

$$\begin{aligned} \mathbf{Q}_{i,j,k}^* &= \mathbf{Q}_{i,j,k}^n + \Delta t \mathcal{R}(\mathbf{Q}^n), \\ \mathbf{Q}_{i,j,k}^{n+1} &= \frac{1}{2} (\mathbf{Q}_{i,j,k}^n + \mathbf{Q}_{i,j,k}^* + \Delta t \mathcal{R}(\mathbf{Q}^*)), \end{aligned} \quad (2.8)$$

and the third order schemes:

$$\begin{aligned} \mathbf{Q}_{i,j,k}^* &= \mathbf{Q}_{i,j,k}^n + \Delta t \mathcal{R}(\mathbf{Q}^n), \\ \mathbf{Q}_{i,j,k}^{**} &= \frac{1}{4} (3\mathbf{Q}_{i,j,k}^n + \mathbf{Q}_{i,j,k}^* + \Delta t \mathcal{R}(\mathbf{Q}^*)), \\ \mathbf{Q}_{i,j,k}^{n+1} &= \frac{1}{3} (3\mathbf{Q}_{i,j,k}^n + 2\mathbf{Q}_{i,j,k}^{**} + 2\Delta t \mathcal{R}(\mathbf{Q}^{**})), \end{aligned} \quad (2.9)$$

where Δt is the time-step, that is usually computed using the standard CFL criterion (Courant et al., 1928) formula:

$$\Delta t = \mathcal{C} \times \min \left(\frac{\Delta x}{\max(|\lambda_{\pm}^x|)}, \frac{\Delta y}{\max(|\lambda_{\pm}^y|)}, \frac{\Delta z}{\max(|\lambda_{\pm}^z|)} \right), \quad (2.10)$$

where $\max(|\lambda_{\pm}|)$ are the maximum absolute value of the characteristic velocities along each direction and \mathcal{C} is the Courant number, which has a typical value less than 1.

2.1.5 Primitive variable recovery

After the temporal evolution of the conservative variables for one time step, updated values for the primitive variables need to be recovered. This step depends on the functional form of \mathbf{q} and on whether it is possible to obtain $\mathbf{u}(\mathbf{q})$ analytically. In case there is not an analytic recovery of the primitive variables, like in the relativistic hydrodynamics case, a transcendental algebraic equation has to be solved (Riccardi & Durante, 2008).

As a different approach to overcome this, sometimes, thorny step, we developed, along with AZTEKAS, the Primitive Variable Recovery Scheme (PVRS) (see Aguayo-Ortiz et al., 2018), in which a direct time integration over the primitive variables is performed. The semi-discrete form of the PVRS is written as:

$$\begin{aligned} \frac{d\mathbf{U}_{i,j,k}}{dt} = & -\frac{1}{\Delta x} \mathcal{A}_{i,j,k} \cdot [\mathbf{F}_{i+1/2,j,k}^x - \mathbf{F}_{i-1/2,j,k}^x] \\ & -\frac{1}{\Delta y} \mathcal{A}_{i,j,k} \cdot [\mathbf{F}_{i,j+1/2,k}^y - \mathbf{F}_{i,j-1/2,k}^y] \\ & -\frac{1}{\Delta z} \mathcal{A}_{i,j,k}^n \cdot [\mathbf{F}_{i,j,k+1/2}^z - \mathbf{F}_{i,j,k-1/2}^z] \\ & + \mathcal{A}_{i,j,k} \cdot \mathbf{S}_{i,j,k} := \mathcal{R}(\mathbf{U}), \end{aligned} \quad (2.11)$$

where $\mathbf{U}_{i,j,k}$ is the cell average value of the primitive variables \mathbf{u} , $\mathcal{A}_{i,j,k} := (\partial\mathbf{q}/\partial\mathbf{u})^{-1}$ and where the numerical fluxes \mathbf{F} may be computed using an approximate Riemann solver. This algorithm is also implemented as an alternative scheme in AZTEKAS and is used for some numerical tests presented in this work.

2.1.6 Ghost cells

In order to implement the boundary conditions, it is necessary to extend the numerical domain further away from the original region of interest. These extended cells are often referred to as *ghost cells* (see LeVeque, 2002). The number of ghost cells needed for a problem depends on the stencil used to reconstruct the primitive variables. For example, for linear reconstructions as Minmod or MC, only 1 ghost cell is needed for the boundary conditions, but for a WENO5 reconstruction, which uses three stencils of three cells each, at least three ghost cells are needed in order to implement the boundary conditions.

2.2 AZTEKAS-HD: non-relativistic hydrodynamics

2.2.1 Euler equations

The Euler equations in the non-relativistic regime can be written in a balanced form, and using general curvilinear coordinates, as:

$$\frac{\partial \rho}{\partial t} + \nabla_j (\rho u^j) = 0, \quad (2.12a)$$

$$\frac{\partial E}{\partial t} + \nabla_j (u^j [E + P]) = \Gamma - \Lambda + f_j u^j, \quad (2.12b)$$

$$\frac{\partial (\rho u^i)}{\partial t} + \nabla_j (\rho u^i u^j) + \nabla^i P = f^i, \quad (2.12c)$$

where $\nabla^i = \gamma^{ij} \nabla_j$ is the three-dimensional covariant derivative, γ^{ij} is the inverse three-dimensional metric tensor⁵, ρ is the mass density, P is the pressure, E is the total energy density and u^i is the velocity vector defined in a non-unitary basis. $\Gamma - \Lambda$ represents the net energy gain/loss per unit volume, and f^i are the external forces per unit of mass acting on the fluid, such as gravity. In all the simulations presented in this work, we assume that the gains or losses in energy due to external factors are balanced ($\Gamma - \Lambda = 0$), in particular, we assume $\Gamma = \Lambda = 0$, and hence, the fluid is assumed to be adiabatic. Note also that we are using the Einstein's index notation, so the indices $\{i, j, k\}$ are no longer referring to locations on a grid cell, but directions in space. The velocity vector is defined as

$$u^i = \frac{dx^i}{dt}. \quad (2.13)$$

We can define the unit velocity vector as

$$v^i = \sqrt{\gamma_{(ii)}} u^i, \quad (2.14)$$

where $\gamma_{(ii)}$ are the diagonal components of the three-dimensional metric and the parenthesis in the indices implies that no Einstein summation is assumed.

The gradient of the pressure $\nabla^i P$ can be written, using the definition of covariant derivative, as

$$\nabla^i P = \gamma^{ij} \nabla_j P = \nabla_j (\gamma^{ij} P), \quad (2.15)$$

which can be added to the $\nabla_j (\rho u^i u^j)$ term.

On the other hand, the divergence terms can be expanded using the Christoffel symbols as

$$\nabla_j (\rho u^j) = \frac{1}{\sqrt{\gamma}} \frac{\partial}{\partial x^j} (\sqrt{\gamma} \rho u^j), \quad (2.16a)$$

⁵In this case, the three-dimensional metric correspond to a flat space but in arbitrary coordinates.

$$\nabla_j (\rho u^i u^j + \gamma^{ij} P) = \frac{1}{\sqrt{\gamma}} \frac{\partial}{\partial x^j} (\sqrt{\gamma} [\rho u^i u^j + \gamma^{ij} P]) + \Gamma_{ab}^i \rho u^a u^b, \quad (2.16b)$$

where $\gamma = \det(\gamma_{ij})$. In this way, the non-relativistic Euler equations can be written in general curvilinear coordinates as

$$\frac{\partial \rho}{\partial t} + \frac{1}{\sqrt{\gamma}} \frac{\partial}{\partial x^j} (\sqrt{\gamma} \rho u^j) = 0, \quad (2.17a)$$

$$\frac{\partial E}{\partial t} + \frac{1}{\sqrt{\gamma}} \frac{\partial}{\partial x^j} (\sqrt{\gamma} u^j [E + P]) = f_j u^j, \quad (2.17b)$$

$$\frac{\partial}{\partial t} (\rho u^i) + \frac{1}{\sqrt{\gamma}} \frac{\partial}{\partial x^j} (\sqrt{\gamma} [\rho u^i u^j + \gamma^{ij} P]) = \Gamma_{ab}^i \rho u^a u^b + f^i, \quad (2.17c)$$

These equations constitute a set of five hyperbolic partial differential equations with six variables (ρ, P, E, u^i) . In order to close the system, we need an equation that relates all the thermodynamical variables. In general,

$$E = \frac{1}{2} (u_j u^j) + \rho \epsilon, \quad (2.18)$$

where we have defined $u_i = \gamma_{ij} u^j$ and ϵ is the specific internal energy of the fluid, which follows an equation of state (EoS) of the form $\epsilon = \epsilon(\rho, P)$. For AZTEKAS, we have adopted an ideal gas equation of state:

$$P = \frac{\rho k_B T}{\bar{m}}, \quad (2.19)$$

where k_B is the Boltzmann constant, \bar{m} is the average mass of a fluid particle and T is the gas temperature. In order to describe a wide variety of thermodynamical processes in the gas, we use the polytropic relation

$$P = K \rho^\kappa, \quad (2.20)$$

where K is a constant and κ is the polytropic index. With this equation it is possible to describe different kinds of thermodynamical processes by varying a single parameter. For example, $\kappa = 1$, following the ideal gas EoS, describes an isothermal process. On the other hand, if $\kappa = c_P/c_V$, where c_P/c_V is the ratio between the heat capacity at constant pressure and the heat capacity at constant volume, describes an isentropic process, which corresponds to a reversible, adiabatic process in which the gas does not exchange heat with its surroundings. This ratio is often referred to as the adiabatic index γ .

By assuming an ideal gas EoS, we can write the internal energy per unit mass as

$$\epsilon = \frac{P}{\rho(\gamma - 1)}. \quad (2.21)$$

The adiabatic index γ depends on the nature of the gas itself, which allow us to study different types of gasses. For example, $\gamma = 5/3$ describes a monoatomic, $\gamma = 7/5$ a diatomic gas and $\gamma = 4/3$ an ultra-relativistic monoatomic gas.

The polytropic equation (2.20) can be used to replace the energy equation (2.17b) in cases where no shocks are developed. Nevertheless, in AZTEKAS we only use this relation explicitly to define the value of the pressure at both initial and boundary conditions, and evolve the whole system of equations numerically.

More realistic both analytic and numerical EoS have been developed to study a relativistic monoatomic gas (cf. [Synge, 1957](#), which is also implemented in AZTEKAS) or more complex systems like neutron stars (cf. [Zhu et al., 2018](#)), nevertheless the polytropic gas approximation results useful to describe many astrophysical phenomena.

2.2.2 HD in balanced form

The Euler equations are written in balanced form as:

$$\frac{\partial(\mathbf{Q}(\mathbf{u}))}{\partial t} + \frac{1}{\sqrt{\gamma}} \frac{\partial(\sqrt{\gamma}\mathbf{F}^i(\mathbf{u}))}{\partial x^i} = \mathbf{S}(\mathbf{u}), \quad (2.22)$$

where the primitive and conservative variables, as well as the fluxes and source terms for this system are:

$$\mathbf{u} = (\rho, P, u^i), \quad (2.23)$$

$$\mathbf{Q} = (\rho, E, \rho u^i), \quad (2.24)$$

$$\mathbf{F}^j = (\rho u^j, [E + P]u^j, \rho u^i u^j + \gamma^{ij}P), \quad (2.25)$$

$$\mathbf{S} = (0, f_j u^j, \Gamma_{ab}^i \rho u^a u^b + f^i). \quad (2.26)$$

2.3 AZTEKAS-HD: code validation

In this section we present a number of HD numerical tests and comparisons with analytic solutions in the non-relativistic regime. All simulations presented here were computed using a second order Runge-Kutta method. The specific flux calculation, Courant number, primitive variable reconstruction and recovery scheme will be specified for each test.

2.3.1 Shock tube

One dimensional shock tube

The shock tube test, first presented by [Sod \(1978\)](#), consists of a Riemann problem along the entire integration domain. The 1D problem in Cartesian coordinates has an exact solution which is presented, for the non-relativistic case, by [Toro \(2009\)](#).

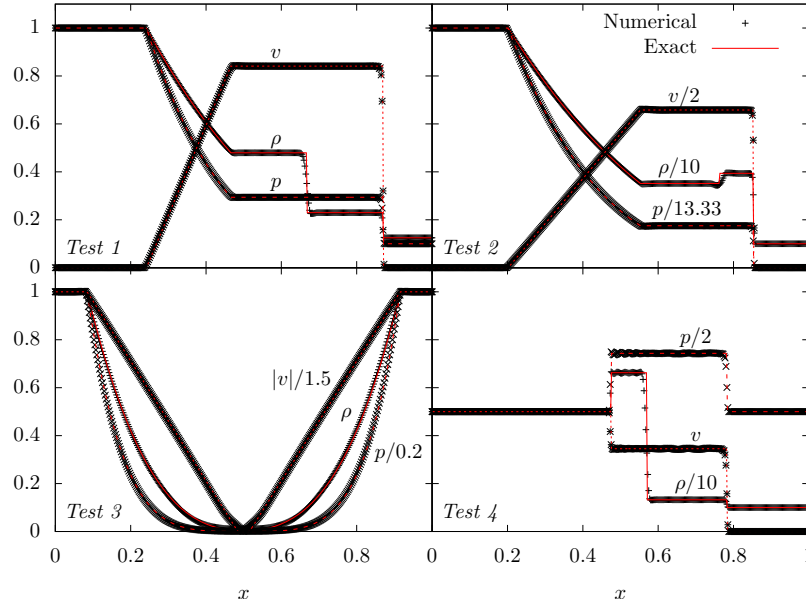


Figure 2.3: Results of the 1D shock tube tests for the four sets of initial conditions listed in Table 2.1. Each panel corresponds to a different test and compares the density, pressure and velocity as obtained numerically against their corresponding analytic values (Toro, 2009). In all cases the resolution is $N = 400$ and the evolution time is $t = 0.2$.

The numerical solution was computed for various tests, changing the initial density, pressure and velocity. All the results presented for the shock tube test use the HLLE formula, an MC limiter for the linear reconstruction of the primitive variables, a domain $[0,1]$ with $N = 400$ identical cells, and a Courant number of 0.9. The initial discontinuity is placed at $x = 0.5$. Unless specified otherwise, all simulations were performed using the classical primitive variable recovery, this is, \mathbf{u} is recovered directly from \mathbf{q} .

In Table 2.1 we show the initial parameters for the left ($x < 0.5$) and right ($x \geq$

Table 2.1: Initial parameters for the four tests of the 1D shock tube problem. The labels L and R represent the initial left and right states, respectively.

Parameters	Test 1	Test 2	Test 3	Test 4
ρ_L	1.0	10.0	1.0	5.0
p_L	1.0	13.33	0.2	1.0
v_L	0.0	0.0	-1.5	0.5
ρ_R	0.125	1.0	1.0	1.0
p_R	0.1	0.01	0.2	1.0
v_R	0.0	0.0	1.5	0.0
γ	5/3	5/3	5/3	1.4

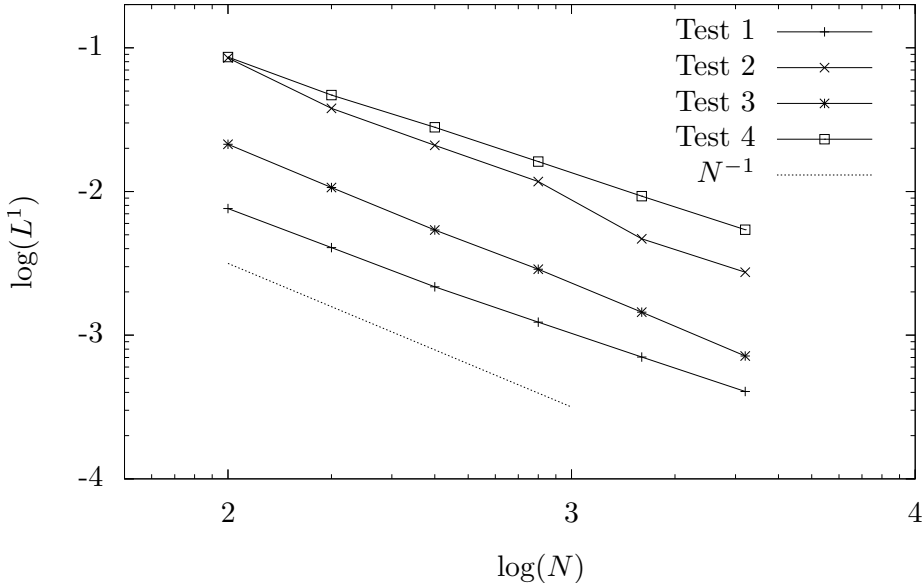


Figure 2.4: L^1 – norm of the error in the density versus the resolution N for all tests presented in Table 2.1. With a dotted line, for comparison, we present the slope of a first order convergence.

0.5) states of the shock tube problem. These tests were selected in order to obtain different kinds of intermediate states. In Test 1 and 2 two different types of working surfaces with a rarefaction wave are created. In Test 3 two rarefaction waves induce a lower density zone and in Test 4 a strong shock without a rarefaction wave is formed. The boundary conditions are set as free outflow in both directions by copying the value of the last evolved cell onto the adjacent ghost cells (zero order extrapolation).

In Figure 2.3 we show the density, pressure and velocity at the time $t = 0.2$ for the four tests. The figure shows the results of the numerical simulations compared against the corresponding exact, analytic values (Toro, 2009). As can be seen from this figure, for all cases there is a good agreement between the numerical and the analytic solutions all over the domain.

In order to determine the convergence rate of the code, we repeated the same four tests presented in Table 2.1, using six different resolutions $N_1 = 100$, $N_2 = 200$, $N_3 = 400$, $N_4 = 800$, $N_5 = 1600$ and $N_6 = 3200$. We then compute the L^1 -norm of the error between the numerical and analytical solutions:

$$L^1\text{-norm} = \frac{1}{N} \sum_{i=0}^N |\rho_n - \rho_e|, \quad (2.27)$$

where ρ_n and ρ_e are the numerical and exact values of the density.

The L^1 -norm is a natural metric for measuring the absolute difference between the components of two vectors; in this case, between each point of our simulation with its corresponding one in the analytic solution. In Figure 2.4 we show the L^1 -

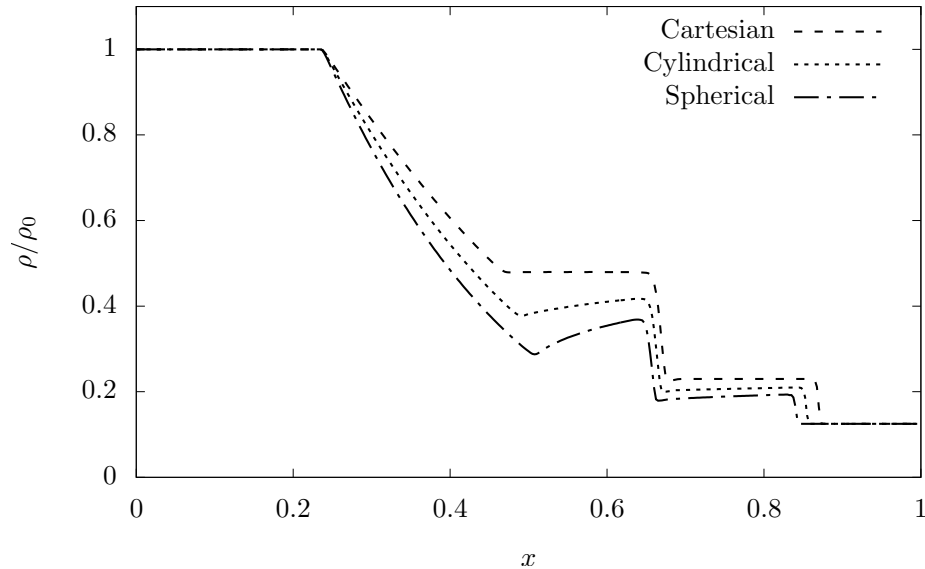


Figure 2.5: Comparison of the density profile in Cartesian, cylindrical and spherical coordinates for the Test 1 in Table 2.1.

norm of the difference between the analytic and numerical solutions. As expected due to the presence of discontinuities, the order of convergence is ~ 1 for all tests.

Shock tube test in cylindrical and spherical coordinates

In addition to Cartesian coordinates, we have also implemented within AZTEKAS the use of cylindrical and spherical coordinate systems. Here we present the results of the 1D shock tube test for these geometries. Each coordinate system represents a different shock tube problem, so we should expect to get different results. This kind of tests have been presented by other authors (eg. [Radice & Rezzolla, 2012](#); [Lora-Clavijo et al., 2015](#)), although it is not commonly considered as part of a test suite because there are no known analytic solutions to this problem in cylindrical and spherical geometries. All simulations for this case were done with the HLLE flux calculator, the MC reconstruction, the standard primitive variable recovery and a grid of $N = 400$ points.

In Figure 2.5 we show the results of the density for the cylindrical and spherical versions of Test 1 in Table 2.1 at $t = 0.25$. For comparison, we also show in this figure the result obtained with Cartesian coordinates discussed in the previous Subsection. As can be seen, due to the geometrical source terms in the balanced equations, the form of the density profile shows a notable difference between the different geometries. These results show that the choice of coordinate system is really important, giving substantial differences in the resulting simulations.

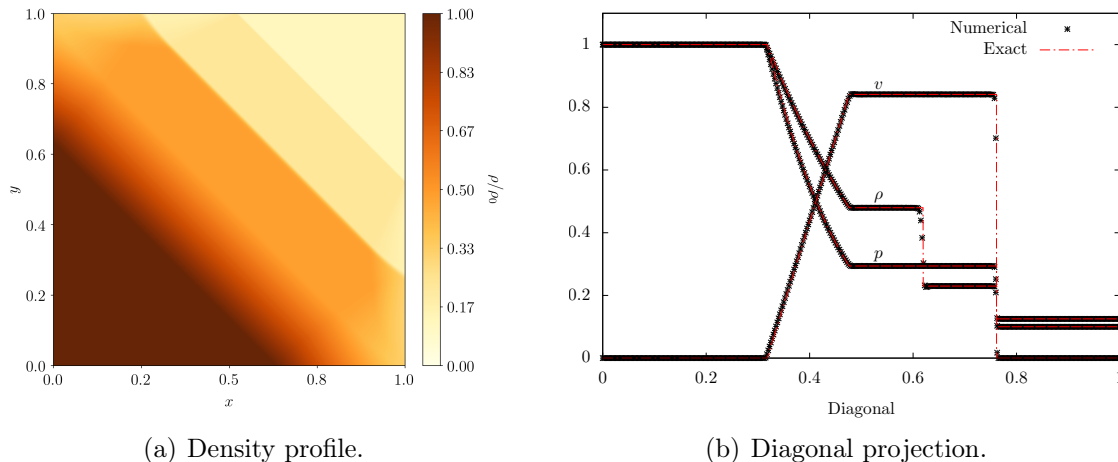


Figure 2.6: *Left panel:* Density profile of the evolution of Test 1 with an interface located at $x + y = 1$ at time $t = 0.2$. *Right panel:* Density, pressure and velocity profile along the diagonal $x = y$ compared with the exact solution (Marti & Muller, 1994).

Two-dimensional shock tube

We performed the shock tube problem for one of the tests of Table 2.1 along a diagonal in a 400×400 Cartesian grid in order to analyse the flux calculation along two dimensions simultaneously (see Lora-Clavijo et al., 2015, where a similar study was implemented for the relativistic case).

In Figure 2.6(a) we show the snapshot of the shock tube evolution at time $t = 0.2$ for Test 1 of Table 2.1. We use the HLLC flux formula, the MC limiter and the standard primitive variable recovery. The left and right states are delimited by the diagonal $x + y = 1$. The boundary conditions were set as outflow in all directions. For this case we implemented a linear extrapolation to the ghost cells at the boundaries in order to avoid spurious reflections. Nevertheless, as can be seen from Figure 2.6(a), the solution still shows a problem at the boundaries, specifically close to the bottom-right and upper-left corners, where a small diminishing in the density is observed. It is likely that this is because the extrapolation was done independently for each direction. In Figure 2.6(b) we show the density, pressure and velocity profile along the diagonal $x = y$, and compare the numerical results against the analytic solution (Toro, 2009).

2.3.2 Double Mach reflection

The HRSC methods are designed not only for accurately tracking of the position and sharpness of discontinuities, like shock waves, but also to avoid spurious numerical

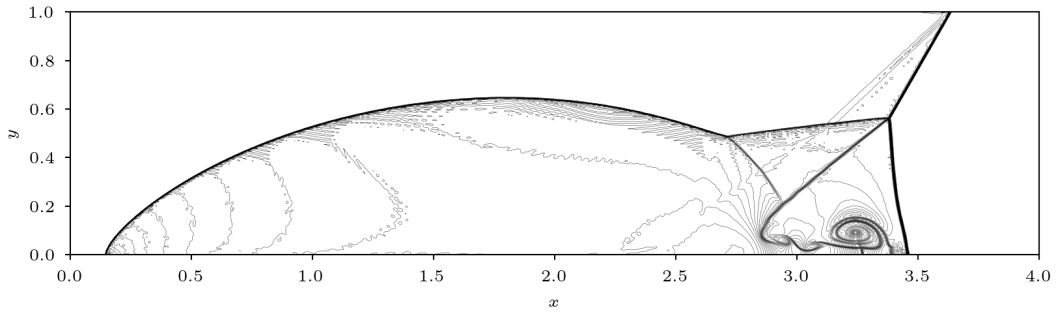


Figure 2.7: Contour density plot of the double Mach reflection test at time $t = 0.25$.

instabilities, as the *carbuncle instability* (Rodionov, 2018).⁶ This instability appears when a shock wave interacts with other shocks or reflecting walls, and it manifests as a growing protuberance ahead of the discontinuity. This spurious problem seems to appear when a less dissipative method is used in the simulation (Woodward & Colella, 1984).

The double Mach reflection test was first described by Woodward & Colella (1984), and it is part of some code test suites (e.g., the Athena++ code, Stone et al., 2008). The problem consists of a strong shock wave moving diagonally toward a reflecting wall. Although there is no analytic solution for this problem, it is a commonly used problem for testing that shocks propagate at the correct speed in all directions (avoid the carbuncle instability) and the proper reflective boundaries' implementation.

In order to test the stability of the solution, this test was performed using the WENO5 reconstructor and the HLLC flux calculator, which is a less dissipative method (compared with the HLL). We also performed a high resolution simulation on a Cartesian domain $[0, 4] \times [0, 1]$, with 1200×300 uniformly distributed grid cells. The fluid is described using an ideal gas EoS under an adiabatic process with index $\gamma = 1.4$. Finally, we use a standard primitive variable recovery and a fixed Courant number of 0.5.

The initial and boundary conditions closely follow those proposed by Stone et al. (2008). The domain was divided into a pre-shock and post-shock regions, delimited by a discontinuity that forms a 60° angle with the x -axis, intersecting it at $x_0 = 1/6$. The shock front moves diagonally towards the lower boundary with a Mach number of 10, so the initial conditions are

$$(\rho, p) = \begin{cases} (8, 116.5) & \text{if } x < x_0 + y/\sqrt{3} \\ (1.4, 1) & \text{if } x \geq x_0 + y/\sqrt{3}, \end{cases} \quad (2.28)$$

⁶Some authors (e.g. Moschetta et al., 2001) claim that, rather to be a numerical pathology, the carbuncle instability is intrinsically associated to the Euler equations.

with velocity components for the post-shock zone

$$\begin{aligned} v_x &= 8.5 \cos(30^\circ), \\ v_y &= -8.5 \sin(30^\circ), \end{aligned} \tag{2.29}$$

and the pre-shocked zone initially at rest.

We set free outflow conditions at the left and right boundaries and reflection at the lower boundary for $x > x_0$. For $x < x_0$ we fill the ghost cells with the values of the post-shock zone. For the upper boundary, we impose the ghost cells to follow the movement of the diagonal shock, so we set the pre-shock conditions for $x \geq x_s(t)$ and the post-shock conditions for $x < x_s(t)$ where

$$x_s(t) = x_0 + \frac{1 + 20t}{\sqrt{3}}, \tag{2.30}$$

is the position of the shock at the upper boundary. These initial conditions were taken from [Woodward & Colella \(1984\)](#).

In [Figure 2.7](#) we show the density contour levels of the double Mach reflection for a time $t = 0.25$. This result is qualitatively comparable with the one presented in other works (e.g [She-Ming Lau-Chapdelaine & Radulescu, 2016](#)): the contact surface curly jet, that appears along the reflecting wall, does not reach the shock front, avoiding the carbuncle instability (see [Kemm, 2015](#), for an example of the instability development, and further discussion on this topic).

2.3.3 Sedov-Taylor blast wave

The Sedov-Taylor blast wave ([Taylor, 1950](#); [Sedov, 1959](#)) consists of an intense explosion caused by an enormous amount of energy deposited in a small volume at the centre of the domain, which generates a strong spherically symmetric shock which propagates through a homogeneous medium.

This problem was studied by [Sedov \(1959\)](#), finding a self-similar solution in which the front shock radius expands in time as ([Sedov, 1959](#); [Landau, 1987](#)):

$$r(t) = \left(\frac{E_0}{\alpha \rho_0} \right)^{1/5} t^{2/5}, \tag{2.31}$$

where E_0 is the initial energy injected, ρ_0 is the background density and α is a constant that depends on the equation of state. This solution is relevant in astrophysics as it helps to understand the physics behind a supernovae explosion. The Sedov-Taylor blast wave is a commonly used benchmark test for hydrodynamic codes ([Tasker et al., 2008](#)).

Continuing with the 2D tests, for this simulation we implement a 2D spherically axisymmetric grid with 400×20 cells uniformly distributed over a $[0, 8] \times [0, \pi/2]$ domain. We use the HLLC flux calculator, the MC reconstructor and a Courant number of 0.25, as well as the standard primitive variable recovery. We set an initial

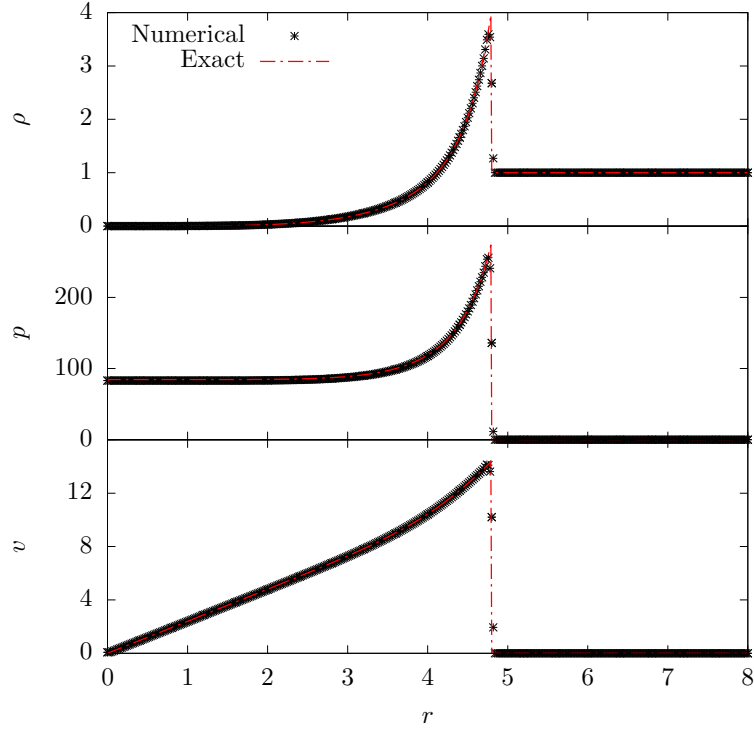


Figure 2.8: Comparison between numerical results and the analytic solution of the density, pressure and velocity for the 2D spherical axisymmetric simulation of the Sedov blast wave at time $t = 0.1$. We only plot the profiles along $\theta = \pi/4$ as no angular dependence was found.

explosion energy of $E_0 = 1.25 \times 10^5$ inside a radius r_0 that corresponds to 8 numerical cells near the origin. The initial pressure P_0 is computed using the ideal gas EoS and the polytropic relation for an adiabatic process ($\kappa = \gamma$) as

$$P_0 = \frac{3(\gamma - 1)E_0}{4\pi\rho_0 r_0^3}, \quad (2.32)$$

where the adiabatic index corresponds to a monoatomic gas ($\gamma = 5/3$). The gas is set initially at rest and $\rho_0 = 1$. The explosion shock front propagates through a uniform medium with $P_m = 10^{-5}$ and $\rho_m = \rho_0$.

In Figure 2.8 we show the density, pressure and velocity profiles of the Sedov explosion at $t = 0.1$ along the $\theta = \pi/4$ direction. For comparison, we also show the corresponding analytic solution (Kamm, 2000). As can be seen, there is a qualitatively good comparison between the numerical results and the analytic solution; the shock is well resolved, as expected for the HLLC Riemann solver.

In order to determine the convergence rate for this test, we repeated the simulation using different radial resolutions, maintaining the same number of cells along θ . We compute the L^1 -norm using the standard primitive variable recovery and the PVRS method (2.11). In Figure 2.9, we show that, for both methods, the order of

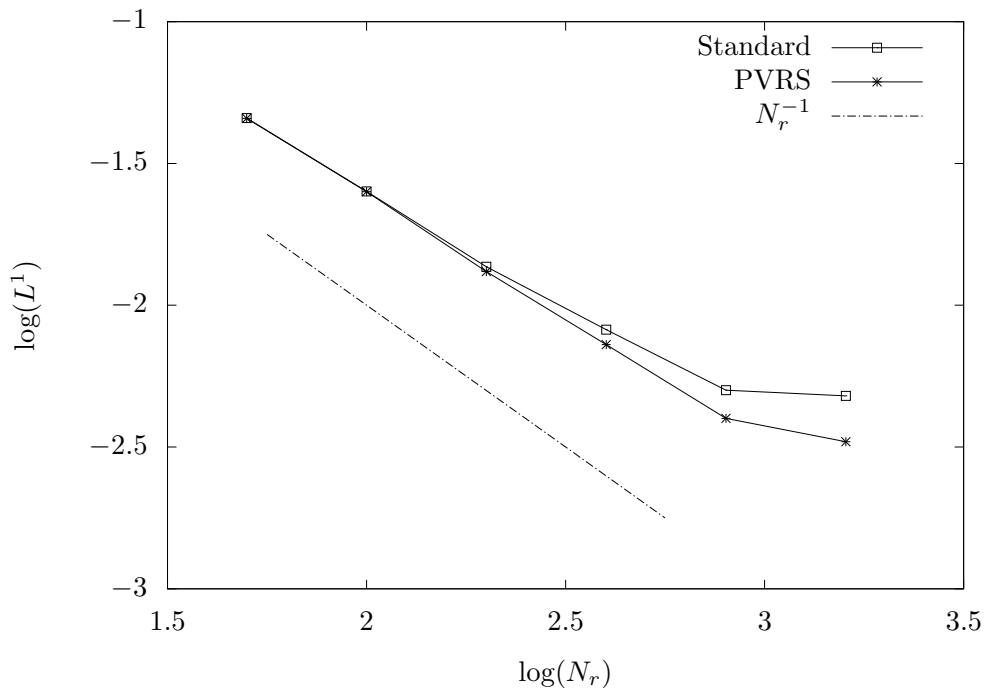


Figure 2.9: L^1 -norm of the error between the numerical and analytic solutions of the Sedov-Taylor blast wave for resolutions $N_r = 50, 100, 200, 400$ and 800 . We compare here the convergence for different schemes of primitive variable recovery: the standard way, recovering \mathbf{u} directly from \mathbf{q} , and the PVRS using direct integration over the primitive variables (2.11).

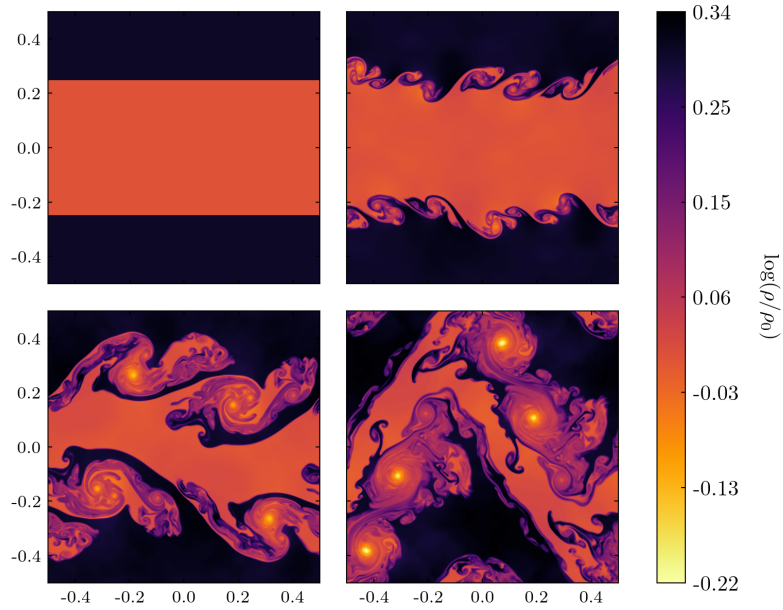


Figure 2.10: Onset of the Kelvin-Helmholtz instability. The panels show the time evolution of the density following a one-mode perturbation on the velocity field (see Eq 2.33). From top to bottom and left to right, the times are $t = 0.0, 1.5, 2.5$ and 3.5 , with an amplitude perturbation $\eta = 0.01$.

convergence is 1, which is expected due to the strong shock front. For a higher resolution, the convergence rate decreases in both cases: this is the result of the truncation error being dominated by the rounding error⁷.

2.3.4 Hydrodynamic instabilities

In astrophysics, the non-linear nature of the hydrodynamic equations is responsible for the turbulence observed in different scenarios like stellar atmospheres (see Jeffrey et al., 2018) or accretion disks (see Wienkers & Ogilvie, 2018). It is important for a code to be able to resolve the fine structure of the turbulence in a simulation, since it is in this zone where important physical process occur (eg. Duffell & Kasen, 2016). In this subsection we analyse the behaviour of AZTEKAS in the non-linear regime with two classical tests: the Kelvin-Helmholtz and the Rayleigh-Taylor instabilities (Chandrasekhar, 1981).

Kelvin-Helmholtz instability

The Kelvin-Helmholtz (KH) instability is the result of perturbing the interface between two fluids that are moving in opposite directions. This interaction drives the fluid to enter a non-linear regime where the turbulence starts to dominate.

The KH instability is a usual phenomenon in astrophysics. It appears at different scales in the Universe, from solar flares (Ruan et al., 2018) and molecular clouds (Pandey & Vladimirov, 2019), up to relativistic jets in active galactic nuclei (Perucho et al., 2006) and even at cosmological scales (Malik & Matravers, 2003).

This test was performed using the HLLC Riemann solver, the WENO5 primitive variable reconstructor, the standard primitive variable recovery, a Courant factor of 0.5 and an ideal gas under an adiabatic process with index $\gamma = 1.4$. We implemented a Cartesian square domain $[-0.5, 0.5] \times [-0.5, 0.5]$ with a uniformly distributed grid of 600×600 cells and periodic conditions for all boundaries.

We divided the domain into three zones with fluids moving in opposite directions along the x direction. The initial conditions were then set as

$$(\rho, p, v_x, v_y) = \begin{cases} (2, 2.5, 0.5v, \delta v) & \text{if } |y| \geq 0.25, \\ (1, 2.5, -0.5v, \delta v) & \text{if } |y| < 0.25, \end{cases} \quad (2.33)$$

where $v = 1 + \delta v$ and $\delta v = \eta \cos(2\pi x/L_x) \sin(2\pi y/L_y)$ is the perturbation, with η its amplitude that, in this case, was set to 0.01. $L_x = 1$ and $L_y = 1$ are the extensions of the domain along each direction. This corresponds to a one-mode perturbation for the velocity over the $x - y$ plane.

In Figure 2.10 we show the resulting time evolution in the density field at times $t = 0.5, 1, 1.5$ and 2. As can be seen from the bottom right panel of the figure, the upper eddies are exactly the same as the ones below, only inverted left to right, i.e. even though a full non-linear regime has been developed, the simulation keeps this symmetry at all times. The fact that there is a clear distinction between the high and low density regions shows the non-dissipative nature of the HLLC Riemann solver.

Rayleigh-Taylor instability

The Rayleigh-Taylor (RT) instability is the result of perturbing the interface between a high density fluid on the top of a low density fluid with a gravitational force pointing downward. This instability appears in astrophysical scenarios like supernovae where a dense shell, created by the explosion, is decelerated by the external medium and the gravity of the remnant star (Fraschetti et al., 2010). The turbulence generated has been shown to be an important mechanism from which the magnetic field is intensified and where the synchrotron radiation is obtained (Duffell & Kasen, 2016).

For this test we use an HLLC Riemann solver, a WENO5 reconstructor, a standard primitive variable recovery method (although we also use the PVRS scheme

⁷The truncation error is the difference between the exact solution and an approximation obtained with a given numerical method. The rounding error is due to the precision of the computer (LeVeque, 2002).

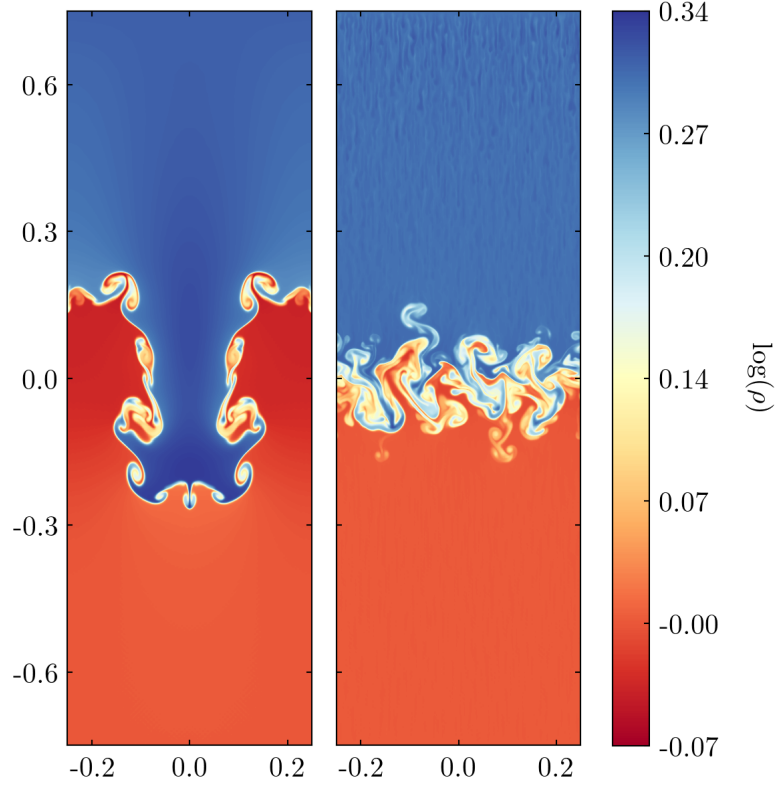


Figure 2.11: Rayleigh-Taylor instability of a one mode perturbation (left) with an amplitude $\eta = 0.01$, and a random perturbation of the same amplitude (right).

for comparison), a Courant factor of 0.5 and an ideal gas under an adiabatic process with index $\gamma = 1.4$. We set a 300×900 uniformly spaced grid in a rectangular domain $[-0.25, 0.25] \times [-0.75, 0.75]$, using periodic conditions in both x boundaries, and reflection in the y boundaries. We also implemented a uniform gravitational acceleration going downward $g = -1$ as a source term.

The domain was divided into two zones with different density fluids. The general initial conditions were set as

$$(\rho, p, v_x, v_y) = \begin{cases} (2.0, p_h, 0.0, \delta v) & \text{if } |y| \geq 0, \\ (1.0, p_h, 0.0, \delta v) & \text{if } |y| < 0, \end{cases} \quad (2.34)$$

where $p_h = 2.5 - \rho g y$, with $g = -1$ is the pressure a fluid in hydrostatic equilibrium, in order to balance the forces between pressure gradients and gravity. For the velocity fluctuation δv , we use a one mode perturbation of the form $-\eta(1 + \cos(2\pi x/L_x))(1 + \cos(2\pi y/L_y))/4$, similar to the one use for the KH instability, and a random perturbation.

In Figure 2.11 we show the density evolution of the RT instability at $t = 3.0$ for the one mode perturbation, with an amplitude $\eta = 0.01$ (left) and a random perturbation of the same amplitude (right). As can be seen in the left panel, the

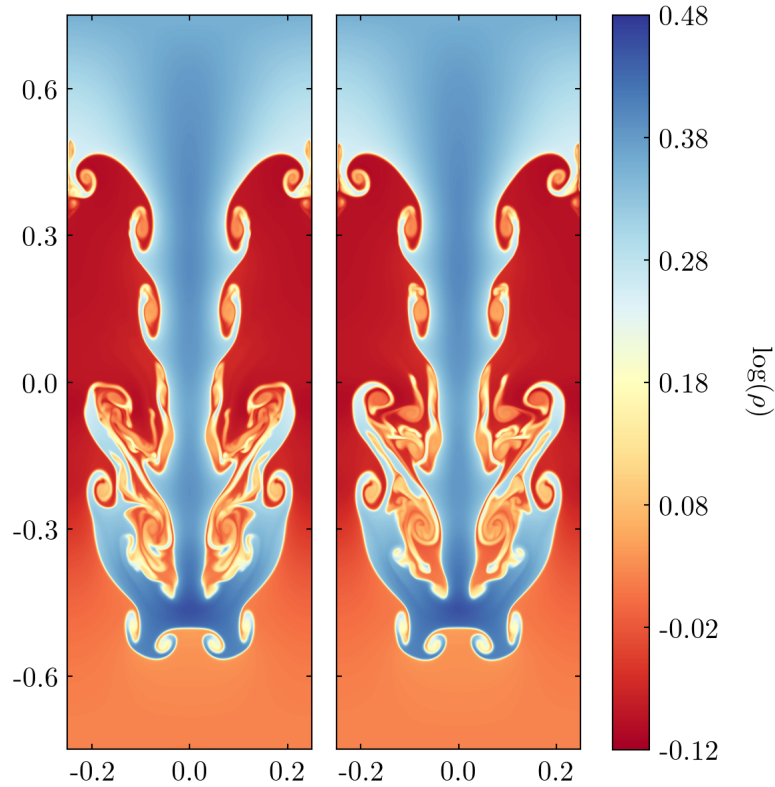


Figure 2.12: Comparison between the standard scheme (left) and the PVRS method (right) for the primitive variable recovery for a one mode perturbation with amplitude $\eta = 0.1$.

fluctuation at the interface, along with the constant gravitational field, leads the higher density fluid to stream down without mixing with the lower density one, even though, the KH instability shows up at the layer between both fluids. On the right panel, the random perturbation leads to a mixing that propagates more slowly. In both cases, the transition to non-linear turbulence is observed.

In Figure 2.12 we show the comparison between a one mode perturbation model, with an amplitude $\eta = 0.1$, for the standard finite volume method (left) and for the PVRS method (right), at a time $t = 0.3$. Due to the larger amplitude of the fluctuation, the higher density fluid sunk deeper in less time. In both cases the non-linear turbulence regime is reached showing similar behaviours, with slight differences in the mixture at small scales.

2.3.5 Astrophysical jet

One of important use of a hydrodynamical code, is the simulation of relativistic and non-relativistic astrophysical jets, which are ubiquitous structures in the Universe.

For this test we closely follow the work of [Stone & Hardee \(2000\)](#), for the case of

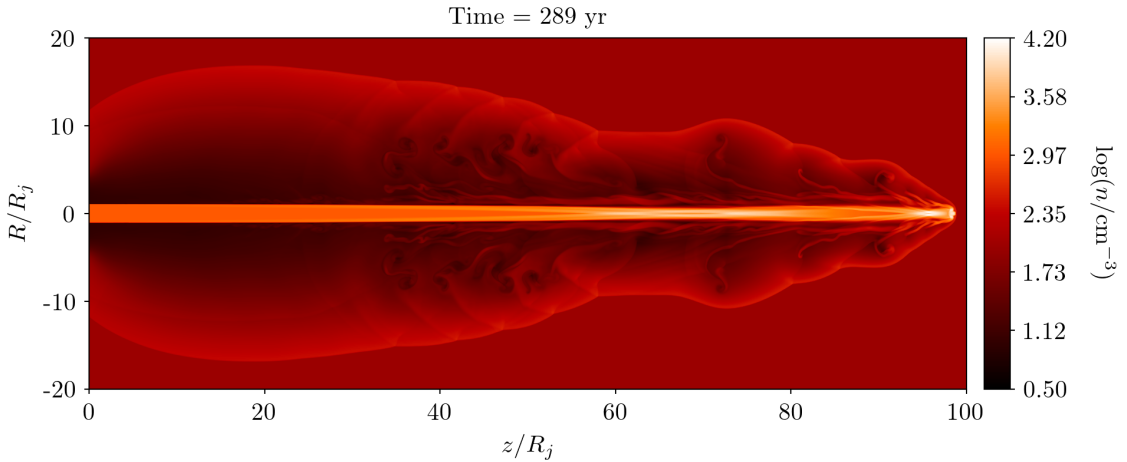


Figure 2.13: Logarithmic numerical density map of the adiabatic over dense jet.

a not-magnetized adiabatic over-dense jet, which is consistent with detailed observations of a number of protostellar jet systems (Nagar et al., 1997). This simulation was performed in a 200×2000 cylindrical axisymmetric grid of size $0 \leq r \leq 20 R_j$ and $0 \leq z \leq 100 R_j$, where $R_j = 2.5 \times 10^{15}$ cm. We use an HLLC Riemann solver for the fluxes, an MC reconstructor, a standard primitive variable recovery scheme and a Courant factor of 0.5.

The initial condition consists of an ideal monoatomic gas with adiabatic index $\gamma = 5/3$, a numerical density $n_m = 100 \text{ cm}^{-3}$ and a pressure $p_m = 1.38 \times 10^{-10} \text{ dyna cm}^{-2}$. The jet injection is set as a boundary condition where all the cells inside $r \leq 1.0 R_j$ and $z \leq 1.0 R_j$ are filled with a numerical density $n_j = 1000 \text{ cm}^{-3}$, a pressure $p_j = p_m$ and a velocity $v_j = 332 \text{ km s}^{-1}$ along the positive z direction. For the remaining boundaries, we set outflow conditions everywhere except for the symmetry axis $r = 0$, where reflection conditions are imposed. The relation between the particle number density and the mass density is given by $\rho = m_H n$, where m_H is the hydrogen atomic mass.

In Figure 2.13 we show the numerical density map for the evolution of the adiabatic over-dense jet at a time $t = 289 \text{ yr}$. The morphology of the cocoon is in good agreement with the one presented by Stone & Hardee (2000), showing similar filamentary structures inside the cocoon, as well as the same length of the jet at 300 yr. Due to the high resolution of the simulation, and the MC reconstructor, we are able to see some KH instabilities developing inside the cocoon. These instabilities form because the material entering the cocoon slows down its velocity, and interacts with the inner part of the jet, which is moving upwards. In the inner structure of the jet we can see re-collimation shocks, which has been suggested as one of the reasons why astrophysical jets can remain tightly collimated over large distances (Kaye et al., 2018). Likewise, these shocks should leave polarization signatures in the emission of jets (Cawthorne & Cobb, 1990), which is important in order to compare simulations

with observations.

2.3.6 Bondi spherical accretion

The [Bondi \(1952\)](#) analytic model is a useful analytic solution to validate a hydrodynamic numerical code. This problem, mentioned in [Section 1.1.1](#), studies the accretion of an infinite spherically symmetric gas cloud onto a Newtonian massive object of mass M . Under the assumption of steady state and by considering a perfect fluid, [Bondi \(1952\)](#) found the equations governing the accretion flow. Assuming a transonic solution, i.e., that the fluid velocity equals the speed of sound at some point, Bondi found that the massive object accretes at a maximum rate

$$\dot{M}_B = 4\pi\lambda_B \frac{G^2 M^2 \rho_\infty}{a_\infty^3}, \quad (2.35)$$

where ρ_∞ and a_∞ are the values of the density and speed of sound at infinity, respectively; and λ_B is a numerical factor that depends on the adiabatic index (γ). From this value of \dot{M} and using the governing equations (see [Chapter 3](#) for a condensed explanation of the solution) a set of algebraic equations is obtained which can be solved numerically in order to get ρ , P and v as a function of radius. We can use this model to validate the addition of gravity in a hydrodynamic code, as well as to test the implementation of spherical coordinates.

For this validation, we perform a series of 2D-spherical axisymmetric numerical simulations of the Bondi problem. The initial conditions consist of a constant density, static gas cloud modelled as a perfect fluid following a polytropic relation. In order to compare our numerical results, we implement a numerical code to obtain the analytic solution (see, [Aguayo-Ortiz, Tejada, et al., 2021](#)), which is used at the boundary to set the values of the density, pressure and velocity at $r = 10 r_B$, where $r_B = GM/a_\infty^2$ is the Bondi radius. We perform three sets of simulations using an ideal gas EoS for three different values of the adiabatic index γ (1, 4/3, 7/5) and different resolutions, in order to perform a L^1 -norm convergence test. For these tests, we fix r_B , a_∞ and ρ_∞ as the units of distance, velocity and density, respectively. All simulations evolve until a steady-state is reached, which is monitored by measuring the evolution of the average mass accretion rate calculated as:

$$\dot{M} = 2\pi \int_0^\pi \rho v_r r^2 \sin \theta d\theta, \quad (2.36)$$

and waiting until the variations in \dot{M} fall below 1 part in 10^4 . We use a standard primitive variable recovery scheme, a Courant factor of 0.5, an HLL Riemann solver, as well as an MC reconstructor.

As mentioned in [Aguayo-Ortiz et al. \(2019\)](#), as a way to avoid numerical problems at the inner boundary, we ensure that, for all of our simulations, the inner radius is set inside the sonic radius. For this reason, we have not included the value $\gamma = 5/3$,

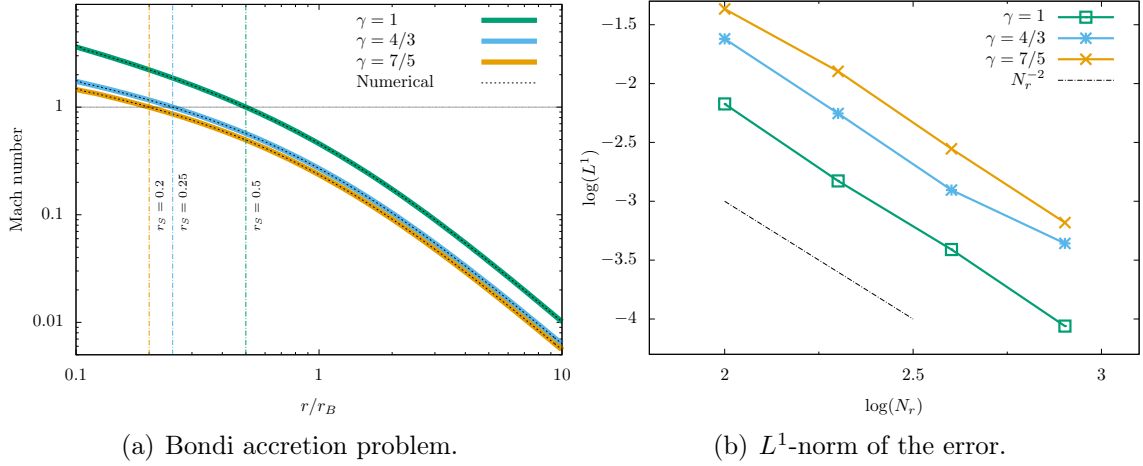


Figure 2.14: *Left panel:* Mach number as a function of radius for the steady-state, spherically symmetric Bondi model. The colour lines represent the analytic solution for three different values of the adiabatic index γ (1, 4/3, 7/5) and the black dashed lines show their respective numerical solution. The vertical lines mark the location of the sonic radius for each value of γ . Taken from [Aguayo-Ortiz et al. \(2019\)](#). *Right panel:* L^1 -norm of the error between the analytic solution and the numerical simulations. The diagonal black dashed line represents an ideal second order convergence trend.

commonly used to describe a monoatomic gas, since for this case $r_s = 0$, meaning that numerical fluctuations are able to travel inside the domain, hence leading to inconsistent results.

In [Figure 2.14\(a\)](#), we show the steady-state solution of the Mach number

$$\mathcal{M} = \frac{v}{c_s} = v \sqrt{\frac{\rho}{\gamma P}}, \quad (2.37)$$

for the three values of γ used for this test.⁸ The colour lines represent the analytic solution, while black dashed lines show their respective numerical steady-state solution. As we can see from this figure, there is a good agreement between both results, even at small radii. As shown in [Aguayo-Ortiz et al. \(2019\)](#), the numerical mass accretion rate remains within an error of less than 0.1% with the corresponding analytic value.

In [Figure 2.14\(b\)](#) we show the L^1 -norm of the error between the analytic and numerical solutions for different resolutions in the radial component, and for the three values of γ . Since the Bondi accretion model does not present shock waves, we expect a second order convergence, which is represented by the black dashed line.

⁸We use the Mach number to compare, since this quantity carries the information of all the primitive variables of the problem.

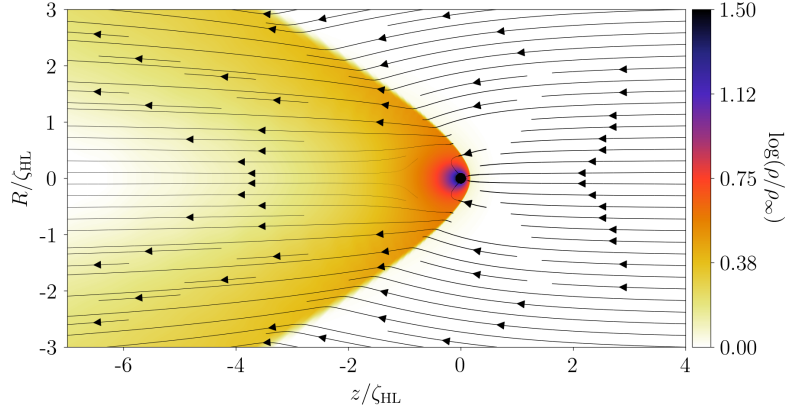


Figure 2.15: Density field of the wind accretion simulation for a $\gamma = 5/3$ fluid and supersonic wind with $\mathcal{M} = 3$. The black solid lines show the fluid streamlines.

2.3.7 Wind accretion

The wind accretion problem, also known as Bondi-Hoyle-Lyttleton (BHL), can be seen as an extension of the spherical accretion model, in which the central object has now a relative velocity with respect to the infinite gas cloud that surrounds it. As mentioned in Section 1.1.2, [Hoyle & Lyttleton \(1939\)](#) and [Bondi & Hoyle \(1944\)](#) give an analytic description of the problem using the ballistic approximation, which does not consider pressure gradients through the gas and, hence, the fluid particles move following free-falling trajectories.

Even though this not a hydrodynamic solution, in [Hoyle & Lyttleton \(1939\)](#), the authors manage to find a value for the mass accretion rate in terms of the impact factor $\zeta_{\text{HL}} = 2GM/v_\infty^2$, which is the radius delimiting all the material that is eventually accreted by the central object, the velocity of the fluid relative to the massive object v_∞ and the density at infinity ρ_∞ :

$$\dot{M}_{\text{HL}} = \pi \zeta_{\text{HL}}^2 v_\infty \rho_\infty = \frac{4\pi G^2 M^2 \rho_\infty}{v_\infty^3}. \quad (2.38)$$

For this test, we extend the BHL problem to the case of a perfect fluid accreted by a Newtonian central potential by means of 2D-axisymmetric numerical simulations. We modelled the fluid as a monoatomic ideal gas with an adiabatic index of $\gamma = 5/3$. Following [Xu & Stone \(2019\)](#), we normalize our simulations units with $GM = \zeta_{\text{HL}} = \rho_\infty = 1$. With this normalization, the wind velocity $v_\infty = \sqrt{2}$, and all the extra required quantities (a_∞, P_∞) can be computed using the Mach number \mathcal{M} and using the EoS. Note that, under this normalization, $\dot{M}_{\text{HL}} = \sqrt{2}\pi$.

Our initial conditions consist, as in the Bondi problem, of a constant density ($\rho = \rho_\infty$) gas cloud, moving with velocity v_∞ along the axis of symmetry:

$$\begin{aligned} v_r &= -v_\infty \cos \theta, \\ v_\theta &= v_\infty \sin(\theta). \end{aligned} \quad (2.39)$$

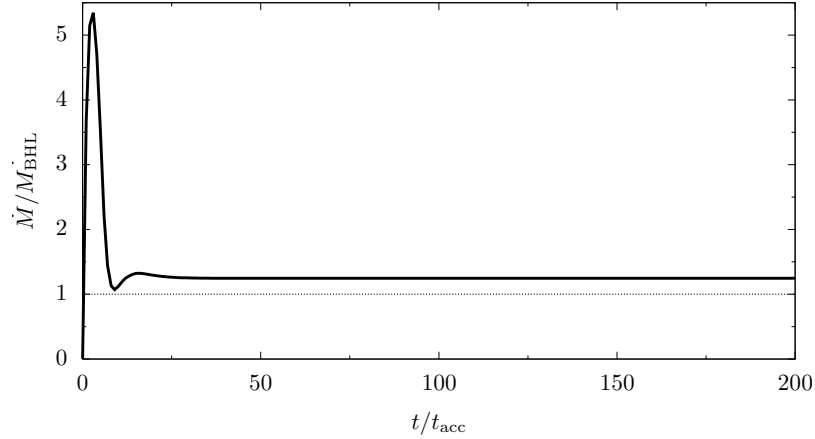


Figure 2.16: Mass accretion rate (in units of \dot{M}_{BHL}) as a function of time (in units of $t_{\text{acc}} = \zeta_{\text{HL}}/v_{\infty}$) for the simulation of the wind accretion problem with $\mathcal{M} = 3$.

For the boundary conditions, at the outer boundary ($r = 10\zeta_{\text{HL}}$), we set an incoming wind, with the same values as the initial conditions for $\theta \in [0, \pi/2]$, and a free-outflow condition at the remaining boundaries. We use an exponential radial mesh grid (see [Aguayo-Ortiz et al., 2019](#)) for 256×128 cells. For the inner boundary ($r = 0.1\zeta_{\text{HL}}$), we set a non-inflow condition, which consists of filling the radial velocity of the ghost cells, with $-|v_r|$, in order to avoid incoming material from this region. The steady-state of the simulation is monitored by measuring the mass accretion rate, as in the Bondi test.

In [Figure 2.15](#), we show the density profile of the steady-state result of a simulation with a Mach number of $\mathcal{M} = 3$. The black solid lines represent the fluid streamlines. As we can see, since the fluid is supersonic ($\mathcal{M} > 1$), a bow-shock forms in front of the massive object, increasing the density over an order of magnitude with respect to ρ_{∞} . In the BHL solution, the fluid streamlines finish at the symmetry axis behind the object, thermalizing the perpendicular component of the velocity and allowing the ones that are bounded to be accreted by the central mass (see [Tejeda & Aguayo-Ortiz, 2019](#)). However, in this case, since we now take into account pressure gradients in the fluid, the fluid streamlines follow a different path and maintain the original direction of the wind, with exception to the ones that pass close to the central mass.

In [Figure 2.16](#), we show the evolution of the mass accretion rate as a function of time. We find that the simulation relaxes in less than $30 t_{\text{acc}}$, and the numerical value of \dot{M} is of the order of magnitude of \dot{M}_{BHL} . These results, both the mass accretion rate and the flow morphology are in very good agreement with other works ([Edgar, 2004](#); [Xu & Stone, 2019](#)).

2.4 AZTEKAS-GRHD: general relativistic hydrodynamics

In this section, we describe the hydrodynamic equations in general relativity i.e., when the fluid is moving inside a curved spacetime, for example, around a black hole. It is important to state that AZTEKAS-GRHD does not take into account the dynamics of the spacetime, in other words, it does not solve the Einstein field equations, but uses a fixed metric instead. The spacetime metrics implemented in AZTEKAS so far are: Minkowski, Schwarzschild and Kerr.

Before writing the general relativistic Euler equations, it is important to introduce the formalism used to evolve the equations. In this section, we adopt geometrized units in which $G = c = 1$.

2.4.1 3+1 formalism

In order to study the evolution in time of any physical system, the problem needs to be formulated as an initial value or Cauchy problem. This means that the set of equations describing the system must predict its evolution in time (future or past) by means of its initial state and boundary conditions (Alcubierre, 2008). In general relativity, the covariant formalism of the theory hinders a direct evolution in time of the system, due to the inherent relation between space and time, and this is a particularly important issue for numerical codes, where we seek to obtain the evolution of the system at specific time intervals.

The 3+1 formalism, popularized by the work of Arnowitt et al. (1962) (seeourgoulhon, 2007, for a complete review of the development of this formalism) is one of the many forms in which spacetime can be foliated in order to establish an initial value problem. In this formulation, we consider that our spacetime with metric $g_{\mu\nu}$ is globally hyperbolic, meaning that it can be foliated into three-dimensional space-like hypersurfaces Σ , identified with a global function of time t , which does not necessarily coincide with the proper time of any particular observer.

The region of spacetime contained between contiguous hypersurfaces can be described by the following parameters (see Alcubierre, 2008):

- A three-dimensional metric γ_{ij} ($i, j = 1, 2, 3$)⁹ that measures the proper distances inside the hypersurface:

$$dl^2 = \gamma_{ij} dx^i dx^j. \quad (2.40)$$

- A lapse of proper time $d\tau$ between each foliated hypersurface, as measured by the observers moving along the direction normal to the hypersurfaces (also

⁹Note that for three-dimensional tensors, we use Roman indices, whereas for four-dimensional ones we use Greek letters.

called *local Eulerian observers* [LEOs]):

$$d\tau = \alpha(t, x^i) dt, \quad (2.41)$$

where α is known as the *lapse gauge function* (Wheeler, 1964).

- And a relative velocity vector β^i that measures the displacement between the LEOs and the lines of constant spatial coordinates:

$$x_{t+dt}^i = x_t^i - \beta^i(t, x^j) dt, \quad (2.42)$$

where β^i is known as the *shift gauge function* (Wheeler, 1964).

Using the above ingredients, the line element of spacetime is written as:

$$ds^2 = (-\alpha^2 + \beta_i \beta^i) dt^2 + 2\beta_i dt dx^i + \gamma_{ij} dx^i dx^j, \quad (2.43)$$

and hence, the metric tensor $g_{\mu\nu}$ in the 3+1 formalism takes the form:

$$g_{\mu\nu} = \begin{pmatrix} -\alpha^2 + \beta_k \beta^k & \beta_i \\ \beta_j & \gamma_{ij} \end{pmatrix}, \quad (2.44a)$$

$$g^{\mu\nu} = \begin{pmatrix} -1/\alpha^2 & \beta^i/\alpha^2 \\ \beta^j/\alpha^2 & \gamma^{ij} - \beta^i \beta^j/\alpha^2 \end{pmatrix}. \quad (2.44b)$$

From these expressions we can show that the four-dimensional volume element in the 3+1 formalism turns out to be given by

$$\sqrt{-g} = \alpha \sqrt{\gamma}, \quad (2.45)$$

where g and γ are the determinants of $g_{\mu\nu}$ and γ_{ij} respectively.

In a more general description, we can state that the three-dimensional space in the Σ hypersurfaces changes as a function of t , which implies that the metric is dynamic. In our case, since we are assuming a fixed metric, this is no longer needed. See Alcubierre (2008) for a more complete description of the 3+1 formalism.

2.4.2 General relativistic hydrodynamics

The general relativistic hydrodynamic evolution equations for a perfect fluid, written in covariant form are

$$\nabla_\mu (\rho U^\mu) = 0, \quad (2.46a)$$

$$\nabla_\mu (T^{\mu\nu}) = 0, \quad (2.46b)$$

with the stress-energy tensor defined as

$$T^{\mu\nu} = \rho h U^\mu U^\nu + P g^{\mu\nu}, \quad (2.47)$$

where U^μ is the 4-velocity of the fluid elements and h , ρ and P are the specific enthalpy, rest-mass density and pressure as measured in the fluid's rest frame. The general form of h is

$$h = 1 + \epsilon + \frac{P}{\rho}, \quad (2.48)$$

where ϵ is the specific internal energy. The rest-mass density can be written in terms of the particle number density n as

$$\rho = nm, \quad (2.49)$$

where m is the average baryonic rest-mass of the fluid.

The state of the fluid at any given time is given in terms of the six primitive variables (ρ, ϵ, p, v^i) . The set of equations is closed assuming an equation of state (EoS) that relates ϵ with the other thermodynamic variables (ρ, P) , e.g.,

$$\epsilon = \epsilon(\rho, P). \quad (2.50)$$

As in the non-relativistic case, by assuming an ideal gas EoS under an adiabatic process with index γ , the specific internal energy could be written as in equation (2.21). Nevertheless, in this case, the values of $\gamma = 4/3$ and $\gamma = 5/3$ describe a monoatomic gas in the ultra-relativistic ($\Theta = P/\rho \gg 1$) and non-relativistic ($\Theta = P/\rho \ll 1$)¹⁰ regimes, respectively. In order to describe a monoatomic ideal gas in the intermediate relativistic regime, we need to use a correct EoS as derived by [Synge \(1957\)](#). We implemented this EoS by using the approximate form proposed by [Ryu et al. \(2006\)](#).

Let us now describe the velocity (both four and three-dimensional vectors) in terms of the gauge functions $\{\alpha, \beta^i\}$ and the three-dimensional metric tensor γ_{ij} . Let's define the scalar parameter Γ as

$$\Gamma := \alpha U^0, \quad (2.51)$$

and the three-dimensional velocity vector

$$v^i := \frac{U^i}{\Gamma} + \frac{\beta^i}{\alpha}. \quad (2.52)$$

With this definition, v^i corresponds to the velocity of a fluid element as seen by the LEOs ([Alcubierre, 2008](#)). Notice that

$$\frac{U^i}{U^0} = \frac{d\tau}{dx^0} \frac{dx^i}{d\tau} = \frac{dx^i}{dx^0}, \quad (2.53)$$

¹⁰The parameter Θ is a temperature-like variable (see for example [Ryu et al., 2006](#); [Aguayo-Ortiz, Sarbach, & Tejada, 2021](#)).

is the coordinate speed of the fluid elements, so we first need to add the shift to convert to the Eulerian reference frame and then divide by the lapse to use the proper time of the LEOs instead of coordinate time. Using this, we can show that

$$U^0 = \frac{\Gamma}{\alpha}, \quad (2.54a)$$

$$U^i = \Gamma \left(v^i - \frac{\beta^i}{\alpha} \right), \quad (2.54b)$$

$$U_0 = \Gamma (v_i \beta^i - \alpha), \quad (2.54c)$$

$$U_i = \Gamma v_i, \quad (2.54d)$$

where $v_i = \gamma_{ij} v^j$. Using the fact that $U_\mu U^\mu = -1$, we find that Γ is equal to

$$\Gamma = \frac{1}{\sqrt{1 - v^2}}, \quad (2.55)$$

where $v^2 = \gamma_{ij} v^i v^j$. This means that Γ is the Lorentz factor as seen by the LEOs.

Now that we have all the primitive variables of the problem, as well as an equation of state, we can write the GRHD equations in conservative form.

2.4.3 GRHD in balanced form

Following the variation of the Valencia formulation (Banyuls et al., 1997) proposed by Del Zanna et al. (2007) (see also Porth et al., 2017) for the general relativistic magneto-hydrodynamic set of equations, we can write the GRHD equations in balanced form as

$$\frac{1}{\sqrt{\gamma}} \left[\frac{\partial(\sqrt{\gamma} \mathbf{Q}(\mathbf{u}))}{\partial t} + \frac{\partial(\sqrt{\gamma} \mathbf{F}^i(\mathbf{u}))}{\partial x^i} \right] = \mathbf{S}(\mathbf{u}), \quad (2.56)$$

where the primitive variables \mathbf{u} , the conserved variables \mathbf{Q} , fluxes \mathbf{F}^i and source terms \mathbf{S} are defined as

$$\mathbf{u} = \begin{bmatrix} \rho \\ P \\ v_j \end{bmatrix}, \quad (2.57a)$$

$$\mathbf{Q} = \begin{bmatrix} D \\ \varepsilon \\ S_j \end{bmatrix}, \quad (2.57b)$$

$$\mathbf{F}^i = \begin{bmatrix} D(\alpha v^i - \beta^i) \\ \alpha(S^i - v^i D) - \beta^i \varepsilon \\ \alpha W_j^i - \beta^i S_j \end{bmatrix}, \quad (2.57c)$$

$$\mathbf{S} = \begin{bmatrix} 0 \\ \frac{1}{2} W^{ik} \beta^j \partial_j \gamma_{ik} + W_i^j \partial_j \beta^i - S^j \partial_j \alpha \\ \frac{1}{2} \alpha W^{ik} \partial_j \gamma_{ik} + S_i \partial_j \beta^i - U \partial_j \alpha \end{bmatrix}, \quad (2.57d)$$

where $D = \rho\Gamma$ is the density as measure in the Eulerian frame, $S_j = \rho h\Gamma^2 v_j$ is the covariant three-momentum and $\varepsilon = U - D$ is the re-scaled energy, with $U = \rho h\Gamma^2 - P$ the energy density as seen by the LEOs. The remaining terms correspond to: the purely spatial variant of the stress-energy tensor $W^{ij} = S^i v^j + P\gamma^{ij}$ and the spatial derivatives $\partial_i = \partial/\partial x^i$.

2.4.4 Primitive variable recovery

Contrary to the non-relativistic case, in GRHD there is no trivial way for recovering the primitive variables from the evolved conservative ones. Instead, a transcendental algebraic equation has to be solved numerically for the recovery. In order to obtain the primitive variables, we define an auxiliary variable $\Theta = P/\rho$, which can be seen as a dimensionless temperature (see [Aguayo-Ortiz, Tejada, et al., 2021](#)), and, using the EoS, write the specific enthalpy as $h = h(\Theta)$. Then, we compute the Lorentz factor as

$$\Gamma(\Theta) = \sqrt{1 - \frac{S^2}{D^2 h(\Theta)^2}}, \quad (2.58)$$

where $S^2 = \gamma^{ij} S_i S_j$. Then, from the definition of ε , we obtain the following transcendental algebraic equation

$$h(\Theta)\Gamma(\Theta) - \frac{\Theta}{\Gamma(\Theta)} - \frac{\varepsilon}{D} - 1 = 0, \quad (2.59)$$

which is then solved for Θ using a root finder, like the Newton-Raphson method (e.g. [Porth et al., 2017](#)). With the numerical solution Θ_0 , we construct the primitive variables as follows:

$$\rho = \frac{D}{\Gamma(\Theta_0)}, \quad (2.60a)$$

$$P = Dh(\Theta_0)\Gamma(\Theta_0) - \varepsilon - D, \quad (2.60b)$$

$$v_i = \frac{S_i}{Dh(\Theta_0)\Gamma(\Theta_0)}. \quad (2.60c)$$

We have also implemented in AZTEKAS the PVRS method ([Aguayo-Ortiz et al., 2018](#)) for the relativistic case. In this method, as mentioned previously, a modified version of the conservative equations is solved in order to evolve directly the primitive variables (see Eq. 2.11). Its performance in the special relativistic regime is tested using the shock tube problem in [Aguayo-Ortiz et al. \(2018\)](#). However, in all the GRHD numerical simulations presented in this thesis, we use the standard recovery scheme using a Newton-Raphson technique, since we have found that, especially in numerical simulations with shock waves and discontinuities, the time-step has to be sufficiently small for the velocity to stay below the speed of light, which greatly

increases the computation time. This could be solved by finding a correct Courant condition for this method.

In the next section, we present some validation and comparison tests for the general relativistic version of the AZTEKAS code.

2.5 AZTEKAS-GRHD: code validation

We now present the validation tests for the general relativistic version of the AZTEKAS code. For all the simulations presented in this section, we use a second order Runge-Kutta method for time integration and a standard primitive variable recovery (2.60). The metric, flux calculation, Courant number and reconstructor will be specified at each test.

2.5.1 Tests in Minkowski spacetime

The spacetime used in the tests presented in this section is described by the Minkowski metric $g_{\mu\nu} = \eta_{\mu\nu} = \text{diag}(-1, 1, 1, 1)$, which is also known as the special relativistic regime. In these cases, we are not considering the curvature of spacetime, but only velocities comparable to the speed of light.

Relativistic shock tube

The relativistic shock tube problem has, essentially, exactly the same setup as in the non-relativistic version. However, in this case the velocity has a natural limit, which is the speed of light, which makes it more complicated to be solved analytically. The analytic solution for the relativistic shock tube problem was first presented by [Marti & Muller \(1994\)](#) (also see [Lora-Clavijo et al., 2013](#), for a more detailed explanation for both the relativistic and non-relativistic cases) and, since then, became the main numerical test for relativistic hydrodynamic code validations.

Table 2.2: Initial parameters for the four tests of the 1D relativistic shock tube problem. The labels L and R represent the initial left and right states, respectively.

Parameters	Test 1	Test 2	Test 3	Test 4
ρ_L	10.0	1.0	1.0	1.0
p_L	13.33	10^{-3}	10^3	1.0
v_L	0.0	0.999999995	0.0	0.9
ρ_R	1.0	1.0	1.0	1.0
p_R	10^{-8}	10^{-3}	0.01	10.0
v_R	0.0	-0.999999995	0.0	0.0
γ	5/3	4/3	5/3	4/3

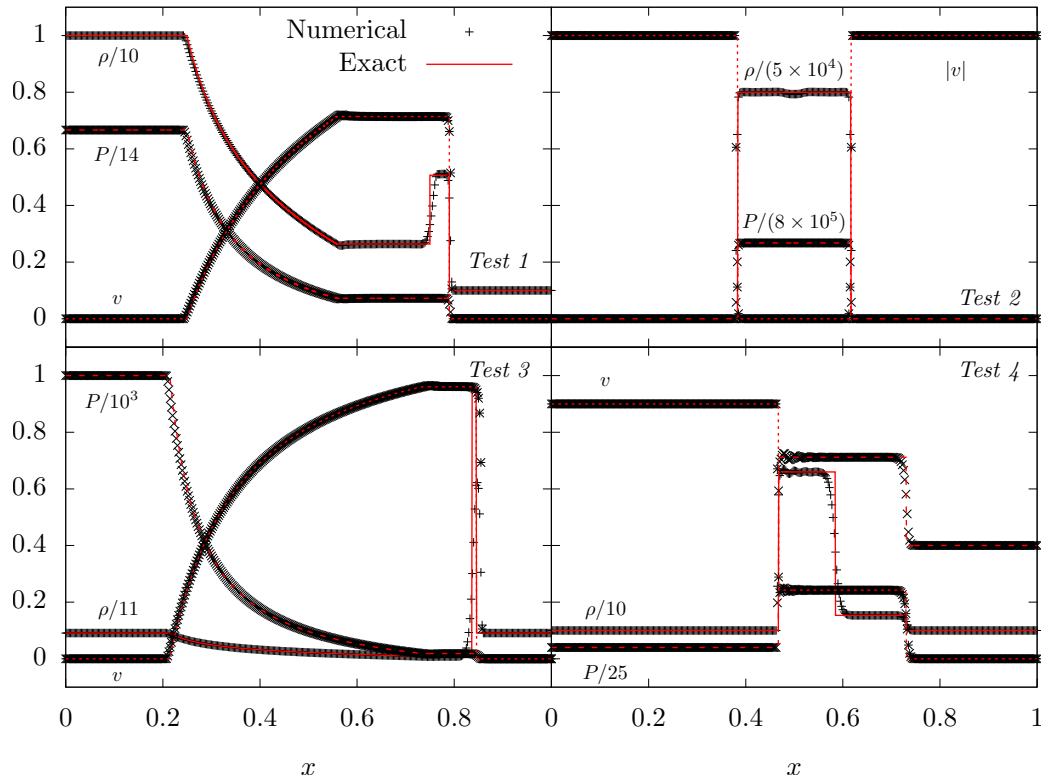


Figure 2.17: Results of the 1D relativistic shock tube tests for the four sets of initial conditions presented in Table 2.2. Each panel corresponds to a different test and compares the density, pressure and velocity as obtained against their corresponding analytic values (Marti & Muller, 1994). In all cases the evolution time is $t = 0.35$.

For this test, as in the non-relativistic case, we perform four simulations with different initial configurations of the problem, in order to study a wide variety of possible outcomes. For all the results presented here we use the HLLE Riemann solver, an MC limiter reconstructor and a Courant factor of 0.5. The initial discontinuity is set at $x = 0.5$.

In Table 2.2 we show the initial conditions for the four tests presented in this section. Test 1 consists of a mildly relativistic shock tube, in which a gas initially at rest in the whole box has a slightly denser and a substantially higher pressure on the left side. In Test 2, the initial state consists of the strong ultra-relativistic flows in a head-on collision at the interface. For Test 3 we have a strong relativistic shock tube configuration, in which there is the same density everywhere, but there is an important difference in pressures at each side. Finally, Test 4 consists of a fluid coming from the left side and encountering static gas with a higher pressure. The boundary conditions in all cases are set as free-outflow in both boundaries.

In Figure 2.17 we show the density, pressure and velocity of the four tests at time $t = 0.35$ with a resolution $N = 400$. The black dotted lines represent the numerical

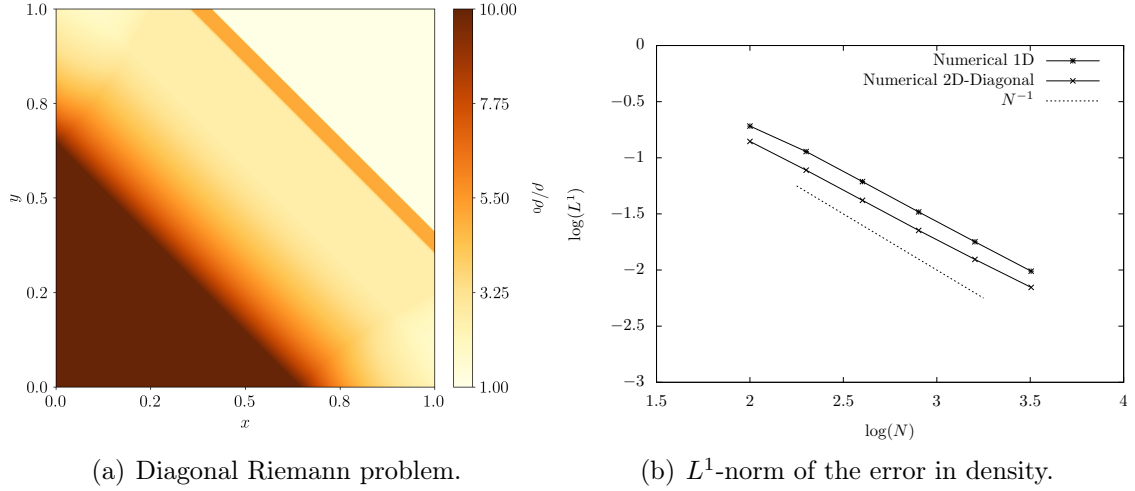


Figure 2.18: *Left panel:* Density map of the evolution of the initial configuration for Test 1, with an interface located at $x + y = 1$, at time $t = 0.35$. *Right panel:* L^1 -norm of the error in the density between the numerical and analytic solutions, and different values of the resolution for the Test 1 in the 1D version and in the 2D-diagonal one. The dotted line show the slope that a first order convergence must have.

solutions, while the red lines are the analytic solution (Marti & Muller, 1994). As can be seen from this figure, in most cases there is a very good agreement between the numerical and analytic solutions. In Test 3, we can see that the contact discontinuity is not well resolved by the numerical simulation, however this problem is also found by other authors with their own numerical codes (e.g. Lora-Clavijo et al., 2015).

We also repeat the 2D simulation of the shock tube problem along the diagonal, but now for the relativistic version. In this case we use the Test 1 presented in Table 2.2, setting the interface at the diagonal $x + y = 1$. In Figure 2.18(a) we show the density colour-map of the numerical solution at $t = 0.35$. As we can see, the contact discontinuity remains stable, showing no problem with the boundaries $x = 1$ and $y = 1$, and the rarefaction wave shows no spurious reflection, by using a zero-order interpolation for the ghost cells.

Regarding the convergence rate of the numerical code for these tests, since we obtain the same first order convergence in all cases, analogous to the non-relativistic ones, we prefer to show the convergence of the Test 1 in the 1D case and in the 2D-diagonal case. In Figure 2.18(b) we show the convergence of the L^1 -norm of the error in density for different resolutions for these two tests. In the 2D-diagonal case, we increase the resolution at both dimensions. As we can see, in both cases we obtain a convergence close to first-order (see the dotted line which follows N^{-1}).

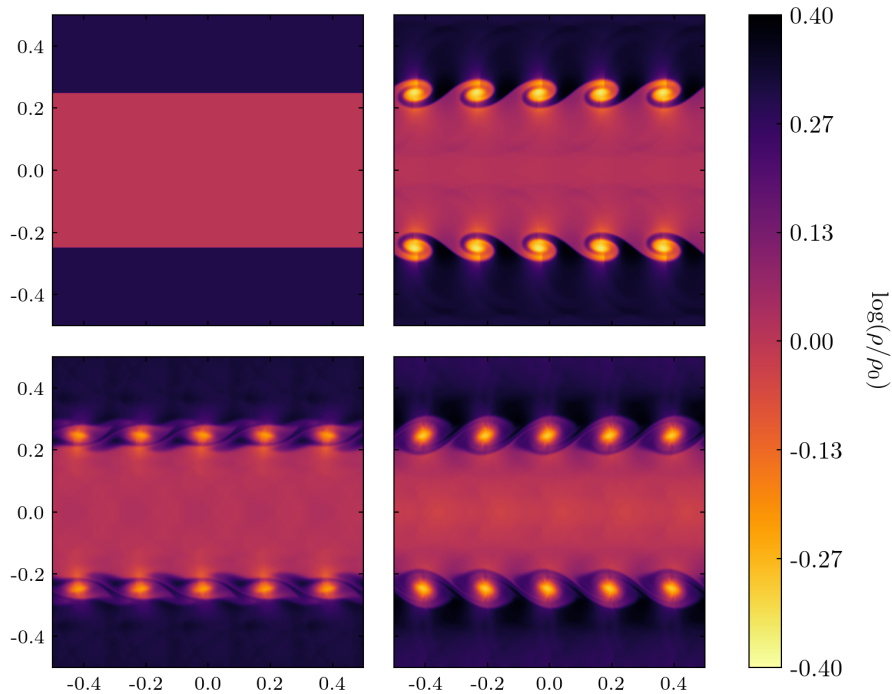


Figure 2.19: Snapshots of the evolution in the rest-mass density of the relativistic Kelvin-Helmholtz instability. From top to bottom and left to right the times are $t = 0, 0.1, 0.2$ and 0.3 .

Relativistic Kelvin-Helmholtz instability

For the relativistic KH instability test we set the same initial configuration as in the non-relativistic case (see Section 2.3.4), but now the relative velocity of the shearing flows is near the speed of light, which may affect the dynamics of the instability. For this test we closely follow the configuration presented in [Lora-Clavijo et al. \(2015\)](#), which has the same initial configuration as in the non-relativistic version presented in Section 2.3.4, but now the relative velocity is $v = |0.5|$, in units of the speed of light. In this case we use an MC primitive variable reconstructor, a Courant factor of 0.5 and an ideal gas under an adiabatic process with index $\gamma = 5/3$. The simulation performed in this test uses a Cartesian square domain of $[-0.5, 0.5] \times [-0.5, 0.5]$ with a uniformly distributed grid of 400×400 cells with periodic boundaries.

In Figure 2.19 we show different stages of the evolution of the relativistic KH instability for times $t = 0, 0.1, 0.2$ and 0.3 . As can be seen from these figures and, comparing with the non-relativistic case (see Figure 2.10), this version has a less chaotic evolution of the instability, maintaining symmetrical eddies at the shear boundaries. This behaviour is also found in simulations by [Lora-Clavijo et al. \(2015\)](#).

Relativistic astrophysical jet

For the relativistic jet test, we closely follow one of the axisymmetric cylindrical jet configurations presented by [Martí et al. \(1997\)](#) (see also [Lora-Clavijo et al., 2015](#)), in which the authors show the morphology at different states of the evolution of a wide range of jets with different parameters.

In this case, we choose the Model C2 of [Martí et al. \(1997\)](#), in which the authors injected a perfect adiabatic fluid with $\gamma = 5/3$ inside a region of size $R = R_j$ and $z = R_j$, with a velocity $v_j = 0.99$ and density $\rho_j = 0.01$ to an ambient medium with density $\rho_m = 1.0$. The jet is injected with a Mach number of $\mathcal{M}_m = 6$, where

$$\mathcal{M} = \frac{v\sqrt{1-c_s^2}}{c_s\sqrt{1-v^2}}, \quad (2.61)$$

i.e., a supersonic jet, from which we can compute the jet pressure using the EoS and the definition of the speed of sound. The numerical domain consists of a rectangular cylindrical grid $[0, 15] \times [0, 50]$ with a high resolution of 576×1920 cells. We use an MC primitive variable reconstructor and a Courant factor of 0.25.

In [Figure 2.20](#) we show the rest-mass density of the relativistic jet evolution at time $t = 115$. Since this is a supersonic jet, we can see the re-collimation shocks in the central part of the jet, covered with a mixing layer where hydrodynamic instabilities can be spotted. Moreover, a cocoon forms between the jet and the medium. Note that, due to the high resolution of the simulation, it is possible to see the shape of waves bouncing back and forth inside the jet region. These results are in very good agreement with the ones presented by different authors (cf. [Martí et al., 1997](#); [Del Zanna & Bucciantini, 2002](#); [Lora-Clavijo et al., 2015](#)), showing a similar structure and length of the jet for $t \approx 120$.

2.5.2 Tests in black hole spacetimes

In this section, we test our numerical code using two different problems regarding the accretion of gas onto a black hole: spherical accretion and wind accretion. In AZTEKAS we have implemented the Schwarzschild and Kerr black hole metrics using the following coordinate systems:

- Schwarzschild coordinates (t, r, θ, φ) :

These describe a Schwarzschild black hole, with non-horizon penetrating coordinates, i.e., there is a divergence at the event horizon:

$$g_{\mu\nu} = \text{diag} \left(- \left[1 - \frac{2M}{r} \right], \left[1 - \frac{2M}{r} \right]^{-1}, r^2, r^2 \sin^2 \theta \right). \quad (2.62)$$

These coordinates are implemented in AZTEKAS using the original spherical symmetry description, as well as Cartesian and cylindrical ones.

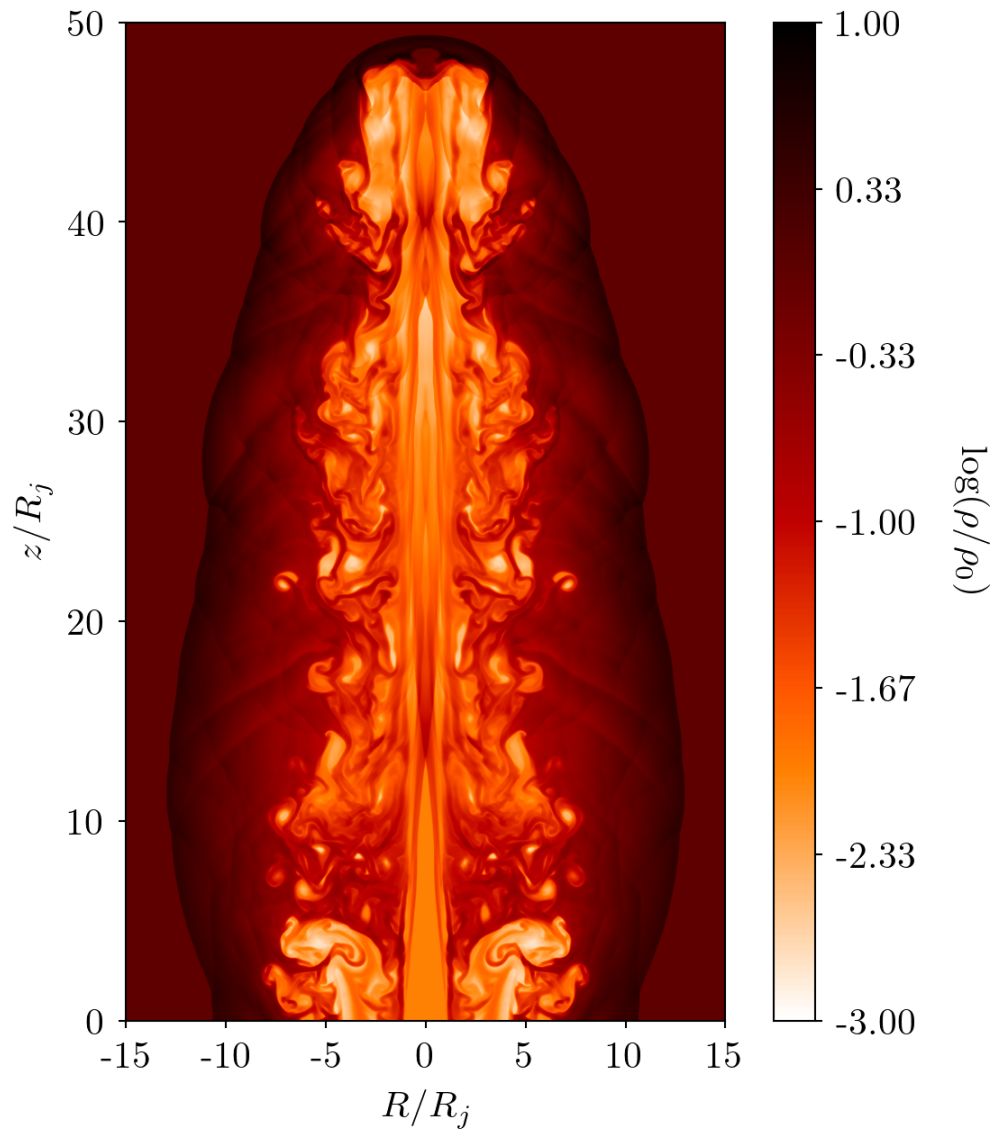


Figure 2.20: Snapshot of the evolution at time $t = 115$ of the rest-mass density for the relativistic jet setup.

- Eddington-Finkelstein coordinates:

These describe a Schwarzschild black hole as well, but now using horizon penetrating coordinates, i.e., the solution is regular across the event horizon:

$$g_{\mu\nu} = \begin{pmatrix} -\left[1 - \frac{2M}{r}\right] & \frac{2M}{r} & 0 & 0 \\ \frac{2M}{r} & 1 - \frac{2M}{r} & 0 & 0 \\ 0 & 0 & r^2 & 0 \\ 0 & 0 & 0 & r^2 \sin^2 \theta \end{pmatrix}, \quad (2.63)$$

which is as well implemented in a Cartesian, cylindrical and spherical description.

- Boyer-Lindquist coordinates (t, r, θ, φ) :

These describe a rotating Kerr black hole of mass M and with spin parameter a , with non-horizon penetrating coordinates:

$$g_{\mu\nu} = \begin{pmatrix} -\frac{\Delta - a^2 \sin^2 \theta}{\varrho^2} & 0 & 0 & -\frac{2Mar \sin^2 \theta}{\varrho^2} \\ 0 & \frac{\varrho^2}{\Delta} & 0 & 0 \\ 0 & 0 & \varrho^2 & 0 \\ -\frac{2Mar \sin^2 \theta}{\varrho^2} & 0 & 0 & \frac{\Sigma}{\varrho^2} \sin^2 \theta \end{pmatrix}, \quad (2.64)$$

where $\Delta = r^2 - 2Mr + a^2$, $\varrho^2 = r^2 + a^2 \cos^2 \theta$ and $\Sigma = (r^2 + a^2) - a^2 \Delta \sin^2 \theta$. This coordinate system reduces to the Schwarzschild one when $a = 0$.

- Kerr-Schild coordinates $(t', r, \theta, \varphi')$:

These describe a rotating Kerr black hole with spin parameter a , with horizon penetrating coordinates:

$$g_{\mu\nu} = \begin{pmatrix} -\left(1 - \frac{2Mr}{\varrho^2}\right) & \frac{2Mr}{\varrho^2} & 0 & -\frac{2Mar \sin^2 \theta}{\varrho^2} \\ \frac{2Mr}{\varrho^2} & \left(1 + \frac{2Mr}{\varrho^2}\right) & 0 & -a \left(1 + \frac{2Mr}{\varrho^2}\right) \sin^2 \theta \\ 0 & 0 & \varrho^2 & 0 \\ -\frac{2Mar \sin^2 \theta}{\varrho^2} & -a \left(1 + \frac{2Mr}{\varrho^2}\right) \sin^2 \theta & 0 & \sin^2 \theta \left[\varrho^2 + a^2 \left(1 + \frac{2Mr}{\varrho^2}\right) \sin^2 \theta\right] \end{pmatrix}. \quad (2.65)$$

As in the previous case, this coordinate system reduces to the Eddington-Finkelstein one when $a = 0$.

Since the metrics describing a rotating black hole are just an extension of the non-rotating ones, and because the horizon-penetrating coordinates have an advantage while dealing with numerical errors coming from the inner boundary of the numerical domain, for all the tests presented in this section, we use the Kerr-Schild metric for the description of the spacetime around the black hole.

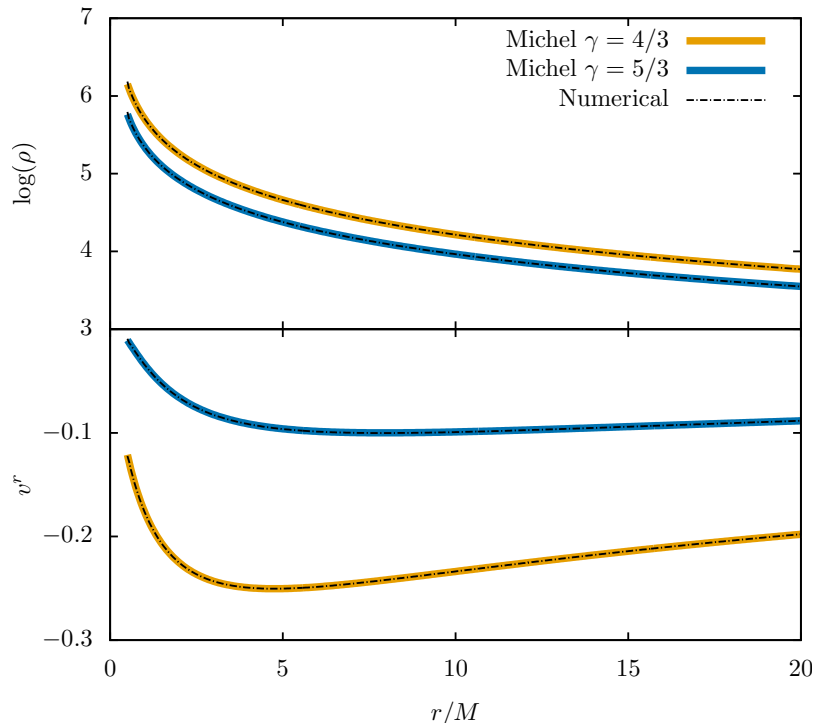


Figure 2.21: Comparison between the numerical simulations (black dashed lines) and the Michel (1972) analytic solution (coloured lines) for the rest-mass density (top panel) and the radial velocity (bottom panel) and two different values of γ . Taken from Tejeda & Aguayo-Ortiz (2019).

Relativistic spherical accretion

Michel (1972) solution is the general relativistic extension of the Bondi (1952) spherical accretion model. In this case, the central massive object corresponds to a non-rotating black hole, which is responsible for the gas accretion. As in the Newtonian case, this solution deals with the accretion of an infinite spherically symmetric gas cloud, under the assumption of steady state and by considering a perfect fluid. In the relativistic regime, the mass accretion rate found by Michel is given by:

$$\dot{M}_M = 4\pi\lambda_M M^2 \frac{\rho_\infty}{\mathcal{C}_\infty^3}, \quad (2.66)$$

where ρ_∞ is the rest-mass density of the gas at infinity, \mathcal{C}_∞ is the speed of sound at infinity and λ_M is a numerical factor that depends on the adiabatic index γ and the asymptotic state of the fluid at infinity (see Aguayo-Ortiz, Tejeda, et al., 2021).

As its non-relativistic counterpart, the Michel analytic solution is a useful model to validate general relativistic hydrodynamic codes. To do this, we develop a numerical code that solves the algebraic equations related to this solution (see Aguayo-Ortiz, Tejeda, et al., 2021).

For this test, we perform a series of 2D spherically axisymmetric numerical simu-

lations of the Michel problem. We use a mesh grid of 400×400 uniformly distributed cells over a domain $[0.5 M, 20 M] \times [0, \pi/2]$. The boundary conditions consist of a free-outflow inner boundary, intentionally set inside the event horizon, in order to prevent spurious numerical error propagation, and a fixed set of values at the outer boundary. These values correspond exactly to the analytical values at that radius. For the initial conditions, we use a constant density, static gas cloud, with the same values of density and pressure as in the boundaries. We evolve the solution for two different values of γ , monitoring the mass accretion rate until a steady-state is reached.

In Figure 2.21 we show the comparison between the analytic solution found by Michel (1972) (colored lines) and the steady-state reached by the simulations performed with AZTEKAS (black dashed lines). As we can see, even for points inside the event horizon, the agreement between both solutions is remarkable. We have found that the relative error in the mass accretion rate between both solutions is below 0.2%. For a convergence analysis, see the Appendix A of Tejada & Aguayo-Ortiz (2019).

This solution is extensively studied from the non-relativistic to the ultra-relativistic regimes in the article presented in chapter 3 (Aguayo-Ortiz, Tejada, et al., 2021), where we also extend the solution, by means of numerical simulations using AZTEKAS, to the case of a rotating Kerr black hole.

Relativistic wind accretion

The wind accretion problem as described by Hoyle & Lyttleton (1939) and Bondi & Hoyle (1944), corresponds to an axisymmetric accretion solution of a gas assumed to move in ballistic trajectories towards the massive object. As shown previously in this chapter, in the non-relativistic regime tests, even though this model is not a hydrodynamic solution, it gives an adequate estimate for the rate at which mass is accreted onto the moving mass. This makes the BHL model a qualitative solution to test a hydrodynamic numerical code.

Schwarzschild black hole

The relativistic extension of the BHL, where the accretor is replaced by a non-rotating, Schwarzschild black hole is obtained by Tejada & Aguayo-Ortiz (2019), which is part of this thesis (see Chapter 4). In that article, we also assume the ballistic approximation, obtaining the description for the gas density profile, the fluid streamlines, and the mass accretion rate. The details of the analytic solution can be found in said article.

We use this solution to compare with full-hydrodynamic simulations performed with AZTEKAS. Using a similar setup as the one presented in Section 1.1.2, we perform a series of simulations for varying the wind velocity v_∞ over different percentages of the speed of light. In Figure 2.22, we show one of the numerical results presented in Tejada & Aguayo-Ortiz (2019). In this figure we see the steady-state of the evo-

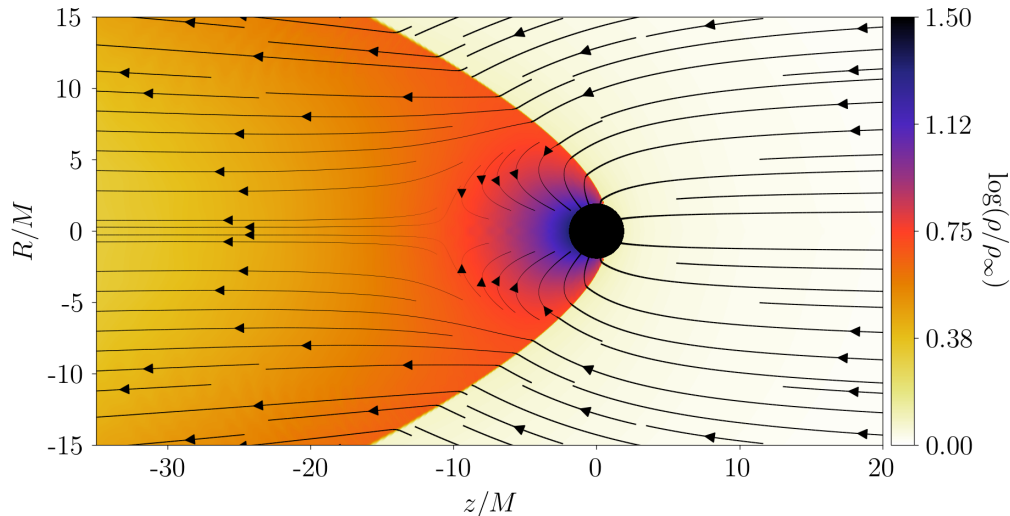


Figure 2.22: Steady-state of the rest-mass density evolution for the relativistic wind accretion problem of a fluid with $\gamma = 5/3$ and a wind velocity $v_\infty = 0.5$. The black line arrows show the fluid streamlines of the wind, their width is proportional to the velocity magnitude. Figure taken from [Tejeda & Aguayo-Ortiz \(2019\)](#).

lution in the rest-mass density for a wind with $v_\infty = 0.5$ and an adiabatic index of $\gamma = 5/3$. As shown in our article, the mass accretion rate of both numerical and analytic results show a very good agreement. We can also see that the morphology of the bow shock is similar to the one seen in the non-relativistic case (see [Figure 2.15](#)). All the details of this comparison, as well as self-convergence, domain extension and validation tests can be found in the Appendix of [Tejeda & Aguayo-Ortiz \(2019\)](#).

Kerr black hole

In order to validate the implementation of the Kerr-Schild metric in our numerical code, we perform a simulation of the relativistic wind accretion problem onto a rotating, Kerr black hole. The black hole rotation drags the spacetime with it, which breaks the axial symmetry of the problem, forcing us to perform a 3D simulation, which is not yet implemented in the code. To overcome this problem, we use polar-like coordinates, which use the radial and azimuthal angle ($\hat{\varphi}$) components. This allows us to study the evolution of a “planar” wind accreted by a rotating black hole. Although this is a rather unlikely flow configuration to find in nature, this might be encountered if a high degree of symmetry between the north and south poles is presented. This particular case has been studied by different authors, which allows us to compare our results with previous simulations. In particular, we follow closely the study presented by [Font et al. \(1999\)](#).

For this test, we use a 2D-planar mesh grid with 512×256 uniformly distributed cells over a domain $(r, \hat{\varphi} \in [1.1r_-, 50M] \times [0, 2\pi])$, where $r_- = M - \sqrt{M^2 - a^2}$ is the

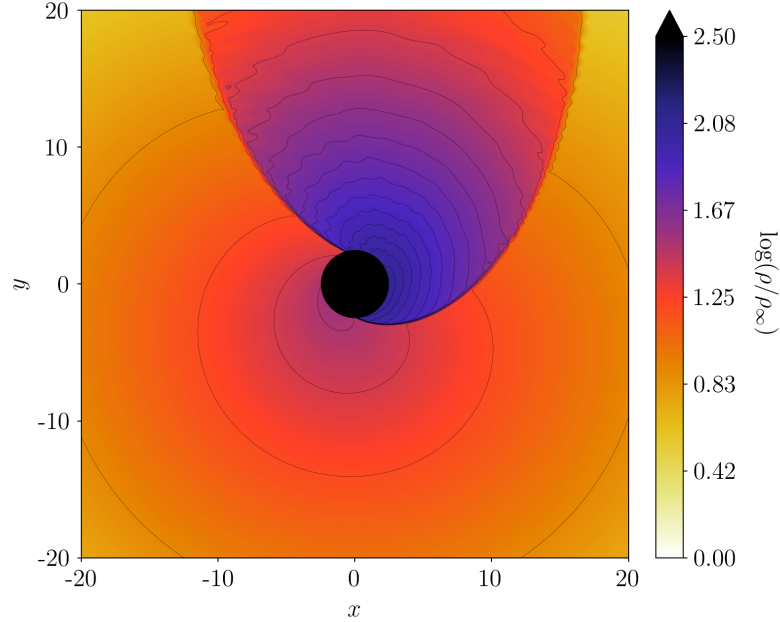


Figure 2.23: Contours of the rest-mass density at the steady-state for the planar wind accretion onto a Kerr black hole with spin parameter $a = 0.99M$. The fluid is described by an adiabatic index of $\gamma = 2$. The simulation uses Kerr-Schild coordinates, but the azimuthal angle is converted to the Boyer-Lindquist system to visualize the frame dragging around the rotating black hole.

inner horizon of the Kerr black hole. The wind distribution used for the initial and boundary conditions are similar to the one presented in the previous test, the wind velocity is $v_\infty = 0.5$, with a Mach number $\mathcal{M} = 5$ (for more detail see [Font et al., 1999](#)). The fluid is described by a perfect fluid with an adiabatic index $\gamma = 2$, which it is known as a stiff EoS. The black hole spin parameter is $a = 0.99M$.

In [Figure 2.23](#) we show contours of the rest-mass density of the evolution of the planar-wind accretion problem when the steady-state is reached. Even though we use the Kerr-Schild coordinates for the space-time metric, in order to visualize the frame dragging of the black hole, we convert the azimuthal angular coordinate to its equivalent in the Boyer-Lindquist coordinate system. As we can see from this figure, near the black hole the wind bow shock is dragged along with the rotating of the black hole (clockwise rotation). Far away from the black hole, the bow shocks recover the original motion of the wind. This result is in very good agreement with the one presented by [Font et al. \(1999\)](#).

Spherical accretion: Bondi, Michel, and rotating black holes

The study presented in this chapter explores the problem of steady-state, spherically symmetric gas accretion onto a Kerr black hole, considering all the possible regimes, from the non-relativistic case to the ultra-relativistic one.

In the first part of the article, we perform a detailed, quantitative comparison between the Bondi and Michel analytic solutions, exploring the models for different values of the adiabatic index (γ) and the dimensionless asymptotic temperature (Θ_∞). We derived appropriate analytic expressions for specific limits in the parameters, analysing when one solution reduces to the other. We also extend the Michel solution by considering a fully relativistic equation of state for an ideal monoatomic gas (Synge, 1957).





Also, using the AZTEKAS code, we extend the spherical accretion problem to the case of a rotating Kerr black hole, by means of 2.5D general relativistic hydrodynamic numerical simulations. We analyse the effect of the black hole spin on the mass accretion rate, as well as on the overall flow morphology. We run over 300 simulations for different values of the temperature, the spin parameter and two different equations of state.

The study presented in this chapter was published in MNRAS in 2021. The details of the paper are:

Aguayo-Ortiz A., Tejeda E., Sarbach O., López-Cámara D., 2021, MNRAS, 504, 5039. [doi:10.1093/mnras/stab1127](https://doi.org/10.1093/mnras/stab1127)



Spherical accretion: Bondi, Michel, and rotating black holes

Alejandro Aguayo-Ortiz ¹★, Emilio Tejada ², Olivier Sarbach ³ and Diego López-Cámara ⁴

¹*Instituto de Astronomía, Universidad Nacional Autónoma de México, AP 70-264, CDMX 04510, México*

²*Cátedras CONACyT – Instituto de Física y Matemáticas, Universidad Michoacana de San Nicolás de Hidalgo, Edificio C-3, Ciudad Universitaria, 58040 Morelia, Michoacán, Mexico*

³*Instituto de Física y Matemáticas, Universidad Michoacana de San Nicolás de Hidalgo, Edificio C-3, Ciudad Universitaria, 58040 Morelia, Michoacán, Mexico*

⁴*Cátedras CONACyT – Universidad Nacional Autónoma de México, Instituto de Astronomía, AP 70-264, CDMX 04510, México*

Accepted 2021 April 16. Received 2021 April 16; in original form 2021 February 24

ABSTRACT

In this work, we revisit the steady-state, spherically symmetric gas accretion problem from the non-relativistic regime to the ultrarelativistic one. We first perform a detailed comparison between the Bondi and Michel models, and show how the mass accretion rate in the Michel solution approaches a constant value as the fluid temperature increases, whereas the corresponding Bondi value continually decreases, the difference between these two predicted values becoming arbitrarily large at ultrarelativistic temperatures. Additionally, we extend the Michel solution to the case of a fluid with an equation of state corresponding to a monoatomic, relativistic gas. Finally, using general relativistic hydrodynamic simulations, we study spherical accretion on to a rotating black hole, exploring the influence of the black hole spin on the mass accretion rate, the flow morphology and characteristics, and the sonic surface. The effect of the black hole spin becomes more significant as the gas temperature increases and as the adiabatic index γ stiffens. For an ideal gas in the ultrarelativistic limit ($\gamma = 4/3$), we find a reduction of 10 per cent in the mass accretion rate for a maximally rotating black hole compared to a non-rotating one, while this reduction is of up to 50 per cent for a stiff fluid ($\gamma = 2$).

Key words: accretion, accretion discs – gravitation – hydrodynamics – methods: numerical.

1 INTRODUCTION

Gas accretion on to a compact gravitating object is one of the most studied problems in astrophysics. In one of the pioneering works of accretion theory, Bondi (1952) found an analytic solution for the spherically symmetric, steady-state accretion flow of an infinite gas cloud on to a Newtonian point-mass potential. This model has been widely extended and applied in many different fields in astrophysics, from the study of star formation to cosmology. See Armitage (2020) for a recent historical review of this subject.

One of the first studies of spherical accretion on to black holes was the extension of the Bondi solution into the general relativistic regime performed by Michel (1972). In this study, Michel found an analytic solution describing the spherical accretion of a polytropic gas on to a Schwarzschild black hole. A formal mathematical analysis of the Michel solution for a generic equation of state (EoS) can be found in Chaverra, Mach & Sarbach (2016). Following Michel's procedure, other authors have found semi-analytic generalizations for different types of spherically symmetric (non-rotating) black hole solutions (e.g. Chaverra & Sarbach 2015; Miller & Baumgarte 2017; Abbas & Ditta 2021; Yang et al. 2021). In a recent work, Richards, Baumgarte & Shapiro (2021a) explore the non-relativistic and ultrarelativistic limits of Michel's solution, mainly focusing on a gas with a stiff EoS (values of the adiabatic index larger than 5/3).

In past decades, the spherical accretion Bondi model has been revisited and extended, by including different additional physical ingredients. For example, some authors have taken into account the fluid's self-gravity by solving the coupled Einstein–Euler system in spherical symmetry, either with an analytical treatment (Malec 1999) or by performing numerical simulations (Lora-Clavijo, Guzmán & Cruz-Osorio 2013). Some works have considered the extension of a Bondi-like solution by introducing a low angular momentum fluid (Abramowicz & Zurek 1981; Proga & Begelman 2003; Mach, Piróg & Font 2018), finding a transition between a quasi-spherical accretion flow and the formation of a thick torus in the equatorial plane. Similarly, there have been works studying spherical accretion in the presence of magnetic fields, either assuming a central dipole (Toropin et al. 1999), or by including a 3D, large-scale weak magnetic field (e.g. Igumenshchev & Narayan 2002; Ressler et al. 2021). Together with magnetic fields, some works have included the effects of a radiation field, addressing the problem either with a simplified approach (Begelman 1978, where the author considered a radiation-dominated fluid) or with a self-consistent, radiative transfer treatment using numerical simulations (McKinney et al. 2014; Weih, Olivares & Rezzolla 2020). In this regard, there have also been studies that extract the shadow of the spherically accreted, optically thin cloud around a non-rotating black hole (Narayan, Johnson & Gammie 2019). Other studies have considered the effects of thermal conduction on magnetized spherical accretion flows (Sharma, Quataert & Stone 2008), vorticity (Krumholz, McKee & Klein 2005), or studied the spherical accretion of a relativistic collisionless kinetic (i.e. a Vlasov) gas (Rioseco & Sarbach 2017a).

* E-mail: aaguayo@astro.unam.mx

Recent works have also studied deviations away from spherical symmetry by introducing large-scale, small amplitude density anisotropies, finding that even a slight equator-to-poles density contrast can drastically modify Bondi's solution, giving rise to an inflow–outflow configuration consisting of equatorial accretion and a bipolar outflow. The resulting steady-state configuration, dubbed choked accretion, was studied in Aguayo-Ortiz, Tejada & Hernandez (2019) at the Newtonian level and, within a general relativistic framework, in Tejada, Aguayo-Ortiz & Hernandez (2020) and Aguayo-Ortiz, Sarbach & Tejada (2021) for Schwarzschild and Kerr black holes, respectively. In these series of works, it was found that the total mass flux that reaches the central accretor is of the order of magnitude of the corresponding Bondi mass accretion rate, while all the excess flux is redirected by the density gradient as outflow. Under the conditions explored so far, the Bondi mass accretion rate acts as a threshold value delimiting whether a given incoming flow becomes choked and prone to the ejection of a bipolar outflow.

Among the astrophysical applications of the spherical accretion model, we mention the study of gas accretion in an expanding Universe (Colpi, Shapiro & Wasserman 1996), the formation and growth of primordial black holes in the early stages of the Universe (Zel'dovich & Novikov 1967; Carr 1981; Karkowski & Malec 2013; Lora-Clavijo et al. 2013), and the accretion on to a mini black hole from the interior of a neutron star (Kouvaris & Tinyakov 2014; Génolini, Serpico & Tinyakov 2020; Richards, Baumgarte & Shapiro 2021b). On the other hand, the Bondi solution allows to estimate, by providing useful characteristic scale tools, the accretion and growth rate of the central supermassive black hole at the centre of galaxies (Maraschi, Reina & Treves 1974; Moscibrodzka 2006; Ciotti & Pellegrini 2017; Moffat 2020) and active galactic nuclei (Krolik & London 1983; Russell et al. 2013, 2015), where observations provide information only from regions far away from the central accretor. Similarly, the Bondi prescription is often used in cosmological simulations as a sub-grid model to estimate the accretion rate of gas on to supermassive black holes at galactic centres (Davé et al. 2019).

On the other hand, the analytic study of accretion flows on to rotating black holes has proven more challenging. Notably, Petrich, Shapiro & Teukolsky (1988) found a full analytic solution that describes the accretion of an irrotational, ultrarelativistic stiff fluid on to a rotating Kerr black hole. However, a main caveat of this solution is that it requires a rather specific, unphysical EoS, in which the sound speed equals the speed of light.¹ Assuming a more general EoS, Beskin & Pidoprygora (1995) studied the problem of spherical accretion on to a slowly rotating black hole by means of a perturbative analysis, and Pariev (1996) extended this work to the case of a rapidly rotating black hole. Both Beskin & Pidoprygora (1995) and Pariev (1996) considered only small deviations away from a Bondi background solution, in other words, these studies were limited to the case of non-relativistic values for the gas temperature at infinity. Even though this assumption might be reasonable in many astrophysical settings, the determination of the effect of the black hole spin on the accretion flow given an arbitrary gas temperature remains an open problem.

The applications of Bondi's model in most of the aforementioned works consider the gas accretion in the non-relativistic regime, not to mention that they neglect the rotation of the black hole. The reason for this is that the Bondi scale factors are estimated and measured

at distances far away from the central black hole, where it is safe to neglect relativistic effects. Nevertheless, in order to analyse the exact differences between the Bondi solution and the relativistic extension performed by Michel, as well as to assess the effect of the black hole spin, it is important to perform a quantitative study of the consequences of having relativistic gas temperatures and strong gravity fields in the vicinity of a rotating black hole.

In this work, we study the spherically symmetric gas accretion problem from the non-relativistic regime to the ultrarelativistic one, considering both rotating and non-rotating black holes.² We first perform a detailed comparison between the Bondi (1952) and Michel (1972) models by studying the behaviour of the relativistic solution across a wide range of values of the gas temperature. In particular, we discuss in detail the isothermal, the non-relativistic, and the ultrarelativistic limits of the Michel solution. We then extend Michel's solution to the case of a monoatomic gas obeying a relativistic EoS (Jüttner 1911; Taub 1948; Synge 1957). We also revisit Petrich et al. (1988)'s analytic solution and apply it to the particular case of a spherically symmetric accretion flow on to a Kerr black hole. Finally, by means of 2D general relativistic hydrodynamic simulations, we perform a quantitative study of the effect that the black hole spin has on the spherical accretion problem, focusing in particular on its effects on the mass accretion rate and on the flow morphology for several EoS. As part of this study, we show how, under the appropriate limits, the obtained numerical results coincide with the analytic solutions of Michel (1972) and Petrich et al. (1988).

The paper is organized as follows. In Section 2, we discuss the analytic solutions of Bondi (1952), Michel (1972), and Petrich et al. (1988). In Section 3, we present our numerical study of the spherical accretion of a perfect fluid on to a rotating black hole. Finally, in Section 4 we present a summary of the main results found in this article and give our conclusions. Technical details regarding the isothermal and non-relativistic limits of the Michel solution, the correct determination of the sonic surface for flows on rotating black holes, and orthonormal frames are discussed in appendices.

2 ANALYTIC SOLUTIONS

In this section, we review three analytic solutions describing a steady-state, spherical accretion flow on to a central massive object. We start by revisiting the Bondi (1952) solution and perform a detailed comparison with the relativistic extension found by Michel (1972). Then, we extend the latter solution by considering the more realistic EoS for a monoatomic relativistic gas introduced by Jüttner (1911). Finally, in order to give a description of accretion on to a rotating black hole, we also discuss the ultrarelativistic, stiff solution found by Petrich et al. (1988) in the case of spherical symmetry.

2.1 Bondi solution

In the Bondi (1952) analytic solution, one considers an infinite, spherically symmetric gas cloud accreting on to a Newtonian central object of mass M . At large distances, the gas cloud is assumed to be at rest and characterized by a homogeneous density ρ_∞ and pressure P_∞ . Note that, using an ideal gas EoS, we can alternatively describe

¹An ultrarelativistic stiff fluid corresponds to the relativistic generalization of an incompressible fluid in Newtonian hydrodynamics (Tejada 2018).

²By 'spherically symmetric' accretion problem on to a rotating black hole, we refer to the gas state being spherically symmetric asymptotically far away from the central black hole. Clearly, a rotating black hole does not admit a spherically symmetric solution at finite radii.

the state of the fluid in terms of the dimensionless gas temperature Θ defined as

$$\Theta = \frac{k_B T}{\bar{m} c^2} = \frac{P}{\rho c^2}, \quad (1)$$

where c is the speed of light, k_B Boltzmann's constant, and \bar{m} the average rest mass of the gas particles. As reference values, $\Theta \simeq T/(10^{13} \text{ K})$ for atomic hydrogen gas and $\Theta \simeq T/(10^{10} \text{ K})$ for an electron–positron plasma.

Under the assumptions of steady-state and spherical symmetry, the equations governing the Bondi accretion flow are the continuity equation and the radial Euler equation, i.e.

$$\frac{1}{r^2} \frac{d}{dr} (r^2 \rho v) = 0, \quad (2a)$$

$$v \frac{dv}{dr} + \frac{1}{\rho} \frac{dP}{dr} + \frac{GM}{r^2} = 0, \quad (2b)$$

where $v = |dr/dt|$ is the radial velocity of the fluid.

Considering that, in addition to the ideal gas EoS, the fluid obeys a polytropic relation $P = K\rho^\gamma$, with $K = \text{const.}$ and γ the adiabatic index (assumed to lie in the range $1 \leq \gamma \leq 2$), equations (2a) and (2b) can be integrated:

$$4\pi r^2 \rho v = \dot{M} = \text{const.}, \quad (3a)$$

$$\frac{v^2}{2} + \hat{h} - \frac{GM}{r} = \hat{h}_\infty = \text{const.}, \quad (3b)$$

where

$$\hat{h} = \left(\frac{\gamma}{\gamma - 1} \right) \frac{P}{\rho} = \frac{\gamma \Theta c^2}{\gamma - 1} = \frac{C^2}{\gamma - 1} \quad (4)$$

is the specific enthalpy and $C := \sqrt{\partial P / \partial \rho}$ the adiabatic speed of sound. Note that equation (4) is only valid for $\gamma > 1$. In the isothermal case, where $\gamma = 1$ and $\Theta \equiv \Theta_\infty = C_\infty^2/c^2$, equation (4) needs to be replaced by

$$\hat{h} - \hat{h}_\infty = C_\infty^2 \ln \left(\frac{\rho}{\rho_\infty} \right). \quad (5)$$

In addition to the steady-state and spherical symmetry conditions, Bondi also assumed that the flow is transonic, i.e. that there exists a radius r_s at which the fluid's radial velocity equals the local speed of sound. From equations (2a) and (2b), it is simple to calculate that the fluid at the sonic radius, r_s , satisfies

$$r_s = \frac{GM}{2v_s^2}, \quad (6a)$$

$$v_s = C_s = C_\infty \left(\frac{2}{5 - 3\gamma} \right)^{1/2}. \quad (6b)$$

The transonic solution found by Bondi is unique and maximises the accretion rate on to the central object, which, in turn, is given by

$$\dot{M}_B = 4\pi \lambda_B (GM)^2 \frac{\rho_\infty}{C_\infty^3}, \quad (7)$$

where λ_B is a numerical factor of order one that depends only on γ and is given by

$$\lambda_B = \frac{1}{4} \left(\frac{2}{5 - 3\gamma} \right)^{\frac{5-3\gamma}{2(\gamma-1)}}. \quad (8)$$

The accretion rate given in equation (7) is only valid for $\gamma \leq 5/3$. In order to discuss the $\gamma > 5/3$ case, one must necessarily account for general relativistic effects as we shall see in Section 2.2. Particular

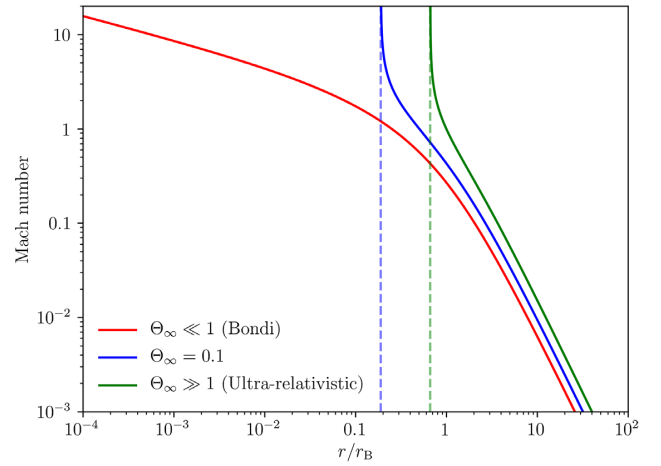


Figure 1. Mach number as a function of radius for the case of a $\gamma = 4/3$ polytrope and for three asymptotic temperatures. Note that the non-relativistic limit ($\Theta_\infty \ll 1$) corresponds to the Bondi solution. The vertical dashed lines show the location of the black hole's event horizon for $\Theta_\infty = 0.1$ and $\Theta_\infty \gg 1$. In all cases, the accretion flow has transitioned from subsonic to supersonic before crossing the event horizon. The horizontal axis is scaled in units of the Bondi radius $r_B = GM/C_\infty^2$.

values for λ_B in equation (8) are

$$\lambda_B(5/3) = 1/4,$$

$$\lambda_B(4/3) = 1/\sqrt{2} \simeq 0.71,$$

$$\lambda_B(1) = e^{3/2}/4 \simeq 1.12.$$

An interesting characteristic of the Bondi solution is that it can be written in a scale-free form with respect to the mass of the central object M and the thermodynamic state of the fluid (ρ_∞ , P_∞) by adopting $r_B = GM/C_\infty^2$, C_∞ , and ρ_∞ as units of length, velocity, and density, respectively. In other words, a global solution of the Bondi accretion problem is fully characterized once a given value for the adiabatic index γ is provided. Once the value for the mass accretion rate of Bondi's solution for a given γ is known, one can go back to equations (3a)–(4) and solve numerically the corresponding algebraic system of non-linear equations to obtain ρ , P , and v as a function of radius. See Fig. 1, for example, where we show the resulting Mach number ($\mathcal{M} = v/C$) as a function of radius, for the solution with $\gamma = 4/3$ (the red line).

2.2 Michel solution

As mentioned in the introduction, a general relativistic extension of the Bondi solution was presented by Michel (1972) who considered a Schwarzschild black hole as central accretor. In what follows, we review Michel's solution and discuss its main differences with respect to the Bondi model. It is important to remark that the Michel solution assumes an ideal gas EoS that follows a polytropic relation $P = K\rho^\gamma$, where, as in the previous section, ρ is the rest-mass density. Note, however, that this assumption is limited in general. For example, for a monoatomic ideal gas, it is only valid at non-relativistic temperatures (for which $\gamma = 5/3$), or at ultrarelativistic temperatures (for which $\gamma = 4/3$). In order to study the whole temperature domain in a consistent way, the polytropic restriction must be dropped and a relativistic EoS (as derived, for example, from relativistic kinetic theory, Sygne 1957) must be adopted. We

discuss the extension of the Michel solution to such a relativistic EoS in Section 2.3.

As in the Newtonian case, the governing equations are the conservation of mass and energy, i.e. the continuity equation and the requirement for the energy–momentum tensor to be divergence-free:

$$(\rho U^\mu)_{;\mu} = 0, \quad (9a)$$

$$(T^{\mu\nu})_{;\mu} = 0, \quad (9b)$$

where the semicolon stands for covariant derivative, U^μ is the fluid four-velocity, $T^{\mu\nu} = \rho h U^\mu U^\nu + p g^{\mu\nu}$ is the stress–energy tensor of a perfect fluid, $h = 1 + \tilde{h}$ is the specific relativistic enthalpy, and $g^{\mu\nu}$ denote the components of the inverse of the Schwarzschild metric:

$$ds^2 = - \left(1 - \frac{2M}{r}\right) dt^2 + \frac{dr^2}{1 - \frac{2M}{r}} + r^2 (d\theta^2 + \sin^2 \theta d\phi^2). \quad (10)$$

In order to ease the notation, we adopt geometrized units in which $G = c = 1$.

It is useful to recall at this point that, in the relativistic regime, the fluid’s sound speed is defined as

$$C^2 := \frac{\rho}{h} \frac{\partial h}{\partial \rho} = \frac{\gamma}{h} \frac{P}{\rho} = \frac{\gamma}{h} \Theta, \quad (11)$$

where, for the second equal sign, we have substituted the polytropic relation for a perfect fluid. Also, note that equation (11) can be recast to express h in terms of C or Θ as

$$h = \frac{1}{1 - C^2/(\gamma - 1)} = 1 + \frac{\gamma}{\gamma - 1} \Theta. \quad (12)$$

Under the conditions of steady-state and spherical symmetry, equations (9a) and (9b) reduce to

$$\frac{d}{dr} (r^2 \rho U^r) = 0, \quad (13a)$$

$$\frac{d}{dr} (r^2 \rho h U_r U^r) = 0, \quad (13b)$$

which, upon integration, can be rewritten as

$$4\pi r^2 \rho u = \dot{M} = \text{const.}, \quad (14a)$$

$$h \left(1 - \frac{2M}{r} + u^2\right)^{1/2} = h_\infty = \text{const.}, \quad (14b)$$

where $u = |U^r|$.

As in the Newtonian case, there exists a unique, transonic solution where the fluid is at rest asymptotically far away from the central object and that is regular across the black hole’s event horizon (Chaverra & Sarbach 2015; Chaverra et al. 2016). In order to find the defining conditions that are satisfied at the sonic point r_s , it is useful to combine equations (13a) and (13b) into the following differential equation:

$$\begin{aligned} & \left[1 - \frac{C^2}{u^2} \left(1 - \frac{2M}{r} + u^2\right)\right] u \frac{du}{dr} \\ &= -\frac{M}{r^2} + 2 \frac{C^2}{r} \left(1 - \frac{2M}{r} + u^2\right). \end{aligned} \quad (15)$$

By requiring that both sides of this equation vanish simultaneously at r_s , the following conditions arise:

$$r_s = \frac{1}{2} \frac{M}{u_s^2}, \quad (16a)$$

$$u_s^2 = \frac{C_s^2}{1 + 3 C_s^2}. \quad (16b)$$

If we introduce V as the norm of the fluid’s three-velocity as measured by local static observers, given in this case by

$$V = \left(1 - \frac{2M}{r}\right)^{-1} \left|\frac{U^r}{U^t}\right|, \quad (17)$$

from equations (16a) and (16b) it follows that $V_s = C_s$, which justifies calling r_s the sonic radius.

On the other hand, a relationship between the fluid state at infinity and at the sonic point can be obtained by substituting equations (16a) and (16b) into equation (14b). Doing this results in the following cubic equation for h_s (see Tejada et al. 2020, Appendix A)

$$h_s^3 - (3\gamma - 2)h_\infty^2 h_s + 3(\gamma - 1)h_\infty^2 = 0, \quad (18)$$

as well as the corresponding equation for the sound speed:

$$C_s^2 = \frac{1}{3} \left(\frac{h_s^2}{h_\infty^2} - 1\right). \quad (19)$$

The polynomial in equation (18) has three real roots but only one satisfies $h_s > 1$ and thus has physical meaning.³ This root is given by

$$h_s = 2 h_\infty \sqrt{\gamma - \frac{2}{3}} \sin\left(\Psi + \frac{\pi}{6}\right), \quad (20)$$

where

$$\Psi = \frac{1}{3} \arccos\left[\frac{3(\gamma - 1)}{2 h_\infty} \left(\gamma - \frac{2}{3}\right)^{-3/2}\right]. \quad (21)$$

Substituting these results back into equation (14a), the mass accretion rate can be expressed in terms of the asymptotic state of the fluid as

$$\dot{M}_M = 4\pi \lambda_M M^2 \frac{\rho_\infty}{C_\infty^3}, \quad (22)$$

where now the numerical factor λ_M depends not only on γ but also on the asymptotic state of the fluid and is given by

$$\lambda_M = \frac{1}{4} \left(\frac{h_s}{h_\infty}\right)^{\frac{3\gamma-2}{\gamma-1}} \left(\frac{C_s}{C_\infty}\right)^{\frac{5-3\gamma}{\gamma-1}}. \quad (23)$$

In Fig. 2, we show the dependence of λ_M on Θ_∞ for several different values of the adiabatic index γ . From this figure, it is clear that for $\gamma \leq 5/3$ in the non-relativistic limit ($\Theta_\infty \ll 1$) $\lambda_M \rightarrow \lambda_B$, as expected. We stress that the mass accretion rate given in equation (22) is only a measure for the flux of rest mass (particle number times the average rest-mass per particle) on to the central black hole. If interested in computing the actual growth rate of the black hole’s mass, the total energy advected by each fluid particle should be taken into account by computing the energy accretion rate (for further details see Aguayo-Ortiz et al. 2021). Since for the present problem the fluid is assumed to be at rest at infinity, one only needs to multiply \dot{M}_M in equation (22) by h_∞ to obtain this rate, i.e.

$$\dot{E}_M = 4\pi \lambda_M M^2 \rho_\infty \left(\frac{1}{\gamma \Theta_\infty} + \frac{1}{\gamma - 1}\right)^{5/2} \gamma \Theta_\infty. \quad (24)$$

In contrast to the Bondi solution, where the asymptotic speed of sound C_∞ is the only characteristic velocity, the Michel solution

³As long as $\gamma > 1$ and $h_\infty > 1$ the cubic polynomial on the left-hand side of equation (18) is positive for $h_s = 0$ and negative for $h_s = 1$, which implies that it has three real roots lying in the intervals $(-\infty, 0)$, $(0, 1)$ and $(1, \infty)$, respectively. See also Chaverra et al. (2016) and Richards et al. (2021a) for alternative ways to characterize the sonic radius using C_s^2 .

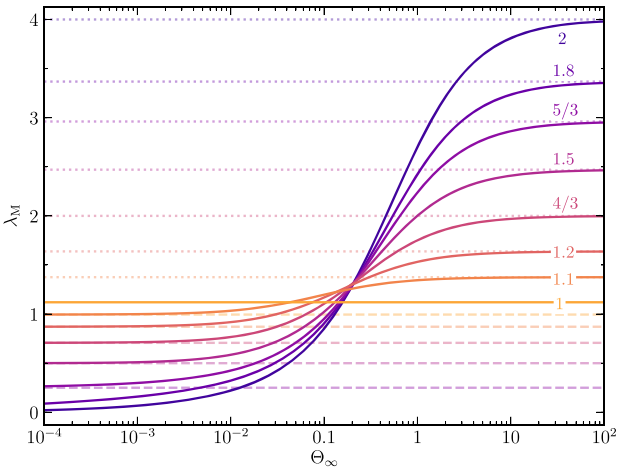


Figure 2. Numerical factor λ_M in the definition of the mass accretion rate of the Michel solution (equation 23) as a function of the dimensionless temperature Θ_∞ and for different values of γ as indicated by the labels on top of each curve. In the non-relativistic limit $\Theta_\infty \ll 1$ and for values of $\gamma \leq 5/3$, the curves asymptotically approach the values corresponding to λ_B (the dashed horizontal lines) of the Bondi solution in equation (7). In the ultrarelativistic limit $\Theta_\infty \gg 1$, the curves asymptotically approach the value given in equation (28).

naturally features the speed of light as an additional characteristic velocity. Consequently, the Michel solution can only be rendered scale invariant with respect to M and ρ_∞ . Therefore, in addition to the adiabatic index γ , to completely describe a given solution one must also specify \mathcal{C}_∞ or, alternatively, Θ_∞ . In what follows, we shall use Θ_∞ as the dynamically relevant parameter describing the state of the fluid asymptotically far away from the central object.

Examples of the resulting Mach number \mathcal{M} for a $\gamma = 4/3$ polytrope and various asymptotic temperatures: $\Theta_\infty = 10^{-4}$, 0.1 , 10^4 are also shown in Fig. 1. Note that, in the relativistic case we have defined

$$\mathcal{M} = \frac{V\sqrt{1-\mathcal{C}^2}}{\mathcal{C}\sqrt{1-V^2}}. \quad (25)$$

As we can see from this figure, in all cases the accretion flow transitions from being subsonic to supersonic before reaching the event horizon (indicated by the dashed lines). Also, the non-relativistic limit ($\Theta_\infty \ll 1$) coincides with the Bondi solution.

In Figs 3 and 4, we show, respectively, the sonic radius r_s and the mass accretion rate \dot{M}_M as functions of Θ_∞ and for several representative values of γ . By examining these figures, and analysing in detail the result obtained in equation (22), three interesting limits can be identified (isothermal, non-relativistic, and ultrarelativistic). In what follows, we list the main conclusions that can be drawn in each case, leaving detailed calculations to Appendix A.

2.2.1 Isothermal limit

The isothermal limit corresponds to the condition when $\gamma \rightarrow 1$. From Fig. 3 we note that, within this limit and for all temperatures Θ_∞ , the sonic radius recedes without limit from the event horizon. As we prove in Appendix A, the Michel solution (with a suitable rescaling) converges to the Newtonian Bondi solution with an EoS as given by equation (5). Thus, the isothermal case can be entirely described within the context of Newtonian physics, even for large temperatures that would ordinarily be associated with an ultrarelativistic regime.

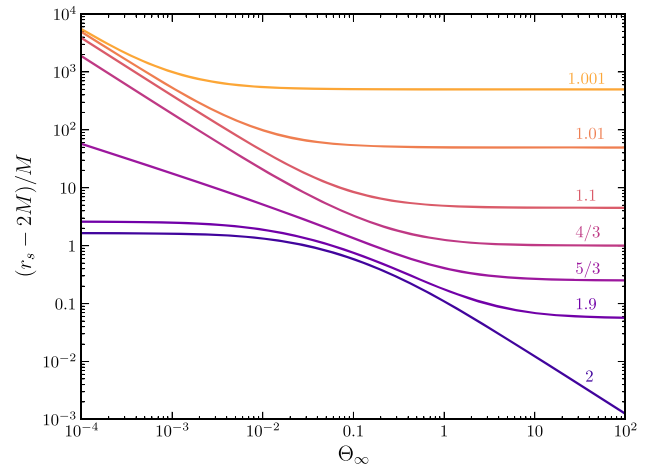


Figure 3. Distance between the sonic radius r_s and the black hole's event horizon radius $r_+ = 2M$ in the Michel solution as a function of the dimensionless temperature Θ_∞ and for different values of γ as indicated by the labels on top of each curve.

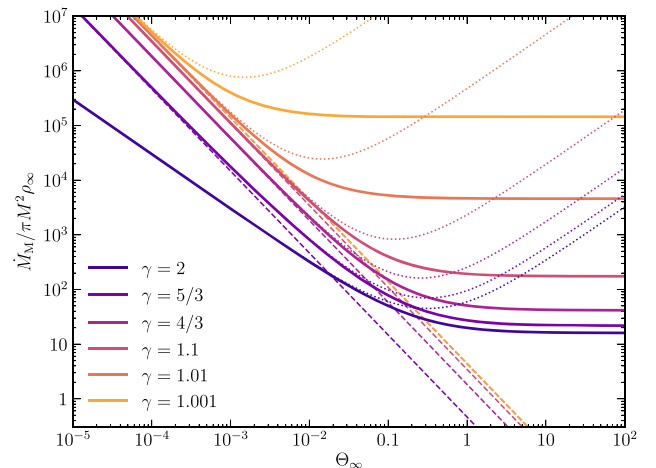


Figure 4. Mass accretion rate of the Michel solution \dot{M}_M as a function of Θ_∞ and for several representative values of γ . The dashed lines represent the corresponding Bondi mass accretion rate \dot{M}_B in cases with $\gamma \leq 5/3$. The dotted lines show the corresponding energy accretion rate (see equation 24). Note that once $\Theta_\infty \gtrsim 10^{-2}$, the differences between Bondi's and Michel's solutions become of order one and that this difference actually diverges as $\Theta_\infty \rightarrow \infty$.

2.2.2 Non-relativistic limit

This limit is described by the condition $\Theta_\infty \ll 1$ which implies $h_\infty \rightarrow 1$. As expected, and as is already apparent from Figs 1 and 2, in this limit the Michel solution converges to the Bondi one and expressions like the mass accretion rate (equation 22) reduce to their non-relativistic counterparts (equation 7). Nevertheless, this is only true for $\gamma \leq 5/3$. When $\gamma > 5/3$ a qualitative change takes place in Michel's solution. From Fig. 3 it is clear that for $\gamma < 5/3$ the value of r_s grows to infinity as Θ_∞^{-1} (as in the Bondi solution), while it converges to a finite distance from the event horizon for $\gamma > 5/3$. This is indicative that the cases with $\gamma > 5/3$ cannot be described with Newtonian physics, even in the low temperature limit. As shown in Appendix A, when $\Theta_\infty \ll 1$ and $\gamma > 5/3$, one finds that r_s converges to a finite value and $h_s > 1$, while the resulting mass accretion rate

converges to

$$\dot{M}_M \rightarrow \pi h_s^{\frac{3\gamma-2}{\gamma-1}} C_s^{\frac{5-3\gamma}{\gamma-1}} M^2 \rho_\infty C_\infty^{-\frac{2}{\gamma-1}}. \quad (26)$$

2.2.3 Ultrarelativistic limit

Finally, we discuss the case where $\Theta_\infty \gg 1$. From Fig. 3, it is clear that r_s converges to a finite value strictly larger than the event horizon radius for all values of γ , with the exception of a stiff EoS $\gamma = 2$, in which case $r_s \rightarrow r_+$ as $\Theta_\infty \rightarrow \infty$. Moreover, within this limit equation (20) reduces to

$$\frac{h_s}{h_\infty} \rightarrow \sqrt{3\gamma - 2}, \quad (27)$$

from which one also obtains $C_s/C_\infty \rightarrow 1$ and, hence,

$$\lambda_M \rightarrow \frac{1}{4}(3\gamma - 2)^{\frac{3\gamma-2}{2(\gamma-1)}}. \quad (28)$$

This limit value grows monotonically from $e^{3/2} \simeq 1.12$ to 4 as γ increases from 1 to 2 (see Fig. 2). From this result, and as is also clear from Fig. 4, one sees that the mass accretion rate becomes independent of Θ_∞ , rapidly approaching the constant value

$$\dot{M}_M \rightarrow \pi M^2 \rho_\infty (3\gamma - 2)^{\frac{3\gamma-2}{2(\gamma-1)}} (\gamma - 1)^{-3/2}. \quad (29)$$

In comparison, the Bondi mass accretion rate steadily decreases as $\Theta_\infty^{-3/2}$ as the temperature increases. Therefore, the difference between \dot{M}_B and \dot{M}_M becomes arbitrarily large when $\Theta_\infty \gg 1$. Also note that the energy accretion rate is not monotonic; it decreases for small temperatures but increases for large ones, eventually growing linearly in Θ_∞ (see equation 24 and Fig. 4). A similar qualitative behaviour has been observed for the accretion of a Vlasov gas (Rioseco & Sarbach 2017b). This is a remarkable difference between the Bondi and Michel solutions that, to the best of our knowledge, had not been discussed in the literature before.⁴ We can track the reason behind this behaviour by examining equations (7) and (22). Even though the factor C_∞^{-3} appears in both expressions, this factor behaves drastically differently when $\Theta_\infty \gtrsim 1$. For a perfect fluid in Newtonian hydrodynamics, one simply has $C^2 = \gamma \Theta$ and, thus, as the temperature increases so does the speed of sound without limit. Consequently, and as can be seen in Fig. 4, the Bondi mass accretion rate decreases to small values as the asymptotic gas temperature increases. On the other hand, in relativistic hydrodynamics one has

$$C^2 = \frac{\gamma(\gamma - 1)\Theta}{\gamma - 1 + \gamma\Theta},$$

that, in the limit $\Theta_\infty \gg 1$, implies that the speed of sound attains a maximum value given by $C_\infty \rightarrow \sqrt{\gamma - 1}$. Therefore, when $\Theta_\infty \gg 1$, \dot{M}_M becomes independent of Θ_∞ .

2.3 Michel solution with relativistic EoS

In the previous subsection, we revisited spherical accretion of a fluid that follows an ideal gas EoS and that is restricted to obey a polytropic relation. As mentioned before, assuming a monoatomic gas, this restriction is only valid in the non-relativistic limit ($\Theta_\infty \ll 1$) with

⁴In the comparison presented in Malec (1999) it is stated that, due to relativistic effects, the Michel mass accretion is enhanced by, at most, a factor of 10 compared to the Bondi value, whereas in our case this factor is unbounded. Note, however, that the adopted EoS in that work is $P = K\epsilon^\gamma$, with ϵ the energy density.

$\gamma = 5/3$ or in the ultrarelativistic one ($\Theta_\infty \gg 1$) with $\gamma = 4/3$. Nevertheless, as it was shown by Taub (1948), in the relativistic case ($\Theta_\infty \sim 1$) the polytropic restriction is not physical and has to be dropped.

In this subsection, we extend the Michel solution to the case of a gas obeying an appropriate EoS for the relativistic regime. As derived from relativistic kinetic theory, the EoS of an ideal, monoatomic gas can be written as (Jüttner 1911; Sygne 1957; Falle & Komissarov 1996)

$$h = \frac{K_3(1/\Theta)}{K_2(1/\Theta)}, \quad (30)$$

where, as before $\Theta = P/\rho$, and K_n is the n th-order modified Bessel function of the second kind.⁵

By additionally imposing the adiabatic condition (i.e. isentropic flow), one obtains the following relation between ρ and Θ (see e.g. Appendix B of Chavez Nambo & Sarbach 2020)

$$\frac{\rho}{\rho_\infty} = \frac{f(\Theta)}{f(\Theta_\infty)}, \quad (31a)$$

$$f(\Theta) = \Theta K_2(1/\Theta) \exp\left[\frac{1}{\Theta} \frac{K_1(1/\Theta)}{K_2(1/\Theta)}\right]. \quad (31b)$$

Meanwhile, the speed of sound in this case is given by

$$C^2 = \frac{\bar{\gamma}\Theta}{h}, \quad (32)$$

where $\bar{\gamma}$ is the effective adiabatic index, defined as

$$\bar{\gamma} := \frac{\rho}{P} \frac{\partial P}{\partial \rho} = \frac{h}{\Theta} C^2. \quad (33)$$

In contrast to the polytropic gas treatment discussed before, $\bar{\gamma}$ is not a constant but rather a function of the temperature that can be calculated explicitly as

$$\bar{\gamma} = \frac{h'}{h' + \Theta^2}, \quad (34)$$

where the prime refers to derivatives with respect to the argument of the modified Bessel functions, i.e. $h' = d[K_3(x)/K_2(x)]/dx$. With this definition of $\bar{\gamma}$ it follows that, as expected, for non-relativistic temperatures, $\bar{\gamma} \rightarrow 5/3$ while, in the ultrarelativistic limit, $\bar{\gamma} \rightarrow 4/3$.

In order to derive the appropriate governing equations in this case, we first notice that equation (18) should be replaced with

$$h_s^2 = h_\infty^2(1 + 3C_s^2) = h_\infty^2 \left[1 + \frac{3\Theta_s}{h_s} \left(\frac{h'_s}{h'_s + \Theta_s^2}\right)\right], \quad (35)$$

which, in contrast to equation (18), does not allow for an analytic solution. Nevertheless, it can be easily solved numerically using any standard root finding algorithm.

The corresponding mass accretion rate is obtained by evaluating equation (14a) at the sonic point, i.e.

$$\dot{M} = 4\pi r_s^2 \rho_s u_s, \quad (36)$$

and, by applying the conditions given by equations (16a) and (16b) that, together with equation (31a), result in

$$\dot{M} = \pi M^2 \rho_\infty \frac{(1 + 3C_s^2)^{3/2}}{C_s^3} \frac{f(\Theta_s)}{f(\Theta_\infty)}. \quad (37)$$

In practice, to calculate the resulting mass accretion rate for a given asymptotic state ($\rho_\infty, \Theta_\infty$), we numerically solve equation (35) to

⁵We adopt the definition of the modified Bessel function as presented in <https://dlmf.nist.gov/10.25>.

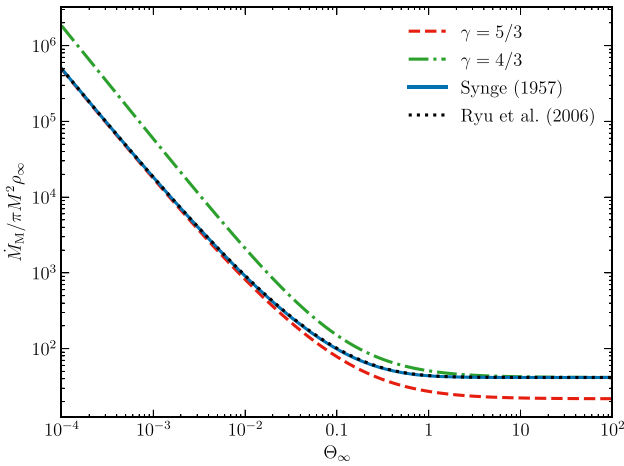


Figure 5. Mass accretion rate in Michel’s model for a gas described by a relativistic EoS (Sygne 1957). The resulting rate converges to a $\gamma = 5/3$ polytrope when $\Theta_\infty \ll 1$ while it behaves as a $\gamma = 4/3$ polytrope for $\Theta_\infty \gg 1$. Also shown is the result of using the approximation to the relativistic EoS by Ryu et al. (2006).

obtain Θ_s , from which we can compute h_s and C_s via equations (30) and (32), respectively, and then substitute these values into equation (37).

In Fig. 5, we show the resulting mass accretion rate as a function of Θ_∞ for the relativistic EoS and compare it with the corresponding values for $\gamma = 5/3, 4/3$ polytropes. From this figure, we can see that the result obtained with the relativistic EoS provides a smooth transition between the polytropic approximations as the temperature transitions from non-relativistic values to the ultrarelativistic regime. We also show the approximation to the relativistic EoS proposed by Ryu, Chattopadhyay & Choi (2006), where

$$h = 2 \frac{6\Theta^2 + 4\Theta + 1}{3\Theta + 2}, \quad (38)$$

and which provides an accurate estimate to the mass accretion rate to within 2 per cent. This comparison is relevant for this work, given that, for some of the numerical simulations presented in Section 3, we have adopted this proxy for the implementation of the relativistic EoS.

2.4 Ultrarelativistic, stiff fluid in Kerr space–time

The analytic solutions revisited so far consider a non-rotating black hole as the central accretor. The inclusion of the black hole’s spin breaks the spherical symmetry of the problem, resulting in a new scenario for which it is not clear whether it admits a closed, analytic solution in general.⁶ As mentioned in the Introduction, a notable exception is the solution derived by Petrich et al. (1988; PST henceforth), which we shall now briefly review. In that work, the authors found a full analytic solution for accretion on to a Kerr black hole that is, however, restricted to the special case of an ultrarelativistic stiff fluid. Within this approximation, the fluid rest-mass energy is neglected compared to its internal energy, while the

⁶Both Shapiro (1974) and Zanotti et al. (2005) have proposed a Michel-like solution for spherical accretion on to a rotating Kerr black hole that is built on the assumption that the polar angular velocity vanishes everywhere. However, as we show in Section 3, this condition is not satisfied for a general perfect fluid.

stiff condition means that a $\gamma = 2$ polytrope is being considered. Under these conditions, the thermodynamic variables of the fluid are simply related as

$$P = K \rho^2, \quad h = 2K \rho. \quad (39)$$

Moreover, the space–time metric is considered as fixed and corresponding to a Kerr black hole of mass M and spin parameter a , in other words, the accreting gas is assumed to be a test fluid with a negligible self-gravity contribution. With the further assumptions of steady-state and irrotational flow, the fluid is described as the gradient of a scalar potential Φ such that

$$h U_\mu = \Phi_{,\mu}, \quad (40)$$

and, by imposing the normalization condition of the four-velocity,

$$h = \sqrt{-\Phi_{,\mu} \Phi^{,\mu}}. \quad (41)$$

By substituting equation (40) into equation (9a), it follows that Φ satisfies the linear wave equation

$$\Phi_{,\mu}{}^{;\mu} = \frac{1}{\sqrt{-g}} (\sqrt{-g} g^{\mu\nu} \Phi_{,\mu})_{,\nu} = 0, \quad (42)$$

where $g^{\mu\nu}$ and $\sqrt{-g}$ are, respectively, the inverse and the determinant of the Kerr metric. In what follows, we shall adopt Kerr-type coordinates (t, r, θ, ϕ) in which the line element assumes the form

$$\begin{aligned} ds^2 = & - \left(1 - \frac{2Mr}{\rho^2}\right) dt^2 + \left(1 + \frac{2Mr}{\rho^2}\right) dr^2 \\ & + \frac{4Mr}{\rho^2} dt dr - \frac{4aMr}{\rho^2} \sin^2 \theta dt d\phi \\ & - 2a \left(1 + \frac{2Mr}{\rho^2}\right) \sin^2 \theta dr d\phi \\ & + \rho^2 d\theta^2 + \frac{\Sigma \sin^2 \theta}{\rho^2} d\phi^2, \end{aligned} \quad (43)$$

with the functions⁷

$$\rho^2 = r^2 + a^2 \cos^2 \theta, \quad (44a)$$

$$\Sigma = (r^2 + a^2)^2 - a^2 \Delta \sin^2 \theta, \quad (44b)$$

$$\Delta = r^2 - 2Mr + a^2. \quad (44c)$$

By requiring that the fluid is uniform and at rest asymptotically far away from the central object, the solution is given by Aguayo-Ortiz et al. (2021):

$$\Phi = h_\infty \left[-t + 2M \ln \left(\frac{r - r_-}{r_+ - r_-} \right) \right], \quad (45)$$

where $r_\pm = M \pm \sqrt{M^2 - a^2}$ are the roots of the equation $\Delta = 0$, with r_+ corresponding to the event horizon and r_- to the Cauchy horizon of the Kerr black hole. It is clear that Φ is regular everywhere outside the Cauchy horizon $r > r_-$.

Substituting the velocity potential in equation (45) into equation (40), leads to

$$\frac{h}{h_\infty} U^t = 1 + \frac{2Mr}{\rho^2} \left(\frac{r + r_+}{r - r_-} \right), \quad (46a)$$

⁷We use the same notation as Aguayo-Ortiz et al. (2021) and warn the reader that the symbol ρ refers to the metric coefficient defined in equation (44a) that should be distinguished from the similar-looking symbol ρ which denotes the rest-mass density.

$$\frac{h}{h_\infty} U^r = -\frac{2Mr_+}{\varrho^2}, \quad (46b)$$

$$\frac{h}{h_\infty} U^\theta = 0, \quad (46c)$$

$$\frac{h}{h_\infty} U^\phi = \frac{2aMr}{\varrho^2(r-r_-)}, \quad (46d)$$

while, by combining equations (39) and (41), one obtains

$$\frac{\rho}{\rho_\infty} = \frac{h}{h_\infty} = \sqrt{1 + \frac{2M}{\varrho^2} \frac{r(r+r_+) + 2Mr_+}{r-r_-}}. \quad (47)$$

Note that, although the fluid's four-velocity has a non-vanishing azimuthal component when $a \neq 0$, its angular momentum is zero since $U_\mu \xi_{(\phi)}^\mu = U_\phi = 0$, where $\xi_{(\phi)}^\mu = \delta_3^\mu$ is the Killing vector field associated with the axisymmetry of Kerr space–time. Also note that, both the four-velocity and the fluid density, are well-defined for all $r > r_-$ (including at the event horizon) but diverge as one approaches the Cauchy (inner) horizon $r \rightarrow r_-$.

In the non-rotating case equation (47) reduces to

$$\rho = \rho_\infty \sqrt{1 + \frac{2M}{r} + \left(\frac{2M}{r}\right)^2 + \left(\frac{2M}{r}\right)^3}, \quad (48)$$

which agrees with the findings in Section 4.2 of Chaverra & Sarbach (2015), with a compression rate of $\rho(r_+)/\rho_\infty = 2$ at the horizon. In the rotating case, this compression rate can be considerably higher, with $\rho(r_+)/\rho_\infty \rightarrow \infty$ in the maximally rotating limit $|a| \rightarrow M$.

The resulting mass accretion rate for the potential flow described by equation (45) is given by

$$\dot{M}_{\text{PST}} = 8\pi M r_+ \rho_\infty = 4\pi (r_+^2 + a^2) \rho_\infty. \quad (49)$$

Interestingly, from equation (49) we see that, in this special case of an ultrarelativistic stiff fluid, the resulting mass accretion rate is proportional to the event horizon area $A = 4\pi(r_+^2 + a^2)$ (Carroll 2003), and, consequently, for fixed M and ρ_∞ , \dot{M}_{PST} decreases as $|a|$ increases, having the finite limit $\dot{M}_{\text{PST}} = 8\pi M^2 \rho_\infty$ when $|a| \rightarrow M$. We also note that, for a non-rotating black hole, $\dot{M}_{\text{PST}} = 16\pi M^2 \rho_\infty$, which coincides exactly with the result given in equation (29) when $\gamma = 2$.

One inconvenience of assuming an ultrarelativistic stiff EoS, is that the speed of sound equals the speed of light, leading to a model with a limited applicability in astrophysics. Nevertheless, it represents a fully hydrodynamic exact solution that is very useful as a benchmark test for the validation of general relativistic hydrodynamic numerical codes in a fixed Kerr space–time. In the next section we relax this restriction on the EoS.

3 PERFECT FLUID IN KERR SPACE–TIME

In the previous sections we reviewed, along with the Bondi and Michel models, the analytic PST solution. This is the only exact solution that considers a rotating black hole as central accretor. This solution corresponds to an upper limit in both the temperature of the gas ($\Theta_\infty \gg 1$) and in the adiabatic index ($\gamma = 2$). Unfortunately, for a more general EoS, or even just a different value of γ , it is apparently not possible to find a closed analytic solution. Therefore, we explore the spherical accretion of a perfect fluid with a more general EoS on to a rotating Kerr black hole by means of general

relativistic hydrodynamic numerical simulations.⁸ Specifically, we shall focus on the dependence of the resulting accretion flow on the spin parameter a , the asymptotic gas temperature Θ_∞ , and the fluid EoS. We also compare the results with the analytic solutions presented in Section 2.

3.1 Numerical set-up and code description

We perform a total of 311 numerical simulations using the open source code AZTEKAS.⁹ This code solves the general relativistic hydrodynamic equations, written in a conservative form using a variation of the ‘3+1 Valencia formulation’ (Banyuls et al. 1997) for time-independent, fixed metrics (Del Zanna et al. 2007). The spatial integration is carried out using a grid-based, finite volume scheme coupled with a high resolution shock capturing method for the flux calculation, and a monotonically centred second order spatial reconstructor. The time integration is performed using a second order total variation diminishing Runge–Kutta method (Shu & Osher 1988). The evolution of the equations is performed on a Kerr background metric, using the same horizon penetrating Kerr-type coordinates as in Section 2.4.

The set of primitive variables used in the code consists of the rest-mass density ρ , pressure P , and the three-velocity vector v_i as measured by Local Eulerian Observers associated with the chosen coordinate system. Both ρ and P are thermodynamic quantities measured at the co-moving reference frame, and the vector v_i is computed as $v_i = \gamma_{ij} v^j$, where

$$v^i = \frac{U^i}{\alpha U^t} + \frac{\beta^i}{\alpha}, \quad i = r, \theta, \phi \quad (50)$$

with α , β^i and γ_{ij} the lapse, shift vector, and three-metric of the 3+1 formalism (Alcubierre 2008), respectively.

3.2 Initial and boundary conditions

For all the simulations, we adopt a spherical axisymmetric 2.5D¹⁰ domain with coordinates $(r, \theta) \in [\mathcal{R}_{\text{in}}, \mathcal{R}_{\text{out}}] \times [0, \pi/2]$, where \mathcal{R}_{in} and \mathcal{R}_{out} are the inner and outer radial boundaries, respectively. We use a uniform polar grid and an exponential radial grid (see Aguayo-Ortiz et al. 2019, for details) and fix the numerical resolution to 128×64 grid cells, unless otherwise stated. Reflective boundaries are set at $\theta = 0$ and $\theta = \pi/2$. The inner radial boundary, at which we impose a free-outflow condition, is placed within the event horizon ($\mathcal{R}_{\text{in}} < r_+$). On the other hand, the outer radial boundary is set with the corresponding Michel solution. With this external boundary condition, the domain size must be sufficiently large as to avoid introducing numerical artefacts in the resulting steady-state solution. By performing a quantitative study varying \mathcal{R}_{out} , we find that we can be confident of the independence on the domain size

⁸Recall that by ‘spherical accretion on to a rotating black hole’ we mean a solution which is asymptotically spherically symmetric.

⁹The code can be downloaded from <https://github.com/aztekas-code/aztekas-s-main>. See Aguayo-Ortiz, Mendoza & Olvera (2018), Tejada & Aguayo-Ortiz (2019), Aguayo-Ortiz et al. (2019), and Tejada et al. (2020), for further details regarding the characteristics, test suite and discretization method of AZTEKAS.

¹⁰The 2.5D scheme consists in evolving the full 3D system of equations, but imposing the condition that the fields are independent of ϕ , such that it is sufficient to consider a 2D grid. The code is not precisely 2D because the azimuthal component v^ϕ of the three-velocity is allowed to evolve instead of being set to zero.

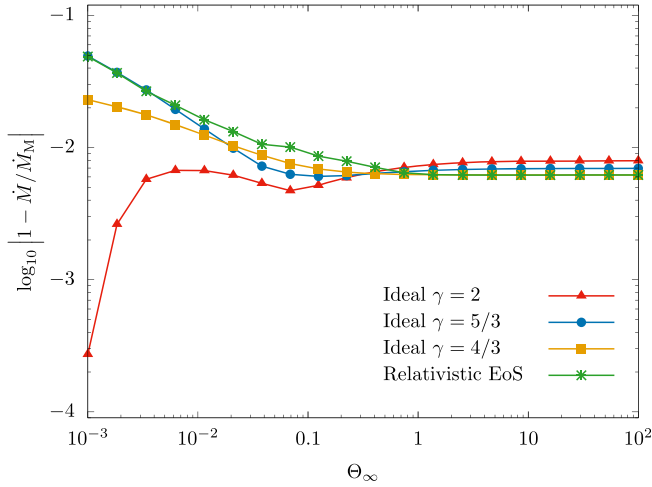


Figure 6. Relative error in the mass accretion rate between the numerical results (\dot{M}) and the Michel analytic solution (\dot{M}_M), as a function of the asymptotic temperature Θ_∞ . We plot the results for $\gamma = 4/3, 5/3, 2$ and the relativistic EoS.

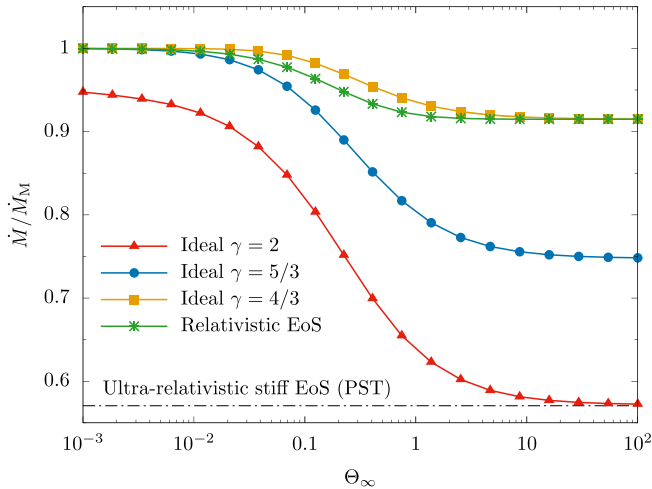


Figure 7. Mass accretion rate as a function of Θ_∞ , for a rotating black hole with $a/M = 0.99$. The first three lines show the results for an ideal gas EoS with different values of γ , and the last line represents the relativistic EoS. The black-dashed line represents the ultrarelativistic stiff EoS lower limit. The mass accretion rate is normalized using the corresponding value in the non-rotating case (\dot{M}_M).

by taking $\mathcal{R}_{\text{out}} = 10 r_B$ in the non-relativistic regime ($\Theta_\infty \lesssim 10^{-2}$), and $\mathcal{R}_{\text{out}} = 40 r_s$ in the relativistic one ($\Theta_\infty \gtrsim 10^{-2}$), where r_B and r_s are the Bondi and sonic radii, respectively. In other words, for a given Θ_∞ , we set $\mathcal{R}_{\text{out}} = 10 \max(r_B, 4r_s)$. In what regards the initial conditions, we start our simulations with a static ($v_i = 0$) and uniform ($\rho = \rho(\mathcal{R}_{\text{out}})$, $P = P(\mathcal{R}_{\text{out}})$) gas distribution.

The mass accretion rate evolves as a function of time with periodic and exponentially damped oscillations (in agreement with the results from Aguayo-Ortiz et al., 2019). The numerical simulations are left to run until the time variation of the resulting mass accretion rate drops below 1 part in 10^4 , a criterion that we take as signalling the onset of the steady-state condition. We compute the mass accretion rate according to

$$\dot{M} = 4\pi \int_0^{\pi/2} \rho \Gamma \left(v^r - \frac{\beta^r}{\alpha} \right) \sqrt{-g} d\theta, \quad (51)$$

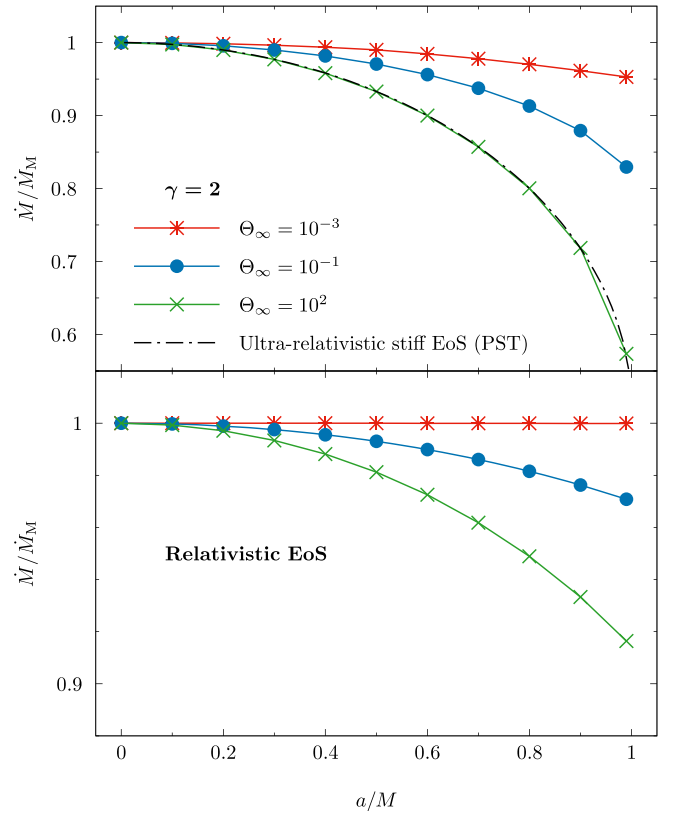


Figure 8. Mass accretion rate as a function of the spin parameter for the $\gamma = 2$ (top panel) and the relativistic EoS (bottom panel), and different values of the asymptotic temperature Θ_∞ . The mass accretion rate is normalized by its value in the non-rotating case \dot{M}_M . The black-dashed line in the top panel represents the solution obtained with the ultrarelativistic stiff EoS (PST) model.

where $\Gamma = 1/\sqrt{1 - \gamma_{ij} v^i v^j}$ is the Lorentz factor.

3.3 Code validation

In order to validate our numerical results, we exploit the known analytic solutions discussed in Section 2 and use them as benchmark in our test runs.

Considering first a non-rotating black hole, in Fig. 6 we show the relative error in the steady-state mass accretion rate between the Michel analytical solution (\dot{M}_M) and the numerical results as a function of the asymptotic temperature Θ_∞ . We show the results for $\gamma = 4/3, 5/3, 2$ as well as the fit to the relativistic EoS given by Ryu et al. (2006). For simplicity, in what follows we shall refer to this fit as the ‘relativistic EoS’. In all cases the numerical error is less than 5 per cent in the non-relativistic regime ($\Theta_\infty \ll 1$) and less than 1 per cent in the relativistic regime ($\Theta_\infty \gg 1$), which is consistent with the numerical resolution being used.

We also perform additional numerical tests to validate the implementation of a non-zero spin parameter in our set-up. In order to approximate the ultrarelativistic stiff EoS and to compare with the PST analytic solution, we perform simulations using an adiabatic index $\gamma = 2$ and an asymptotic temperature $\Theta_\infty = 10^2$, for different values of a . The result of this comparison is shown in Figs 7 and 8, from where we find an excellent agreement between both solutions, with a relative error of less than 1 per cent. We explain these two figures in further detail in the next subsection.

3.4 Results

In order to quantify the spherical accretion flow on to a rotating Kerr black hole and analyse its dependence on the black hole's spin parameter a , we perform a series of simulations varying both a and Θ_∞ , both for a polytrope with $\gamma = 4/3, 5/3, 2$ as well as for the relativistic EoS.

For the spin parameter, we take a uniformly distributed set of values between $a = 0$ (non-rotating black hole) and $a/M = 0.99$. On the other hand, for the temperatures we choose a list of representative values between $\Theta_\infty = 10^{-3}$ and 10^2 , in order to study the behaviour of the solution in the transition from the non-relativistic regime to the ultrarelativistic one.

3.4.1 Temperature dependence: rotating black hole case

We explore the variation in the mass accretion rate for the rotating black hole case $a > 0$, as compared with the non-rotating case. We find that the larger difference is obtained for a maximally rotating black hole, as is to be expected considering the analytic PST solution (see equation 49).

In Fig. 7, we show the steady-state mass accretion rate as a function of the asymptotic temperature (for $\gamma = 4/3, 5/3, 2$ and the relativistic EoS) for the case of a rotating black hole with a spin parameter $a/M = 0.99$. The mass accretion rate is normalized by the corresponding Michel value ($a = 0$). As can be seen from this figure, all simulations are bounded between the non-rotating black hole value ($\dot{M}/\dot{M}_M = 1$) and the ultrarelativistic stiff EoS case ($\dot{M}/\dot{M}_M \simeq 0.57$). In the non-relativistic regime ($\Theta_\infty \ll 1$), the mass accretion rate for all γ values converges to the corresponding Michel solution, although this convergence appears to be much slower in the case $\gamma = 2$. Thus, we conclude that in this regime the effects of the spin on \dot{M} are negligible for $\gamma \leq 5/3$. In the ultrarelativistic regime ($\Theta_\infty \gg 1$), \dot{M} decreases by a factor of $\sim 10, 25$, and 43 per cent for the solutions with $\gamma = 4/3, 5/3$, and 2, respectively. Note how the solution for $\gamma = 2$ in the $\Theta_\infty \gg 1$ limit matches the ultrarelativistic stiff analytical value.

3.4.2 Spin dependence

In order to study the dependence of the spherical accretion solution on the spin parameter, we perform a series of simulations varying the value of a . For these runs, we also consider three values of the asymptotic temperature corresponding to the non-relativistic, intermediate, and ultrarelativistic regimes. In Fig. 8, we show our analysis of this dependence adopting two fluid models: the stiff fluid ($\gamma = 2$, top panel) and the relativistic EoS (bottom panel). The former case allows us to study the behaviour of the simulations for an extreme adiabatic index (for which the spin effects are more noticeable), while the latter constitutes a more realistic EoS. As in Fig. 7, the $\gamma = 2$ and $\Theta_\infty = 10^2$ case matches the analytic PST solution, providing yet another code validation, but now for a wide range of spin values.

As can be seen in Fig. 8, the mass accretion rate decreases as the spin parameter a increases. Moreover, the dependence on a becomes more significant as higher temperatures are considered. In the case of the stiff fluid (top panel), we find that the mass accretion rate is reduced by up to a factor of 50 per cent for a maximally rotating black hole compared to a non-rotating one. On the other hand, this reduction is at most of ~ 10 per cent in the case of the relativistic EoS (bottom panel). It is interesting to note that all the numerical results follow a qualitatively similar dependence on a as the analytic

PST solution: the accretion rate decreasing as the spin parameter increases.¹¹

3.4.3 Global effect of the spin

The dependence on the spin parameter has been studied so far by considering only its effect on the mass accretion rate. This is important since one of the most relevant results of any accretion model is the associated mass growth of the central object. Nevertheless, it is also of interest to study the overall morphology of the resulting accretion flow in order to understand the global effect of the spin.

To study the effect of the spin on the velocity field, as well as on the rest-mass density profile, we take as a representative example one of the simulations discussed in Section 3.4.2, namely that of a fluid obeying the relativistic EoS, with an asymptotic temperature $\Theta_\infty = 0.1$, and a spin parameter $a/M = 0.99$.

In Fig. 9, we show the steady-state rest-mass density ρ/ρ_∞ at the equatorial plane and the spatial components of the velocity field $U^{\hat{r}}, U^{\hat{\theta}}, U^{\hat{\phi}}$ (measured in an orthonormal reference frame, see Appendix B). The solid black arrows show the fluid streamlines, and the solid white line represents the location of the sonic surface (see Appendix C for its invariant determination). Note that the azimuthal flow shown in the rest-mass density and in the $U^{\hat{\phi}}$ field, is due exclusively to the frame dragging of the black hole.

As can be seen from Fig. 9, the polar component $U^{\hat{\theta}}$ exhibits a quadrupolar-like morphology, which is in contrast to the non-rotating case where $U^{\hat{\theta}} = 0$. This is interesting since in the PST solution this component of the four-velocity is exactly zero, independent of the value of the spin parameter (see equation 46c). On the other hand, the isocontours for $U^{\hat{r}}$ depart from spherical symmetry close to the event horizon, in particular inside the sonic surface. However, apart from the inspiraling effect due to the frame dragging, the fluid streamlines do not deviate significantly from those of the spherically symmetric inflow.

In order to analyse the behaviour of the fluid velocity, we compute the latitudinal average at each radius, defined as

$$\langle U^{\hat{i}} \rangle_\theta = \frac{\int_0^{\pi/2} U^{\hat{i}} \sqrt{-g} \, d\theta}{\int_0^{\pi/2} \sqrt{-g} \, d\theta}. \quad (52)$$

In Fig. 10, we show this average for $U^{\hat{r}}$ (upper-panel) and $U^{\hat{\theta}}$ (lower-panel) as a function of r for $a/M = 0.99$ and $\Theta_\infty = 0.1$. We also use two different numerical resolutions in order to show that our results are robust with respect to the grid size. The black-dotted line represents the non-rotating Michel solution in the radial velocity case (top-panel), and the average numerical error that we obtain from our simulations in the polar velocity (bottom panel). We find that the average of $U^{\hat{r}}$ is larger for a rotating black hole than for a non-rotating one. Also, in the rotating case, the average of $U^{\hat{\theta}}$ is comparable in size to $U^{\hat{r}}$ at the horizon and decreases approximately as $1/r^3$ for $r > r_+$. The fact that $U^{\hat{\theta}}$ is different from zero is relevant

¹¹In this regard, it is interesting to mention the recent work by Cieřlik & Mach (2020) who study the spherical accretion of a Vlasov gas on to a (charged) Reissner-Nordström black hole which is often considered as a simpler model for the Kerr space-time since it shares many of its qualitative properties. In this model, the charge parameter plays the role of the spin parameter, and similar to our findings, the authors of that study find that the mass accretion rate decreases as the charge parameter increases.

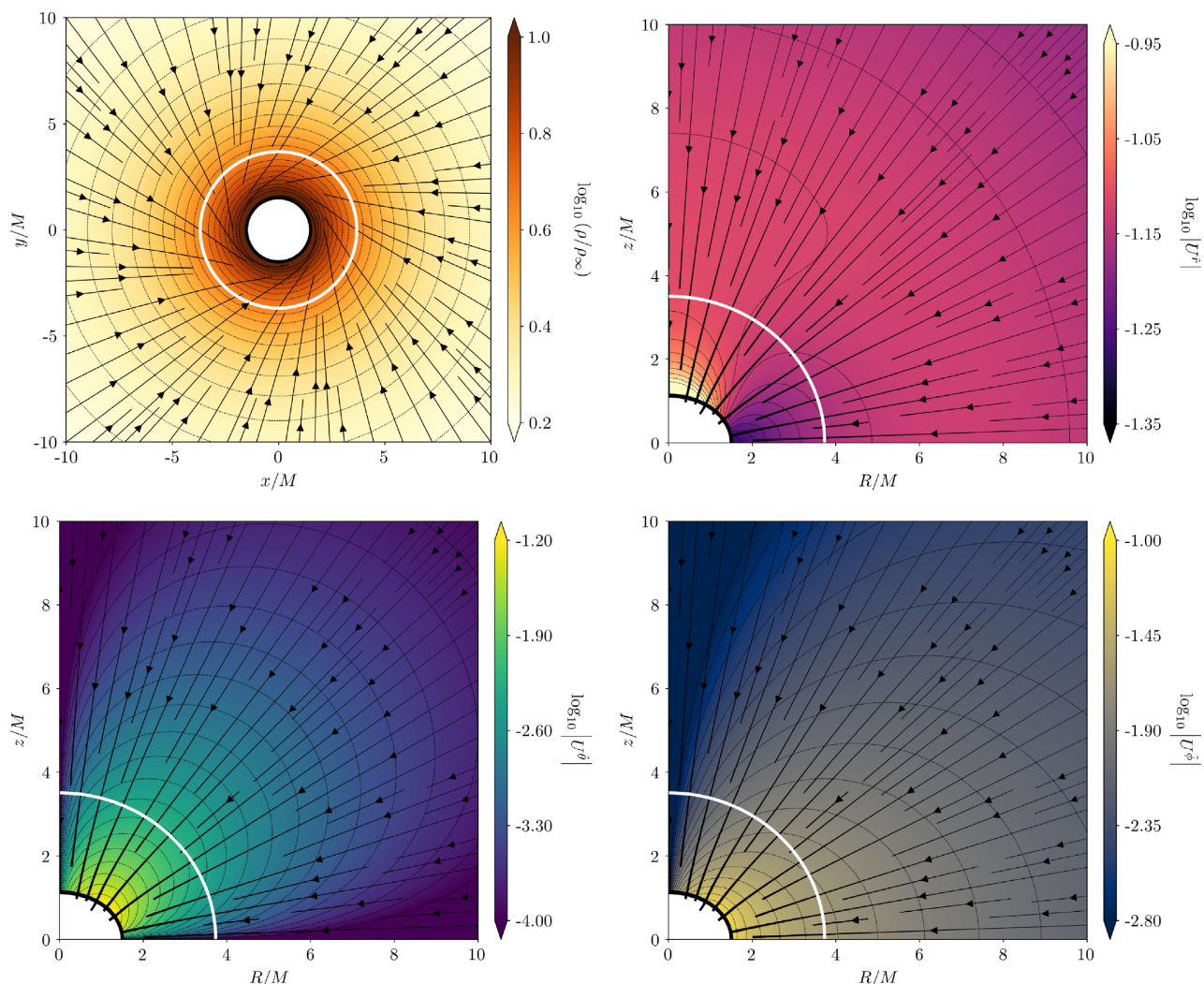


Figure 9. Isocontour plots of the steady state of a simulation of the spherical accretion problem on to a rotating black hole with $a/M = 0.99$, for a gas obeying the relativistic EoS and $\Theta_\infty = 0.1$. The figures show the normalized rest-mass density ρ/ρ_∞ at the equatorial plane (top left) and the spatial orthonormal components of the four-velocity [U^r (top right), U^θ (bottom-left), and U^ϕ (bottom right)] projected on the R - z plane, where $R = \sqrt{r^2 + a^2} \sin \theta$ and $z = r \cos \theta$. The black solid arrows show the fluid streamlines, whereas the black-dashed lines the isocontour levels. The white solid line shows the location of the sonic surface, see Fig. 11 for further details. The outer boundary in this simulation is $\mathcal{R}_{\text{out}} \approx 147 M$.

in view of previous work (see Shapiro 1974; Zanotti et al. 2005), which discuss spherical accretion models in Kerr space-time based on the assumption $U^\theta = 0$.

Finally, we explore in more detail the effect of the black hole spin on the sonic surface. As shown in Appendix C, this surface can be defined in an invariant way as those points at which the magnitude of the three-velocity as measured by zero angular momentum observers (ZAMOs, Bardeen 1970) equals the local sound speed. In Fig. 11, we show the shape of the sonic surface by plotting the sonic radius as a function of the polar angle, for different values of the spin parameter. As can be seen from this figure, for the non-rotating case the sonic surface corresponds to the sphere $r_s = \text{const.}$, as expected since in this case the ZAMOs reduce to static observers. As the spin parameter increases, the sonic surface contracts unevenly giving rise to a slightly oblate shape in the $R - z$ plane. This flattening at the poles is more significant as $a/M \rightarrow 1$. For the maximum value explored in this work ($a/M = 0.99$), the equator-to-poles difference in radii is of around 5 per cent.

4 SUMMARY AND CONCLUSIONS

In this work, we have studied the spherical accretion problem from the non-relativistic regime to the ultrarelativistic one, for both rotating and non-rotating black holes. We have focused on steady-state solutions for a perfect fluid obeying an ideal gas EoS and parametrized its thermodynamic state far away from the black hole using the dimensionless temperature $\Theta_\infty = P_\infty/(\rho_\infty c^2)$. We have also assumed that the gravitational field is dominated by the black hole, such that the fluid’s self-gravity can be neglected. We first revisited the analytic solutions of Bondi (1952) and Michel (1972), and provided a quantitative comparison between them. Next, we extended Michel’s solution to the case of an ideal gas obeying a relativistic EoS (Jüttner 1911; Sygne 1957). Finally, we studied the spherical accretion problem in the case of a rotating black hole, first by writing the exact ultrarelativistic, stiff solution (Petrich et al. 1988) in the spherically symmetric case and then by performing general relativistic hydrodynamic simulations of a general perfect fluid.

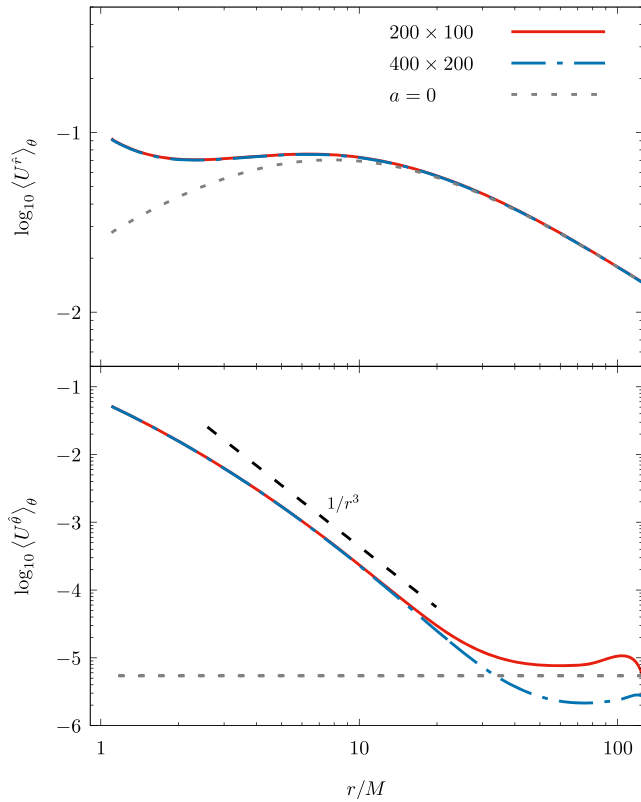


Figure 10. Solutions of the angular averaged values of $U^{\hat{r}}$ (top panel) and $U^{\hat{\theta}}$ (bottom panel) as a function of r , for $a/M = 0.99$ and for two different resolutions. The parameters used in this plots are $\Theta_{\infty} = 0.1$ and the relativistic EoS. The grey-dotted lines show the Michel’s $a = 0$ solution in the top panel, and the average numerical error in the polar velocity in the bottom panel. Note that the difference between the two resolutions in the bottom panel for large radii is of the same order as the average numerical error. The black dashed represents the approximate behaviour of $\langle U^{\hat{\theta}} \rangle_{\theta}$.

Concerning the comparison between the Bondi and Michel solutions, we have shown rigorously that Michel’s solution reduces to the Bondi one when the non-relativistic limit is considered ($\Theta_{\infty} \ll 1$) and when $\gamma \leq 5/3$, as expected. Importantly, when $\gamma > 5/3$, the obtained global solution is intrinsically relativistic, even for non-relativistic asymptotic temperatures, in accordance with Richards et al. (2021a). Additionally, we derived appropriate analytic expressions for the mass accretion rate for the Michel solution in the ultrarelativistic limit ($\Theta_{\infty} \gg 1$). Moreover, within this limit and for a stiff EoS ($\gamma = 2$), we have shown that the resulting mass accretion rate coincides exactly with the result obtained by Petrich et al. (1988). Furthermore, we have shown that in the isothermal limit, in which $\gamma \rightarrow 1$, the entire accretion flow can be described in a Newtonian way, i.e. the Michel solution reduces to the Bondi one for all asymptotic temperatures Θ_{∞} .

Regarding the relativistic regime, we have found that the difference between the mass accretion rates as obtained in the Bondi and Michel solutions grows arbitrarily as the asymptotic temperature increases. The reason behind this relies in the fact that, at ultrarelativistic temperatures ($\Theta_{\infty} \gg 1$), the Michel mass accretion rate reaches a minimum constant value, whereas the Bondi one decreases without limit (Fig. 4). The discrepancy between these two values is already noticeable (of order one) for $\Theta_{\infty} \sim 0.1$. Moreover, we have extended the Michel solution by considering the relativistic EoS of an ideal,

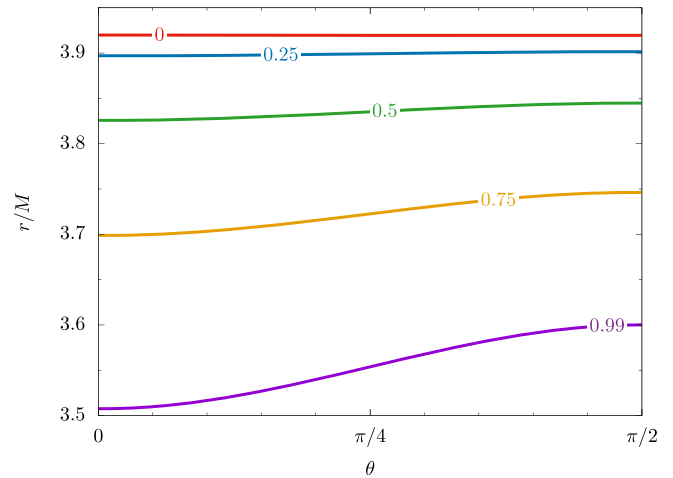


Figure 11. Resulting sonic surface as a function of the polar angle, for different values of the spin parameter a/M (as indicated by the label on top of each curve). All cases correspond to the relativistic EoS with $\Theta_{\infty} = 0.1$. This figure shows that, for a rotating black hole, the sonic surface contracts to smaller radii and ceases to be characterized by a constant radius.

monoatomic gas (Jüttner 1911; Synge 1957), which is a more accurate description for a perfect fluid in this regime (Fig. 5).

We have also extended, by means of numerical simulations, the Michel solution to the case of a rotating Kerr black hole. The main purpose of this numerical exploration was to analyse the effect of the black hole spin on the mass accretion rate and the flow morphology. We ran a series of 2.5D general relativistic hydrodynamic simulations varying different parameters including the asymptotic temperature Θ_{∞} , the gas EoS, and the spin parameter of the black hole. We have validated our results by comparing them with the known analytic solutions, as well as by performing a series of careful resolution and domain-size convergence tests.

The numerical results show that the influence of the black hole’s rotation is only larger than a few percent in the relativistic regime ($\Theta_{\infty} \gtrsim 0.1$) or for $\gamma > 5/3$ (Fig. 7). As the spin parameter increases, the mass accretion rate decreases as compared with the non-rotating case. This effect is stronger for larger values of Θ_{∞} and γ . Nevertheless, even in the most extreme case ($\Theta_{\infty} \gg 1$ and $\gamma = 2$), the reduction in the accretion rate is no larger than 50 per cent (Fig. 8). The simulations in this work allowed us to study the morphology of the fluid’s density profile and velocity field near the event horizon, showing in the latter a behaviour considerably different from the non-rotating black hole case, even for mildly relativistic temperatures. We have shown that the black hole rotation induces an azimuthal velocity component (entirely due to relativistic frame-dragging), a non-zero polar angular velocity component, as well as a non-spherically symmetric radial component (Figs 9 and 10). Furthermore, the sonic surface ceases to be characterized by a constant radial coordinate (Fig. 11).

Our results imply that the relativistic features of a black hole can be safely neglected when considering the spherical accretion of a fluid with a non-relativistic asymptotic temperature ($\Theta_{\infty} \ll 1$) and $\gamma \leq 5/3$. However, this is not true for relativistic and ultrarelativistic values of the asymptotic temperature ($\Theta_{\infty} \gtrsim 0.1$). In this regime, a proper relativistic description must be used in order to compute the mass accretion rate, as the Bondi and Michel solutions lead to completely different values. On the other hand, the black hole’s rotation, even in the ultrarelativistic case and for a close-to-maximally rotating black hole, does not change the resulting mass accretion rate by more

than 50 per cent (for $\gamma \leq 2$) with respect to the non-rotating case. For a more realistic EoS ($\gamma = 4/3$) this change is even smaller and lies below 10 per cent. Thus, it is safe to neglect the black hole spin when considering an order of magnitude estimation, but it should be taken into account when performing a more accurate calculation.

The results presented in this work could be useful for studying spherical accretion on to rotating and non-rotating black holes in extreme environments where the ambient gas approaches relativistic temperatures ($\Theta_\infty \sim 1$), or that are well approximated by a stiff EoS ($\gamma > 5/3$). Examples of such scenarios might range from primordial black holes accreting during the radiation era in the early universe evolution (especially between the quark and lepton epochs when $10^{10} \text{ K} < T < 10^{15} \text{ K}$; Jedamzik 1997; Lora-Clavijo et al. 2013), to mini black holes accreting from within a neutron star (whose core can be modelled, as a first approximation, with a $\gamma = 2$ polytrope; Capela, Pshirkov & Tinyakov 2013; Génolini et al. 2020).

ACKNOWLEDGEMENTS

We thank John Miller for insightful discussions and critical comments on the manuscript. The authors also acknowledge useful comments from an anonymous referee. This work was partially supported by CONACYT Ciencia de Frontera Project No. 376127 ‘Sombras, lentas y ondas gravitatorias generadas por objetos compactos astrofísicos’ and by a CIC grant to Universidad Michoacana. The authors acknowledge the support from the Miztli-UNAM supercomputer (project LANCAD-UNAM-DGTIC-406). AAO acknowledge support from CONACYT scholarship (No. 788898).

DATA AVAILABILITY

All of the simulations presented in this work can be reproduced using the ‘Spherical accretion’ set-up of the AZTEKAS code that can be found on the Github repository (<https://github.com/aztekas-code/aztekas-main>). Any further data underlying this paper will be shared upon request to the corresponding author.

REFERENCES

Abbas G., Ditta A., 2021, *New Astron.*, 84, 101508
 Abramowicz M. A., Zurek W. H., 1981, *ApJ*, 246, 314
 Aguayo-Ortiz A., Mendoza S., Olvera D., 2018, *PLOS One*, 13, e0195494
 Aguayo-Ortiz A., Tejada E., Hernandez X., 2019, *MNRAS*, 490, 5078
 Aguayo-Ortiz A., Sarbach O., Tejada E., 2021, *Phys. Rev. D*, 103, 023003
 Alcubierre M., 2008, *Introduction to 3+1 Numerical Relativity*. International Series Of Monographs on Physics. Oxford Univ. Press, Oxford
 Armitage P. J., 2020, *A&G*, 61, 2.40
 Banyuls F., Font J. A., Ibáñez J. M., Martí J. M., Miralles J. A., 1997, *ApJ*, 476, 221
 Bardeen J. M., 1970, *ApJ*, 162, 71
 Begelman M. C., 1978, *MNRAS*, 184, 53
 Beskin V. S., Pidoprygora Y. N., 1995, *J. Exp. Theor. Phys.*, 80, 575
 Bondi H., 1952, *MNRAS*, 112, 195
 Capela F., Pshirkov M., Tinyakov P., 2013, *Phys. Rev. D*, 87, 123524
 Carroll S., 2003, *Space–time and Geometry: An Introduction to General Relativity*. Benjamin Cummings, San Francisco, United States
 Carr B. J., 1981, *MNRAS*, 194, 639
 Chaverra E., Sarbach O., 2015, *Class. Quantum Gravity*, 32, 155006
 Chaverra E., Sarbach O., 2016, *Gen. Relativ. Gravity*, 48, 12
 Chaverra E., Mach P., Sarbach O., 2016, *Class. Quantum Gravity*, 33, 105016
 Chavez Nambo E., Sarbach O., 2020, *Static Spherical Perfect Fluid Stars with Finite Radius in General Relativity: A Review*, preprint (arXiv:2010.02859)
 Cieřlik A., Mach P., 2020, *Phys. Rev. D*, 102, 024032

Ciotti L., Pellegrini S., 2017, *ApJ*, 848, 29
 Colpi M., Shapiro S. L., Wasserman I., 1996, *ApJ*, 470, 1075
 Davé R., Anglés-Alcázar D., Narayan D., Li Q., Rafieferantsoa M. H., Appleby S., 2019, *MNRAS*, 486, 2827
 Del Zanna L., Zanotti O., Bucciantini N., Londrillo P., 2007, *A&A*, 473, 11
 Falle S. A. E. G., Komissarov S. S., 1996, *MNRAS*, 278, 586
 Génolini Y., Serpico P. D., Tinyakov P., 2020, *Phys. Rev. D*, 102, 083004
 Heusler M., 1996, *Black Hole Uniqueness Theorems*. Cambridge Univ. Press, Cambridge
 Igumenshchev I. V., Narayan R., 2002, *ApJ*, 566, 137
 Jedamzik K., 1997, *Phys. Rev. D*, 55, R5871
 Jüttner F., 1911, *Das Maxwell’sche Gesetz der Geschwindigkeitsverteilung in der Relativtheorie*. Ann. Phys. Annalen der Physik, Germany. p. 856
 Karkowski J., Malec E., 2013, *Phys. Rev. D*, 87, 044007
 Kouvaris C., Tinyakov P., 2014, *Phys. Rev. D*, 90, 043512
 Krolik J. H., London R. A., 1983, *ApJ*, 267, 18
 Krumholz M. R., McKee C. F., Klein R. I., 2005, *ApJ*, 618, 757
 Lora-Clavijo F. D., Guzmán F. S., Cruz-Osorio A., 2013, *J. Cosmol. Astropart. Phys.*, 2013, 015
 Mach P., Piróg M., Font J. A., 2018, *Class. Quantum Gravity*, 35, 095005
 Malec E., 1999, *Phys. Rev. D*, 60, 104043
 Maraschi L., Reina C., Treves A., 1974, *A&A*, 35, 389
 McKinney J. C., Tchekhovskoy A., Sadowski A., Narayan R., 2014, *MNRAS*, 441, 3177
 Michel F. C., 1972, *Ap&SS*, 15, 153
 Miller A. J., Baumgarte T. W., 2017, *Class. Quantum Gravity*, 34, 035007
 Moffat J. W., 2020, *Supermassive Black Hole Accretion and Growth*, preprint (arXiv:2011.13440)
 Moncrief V., 1980, *ApJ*, 235, 1038
 Moscibrodzka M., 2006, *A&A*, 450, 93
 Narayan R., Johnson M. D., Gammie C. F., 2019, *ApJ*, 885, L33
 Pariev V. I., 1996, *MNRAS*, 283, 1264
 Petrich L. I., Shapiro S. L., Teukolsky S. A., 1988, *Phys. Rev. Lett.*, 60, 1781
 Proga D., Begelman M. C., 2003, *ApJ*, 582, 69
 Ressler S. M., Quataert E., White C. J., Blaes O., 2021, *MNRAS*, preprint (arXiv:2102.01694)
 Richards C. B., Baumgarte T. W., Shapiro S. L., 2021a, *MNRAS*, 502, 3003
 Richards C. B., Baumgarte T. W., Shapiro S. L., 2021b, preprint (arXiv:2102.09574)
 Rioseco P., Sarbach O., 2017a, *Class. Quantum Gravity*, 34, 095007
 Rioseco P., Sarbach O., 2017b, *J. Phys.*, 831, 012009
 Russell H. R., McNamara B. R., Edge A. C., Hogan M. T., Main R. A., Vantyghem A. N., 2013, *MNRAS*, 432, 530
 Russell H. R., Fabian A. C., McNamara B. R., Broderick A. E., 2015, *MNRAS*, 451, 588
 Ryu D., Chattopadhyay I., Choi E., 2006, *ApJS*, 166, 410
 Shapiro S. L., 1974, *ApJ*, 189, 343
 Sharma P., Quataert E., Stone J. M., 2008, *MNRAS*, 389, 1815
 Shu C.-W., Osher S., 1988, *J. Comput. Phys.*, 77, 439
 Synge J., 1957, *The Relativistic Gas*. North-Holland, Amsterdam
 Taub A. H., 1948, *Phys. Rev.*, 74, 328
 Tejada E., 2018, *Rev. Mex. Astron. Astrofis.*, 54, 171
 Tejada E., Aguayo-Ortiz A., 2019, *MNRAS*, 487, 3607
 Tejada E., Aguayo-Ortiz A., Hernandez X., 2020, *ApJ*, 893, 81
 Toropin Y. M., Toropina O. D., Savelyev V. V., Romanova M. M., Chechetkin V. M., Lovelace R. V. E., 1999, *ApJ*, 517, 906
 Weih L. R., Olivares H., Rezzolla L., 2020, *MNRAS*, 495, 2285
 Yang S., Liu C., Zhu T., Zhao L., Wu Q., Yang K., Jamil M., 2021, *Chin. Phys. C*, 45, 015102
 Zanotti O., Font J. A., Rezzolla L., Montero P. J., 2005, *MNRAS*, 356, 1371
 Zel’dovich Y. B., Novikov I. D., 1967, *Soviet Astron.*, 10, 602

APPENDIX A: LIMITS OF THE MICHEL SOLUTION

In this appendix, we make a few remarks regarding the following two limits of the Michel solution: the isothermal limit for which the

adiabatic index $\gamma \rightarrow 1$ and the non-relativistic limit for which the asymptotic temperature is $\Theta_\infty \ll 1$.

(i) *Isothermal limit*

In the limit when $\gamma \rightarrow 1$, we show that the Michel solution approaches the Newtonian (Bondi) flow solution with an EoS given by equation (5). To this end, we first use the cubic equation (18) and find, for small values of $\delta := \gamma - 1 > 0$,

$$\frac{h_s}{h_\infty} = 1 + \frac{3}{2}\delta - \left(\frac{9}{8} + \frac{3}{2\Theta_\infty}\right)\delta^2 + \mathcal{O}(\delta^3), \quad (\text{A1a})$$

$$c_s^2 = \delta \left[1 - \frac{\delta}{\Theta_\infty} + \mathcal{O}(\delta^2) \right], \quad (\text{A1b})$$

$$\frac{C_s}{C_\infty} = 1 + \mathcal{O}(\delta)^2, \quad (\text{A1c})$$

from which

$$\frac{\dot{M}_M}{4\pi M^2 \rho_\infty C_\infty^{-3}} \rightarrow \frac{1}{4} e^{3/2}, \quad (\text{A2})$$

which coincides with the Bondi solution in equation (7).

Next, we introduce the dimensionless quantities

$$x := \frac{r}{M} C_\infty^2, \quad z := \frac{\rho}{\rho_\infty}, \quad v := \frac{u}{c}, \quad \lambda := \frac{\dot{M}_M}{4\pi M^2} \frac{C_\infty^3}{\rho_\infty}. \quad (\text{A3})$$

in terms of which equations (14a,14b) can be rewritten as

$$x^2 v z^{\frac{\gamma+1}{2}} = \lambda \left(\frac{h}{h_\infty} \right)^{1/2}, \quad (\text{A4a})$$

$$-\frac{2}{x} + \frac{h_\infty}{h} z^{\gamma-1} v^2 = \frac{1}{C_\infty^2} \left[\left(\frac{h_\infty}{h} \right)^2 - 1 \right]. \quad (\text{A4b})$$

For small values of δ , one finds, using $h = 1 + \gamma \rho^\delta / \delta$,

$$\frac{h}{h_\infty} = 1 + \delta \log(z) + \mathcal{O}(\delta^2). \quad (\text{A5})$$

Introduced into equations (A4a) and (A4b), using equation (A1b) and taking the limit $\delta \rightarrow 0$ yields (assuming that x , z and v have finite values in this limit)

$$x^2 v z = \lambda, \quad -\frac{1}{x} + \frac{1}{2} v^2 = -\log z, \quad (\text{A6})$$

which agrees precisely with the Newtonian equations (3a,3b) with the EoS (5), for x , z and λ defined as in equation (A3) and $v = v/C_\infty$ (note that $c/C_\infty \rightarrow 1$ in the limit $\delta \rightarrow 0$). Taking into account the limit (A2) this yields the transonic flow solution discussed in subsection 2.1, which has been shown in Chaverra & Sarbach (2016) to be the correct $\gamma \rightarrow 1$ limit of the Bondi flow.

(ii) *Non-relativistic limit*

In the low-temperature limit $\Theta_\infty \rightarrow 0$ one has $h_\infty \rightarrow 1$, and in this limit equation (18) has two positive roots

$$h_s = 1, \quad h_s = \frac{1}{2} \left(\sqrt{12\gamma - 11} - 1 \right), \quad (\text{A7})$$

the third one being negative and hence unphysical. For $\gamma < 5/3$, the second positive root is smaller than one, and hence unphysical as well and the correct limit is $h_s = 1$. Computing the first-order correction in Θ_∞ one finds

$$\frac{h_s}{h_\infty} = 1 + \frac{3\gamma}{5-3\gamma} \Theta_\infty + \mathcal{O}(\Theta_\infty)^2, \quad (\text{A8})$$

from which

$$\frac{C_s^2}{C_\infty^2} = \frac{2}{5-3\gamma} + \mathcal{O}(\Theta_\infty), \quad (\text{A9})$$

and substituting into equation (22) it follows that $\dot{M}_M \rightarrow \dot{M}_B$ when $\Theta_\infty \rightarrow 0$ and $\gamma < 5/3$. When $\gamma > 5/3$ it turns out the correct root is the second one in equation (A7), see Chaverra et al. (2016), and the corresponding squared sound speed and radius at the sonic point are

$$C_s^2 = \frac{1}{3}(h_s^2 - 1) > 0, \quad r_s = \frac{3M}{2} \frac{h_s^2}{h_s^2 - 1}. \quad (\text{A10})$$

It follows from equation (22) that

$$\dot{M}_M \rightarrow \pi h_s^{\frac{3\gamma-2}{\gamma-1}} C_s^{\frac{5-3\gamma}{\gamma-1}} M^2 \rho_\infty C_\infty^{-\frac{2}{\gamma-1}}, \quad (\text{A11})$$

and the mass accretion rate decays slower than C_∞^{-3} . Note that $h_s > 1$ and $C_s > 0$ imply that the flow does not lie in the Newtonian regime close to the sonic point when $\gamma > 5/3$.

APPENDIX B: ORTHONORMAL FRAME ADAPTED TO THE KERR-TYPE COORDINATES

The orthonormal frame adapted to the constant time slices in the Kerr-type coordinates (t, ϕ, r, θ) used in this article is given by

$$e_t = \sqrt{1 + \frac{2Mr}{\varrho^2}} \left(\frac{\partial}{\partial t} - \frac{2Mr}{\varrho^2 + 2Mr} \frac{\partial}{\partial r} \right), \quad (\text{B1a})$$

$$e_r = \frac{1}{\sqrt{1 + \frac{2Mr}{\varrho^2}}} \frac{\partial}{\partial r}, \quad (\text{B1b})$$

$$e_\theta = \frac{1}{\varrho} \frac{\partial}{\partial \theta}, \quad (\text{B1c})$$

$$e_\phi = \frac{1}{\varrho \sin \theta} \left(\frac{\partial}{\partial \phi} + a \sin^2 \theta \frac{\partial}{\partial r} \right), \quad (\text{B1d})$$

and it is well defined for all $r > 0$. The corresponding components of the four-velocity vector field, such that

$$U^\mu \frac{\partial}{\partial x^\mu} = U^t e_t + U^r e_r + U^\theta e_\theta + U^\phi e_\phi \quad (\text{B2})$$

are given by

$$U^t = \frac{1}{\sqrt{1 + \frac{2Mr}{\varrho^2}}} U^t, \quad (\text{B3a})$$

$$U^r = \sqrt{1 + \frac{2Mr}{\varrho^2}} \left(U^r + \frac{2Mr}{\varrho^2 + 2Mr} U^t - a \sin^2 \theta U^\phi \right), \quad (\text{B3b})$$

$$U^\theta = \varrho U^\theta, \quad (\text{B3c})$$

$$U^\phi = \varrho \sin \theta U^\phi. \quad (\text{B3d})$$

APPENDIX C: INVARIANT DETERMINATION OF THE SONIC SURFACE

In relativistic fluids, it is not immediately obvious how to determine the sonic surfaces, that is, the boundary separating the events at which the flow is subsonic from those at which it is supersonic. Indeed, the fluid's sound speed C is a scalar, while the velocity U^μ of the fluid is a four-vector. One could consider instead of U^μ the magnitude of the three-velocity V with respect to a specific family of observers and define the sonic surface by those events for which $V = C$, but this definition would clearly be observer dependent.

A definition that does provide an invariant characterization of the sonic surface is based on the sonic metric:

$$\mathfrak{G}_{\mu\nu} := \frac{\rho}{h} \frac{1}{\mathcal{C}} [g_{\mu\nu} + (1 - \mathcal{C}^2) U_\mu U_\nu], \quad (\text{C1})$$

first introduced by Moncrief (1980), for the purpose of analysing the propagation linearised, acoustic perturbations of an isentropic, vorticity-free flow on a background space–time with metric $g_{\mu\nu}$. The sonic metric (C1) is a Lorentzian metric whose set of null vectors at a given space–time event e form a cone (the sound cone) that can be shown to lie inside the light-cone at e provided $\mathcal{C}^2 < 1$. Another useful property of the sonic metric is that it inherits the symmetries of the space–time and the flow configuration: if X is a Killing vector field, such that the Lie derivative \mathfrak{L}_X of $g_{\mu\nu}$, U^μ , ρ and h vanish, then it follows that $\mathfrak{L}_X \mathfrak{G}_{\mu\nu} = 0$, that is, the sonic metric is invariant with respect to X .

For the solutions described in this article, where both the space–time metric and the flow are steady-state and axisymmetric, it follows that equation (C1) describes a steady-state and axisymmetric geometry that is asymptotically flat since the flow’s four-velocity is constant at infinity. A sonic surface corresponds to the ‘event horizon’ of this geometry, that is, the surface that separates those events that can send an acoustic signal to infinity from those that cannot. Due to the aforementioned symmetries of the sonic geometry, this surface must be a Killing horizon, i.e. a null surface of the form (see, e.g. Heusler 1996)

$$\mathcal{H} := \{x : \mathfrak{G}_{\mu\nu}(x) X^\mu X^\nu = 0\}, \quad (\text{C2})$$

whose normal vector,

$$X^\mu = \delta^\mu_t + \Omega_{\mathcal{H}} \delta^\mu_\phi, \quad (\text{C3})$$

is a superposition of the Killing vector fields of the Kerr metric, where here the constant $\Omega_{\mathcal{H}}$ describes the angular velocity of the horizon. The requirement of \mathcal{H} being a null surface (with respect to the sonic metric) with normal X^μ implies the condition

$$\nabla^\alpha [\mathfrak{G}_{\mu\nu}(x) X^\mu X^\nu] = -2\kappa X^\alpha, \quad (\text{C4})$$

the proportionality factor κ describing the ‘surface gravity’ associated with the horizon. Assuming a regular horizon, such that $\kappa \neq 0$, the four equations (C4) imply

$$\mathfrak{G}_{tt} + \Omega_{\mathcal{H}} \mathfrak{G}_{t\phi} = 0, \quad (\text{C5a})$$

$$\mathfrak{G}_{t\phi} + \Omega_{\mathcal{H}} \mathfrak{G}_{\phi\phi} = 0, \quad (\text{C5b})$$

$$\mathfrak{G}_{rr} + \Omega_{\mathcal{H}} \mathfrak{G}_{\phi r} = -\frac{1}{2\kappa} \frac{\partial N}{\partial r}, \quad (\text{C5c})$$

$$\mathfrak{G}_{t\theta} + \Omega_{\mathcal{H}} \mathfrak{G}_{\phi\theta} = -\frac{1}{2\kappa} \frac{\partial N}{\partial \theta} \quad (\text{C5d})$$

with $N := \mathfrak{G}_{\mu\nu} X^\mu X^\nu = \mathfrak{G}_{tt} + 2\Omega_{\mathcal{H}} \mathfrak{G}_{t\phi} + \Omega_{\mathcal{H}}^2 \mathfrak{G}_{\phi\phi}$. Note that the first two conditions (C5a,C5b) imply that X^μ is null on \mathcal{H} , i.e. $N = 0$, as required. They determine the location of the sonic surface \mathcal{H} through the requirement that the determinant of the 2×2 matrix $(\mathfrak{G}_{ab})_{a,b=t,\phi}$ vanishes. In view of definition (C1), this yields

$$\det [g_{ab} + (1 - \mathcal{C}^2) U_a U_b] = 0. \quad (\text{C6})$$

In turn, either equation (C5c) or equation (C5d) can be used to determine the surface gravity κ , but this will not be needed here.¹²

In terms of the Kerr-type coordinates (t, ϕ, r, θ) used in this article, the determinant condition (C6), together with the property $U_\phi = 0$ satisfied by the flow, leads to the condition

$$g_{tt} - \frac{g_{t\phi}^2}{g_{\phi\phi}} + (1 - \mathcal{C}^2) U_t^2 = 0, \quad (\text{C7})$$

which yields an implicit relation between r and θ . This condition acquires a much clearer interpretation when rewriting it in terms of the flow’s Lorentz factor Γ measured by a ZAMO, which gives

$$(1 - \mathcal{C}^2) \Gamma^2 = 1, \quad (\text{C8})$$

i.e. the sonic surface is determined by those events for which the flow, as measured by ZAMOs, changes from sub- to supersonic. From equation (C5b) and $U_\phi = 0$ it also follows that $\Omega_{\mathcal{H}} = -g_{t\phi}/g_{\phi\phi} = \Omega_{\text{ZAMO}}$, i.e. the angular velocity of the sonic horizon is equal to the angular velocity of the ZAMO at \mathcal{H} .

¹²Note that the condition $N = 0$ on \mathcal{H} implies that equation (C4), when contracted with a tangent vector to \mathcal{H} is automatically satisfied, such that only one of the two equations (C5c,C5d) needs to be considered.

This paper has been typeset from a $\text{\TeX}/\text{\LaTeX}$ file prepared by the author.

Relativistic wind accretion on to a Schwarzschild black hole

In this chapter, we present a general relativistic extension of the Bondi, Hoyle and Lyttleton (BHL, [Hoyle & Lyttleton, 1939](#); [Bondi & Hoyle, 1944](#)) classical wind accretion solution. The model presented in this article, as in BHL, is based on the assumption of steady state, axisymmetry and ballistic motion, but in this case the central mass corresponds to a Schwarzschild black hole, substantially modifying the computing and final expressions for the density field, the fluid streamlines and the mass accretion rate.

We start by giving a brief introduction to the BHL problem in which we establish the conditions and setup of the problem, and then summarize the expressions of the density field, fluid streamlines, and mass accretion rate for the non-relativistic case. Then, we introduce the BHL relativistic extension by writing the equations of motion for a test particle and its conserved quantities, which corresponds to the ballistic approximation. From these equations, we obtain both the fluid streamlines and density field expressions. Finally, using these results, we numerically compute the mass accretion rate as a function of the wind velocity at infinity. From these three physical quantities, we make a comparison between the relativistic and non-relativistic cases, finding that, for the relativistic model, the total accretion rate is greater than the corresponding Newtonian value.

In the second part of the article, we show a comparison between the previously mentioned relativistic wind accretion ballistic model and numerical simulations performed with the numerical code AZTEKAS. The numerical experiments consist of a 2D-axisymmetric setup of the wind accretion problem, in which we run general relativistic hydrodynamic simulations of a perfect fluid evolving on top a fixed Schwarzschild background metric. For these simulations, we consider that the gas follows a polytropic relation, and use two different adiabatic indices ($4/3$ and $5/3$). Moreover, we run different simulations for a wide range of values of the wind velocity at infinity, and two Mach numbers. Even though the analytic model is ballistic, which

is not a hydrodynamic solution, the numerical results found with AZTEKAS show a good agreement for the fluid streamlines in the upstream region of the flow and for the corresponding accretion rates. Furthermore, in the appendix of this article, we show some relevant validation tests for the AZTEKAS code.

The study presented in this chapter was published in MNRAS in 2019. The details of the paper are:

Tejeda E., Aguayo-Ortiz A., 2019, MNRAS, 487, 3607. [doi:10.1093/mnras/stz1513](https://doi.org/10.1093/mnras/stz1513)

Relativistic wind accretion on to a Schwarzschild black hole

Emilio Tejeda^{1,2★} and Alejandro Aguayo-Ortiz^{2★}

¹CONACyT – Instituto de Física y Matemáticas, Universidad Michoacana de San Nicolás de Hidalgo, Edificio C-3, Ciudad Universitaria, 58040 Morelia, Michoacán, Mexico

²Instituto de Astronomía, Universidad Nacional Autónoma de México, AP 70-264, 04510 Ciudad de México, Mexico

Accepted 2019 May 28. Received 2019 May 22; in original form 2019 March 30

ABSTRACT

We present a novel analytic model of relativistic wind accretion on to a Schwarzschild black hole. This model constitutes a general relativistic extension of the classical model of wind accretion by Bondi, Hoyle, and Lyttleton (BHL). As in BHL, this model is based on the assumptions of steady state, axisymmetry, and ballistic motion. Analytic expressions are provided for the wind streamlines while simple numerical schemes are presented for calculating the corresponding accretion rate and density field. The resulting accretion rate is greater in the relativistic model when compared to the Newtonian BHL one. Indeed, it is two times greater for asymptotic wind speeds $v_\infty \geq 0.4c$ and more than an order of magnitude greater for $v_\infty \geq 0.8c$. We have compared this full relativistic model versus numerical simulations performed with the free GNU Public Licensed hydrodynamics code *aztekas* and found a good agreement for the streamlines in the upstream region of the flow and also, to within 10 per cent, for the corresponding accretion rates.

Key words: accretion, accretion discs – black hole physics – gravitation – hydrodynamics – methods: analytical.

1 INTRODUCTION

Accretion physics has become a basic tenet of astrophysics ever since it was recognized that the process of accretion, especially when compact objects are involved, is one of the most efficient mechanisms for converting rest mass energy into luminosity at work in our Universe (Frank, King & Raine 2002). Indeed, it has been established that a thin accretion disc around a non-rotating black hole can reprocess as much as 10 per cent of the accreted gas rest mass into electromagnetic radiation, while for a maximally rotating black hole this figure can reach up to 46 per cent (see e.g. Longair 2011).

The simplest accretion scenario consists of the stationary, spherically symmetric solution first discussed by Bondi (1952), where he considered an infinitely large homogeneous gas cloud steadily accreting on to a central gravitational object. The general relativistic extension of this model was developed by Michel (1972) who took a Schwarzschild black hole as the central accretor.

In the so-called wind accretion scenario, the spherical symmetry approximation is relaxed by considering a non-zero relative velocity between the central object and the accreted medium (cf. Edgar 2004; Romero & Vila 2014). As it turns out, even after assuming a steady state and axial symmetry, the problem becomes sufficiently

complex as not to admit a full analytic solution in general. In the pioneering work of Hoyle & Lyttleton (1939) and Bondi & Hoyle (1944) (BHL hereafter), the authors provided an analytic model for supersonic wind accretion by adopting the so-called ballistic approximation, i.e. by neglecting pressure gradients and assuming that the fluid's dynamics is solely dictated by the central object's gravitational field. This approximation is well suited to describe highly supersonic flows given that, within this regime, incoming fluid elements cannot oppose pressure gradients readily, effectively following nearly free-fall trajectories.

Further analytic solutions to wind accretion problems have been found for a perfect fluid with a stiff equation of state in general relativity (Petrich, Shapiro & Teukolsky 1988) and for the corresponding non-relativistic case of an incompressible fluid (Tejeda 2018).

The problem of wind accretion has also been the focus of various numerical studies, from both a Newtonian perspective (Hunt 1971; Shima et al. 1985; Ruffert & Arnett 1994; El Mellah & Casse 2015; El Mellah, Sundqvist & Keppens 2018) and in general relativity (Petrich et al. 1989; Font & Ibáñez 1998; Zanotti et al. 2011; Lora-Clavijo & Guzmán 2013; Gracia-Linares & Guzmán 2015; Cruz-Osorio & Lora-Clavijo 2016; Cruz-Osorio, Sánchez-Salcedo & Lora-Clavijo 2017).

In this article we introduce a simple, analytic model for a supersonic wind accreting on to a non-rotating black hole (Schwarzschild spacetime). This model is a general relativistic extension of the BHL model and follows closely the methodology outlined in

* E-mail: emilio.tejeda@conacyt.mx (ET); aaguayo@astro.unam.mx (AA-O)

Mendoza, Tejada & Nagel (2009), Tejada, Mendoza & Miller (2012), and Tejada, Taylor & Miller (2013). In that series of works, we presented an analytic model of the accretion flow of a rotating dust cloud infalling towards a central object, first in a Newtonian regime (Mendoza et al. 2009) and then in general relativity for a Schwarzschild black hole (Tejada et al. 2012) and for a Kerr black hole (Tejada et al. 2013). See Schrovén, Hackmann & Lämmerzahl (2017) for a recent extension of this model considering the case of charged dust particles accreting on to a Kerr–Newman black hole.

The article is organized as follows: in Section 2 we give a brief review of the BHL model. In Section 3 we introduce the new relativistic wind model, and in Section 4 we present the comparison against relativistic hydrodynamic numerical simulations performed with the free GNU Public Licensed (GPL) hydrodynamics code *aztekas* (Olvera & Mendoza 2008; Aguayo-Ortiz, Mendoza & Olvera 2018).¹ Finally, in Section 5 we summarize the work and present our conclusions. The Appendix A presents the results of the benchmark test of *aztekas* against Michel’s analytic model, as well as self-convergence and various resolution tests relevant to this study.

2 BONDI–HOYLE–LYTTLETON MODEL

In this section we give a brief overview of the BHL accretion model as its general relativistic extension constitutes the scope of this work. The BHL model deals with a steady, supersonic wind accreting on to a gravitational object of mass M . Considering that the accretor is held fixed at the centre of coordinates, infinitely far away from the central object, the wind is homogeneous and characterized by a uniform density ρ_∞ and wind speed v_∞ .

Under the ballistic approximation, expressions for the streamlines, velocity field, and density for this model are given by (Bisnovatyi-Kogan et al. 1979)

$$r = \frac{b^2 v_\infty^2}{GM(1 - \cos\theta) + b v_\infty^2 \sin\theta}, \quad (1)$$

$$\dot{r} = -\sqrt{v_\infty^2 + \frac{2GM}{r} - \frac{b^2 v_\infty^2}{r^2}}, \quad (2)$$

$$\dot{\theta} = \frac{b v_\infty}{r^2}, \quad (3)$$

$$\rho = \frac{\rho_\infty b^2}{r \sin\theta (2b - r \sin\theta)}, \quad (4)$$

where b is the impact parameter of a given incoming fluid element. Note that we are taking here a reference frame in spherical coordinates such that the polar axis is aligned with the incoming wind direction. The wind comes asymptotically from the direction of the $\theta = 0$ axis. Fig. 1 shows a schematic representation of the model set-up and streamlines.

Given the uniform wind condition at infinity, all of the incoming trajectories have initially a common specific total energy $E = v_\infty^2/2$. In other words, the wind fluid elements follow energetically unbound (hyperbolic) trajectories. From equations (1) and (2) we see that the incoming trajectories reach the downstream axis at $r(\pi) = b^2 v_\infty^2 / (2GM)$ with radial velocity $\dot{r} = v_\infty$. It is expected

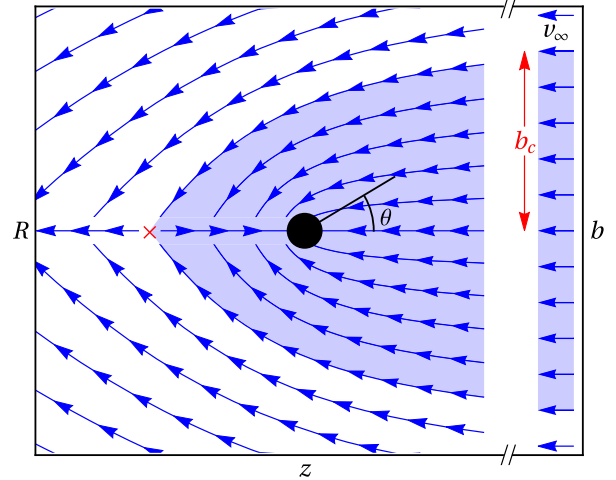


Figure 1. Schematic representation of the BHL model. The incoming wind comes from an infinite distance to the right, corresponding to a polar angle $\theta = 0$. Under the ballistic approximation, fluid streamlines correspond to free-fall trajectories. At their arrival at the so-called accretion axis $\theta = \pi$, mirror symmetric streamlines collide against each other. The kinetic energy corresponding to the normal component of the velocity is efficiently thermalized and lost from the system. After this energy redistribution, streamlines with negative mechanical energy are left bound to the central object and constitute the accretion basin (shaded blue area). The stagnation point, i.e. the point along the accretion axis marking this transition, is marked with a red cross, and the corresponding streamline is characterized by the critical impact parameter b_c . The black circle shows the location of the central accretor. The axes correspond to the usual cylindrical coordinates $R = r \sin\theta$, $z = r \cos\theta$.

that streamlines coming from mirror-reflected points with respect to the symmetry axis will collide with one another along this axis (see Fig. 1). Following this collision, the BHL model envisages that the component of the velocity perpendicular to the axis is instantly transformed into thermal energy and, eventually, lost as radiation.² After this loss of kinetic energy, each fluid element is left with a new specific total energy

$$E' = \frac{1}{2} \dot{r}(\pi)^2 - \frac{GM}{r(\pi)} = \frac{1}{2} v_\infty^2 - \frac{2(GM)^2}{b^2 v_\infty^2}. \quad (5)$$

By equating this energy to zero, the following critical value for the impact parameter is found

$$b_c = \frac{2GM}{v_\infty^2}, \quad (6)$$

such that any fluid element following a streamline with $b < b_c$ is energetically bound to the central object and, hence, eventually accreted. On the other hand, any fluid element following a streamline with $b > b_c$ is energetically unbound to the central object and therefore ultimately escapes to infinity. Following this argument, and accounting for all of the material within the cylinder of radius b_c , the total accretion rate on to the central object in the BHL model

²More precisely, in the Hoyle & Lyttleton (1939) model the fluid streamlines are assumed to focus downstream on to the symmetry axis leading to an infinite density there. The accretion then proceeds along this line. Instead, Bondi & Hoyle (1944) envisioned an accretion flow that spreads out on to a finite density region that they referred to as accretion column. In this work we are adopting the former description.

¹aztekas.org©2008 Sergio Mendoza & Daniel Olvera and ©2018 Alejandro Aguayo-Ortiz & Sergio Mendoza.

is given by

$$\dot{M}_{\text{BHL}} = \pi b_c^2 \rho_\infty v_\infty = 4\pi \rho_\infty \frac{(GM)^2}{v_\infty^3}. \quad (7)$$

Subsequent numerical studies of this problem have found stationary accretion rates that agree remarkably well with those predicted by the simple BHL model (see e.g. Hunt 1971). The resulting flows obtained in full-hydrodynamic simulations of supersonic wind accretion show the development of a bow shock around the central accretor at which the incoming wind streamlines abruptly decelerate and become subsonic. Clearly, the simple analytic description of the streamlines provided by the BHL model is no longer valid inside the bow shock, nevertheless, it provides a qualitatively good description of the streamlines in the supersonic, upwind region.

3 RELATIVISTIC WIND MODEL

In this section we present the extension of the BHL wind model to the case in which the central accretor is a non-rotating black hole of mass M . We shall assume that the mass–energy content of the accreting gas is negligible as compared to the mass of the central black hole and, thus, the overall spacetime metric corresponds to the Schwarzschild solution. For constructing this model we are closely following the methodology described in Tejeda et al. (2012). For the remainder of this work we adopt a geometrized system of units for which $G = c = 1$.

3.1 Velocity field

Adopting the ballistic approximation for test particles in general relativity amounts to describe the incoming streamlines as geodesic trajectories. Due to the symmetries of Schwarzschild spacetime, the trajectory of a test particle is restricted to a plane and governed by the equations of motion (Frolov & Novikov 1998)

$$\frac{dt}{d\tau} = \mathcal{E} \left(1 - \frac{2M}{r}\right)^{-1}, \quad (8)$$

$$\frac{dr}{d\tau} = - \left[\mathcal{E}^2 - \left(1 - \frac{2M}{r}\right) \left(1 + \frac{h^2}{r^2}\right) \right]^{1/2}, \quad (9)$$

$$\frac{d\theta}{d\tau} = \frac{h}{r^2}, \quad (10)$$

where \mathcal{E} is the conserved specific (relativistic) total energy and h is the conserved specific angular momentum. Assuming a uniform wind velocity at infinity v_∞ , these conserved quantities for a given streamline with impact parameter b are given by

$$\mathcal{E} = \frac{1}{\sqrt{1 - v_\infty^2}} = \gamma_\infty, \quad (11)$$

$$h = \frac{b v_\infty}{\sqrt{1 - v_\infty^2}} = b V_\infty, \quad (12)$$

where γ_∞ is the wind's Lorentz factor at infinity and where we have introduced the shorthand notation $V_\infty = \gamma_\infty v_\infty$.

In order for the velocity field in equations (8)–(10) to be useful in practice, we need to provide an expression for the streamlines of the form $r(\theta, b)$ as we discuss in the next subsection.

3.2 Streamlines

An expression for the streamlines can be obtained by combining equations (9) and (10) as

$$\frac{dr}{d\theta} = \frac{\sqrt{\mathcal{R}(r)}}{h}, \quad (13)$$

where

$$\mathcal{R}(r) = r \left[V_\infty^2 r^3 + 2Mr^2 - b^2 V_\infty^2 (r - 2M) \right]. \quad (14)$$

As discussed in detail in Tejeda et al. (2012), equation (13) can be solved in terms of elliptic integrals. For the problem at hand, we need to distinguish between two types of trajectories: (1) unbound trajectories that reach a minimum distance in their descent towards the central object before turning back to infinity and (2) trapped trajectories that plunge on to the black hole's event horizon (located at $r = 2M$). Specifically, streamlines with $b \geq b_0$ belong to type (1) while those with $b < b_0$ belong to type (2) where

$$b_0 = \frac{M \sqrt{27 V_\infty^4 + 18 V_\infty^2 + \gamma_\infty (1 + 9 V_\infty^2)^{3/2} - 1}}{\sqrt{2} V_\infty}. \quad (15)$$

In case (1), the polynomial in equation (14) has three non-trivial real roots. For the particular boundary condition that we have adopted here, it can be proved that one of these roots is negative and the other two are positive. We call them r_1 , r_2 , and r_3 , such that $r_1 < 0 < r_2 < r_3$. These roots can be explicitly given in terms of the constants of motion, see e.g. Tejeda et al. (2012). In terms of these roots, the equation for the streamlines is given by

$$r = \frac{r_1(r_3 - r_2) - r_2(r_3 - r_1)\text{cn}^2(\xi, k)}{r_3 - r_2 - (r_3 - r_1)\text{cn}^2(\xi, k)}, \quad (16)$$

$$\xi = \frac{\sqrt{r_3(r_3 - r_2)}}{2b}(\theta + \theta_\infty), \quad (17)$$

where $\text{cn}(\xi, k)$ is a Jacobi elliptic function with modulus (Lawden 1989)

$$k = \sqrt{\frac{r_2(r_3 - r_1)}{r_3(r_2 - r_1)}}, \quad (18)$$

and

$$\theta_\infty = \frac{2b}{\sqrt{r_3(r_3 - r_2)}} \text{cn}^{-1} \sqrt{\frac{r_3 - r_2}{r_3 - r_1}}, \quad (19)$$

is the polar phase setting $\theta = 0$ as the incoming wind direction, i.e. $r(\theta = 0) \rightarrow \infty$.

In case (2) the polynomial in equation (14) has as roots a negative real number r_1 and a complex conjugate pair $r_2 = r_3^*$. In this case the equation for the streamlines can be written as

$$r = \frac{\delta r_1 [1 - \text{cn}(\tilde{\xi}, \tilde{k})]}{\delta - \eta - (\eta + \delta)\text{cn}(\tilde{\xi}, \tilde{k})}, \quad (20)$$

$$\tilde{\xi} = \frac{\sqrt{\eta \delta}}{b}(\theta + \tilde{\theta}_\infty), \quad (21)$$

where

$$\eta = \sqrt{(r_2 - r_1)(r_3 - r_1)}, \quad (22)$$

$$\delta = \sqrt{r_2 r_3}, \quad (23)$$

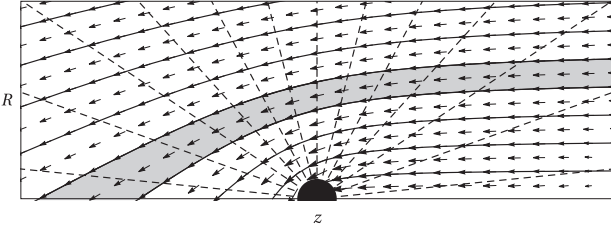


Figure 2. Schematic illustration of the grid used for numerically evaluating the partial derivative involved in the calculation of the density field (equation 30). The shaded area represents one of the streamline tubes used as integration volume for calculating the density field in equation (27).

$$\tilde{k}^2 = \frac{(\eta + \delta)^2 - r_1^2}{4\eta\delta}, \quad (24)$$

and

$$\tilde{\theta}_\infty = \frac{b}{\sqrt{\eta\delta}} \operatorname{cn}^{-1} \left[\frac{\delta - \eta}{\eta + \delta}, \tilde{k} \right]. \quad (25)$$

Equations (16) and (20) constitute the required expressions for the streamlines. As demonstrated by Tejada et al. (2012), these expressions for the streamlines reduce to the usual Newtonian conic-sections in the non-relativistic limit, i.e. for $v_\infty \ll 1$ equation (16) reduces to equation (1), while the velocity field in equations (9) and (10) reduce to equations (2) and (3), respectively.

3.3 Density field

For calculating the density field we follow here a similar strategy as in Tejada et al. (2012, 2013). We start from the continuity equation³

$$\nabla_\mu(\rho U^\mu) = 0, \quad (26)$$

where $U^\mu = dx^\mu/d\tau$ is the four-velocity, ρ is the rest mass density, and ∇ stands for the covariant derivative.

Writing equation (26) for a Schwarzschild spacetime and adopting the stationary condition results in

$$\frac{\partial}{\partial x^i}(r^2 \sin \theta \rho U^i) = 0. \quad (27)$$

Let us now integrate equation (27) over the spatial volume element delimited by a sufficiently small set of streamlines that start from an area element $S_\infty = 2\pi b db$ located at infinity and that end at the intersection with the conic surface defined by $\theta = \text{const.}$, i.e. $S_\theta = 2\pi r \sin \theta dr$, as shown in Fig. 2. By construction, fluid elements enter the integration volume only across S_∞ and leave across S_θ . Therefore, by means of Gauss's theorem, it follows that

$$\rho r U^\theta S_\theta = \rho_\infty \gamma_\infty v_\infty S_\infty, \quad (28)$$

from where

$$\rho r^2 U^\theta \sin \theta dr = \rho_\infty \gamma_\infty v_\infty b db. \quad (29)$$

Finally, substituting U^θ from equation (10) into equation (29) results in

$$\rho = \frac{\rho_\infty}{\sin \theta} \left(\frac{\partial r}{\partial b} \right)^{-1}. \quad (30)$$

³Here and in what follows Greek indices run over spacetime components, Latin indices run over spatial components only, and Einstein's summation convention over repeated indices is adopted.

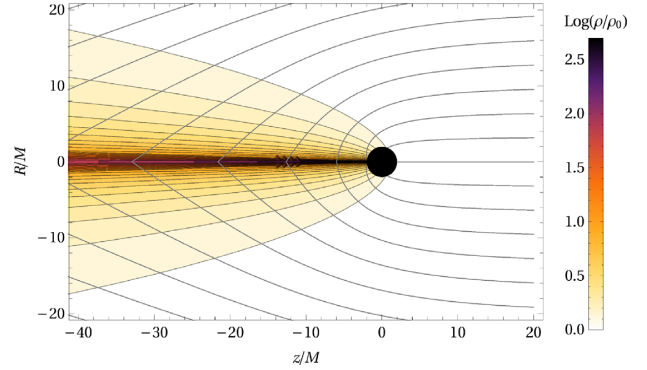


Figure 3. Analytic model of a relativistic wind accreting at $v_\infty = 0.5$ on to a Schwarzschild black hole. Accretion flow streamlines are represented as grey, solid lines, while colour contours correspond to the density field level set.

Calculating explicitly the partial derivative in equation (30) is something trivial to do in the Newtonian case. Indeed, this calculation is the step leading from equation (1) to equation (4). However, this same calculation in the relativistic case represents a complex procedure involving the derivative of an elliptic function with respect to its argument and modulus. Following Tejada et al. (2012), we do not attempt here to calculate this derivative analytically but rather use a finite difference scheme to compute it numerically. A suitable grid for performing this calculation can be constructed as follows: start from a collection of streamlines separated by uniform intervals of Δb at infinity. Follow these streamlines from $\theta = 0$ to $\theta = \pi$ storing the different values of r at uniform steps of $\Delta\theta$. Use these grid values for estimating $\partial r/\partial b$ as a finite difference of the radial coordinate between neighbouring streamlines. Such a grid is schematically represented in Fig. 2.

In Fig. 3 we show an example of a wind accreting at $v_\infty = 0.5$ on to a Schwarzschild black hole. The figure shows the flow streamlines as expressed analytically by equations (16) and (20) together with the density field as calculated numerically from equation (30).

In Fig. 4 we compare the resulting streamlines in Schwarzschild spacetime with those coming from the Newtonian BHL model for different values of the asymptotic wind speed. From this figure it is clear that the accretion cylinder, and thus the total accretion rate, in the relativistic model is greater than the corresponding Newtonian value. In the next subsection we discuss this in further detail.

3.4 Accretion rate

Just as for the density field, the procedure described in Section 2 to compute the total accretion rate in the Newtonian case (BHL model) is not as simple to implement for the relativistic problem. However, the logic behind this calculation remains the same: when the collision of mirror-reflected streamlines along the symmetry axis ($\theta = \pi$) occurs, the flow's kinetic energy associated to the normal component of the velocity (U^θ in this case) is lost from the system as thermal energy and/or radiation. The remaining relativistic energy \mathcal{E}' of a given streamline with impact parameter b will determine whether the gas travelling along the streamline is accreted ($\mathcal{E}' < 1$) on to the central black hole or lost to infinity ($\mathcal{E}' > 1$). The streamline that is left marginally bound with $\mathcal{E}' = 1$ is characterized by the critical impact parameter b_c . Using the normalization condition $U_\mu U^\mu = -1$, together with $U^\theta = 0$ and equation (9), it is simple to show that the condition $\mathcal{E}' = 1$ is

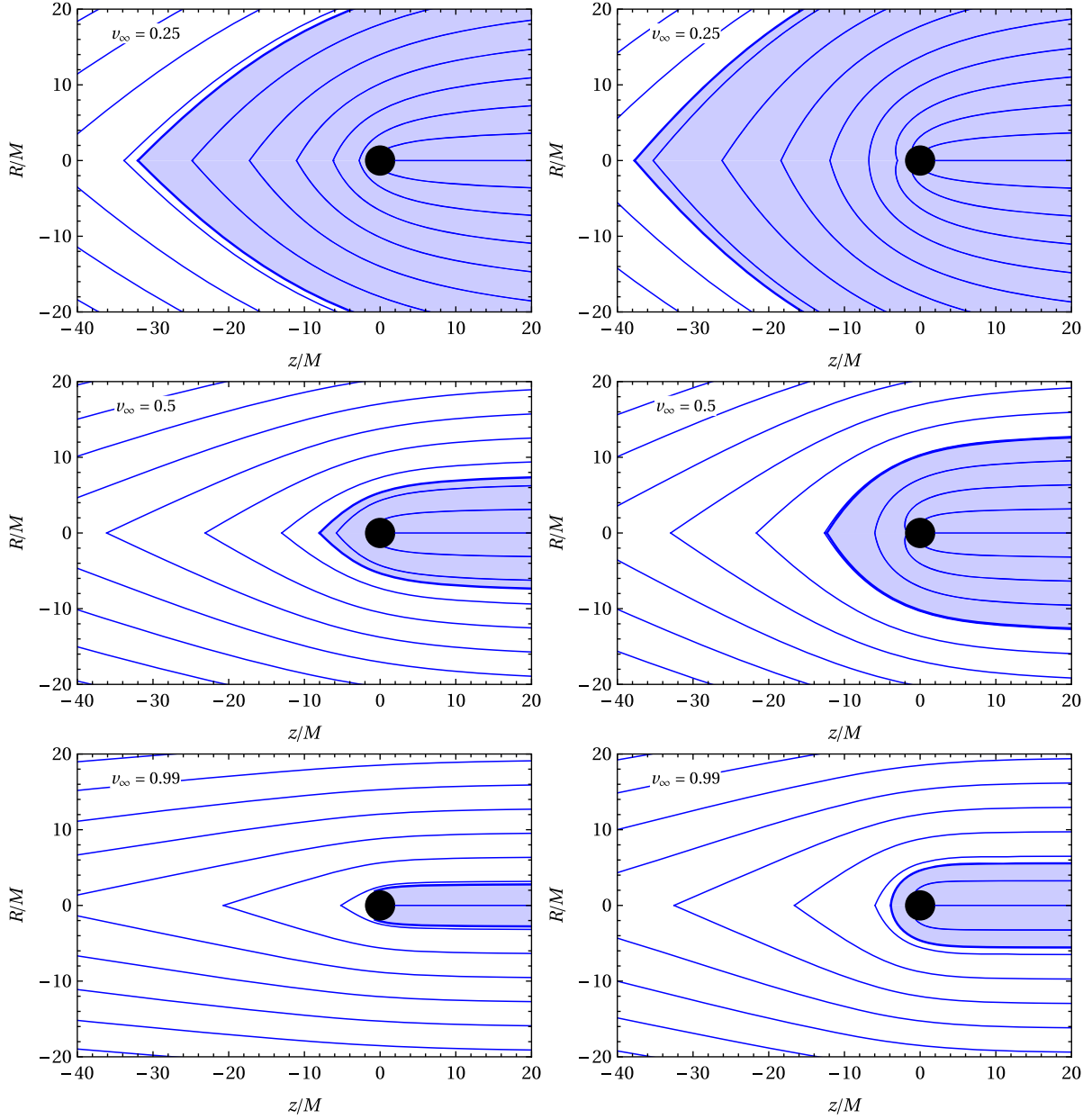


Figure 4. Comparison of the ballistic streamlines as obtained in the BHL model (left-hand column) and in Schwarzschild spacetime (right-hand column). The shaded area in each panel corresponds to the accretion cylinder, i.e. to those streamlines with impact parameter b less than the critical value b_c that end up accreting on to the central object. The wind speed at infinity v_∞ is indicated at the top left of each panel.

equivalent to

$$r(\pi)^3 + [2M - r(\pi)] b_c^2 = 0. \quad (31)$$

Unfortunately, after substituting $r(\pi)$ from either equations (16) or (20), the resulting equation is highly non-linear in b_c and it does not seem possible to solve it for b_c explicitly. None the less, it is straightforward to solve equation (31) numerically using a root-finding algorithm. We have done this using the bisection method for 1000 values of v_∞ uniformly distributed between 0.001 and 0.999 to a precision of 10^{-8} . Now, based on these numerically calculated values, we found the following fit that approximates b_c to an accuracy better than 3 per cent for $v_\infty < 0.999$ and to within

0.5 per cent for $v_\infty < 0.98$:

$$b_c^{\text{fit}} = \frac{2M}{v_\infty^2} (1 + c_1 v_\infty + c_2 v_\infty^2 + c_3 v_\infty^3), \quad (32)$$

with $c_1 = 0.081135$, $c_2 = 3.452826$, and $c_3 = -1.758438$.

All of the streamlines within the cylinder $b \leq b_c$ contribute to the total accretion rate. According to the right-hand side of equation (29), we can therefore express \dot{M} as

$$\dot{M} = \pi b_c^2 \rho_\infty v_\infty \gamma_\infty. \quad (33)$$

In Fig. 5 we show the resulting accretion rate as a function of the wind speed at infinity and compare it to the Newtonian value found in the BHL model (equation 7). As can be seen from this figure, the relativistic accretion rate is greater than the corresponding BHL one for all values of v_∞ , with the difference being more than double

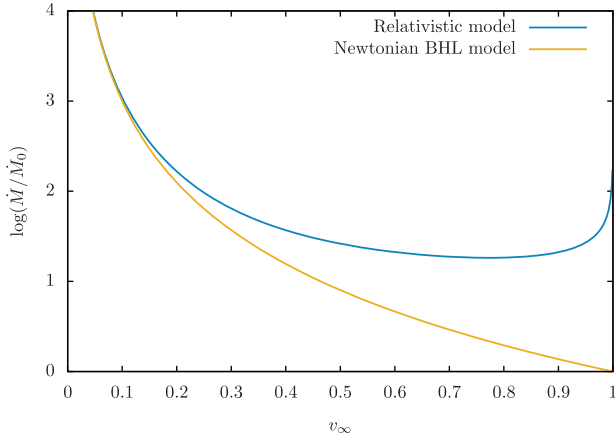


Figure 5. Mass accretion rate as a function of the wind speed at infinity v_∞ . The blue line corresponds to the (fitted) relativistic model as given by equation (32), while the yellow line corresponds to the Newtonian BHL model (equation 7). In both cases the accretion rate is expressed in units of $M_0 = 4\pi M^2 \rho_\infty$.

for $v_\infty \gtrsim 0.4$ and more than 10 times larger for $v_\infty \gtrsim 0.8$. As expected, the relativistic accretion rate converges to the Newtonian value in the non-relativistic limit, i.e. for $v_\infty \ll 1$. Contrary to the Newtonian case in which the accretion rate was a monotonically decreasing function of v_∞ , the relativistic result has an inflection point at around $v_\infty \simeq 0.8$ and becomes arbitrarily large as $v_\infty \rightarrow 1$. The culprit behind this behaviour is the special relativistic effect of Lorentz contraction that compresses the fluid volume elements along the direction of the wind and is represented by the Lorentz factor in equation (33).

4 COMPARISON WITH NUMERICAL SIMULATIONS

In this section we compare the analytic wind accretion model presented in the previous section against numerical hydrodynamic simulations performed with *aztekas*, a free GPL code for solving any conservative set of equations, in particular, relativistic (with a non-trivial fixed metric) and non-relativistic hydrodynamic equations. Some aspects of *aztekas*, together with numerical and convergence tests relevant to this work are discussed in the Appendix A. Further details and tests of the *aztekas* code will be presented elsewhere.

For all of the simulations discussed in this work, we considered a perfect fluid evolving on top a fixed Schwarzschild background metric described in terms of the horizon-penetrating, Kerr–Schild coordinates. Since the problem under study presents axial symmetry, all of the simulations were performed in 2D using polar coordinates r and θ . All of the results presented below were obtained after the numerical simulations had evolved in time from a uniform initial state condition until a relaxed stationary state was reached.

The relativistic hydrodynamic equations consist of the continuity equation (26) together with the local conservation of energy–momentum

$$\nabla_\mu T^{\mu\nu} = 0, \quad (34)$$

where we take the energy–momentum tensor $T^{\mu\nu}$ corresponding to a perfect fluid (Landau & Lifshitz 1975)

$$T^{\mu\nu} = \rho h U^\mu U^\nu + p g^{\mu\nu}, \quad (35)$$

with rest mass density ρ , pressure p , specific internal energy ϵ , and specific enthalpy $h = 1 + \epsilon + p/\rho$. Moreover, we adopt a Bondi–Wheeler equation of state (Tooper 1965) of the form

$$\epsilon = \frac{p}{\rho(\Gamma - 1)}, \quad (36)$$

where Γ is the polytropic index.

In order to integrate numerically equations (26) and (34) with *aztekas*, we recast them in a conservative form based on the 3 + 1 formalism (see e.g. Font 2000; Alcubierre 2008), as follows

$$\frac{1}{\sqrt{-g}} \frac{\partial (\sqrt{\gamma} \mathbf{Q})}{\partial t} + \frac{1}{\sqrt{-g}} \frac{\partial (\sqrt{-g} \mathbf{F}^i)}{\partial x^i} = \mathbf{S}, \quad (37)$$

where γ and g are the determinants of the spatial 3-metric γ_{ij} and the spacetime 4-metric $g_{\mu\nu}$, respectively. \mathbf{Q} is the conservative variable vector, $\mathbf{F}^i = \{\mathbf{F}^r, \mathbf{F}^\theta\}$ are the fluxes along the r and θ coordinates, and \mathbf{S} is the source vector. All of these quantities depend on the primitive variables \mathbf{U} . The functional form of these vectors are presented below:

$$\mathbf{U} = [\rho, v_j, p]^T, \quad (38)$$

$$\mathbf{Q} = [D, S_j, \tau] = [\rho W, \rho h W^2 v_j, \rho h W^2 - p - D]^T, \quad (39)$$

$$\mathbf{F}^i = \left[D \left(v^i - \frac{\beta^i}{\alpha} \right), S_j \left(v^i - \frac{\beta^i}{\alpha} \right) + p \delta_j^i, \right. \\ \left. \tau \left(v^i - \frac{\beta^i}{\alpha} \right) + p v^i \right]^T, \quad (40)$$

$$\mathbf{S} = \left[0, T^{\mu\nu} \left(\frac{\partial g_{\nu j}}{\partial x^\mu} - \Gamma_{\nu\mu}^\sigma g_{\sigma j} \right), \right. \\ \left. \alpha \left(T^{\mu 0} \frac{\partial \ln \alpha}{\partial x^\mu} - T^{\mu\nu} \Gamma_{\nu\mu}^0 \right) \right]^T, \quad (41)$$

where $\Gamma_{\mu\nu}^\lambda$ are the usual Christoffel symbols, v^i is the three-velocity as measured by local Eulerian observers, $W = (1 - \gamma_{ij} v^i v^j)^{-1/2}$ is the associated Lorentz factor, and

$$\alpha = \left(1 + \frac{2M}{r} \right)^{-1/2}, \quad (42)$$

$$\beta^i = \left(\frac{2M}{r} \left(1 + \frac{2M}{r} \right)^{-1}, 0, 0 \right), \quad (43)$$

are the lapse function and the shift vector, respectively, and correspond to the 3 + 1 decomposition of Schwarzschild spacetime in Kerr–Schild coordinates.

For the numerical flux calculation, we use in *aztekas* a high-resolution shock capturing method with an HLLC approximate Riemann solver (Harten, Lax & Leer 1983), combined with a monotonically centred (MC) second-order reconstructor at cell interfaces. For the time integration, we use a second-order Runge–Kutta method of lines in the total variation diminishing version (Shu & Osher 1988). Finally, we adopt a constant time step defined through the Courant–Friedrichs–Lewy (CFL) condition $\Delta t = C \min(\Delta r, r \Delta\theta)$, with $C = 0.1$.

For the relativistic wind simulations, we ran two sets of simulations exploring asymptotic wind speeds from $v_\infty = 0.1$ to 0.9 for two different polytropic indices: $\Gamma = 4/3$ and $5/3$. We took as numerical

domain $[r_{\min}, r_{\max}] \times [0, \pi]$, with $r_{\min} = 0.5 r_{\text{acc}}$, $r_{\max} = 10 r_{\text{acc}}$, and

$$r_{\text{acc}} = \frac{M}{v_{\infty}^2 + a_{\infty}^2}, \quad (44)$$

where a_{∞} is the asymptotic speed of sound. The radius r_{acc} is commonly used in the literature (cf. Font, Ibáñez & Papadopoulos 1999; Cruz-Osorio, Lora-Clavijo & Guzmán 2012), as a good estimate for the extension of the numerical domain necessary for numerical convergence.⁴ Our choice of this numerical domain is based on the convergence and resolution tests discussed in detail in the Appendix A.

For most of these simulations we used a fixed Mach number $\mathcal{M} = v_{\infty}/a_{\infty} = 5$ in order to ensure that we were considering the same supersonic conditions in all cases. As a sanity check, we also considered $\mathcal{M} = 10$ for a reduced number of cases. We used a uniform grid of 400×400 cells except for the cases $v_{\infty} = 0.1, 0.8$, and 0.9 , where we had to use a larger grid of 1000×1000 in order to find converged solutions.

As external boundary condition at the sphere $r = r_{\max}$, we enforced a constant, uniform inflow from the northern hemisphere $\theta \in [0, \pi/2)$ and free outflow from the southern one $\theta \in [\pi/2, \pi]$. As internal boundary condition, we set free outflow across the sphere at $r = r_{\min}$. The incoming wind at the external boundary has uniform thermodynamical variables ρ_{∞} and p_{∞} . We set $\rho_{\infty} = 10^{-10}$ in arbitrary units and take p_{∞} consistent with the chosen Mach number \mathcal{M} and the equation of state, as in Cruz-Osorio et al. (2012):

$$p_{\infty} = \frac{a_{\infty}^2 \rho_{\infty} (\Gamma - 1)}{\Gamma (\Gamma - 1) - a_{\infty}^2 \Gamma}. \quad (45)$$

For the velocity field, we set an incoming wind with a constant velocity $\sqrt{v_i v^i} = v_{\infty}$, and components:

$$v_r = -\sqrt{g_{rr}} v_{\infty} \cos \theta, \quad (46)$$

$$v_{\theta} = \sqrt{g_{\theta\theta}} v_{\infty} \sin \theta, \quad (47)$$

where g_{rr} and $g_{\theta\theta}$ are the radial and polar components of the metric, respectively. As for the initial conditions of the simulation, we set them equal to the constant boundary values over all the numerical domain.

The simulations were left to run until a stationary state was reached. This was monitored by keeping track of the mass accretion rate, which was computed on the fly by integrating the relativistic radial mass flux across a control sphere of radius r according to (Petrich et al. 1989)

$$\dot{M} = 2\pi \int_0^{\pi} D \left(v^r - \frac{\beta^r}{\alpha} \right) r^2 \sin \theta d\theta. \quad (48)$$

It is important to remark that, once the stationary state is reached across all the numerical domain, the mass accretion rate as calculated from equation (48) has to have a constant value (to within numerical precision) independently of where the control radius r is located (see Fig. A3).

⁴Note that with our choice of r_{\min} , simulations with $v_{\infty} \geq 0.5$ are such that $r_{\min} < 2M$, which *aztekas* can handle without any problem due to our choice of horizon-penetrating coordinates. On the other hand, for those simulations with $r_{\min} > 2M$, we performed trial tests to make sure that the resulting steady-state accretion rate was unchanged independently of whether the black hole event horizon ($2M$) was part of the numerical domain or not.

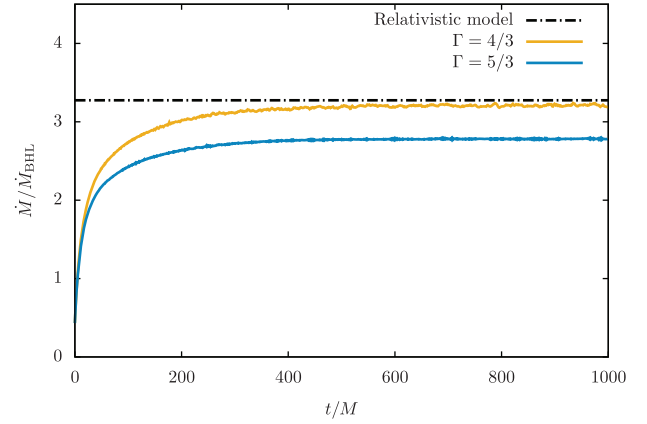


Figure 6. Mass accretion rate as a function of time for two wind simulations with asymptotic velocity $v_{\infty} = 0.5$ and $\Gamma = 4/3, 5/3$. As a reference, the horizontal dashed line shows the corresponding value from the relativistic model (equation 33). The stationary state is reached after $t \approx 600M$. The mass accretion rate has been scaled using the BHL result $\dot{M}_{\text{BHL}} = 4\pi M^2 \rho_{\infty}^3 / v_{\infty}^3$ (equation 7).

The typical simulation time at which steady state was reached depends on the wind velocity at infinity and the domain extension roughly as $t_c \approx r_{\text{acc}}/v_{\infty}$. As an example, in Fig. 6 we show the mass accretion rate as a function of time for $v_{\infty} = 0.5$ and $\Gamma = 4/3, 5/3$, measuring it at the event horizon $r = 2M$.

In Fig. 7, we show the steady-state of the density field and streamlines of a wind accretion flow with $v_{\infty} = 0.5$ and polytropic index $\Gamma = 4/3$ on the left-hand panel and $\Gamma = 5/3$ on the right-hand panel. As expected for a supersonic flow, a bow shock is formed downstream around the accretor, with a smaller shock cone for $\Gamma = 4/3$ than for $\Gamma = 5/3$.

In Fig. 8, we compare the streamlines as obtained from the two simulations discussed in the previous paragraph against the ones from the analytic model. As can be seen from this figure, the ballistic approximation provides a qualitatively good description of the resulting streamlines upstream of the flow and in the region outside the bow shock, while inside the shock cone the streamline behaviour is notably different.

We can also notice from both Figs 6 and 8 that there is a better agreement between the analytic model and the $\Gamma = 4/3$ case than for the $\Gamma = 5/3$ one. This is related to the fact that the relative degree of incompressibility or stiffness of a polytropic fluid is directly proportional to the adiabatic index and, thus, a $\Gamma = 5/3$ fluid resists more effectively the compression due to the gravitational field of the central object (geodesic focusing) than a fluid with $\Gamma = 4/3$.

In order to compare the numerical mass accretion rate with the ballistic model (equation 31), we computed the mean value of equation (48) across all the radial domain. In Fig. 9 we show the comparison between the analytic model presented in the previous section and the simulations for both $\Gamma = 4/3$ and $5/3$.

Moreover, we also explored the dependence of the mass accretion rate on the Mach number by performing 10 additional simulations with $\mathcal{M} = 10$. In Fig. 9, the square marks show the mass accretion rate for these simulations. Note that these results overlay with the $\mathcal{M} = 5$ cases (the relative difference between both results is less than 0.7 per cent). The resulting bow shocks are also very similar in both cases, with slightly smaller cones for the $\mathcal{M} = 10$ case.

As can be seen in Fig. 9, the resulting accretion rate from the numerical simulations is consistently slightly larger for the $\Gamma = 4/3$

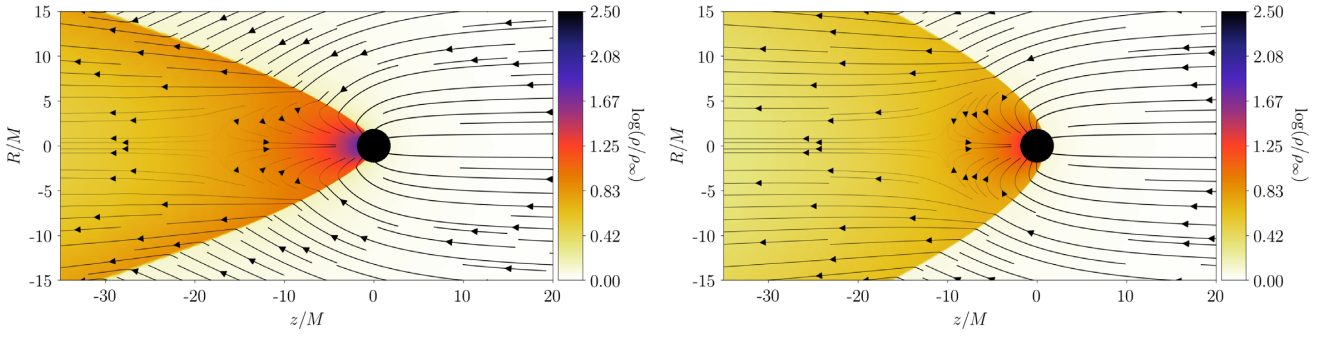


Figure 7. Numerical simulations performed with *aztekas* of a relativistic wind accreting on to a Schwarzschild black hole. The chosen polytropic index is $\Gamma = 4/3$ for the left-hand panel and $\Gamma = 5/3$ for the right-hand one, while the asymptotic wind velocity is $v_\infty = 0.5$. The plot shows the stationary-state streamlines and in colour isocontour levels of the corresponding density field. The width of the streamlines is proportional to the velocity magnitude $v = \sqrt{v_i v^i}$.

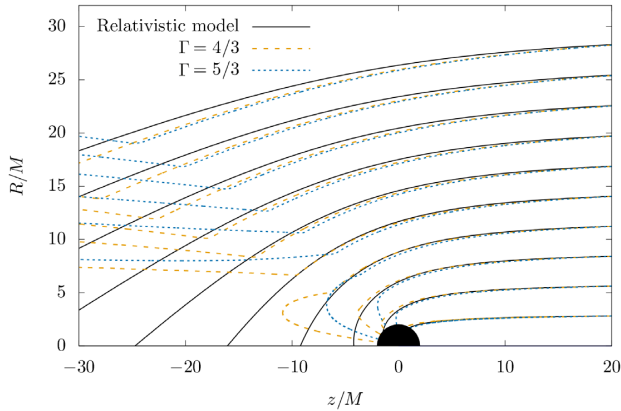


Figure 8. Comparison of the streamlines of the analytic model against the corresponding ones extracted from the numerical simulations for $v_\infty = 0.5$, $\mathcal{M} = 5$, and $\Gamma = 4/3, 5/3$.

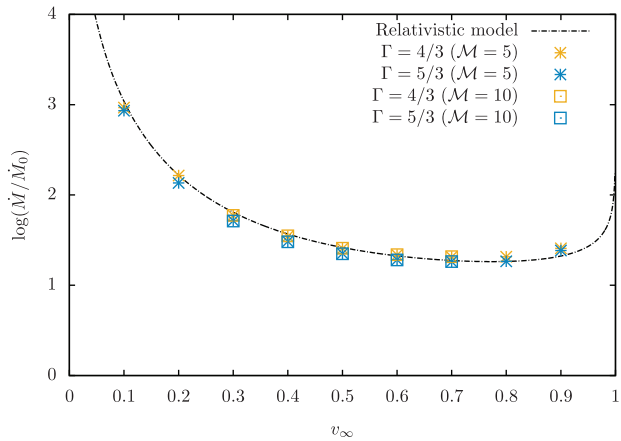


Figure 9. Comparison of the mass accretion rate as obtained from the relativistic model (equation 33) versus the numerical values obtained from the *aztekas* simulations. The colour marks show the results of the 28 simulations discussed in this work for asymptotic wind speeds $v_\infty = 0.1, 0.2, \dots, 0.9$, two polytropic indices $\Gamma = 4/3, 5/3$, and two Mach numbers $\mathcal{M} = 5, 10$. The mass accretion rate is expressed in units of $\dot{M}_0 = 4\pi M^2 \rho_\infty$.

simulations than for the $\Gamma = 5/3$ ones. Moreover, a good agreement is found between the accretion rate as predicted by the relativistic model and the one obtained from the *aztekas* simulations, with a

relative error less than 10 percent for all of the 28 simulations presented in this work.

5 SUMMARY

We have presented a full relativistic, analytic model of a supersonic wind accreting on to a Schwarzschild black hole. In addition to the assumptions of stationarity and axisymmetry, the model is based on the ballistic approximation in which the streamlines of the accretion flow correspond to geodesic trajectories of a Schwarzschild spacetime. Following the methodology presented in Tejada et al. (2012), the streamlines of the model were described analytically in terms of Jacobi elliptic functions. The density field of the resulting accretion flow and the corresponding accretion rate were calculated using simple numerical schemes.

The model presented in this paper constitutes the relativistic generalization of the Newtonian wind accretion model by Bondi–Hoyle–Lyttleton (BHL). Naturally, the relativistic model recovers the BHL model in the non-relativistic limit $v_\infty \ll c$. The enhanced gravitational field of the accreting object in general relativity, together with the special relativistic effect of Lorentz contraction, contribute to a larger accretion rate as compared to that of the BHL model (see Fig. 5). This difference becomes substantial (by a factor of 10–100) for asymptotic wind speeds v_∞ close to the speed of light c . Although these large velocities are not expected to be common in astrophysical settings, they can appear in extreme cases such as the velocity kick imparted on to a newborn black hole following an asymmetrical supernova explosion (Janka 2013) or after the merger of two rotating black holes (Gerosa & Moore 2016).

We have compared the new relativistic model against numerical simulations performed with the *aztekas* code. This code solves numerically the full hydrodynamic evolution of a perfect fluid in Schwarzschild spacetime starting off from a uniform condition until a stationary state is reached. We have used two different polytropic equations of state ($\Gamma = 4/3$ and $\Gamma = 5/3$) and asymptotic wind speeds from $v_\infty = 0.1c$ to $v_\infty = 0.9c$. We have considered two different values for the asymptotic Mach number, $\mathcal{M} = 5$ and 10 , finding virtually no difference between these two values. We have found a good agreement (to within 10 percent) between the accretion rate predicted by the relativistic model and the *aztekas* simulations (see Fig. 9). As expected for these supersonic flows, the ballistic streamlines of the analytic model agree quite well with the resulting streamlines of the numerical simulations in the upwind region outside the bow shock.

ACKNOWLEDGEMENTS

We thank Sergio Mendoza, Alejandro Cruz-Osorio, Olivier Sarbach, and Francisco S. Guzmán for useful discussions and comments on the manuscript. We also thank the anonymous referee for helpful suggestions and remarks. This work was supported by Dirección General de Asuntos del Personal Académico, Universidad Nacional Autónoma de México (DGAPA-UNAM project number IN112616 and IN112019) and Consejo Nacional de Ciencia y Tecnología (CONACyT project ID: CB-2014-01 No. 240512; No. 290941; No. 291113) grants. ET and AAO acknowledge economic support from CONACyT (CVU 673583 and 788898).

REFERENCES

- Aguayo-Ortiz A., Mendoza S., Olvera D., 2018, *PLOS One*, 13, e0195494
 Alcubierre M., 2008, *Introduction to 3 + 1 Numerical Relativity*. Oxford Univ. Press, Oxford
 Bisnovaty-Kogan G. S., Kazhdan I. M., Klypin A. A., Lutskii A. E., Shakura N. I., 1979, *Astron. Zh.*, 56, 359
 Bondi H., 1952, *MNRAS*, 112, 195
 Bondi H., Hoyle F., 1944, *MNRAS*, 104, 273
 Cruz-Osorio A., Lora-Clavijo F. D., 2016, *MNRAS*, 460, 3193
 Cruz-Osorio A., Lora-Clavijo F. D., Guzmán F. S., 2012, *MNRAS*, 426, 732
 Cruz-Osorio A., Sánchez-Salcedo F. J., Lora-Clavijo F. D., 2017, *MNRAS*, 471, 3127
 Edgar R., 2004, *New Astron. Rev.*, 48, 843
 El Mellah I., Casse F., 2015, *MNRAS*, 454, 2657
 El Mellah I., Sundqvist J. O., Keppens R., 2018, *MNRAS*, 475, 3240
 Font J. A., 2000, *Living Rev. Relativ.*, 3, 2
 Font J. A., Ibáñez J. M., 1998, *ApJ*, 494, 297
 Font J. A., Ibáñez J. M., Papadopoulos P., 1999, *MNRAS*, 305, 920
 Frank J., King A., Raine D., 2002, *Accretion Power in Astrophysics*, 3rd edn. Cambridge Univ. Press, Cambridge
 Frolov V. P., Novikov I. D., 1998, *Black Hole Physics: Basic Concepts and New Developments*. Kluwer Academic, Dordrecht
 Gerosa D., Moore C. J., 2016, *Phys. Rev. Lett.*, 117, 011101
 Gracia-Linares M., Guzmán F. S., 2015, *ApJ*, 812, 23
 Harten A., Lax P. D., Leer B., 1983, *SIAM Rev.*, 25, 35
 Hoyle F., Lyttleton A., 1939, *Math. Proc. Camb. Phil. Soc.*, 35, 405
 Hunt R., 1971, *MNRAS*, 154, 141
 Janka H.-T., 2013, *MNRAS*, 434, 1355
 Landau L., Lifshitz E., 1975, *The Classical Theory of Fields: Course of Theoretical Physics – Vol. 2*, 4th edn. Elsevier, Oxford, UK
 Lawden D. F., 1989, *Elliptic Functions and Applications*, Springer, New York
 Longair M. S., 2011, *High Energy Astrophysics*. Cambridge Univ. Press, Cambridge
 Lora-Clavijo F. D., Guzmán F. S., 2013, *MNRAS*, 429, 3144
 Mendoza S., Tejada E., Nagel E., 2009, *MNRAS*, 393, 579
 Michel F. C., 1972, *Ap&SS*, 15, 153
 Olvera D., Mendoza S., 2008, in Oscoz A., Mediavilla E., Serra-Ricart M., eds, *EAS Publ. Ser. Vol. 30, A GPL Relativistic Hydrodynamical Code*. Cambridge Univ. Press, Cambridge, p. 399
 Petrich L. I., Shapiro S. L., Teukolsky S. A., 1988, *Phys. Rev. Lett.*, 60, 1781
 Petrich L. I., Shapiro S. L., Stark R. F., Teukolsky S. A., 1989, *ApJ*, 336, 313
 Romero G. E., Vila G. S., eds, 2014, *Lecture Notes in Physics, Vol. 876, Introduction to Black Hole Astrophysics*. Springer-Verlag, Berlin
 Ruffert M., Arnett D., 1994, *ApJ*, 427, 351
 Schroven K., Hackmann E., Lämmerzahl C., 2017, *Phys. Rev. D*, 96, 063015
 Shima E., Matsuda T., Takeda H., Sawada K., 1985, *MNRAS*, 217, 367
 Shu C.-W., Osher S., 1988, *J. Comput. Phys.*, 77, 439
 Tejada E., 2018, *Rev. Mex. Astron. Astrofis.*, 54, 171

- Tejada E., Mendoza S., Miller J. C., 2012, *MNRAS*, 419, 1431
 Tejada E., Taylor P. A., Miller J. C., 2013, *MNRAS*, 429, 925
 Tooper R. F., 1965, *ApJ*, 142, 1541
 Zanotti O., Roedig C., Rezzolla L., Del Zanna L., 2011, *MNRAS*, 417, 2899

APPENDIX: VALIDATION OF THE NUMERICAL HYDRODYNAMIC CODE AZTEKAS

In this appendix we present several numerical tests intended to validate our use of *aztekas* in this work.

A1 Spherical accretion

In order to test *aztekas* in the general relativistic hydrodynamic regime, it is important to compare with a benchmark solution. For this, we employ the analytic model of spherical accretion developed by Michel (1972).

In Fig. A1, we compare the outcome of numerical simulations performed with *aztekas* against Michel’s analytic solution for the same values of polytropic index used in the wind accretion problem ($\Gamma = 4/3, 5/3$) and for an asymptotic sound speed of $a_\infty = 0.01$.

For these simulations, we took a 2D spherical axisymmetric grid of 400×400 uniformly distributed radial bins $r \in [0.5M, 20M]$ and polar bins $\theta \in [0, \pi/2]$. We set the boundary conditions at $r = 20M$ by imposing Michel’s solution there. As initial conditions we populate the entire numerical domain with the boundary constant value and let the system evolve until a stationary regime is reached for $t \gtrsim 100M$. As can be seen from Fig. A1, an excellent agreement is found between Michel’s analytic solution and the *aztekas* simulation results. We compute the mass accretion rate and the relative error between both solutions is below 0.2 per cent.

Also using this benchmark solution, we looked at the convergence rate of *aztekas* by computing the L^1 norm of the density error for

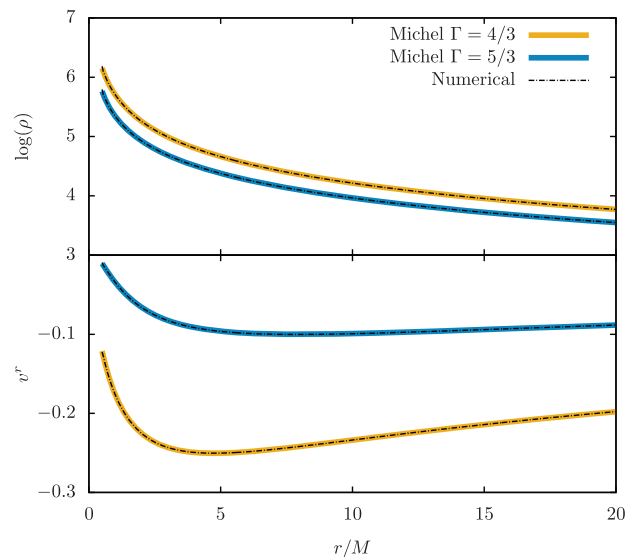


Figure A1. Comparison of the numerical hydrodynamic simulations performed with *aztekas* against the relativistic spherical accretion model of Michel (1972). The top panel shows the density as a function of radius while the bottom panel shows the radial velocity for two different values of the polytropic index $\Gamma = 4/3, 5/3$ and an asymptotic sound speed of $a_\infty = 0.01$.

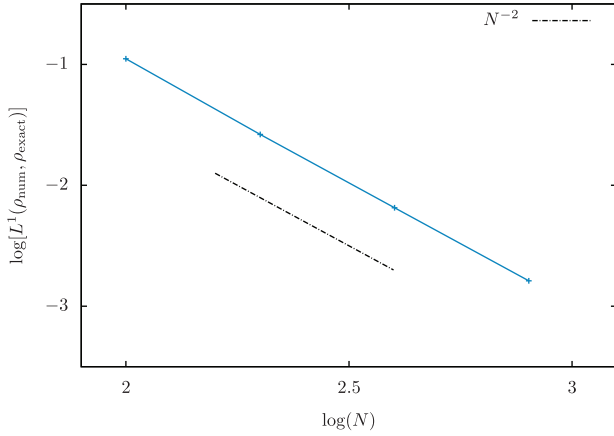


Figure A2. L^1 norm of the density error for the Michel test, using resolutions $N_r = 100, 200, 400,$ and 800 . The dashed line shows the slope that corresponds to a second-order convergence rate.

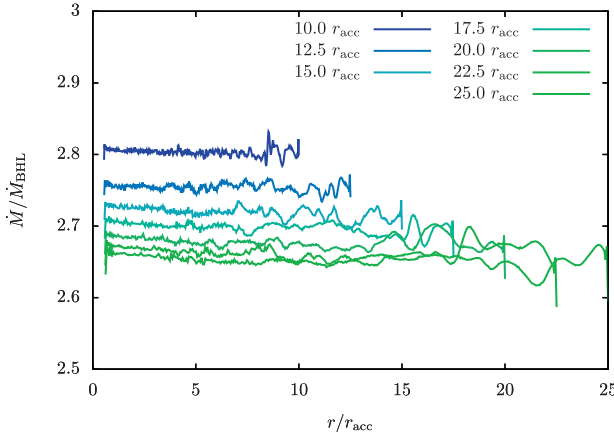


Figure A3. Comparison of the mass accretion rate for different domain extensions. In all cases $v_\infty = 0.5$, $\Gamma = 5/3$, and the simulation time is $t = 1000M$.

different numerical resolutions N_r ,⁵ i.e.

$$L^1(\rho_{\text{num}}, \rho_{\text{exact}}) = \frac{1}{N_r} \sum_{i=1}^{N_r} |\rho_{\text{num}}(r_i) - \rho_{\text{exact}}(r_i)|, \quad (\text{A1})$$

where ρ_{num} and ρ_{exact} are the numerical and exact values of the density, respectively. In Fig. A2, we show the result of this test from where we obtain a convergence rate consistent with a second order, which is to be expected for smooth solutions and for our use of the MC reconstructor.

A2 Dependence on domain extension and resolution

We also want to make sure that the numerical solutions obtained with *aztekas* have converged to physical values and that the results are independent from both numerical resolution and domain extension.

Due to the finite extension of the numerical domain r_{max} , the total accretion rate calculated from the numerical simulations shows a small dependence on r_{max} that gets weaker as larger domain

⁵Since no angular dependence is found for this spherically symmetric test, we only varied the radial resolution while keeping a constant $N_\theta = 400$.

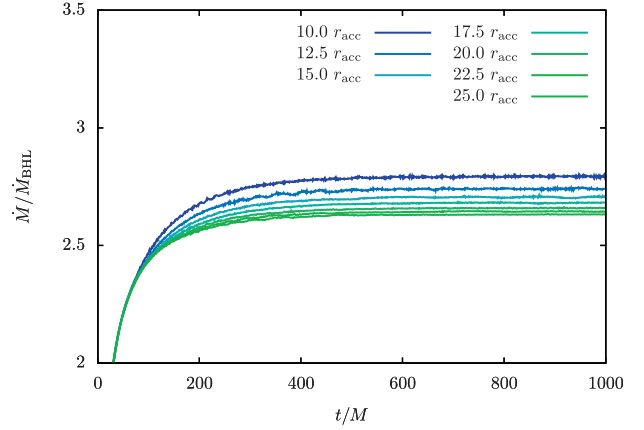


Figure A4. Same as in Fig. A3, but now measuring the mass accretion rate across $r = 2M$ as a function of time.

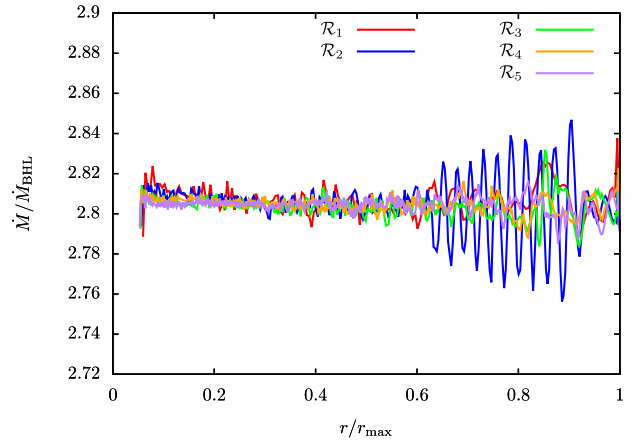


Figure A5. Comparison between the mass accretion rate for different resolutions $\mathcal{R}_1 = 200 \times 200$, $\mathcal{R}_2 = 300 \times 300$, $\mathcal{R}_3 = 400 \times 400$, $\mathcal{R}_4 = 500 \times 500$, and $\mathcal{R}_5 = 600 \times 600$, for $v_\infty = 0.5$, $\Gamma = 5/3$, and $t = 1000M$.

extensions are considered. For example, in Fig. A3 we show the resulting mass accretion rate for simulations with $v_\infty = 0.5$, $\Gamma = 5/3$, and seven different domain extensions, at $t = 1000M$. As can be seen from this figure, our choice of a domain extension of $r_{\text{max}} = 10 r_{\text{acc}}$ leads to an overestimation of the mass accretion rate of the order of ~ 5 per cent, which is an acceptable margin of error for us in this work. We expect the rest of the simulations to behave in a similar way.

Similarly, we also looked at this same domain extension dependence but now by monitoring the mass accretion rate across a fixed radius (in this case across the event horizon at $r = 2M$) as a function of time. As can be seen from Fig. A4, the difference between a domain extension of $10 r_{\text{acc}}$ and of $25 r_{\text{acc}}$ maintains the same margin error of ~ 5 per cent along time.

In what regards the numerical resolution, we found that the grid size does not affect as directly the value of the resulting accretion rate. However, it does contribute to the smoothness of the solution, with larger resolutions leading to less numerical noise. In Fig. A5 we show an example of this again for the case $v_\infty = 0.5$, $\Gamma = 5/3$ and five different numerical resolutions: $\mathcal{R}_1 = 200 \times 200$, $\mathcal{R}_2 = 300 \times 300$, $\mathcal{R}_3 = 400 \times 400$, $\mathcal{R}_4 = 500 \times 500$, and $\mathcal{R}_5 = 600 \times 600$. As discussed in the Section 4, for most of the simulations presented in

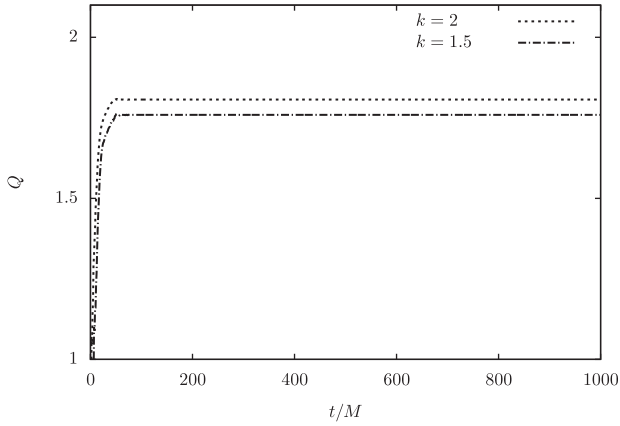


Figure A6. Self-convergence of the wind simulations (see equation A2) for two sets of simulations with a ratio of $k = 1.5$ and 2 between successive resolutions. In both cases the convergence rate Q stays between 1.5 and 2 in the steady-state region, as required for this test due to the presence of shocks.

this work we settled for \mathcal{R}_3 as a good compromise between accuracy and performance.

Finally, in order to estimate the convergence rate of the simulations, and given that there is no analytical solution for the full hydrodynamic wind accretion, we follow Lora-Clavijo & Guzmán (2013) and measure the self-convergence rate using different resolutions. To this purpose, we ran two sets of three simulations each,

with resolutions

$$\mathcal{R}_1 = 200 \times 200, \mathcal{R}_2 = 300 \times 300, \text{ and } \mathcal{R}_3 = 450 \times 450,$$

and

$$\mathcal{R}_1 = 200 \times 200, \mathcal{R}_2 = 400 \times 400, \text{ and } \mathcal{R}_3 = 800 \times 800.$$

Note that, for each set separately, there is a factor of $k = 1.5$ and $k = 2$ between successive resolutions. With the simulation results at hand, we compute the self-convergence factor Q according to

$$k^Q = \frac{L^1(\rho_1, \rho_2)}{L^1(\rho_2, \rho_3)}, \quad (\text{A2})$$

with $L^1(\rho_i, \rho_j)$ as defined in equation (A1) and where ρ_1 , ρ_2 , and ρ_3 are the densities along the accretion axis ($\theta = \pi$) for each of the employed resolutions. The results for this test are shown in Fig. A6. As can be seen from this figure, for both set of resolutions we find an order of convergence between 1.5 and 2 in the steady-state region, which is to be expected for this kind of algorithms due to the presence of shocks.

This paper has been typeset from a $\text{\TeX}/\text{\LaTeX}$ file prepared by the author.

Choked accretion: from radial infall to bipolar outflows by breaking spherical symmetry

In this chapter, we present the *choked accretion* model. The latter consists of an inflow-outflow mechanism obtained by considering deviations from spherical symmetry in an initially, radial gas inflow. Specifically, this non-relativistic model considers axisymmetric, large-scale, small amplitude deviations in the density field in such a way that the equatorial region is over dense as compared with the polar regions. This density gradient breaks the spherical symmetry of the inflow, giving rise to a steady-state solutions characterized by an equatorial inflow and a bipolar outflow.

The first part of the article focuses on the derivation of a simple analytic model that motivates the physical processes involved in the choked accretion mechanism. This analytic solution describes an incompressible fluid from which, under the assumption of irrotational flow, we obtain the potential flow equation that gives us a general solution for the velocity potential that describes both accretion onto a central object and a bipolar outflow.

In the second part of the study, we extend the previous analytic solution to the case of an ideal gas using full-hydrodynamic numerical simulations using the AZTEKAS code. The initial setup for these simulations consists of a uniform density, spherical gas cloud. In order to break the spherical symmetry, we impose a density profile as boundary condition at the injection sphere of the domain. We perform different simulations of an ideal gas under two different thermodynamical processes: isothermal ($\kappa = 1$) and adiabatic ($\kappa = \gamma$), using two values of the adiabatic index. We also explore four values of the density contrast. From these numerical simulations we compute the accretion rate and find that, independently of the density contrasts at the boundary (as well as the adiabatic index), the mass accretion rate remains constant and corresponds to Bondi's value. These results suggest that, given that the material is *choking* at a fixed value, the injected and ejected material are balanced,

providing a direct link between accretion and ejection.

The study presented in this chapter was published in MNRAS in 2019. The details of the paper are:

Aguayo-Ortiz A., Tejada E., Hernandez X., 2019, MNRAS, 490, 5078.

[doi:10.1093/mnras/stz2989](https://doi.org/10.1093/mnras/stz2989)

Choked accretion: from radial infall to bipolar outflows by breaking spherical symmetry

Alejandro Aguayo-Ortiz¹,[★] Emilio Tejada²,[★] and X. Hernandez¹,[★]

¹*Instituto de Astronomía, Universidad Nacional Autónoma de México, AP 70-264, 04510 Ciudad de México, Mexico*

²*Cátedras CONACyT – Instituto de Física y Matemáticas, Universidad Michoacana de San Nicolás de Hidalgo, Edificio C-3, Ciudad Universitaria, 58040 Morelia, Michoacán, Mexico*

Accepted 2019 October 18. Received 2019 October 10; in original form 2019 July 2

ABSTRACT

Steady-state, spherically symmetric accretion flows are well understood in terms of the Bondi solution. Spherical symmetry, however, is necessarily an idealized approximation to reality. Here we explore the consequences of deviations away from spherical symmetry, first through a simple analytic model to motivate the physical processes involved, and then through hydrodynamical, numerical simulations of an ideal fluid accreting on to a Newtonian gravitating object. Specifically, we consider axisymmetric, large-scale, small-amplitude deviations in the density field such that the equatorial plane is overdense as compared to the polar regions. We find that the resulting polar density gradient dramatically alters the Bondi result and gives rise to steady-state solutions presenting bipolar outflows. As the density contrast increases, more and more material is ejected from the system, attaining speeds larger than the local escape velocities for even modest density contrasts. Interestingly, interior to the outflow region, the flow tends locally towards the Bondi solution, with a resulting total mass accretion rate through the inner boundary *choking* at a value very close to the corresponding Bondi one. Thus, the numerical experiments performed suggest the appearance of a maximum achievable accretion rate, with any extra material being ejected, even for very small departures from spherical symmetry.

Key words: accretion, accretion discs – gravitation – hydrodynamics – methods: numerical.

1 INTRODUCTION

The accretion of fluids towards gravitational objects is a topic of general interest in astrophysics, as such phenomena underpin the physics of large classes of systems (Hawley et al. 2015). Notably, the ubiquitous jets observed from young stellar objects (YSOs) to gamma-ray bursts (GRBs) and active galactic nuclei (AGNs) are fuelled by the accretion of gas on to massive objects. Although the detailed physics of accretion problems is complex, including the effects of rotation, magnetic fields, non-ideal fluids, and mixing, to name a few (Pudritz et al. 2007; Tchekhovskoy 2015; Jafari 2019), the availability of simplified analytic solutions where the salient physical ingredients can be transparently traced has always provided valuable insights and well-understood limiting cases for the analysis of these systems.

The first analytic solution to such an accretion problem was the Newtonian spherically symmetric model of Bondi (1952), with the

corresponding extension to general relativity by Michel (1972). In both the cases, the authors assumed stationariness, spherical symmetry, and zero angular momentum for the infalling material, which was in turn described as an ideal fluid.

On the other hand, the origin of jets is typically understood in connection with accretion disc models, where the geometry very strongly deviates from spherical symmetry. In these, rotation and small-scale magnetic fields are considered as fundamental for the stability and evolution of the disc (Shakura & Sunyaev 1973; Balbus & Hawley 1991), while the interplay of these with a large-scale magnetic field is thought to be responsible for the launching and subsequent collimation of the jet (Hawley et al. 2015). This so-called magneto-rotational mechanism has been studied both at a Newtonian level (Blandford 1976; Lovelace 1976; Blandford & Payne 1982) and in general relativity when a central black hole is involved (Blandford & Znajek 1977).

The viability of the magneto-rotational mechanism for launching powerful jets has been successfully demonstrated by means of magnetohydrodynamic (MHD) numerical simulations. This has been done at a non-relativistic level for jets associated with YSOs (Casse & Keppens 2002), as well as with comprehensive,

* E-mail: aaguayo@astro.unam.mx, (AA-O); emilio.ciencias@conacyt.mx, (ET); xavier@astro.unam.mx (XH)

general relativistic-MHD simulations of accretion discs around spinning black holes (Semenov, Dyadechkin & Punsly 2004; Qian, Fendt & Vourellis 2018; Sheikhnezhadi & Fendt 2018; Liska et al. 2019).

The similarity of jets across a vast range of astrophysical scales, from quasars to micro-quasars (e.g. Mirabel & Rodríguez 1994), along with open questions regarding the matter content of relativistic jets (Hawley et al. 2015) or the link between the accretion disc and the acceleration process (Romero et al. 2017), might hint towards the presence in some cases of more simple outflow-producing mechanisms based on hydrodynamical physics. Moreover, it is clear that if some kind of universal mechanism underlies all astrophysical jets, then it cannot rely on the central accretor being a black hole.

Hydrodynamical models have been introduced for collimating and accelerating jets, in the context of AGNs (Blandford & Rees 1974) and of YSOs (specifically H–H objects as studied by Canto & Rodríguez 1980). On the other hand, a purely hydrodynamical mechanism, where a small-amplitude density gradient on the inflow boundary conditions yields to an inflow/outflow steady-state solution, was introduced by Hernandez et al. (2014) based on an analytic perturbation analysis of the hydrodynamic equations for an isothermal fluid.

In Hernandez et al. (2014), the authors consider an originally radial accretion flow that becomes increasingly dense as the fluid approaches the central accretor. As the authors assume that this flow originates from the inner walls of a disc-like configuration, there is a certain degree of inhomogeneity in the density field, with the polar regions being less dense than the disc plane. As a result of this density inhomogeneity, on approaching the central regions the geometrical focusing of the accreted material results in a pressure gradient that deviates some of the fluid elements from their infall trajectories and expels them from the central region along a bipolar outflow.¹ Within this scenario, the resulting bipolar outflow is neither accelerated to large Mach numbers nor collimated as a proper jet.

Following on from Hernandez et al. (2014), in this work we extend the previous results by considering more realistic adiabatic indices for the infalling material. The problem can no longer be treated analytically, so we implement full hydrodynamical numerical simulations using the free GPL hydrodynamical code *aztekas* (Olvera & Mendoza 2008; Aguayo-Ortiz, Mendoza & Olvera 2018).²

We have found with these simulations a flux-limited accretion mode, in which the total mass infall rate on to the central accretor is limited by a fixed value. This value coincides very closely with the mass accretion rate of the spherically symmetric Bondi solution. Whenever the incoming accretion flow surpasses this threshold value, the excess flow is redirected by a density gradient and expelled through the poles. Since the incoming accretion flow is jamming at a gravitational bottleneck, we refer to this ejection mechanism as *choked accretion*.

With the numerical simulations presented in this work, we recover the main result of Hernandez et al. (2014) that a large-scale, small-amplitude inhomogeneity in the density field can lead to

the onset of a bipolar outflow as a generic result. The choked accretion model can then be viewed as a transition bridge between the spherically symmetric condition treated by Bondi and Michel, where no outflows appear, and the disc geometries of the jet-generating models mentioned above.

In a separate work, Tejada, Aguayo-Ortiz & Hernandez (2019), we are proposing a full-analytic, general relativistic model of the choked accretion mechanism. This analytic model describes an ultra-relativistic gas with a stiff equation of state (see Petrich, Shapiro & Teukolsky 1988) and is based on the conditions of steady-state, axisymmetry, and irrotational flow. As shown by Tejada (2018), the non-relativistic limit of such a model corresponds to an incompressible fluid in Newtonian hydrodynamics. With this motivation in mind, we present in this article a simple analytic model of an incompressible fluid.

The remainder of the paper is organized as follows. In Section 2, we present a simple analytic model of the choked accretion that leads to an inflow/outflow configuration. Section 3 presents the hydrodynamical simulations used to extend this model to more general conditions, allowing for a range of plausible adiabatic indices. The code is validated and tested in the spherically symmetric case, where steady-state solutions accurately tracing the corresponding Bondi ones are recovered. In Section 4, we analyse the results obtained and discuss the applicability of the choked accretion mechanism in astrophysical settings. Finally, in Section 5, we present our conclusions.

2 ANALYTIC MODEL

In order to present a simple model where the physics leading from the breakage of spherical symmetry to the establishing of an outflow can be traced transparently, in this section we discuss an analytic model of choked accretion. Following Tejada (2018), this model is based on an incompressible fluid under the approximations of steady-state, axisymmetry, and irrotational flow.

This model can be considered as complementary to the perturbation analysis presented in Hernandez et al. (2014), where isothermal conditions were assumed, and which shows that a spherically symmetric flow on to a point mass is in fact unstable towards the development of the outflow phenomenology discussed here, as soon as a slight perturbation to spherical symmetry is introduced in the inflow conditions.

Under the irrotational flow condition, the fluid's velocity field can be obtained as the gradient of a velocity potential Φ (i.e. $\vec{v} = \nabla\Phi$). For an incompressible fluid, this means that Φ has to be a solution to the Laplace equation $\nabla^2\Phi = 0$. Adopting spherical coordinates and imposing the axisymmetry condition, we know that a general solution for Φ is given by (Currie 2003)

$$\Phi = \sum_{n=0}^{\infty} (A_n r^n + B_n r^{-(n+1)}) P_n(\cos\theta), \quad (1)$$

where A_n and B_n are the constant coefficients and $P_n(\cos\theta)$ is the Legendre polynomial of degree n .

The lowest order solution that describes both accretion on to a central object and an axisymmetric, bipolar outflow has only non-vanishing coefficients B_0 and A_2 .³ Let us re-parametrize these two

¹A similar deviation process by a pressure gradient is incorporated in the circulation model presented by Lery et al. (2002) in the context of molecular outflows in YSOs.

²aztekas.org ©2008 Sergio Mendoza & Daniel Olvera and ©2018 Alejandro Aguayo-Ortiz & Sergio Mendoza. The code can be downloaded from github.com/aztekas-code/aztekas-main.

³A scenario of wind accretion can be studied by taking instead only B_0 and A_1 different from zero, as has been done by Petrich et al. (1988) and Tejada (2018). More complex geometries can be described by considering higher order multipoles of A_n .

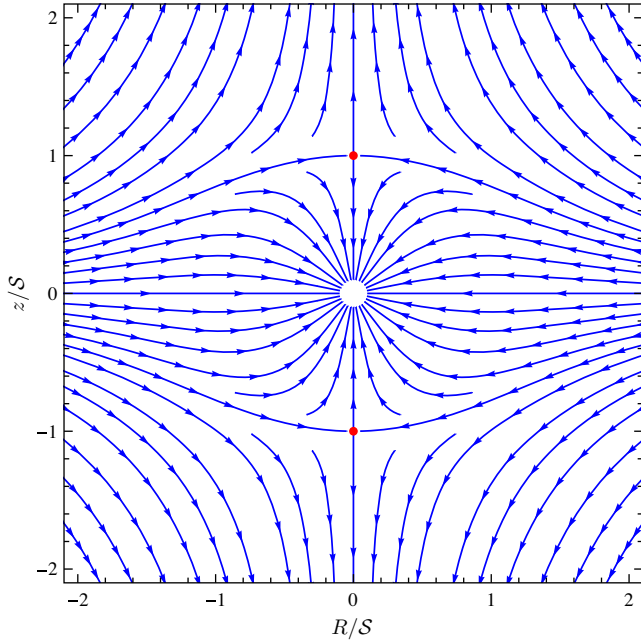


Figure 1. Streamlines of the incompressible analytic model showing an inner quasi-spherical accretion region, and polar stagnation points beyond which a polar outflow solution results. The red dots indicate the location of the stagnation points along the symmetry axis. The axes correspond to the usual cylindrical coordinates $R = r \sin \theta$, $z = r \cos \theta$.

coefficients as $B_0 = \alpha$, $A_2 = \alpha/(2\mathcal{S}^3)$, and write the solution as

$$\Phi = \frac{\alpha}{r} \left[1 + \frac{r^3}{4\mathcal{S}^3} (3 \cos^2 \theta - 1) \right], \quad (2)$$

which leads to the velocity field

$$\frac{dr}{dt} = -\frac{\alpha}{r^2} \left[1 - \frac{r^3}{2\mathcal{S}^3} (3 \cos^2 \theta - 1) \right], \quad (3)$$

$$\frac{d\theta}{dt} = -\frac{3\alpha \sin \theta \cos \theta}{2\mathcal{S}^3}. \quad (4)$$

This velocity profile has the same dependence on the polar angle as the one obtained for the isothermal hydrodynamic solutions of Hernandez et al. (2014), which are also given in terms of Legendre polynomials.

The parameter \mathcal{S} is related to the location of the stagnation point, as from equations (3) and (4) we see that the points ($r = \mathcal{S}$, $\theta = 0$) and ($r = \mathcal{S}$, $\theta = \pi$) correspond to the stagnation points of the flow. In Fig. 1, we show an example of the resulting streamlines.

On the other hand, the parameter α is related to the total accretion rate on to the central object in the following way:

$$\dot{M} = -2\pi \int_0^\pi \rho \frac{dr}{dt} r^2 \sin \theta d\theta = 4\pi\rho\alpha, \quad (5)$$

that is

$$\alpha = \frac{\dot{M}}{4\pi\rho}. \quad (6)$$

At this point, \dot{M} can have any arbitrary value. For the choked accretion model, we shall assume that \dot{M} is given by the Bondi accretion rate, i.e.

$$\alpha = \frac{\dot{M}_B}{4\pi\rho} = \frac{1}{4} \frac{(GM)^2}{a_\infty^3} \left(\frac{2}{5-3\gamma} \right)^{\frac{5-3\gamma}{2(\gamma-1)}}, \quad (7)$$

where M is the mass of the central accretor, γ is the adiabatic index of the fluid, and a_∞ is the speed of sound far away from the central object.

Let us consider that the flow is continuously being injected from a sphere of radius \mathcal{R} that we shall refer to as the injection sphere. Provided that $\mathcal{S} < \mathcal{R}$, from equation (3) we see that the radial velocity changes sign at

$$\cos \theta_0 = \sqrt{\frac{1}{3} \left(1 + 2 \frac{\mathcal{S}^3}{\mathcal{R}^3} \right)}. \quad (8)$$

More specifically, the flow is characterized by an inflow/outflow geometry, with inflow ($\dot{r} < 0$) across the equatorial belt defined by $\theta_0 < \theta < \pi - \theta_0$ and outflow ($\dot{r} > 0$) across the polar caps defined by $\theta < \theta_0$ and $\theta > \pi - \theta_0$.

We can calculate now the mass injection rate across the sphere of radius \mathcal{R} as

$$\begin{aligned} \dot{M}_{\text{in}} &= -4\pi \int_{\theta_0}^{\pi/2} \rho \frac{dr}{dt} \mathcal{R}^2 \sin \theta d\theta, \\ &= 4\pi\rho\alpha \frac{\mathcal{R}^3}{\mathcal{S}^3} \left[\frac{1}{3} \left(1 + 2 \frac{\mathcal{S}^3}{\mathcal{R}^3} \right) \right]^{3/2}. \end{aligned} \quad (9)$$

Similarly, we define the mass ejection rate leaving this same sphere as

$$\begin{aligned} \dot{M}_{\text{ej}} &= 4\pi \int_0^{\theta_0} \rho \frac{dr}{dt} \mathcal{R}^2 \sin \theta d\theta, \\ &= \dot{M}_{\text{in}} - \dot{M}. \end{aligned} \quad (10)$$

Note that if $\mathcal{S} \geq \mathcal{R}$ then $\dot{M}_{\text{in}} = \dot{M}$ and $\dot{M}_{\text{ej}} = 0$.

Finally, an expression for the streamlines can be found by combining equations (3) and (4) as

$$\frac{dr}{d\theta} = \frac{2\mathcal{S}^3 - r^3 (3 \cos^2 \theta - 1)}{3r^2 \sin \theta \cos \theta}, \quad (11)$$

which can be integrated to give

$$r = \mathcal{S} \left(2 \frac{\Psi - \cos \theta}{\cos \theta \sin^2 \theta} \right)^{1/3}, \quad (12)$$

where Ψ is an integration constant (stream function). From this expression, we see that the streamlines corresponding to $\Psi = \pm 1$ are the only ones that arrive at the stagnation points located at $(\mathcal{S}, 0)$ and (\mathcal{S}, π) , respectively. On the other hand, all of the streamlines with $|\Psi| < 1$ accrete on to the central object while those with $|\Psi| > 1$ escape along the bipolar outflow.

3 NUMERICAL SIMULATIONS

The simple toy model presented in the previous section is clearly limited by the assumption of an incompressible fluid. In this section, we relax this condition and use instead full-hydrodynamic numerical simulations of a polytropic fluid obeying

$$P = K \rho^\gamma, \quad (13)$$

where P is the fluid pressure and $K = \text{const}$. In this work, we consider three different values for the adiabatic index, namely $\gamma = 1$ corresponding to an isothermal fluid, $\gamma = 4/3$ describing a gas composed of relativistic particles,⁴ and $\gamma = 7/5$ corresponding to the adiabatic index of a diatomic gas.

⁴This value is relevant not only for relativistic particles, but is also commonly used in astrophysical situations, e.g. for optically thick material where the internal energy is dominated by radiation pressure (e.g. Awe et al. 2011).

In order to capture the basic premise on which the mechanism of choked accretion operates, i.e. breaking spherical symmetry by introducing a small density contrast between the equator and the poles, here we parametrize this anisotropy by imposing the following density profile as boundary condition at the injection sphere ($r = \mathcal{R}$)

$$\rho(\theta) = \rho_0 (1 - \delta \cos^2 \theta), \quad (14)$$

where ρ_0 is an arbitrary value that we set as the density unit and δ is the density contrast between the equator and the poles defined as

$$\delta = 1 - \frac{\rho(0)}{\rho(\pi/2)}. \quad (15)$$

We study this problem by means of numerical simulations performed with the hydrodynamical code *AZTEKAS*. This code numerically solves the inviscid Euler equations in a conservative form,

$$\frac{\partial \rho}{\partial t} + \nabla \cdot (\rho v) = 0, \quad (16)$$

$$\frac{\partial (\rho v)}{\partial t} + \nabla \cdot (\rho v \otimes v) + \nabla P = -\rho \frac{GM}{r^2} \hat{r}, \quad (17)$$

$$\frac{\partial E}{\partial t} + \nabla \cdot [v(E + P)] = -\rho \frac{GM}{r^2} v \cdot \hat{r}, \quad (18)$$

with v the fluid velocity vector and E the total energy density defined as

$$E = \frac{1}{2} \rho |v|^2 + \epsilon, \quad (19)$$

where ϵ is the internal energy density. From equation (13), together with the first law of thermodynamics for an ideal gas, we can close this system of equations with the following equation of state that relates the pressure to the internal energy density

$$\epsilon = \frac{P}{\gamma - 1}. \quad (20)$$

The equations (16)–(20) are spatially discretized using a finite-volume scheme together with a high-resolution shock capturing (HRSC) method that uses a second-order piecewise linear reconstructor (MC) and the HLL (Harten, Lax & Leer 1983) approximate Riemann solver to compute the numerical fluxes. The time evolution of these equations is calculated using a second-order total variation diminishing Runge–Kutta time integrator (RK2) (Shu & Osher 1988), with a Courant factor of 0.25.

Since the density profile in equation (14) is independent of the azimuthal angle, we assume that the problem retains symmetry with respect to both the polar axis (axisymmetry) and the equatorial plane (north–south symmetry). Hence, for the numerical simulations, we adopt a two-dimensional spherical domain consisting of a uniform polar grid on $\theta \in [0, \pi/2]$ and an exponential radial grid with $r \in [\mathcal{R}_{\text{acc}}, \mathcal{R}]$, computed as

$$r_i = \mathcal{R}_{\text{acc}} + \exp\left(\frac{\ln(\mathcal{R} - \mathcal{R}_{\text{acc}})i}{N_r}\right), \quad (21)$$

where \mathcal{R}_{acc} is the radius of the inner boundary. As fiducial values for the numerical resolution, we adopt $N_r = N_\theta = 150$, while for the radial boundaries we take $\mathcal{R}_{\text{acc}} = 0.1 r_B$ and $\mathcal{R} = 10 r_B$, where $r_B = GM/a_\infty^2$ is the Bondi radius. The code uses r_B , a_∞ , and $t_B = r_B/a_\infty$ as units of length, velocity, and time, respectively.

3.1 Initial and boundary conditions

We performed different simulations using three values of the adiabatic index $\gamma = 1, 4/3$, and $7/5$, and four values of the den-

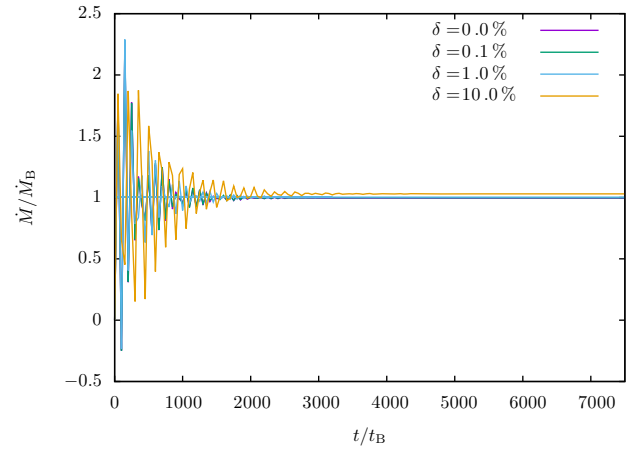


Figure 2. Mass accretion rate as a function of time for the four values of the density contrast δ in the case $\gamma = 4/3$ (similar results were obtained for the other two values of γ). There is a clear convergence towards a steady-state solution.

sity contrast $\delta = 0, 0.1$ per cent, 1 per cent, and 10 per cent. As boundary conditions, we set free outflow⁵ from the grid at \mathcal{R}_{acc} (i.e. free inflow towards the central object) and reflection conditions at both polar boundaries. At the outer boundary, at $\mathcal{R} = 10 r_B$, we impose the density profile described in equation (14) and compute the pressure as $P(\theta) = \rho(\theta)^\gamma / \gamma$, but allow free (as free-outflow condition) evolution on both velocity components. For all the simulations, we set the fluid initially at rest (zero velocities) and uniform initial conditions (constant density and pressure interior to the outer boundary).

We have adopted the free-outflow condition at the inner radial boundary as we are treating the accretor as a featureless Keplerian potential. For alternative assumptions on the accretor, e.g. modelling it as a star, appropriate boundary conditions should be imposed. See, for example, the treatment of a hard inner boundary employed by Velli (1994) and Del Zanna, Velli & Londrillo (1998) for studying time-dependent, inflow/outflow solutions in the context of stellar atmospheres and their interaction with the interstellar medium.

All simulations were run until a stationary state was reached throughout the domain. This was estimated by monitoring the behaviour of the mass accretion rate \dot{M} , with a steady state assumed once the relative temporal fluctuations in this parameter fell below one part in 10^5 . See Fig. 2 for an example of the time evolution of \dot{M} for the case $\gamma = 4/3$. The steady state was reached at times $2000 t_B, 4500 t_B$, and $7500 t_B$ for $\gamma = 1, 4/3$, and $7/5$, respectively.

3.2 Code validation

As a validation of the *AZTEKAS* code in this work, we start by considering $\delta = 0$, in which case spherical symmetry is recovered and the resulting accretion flow should coincide with the Bondi solution. In Fig. 3, we show the results for the Mach number $\mathcal{M} = v/a$ as a function of the radial distance to the central object, as obtained from the three simulations with $\gamma = 1, 4/3$, and $7/5$ and compared to the corresponding analytic solutions. We find a very good agreement with the Bondi solution, with an error of less than 1 per cent in the three cases (see Table 1). Further tests of *aztekas*

⁵The free-outflow condition is implemented by assigning to each ghost cell the value of the nearest active cell.

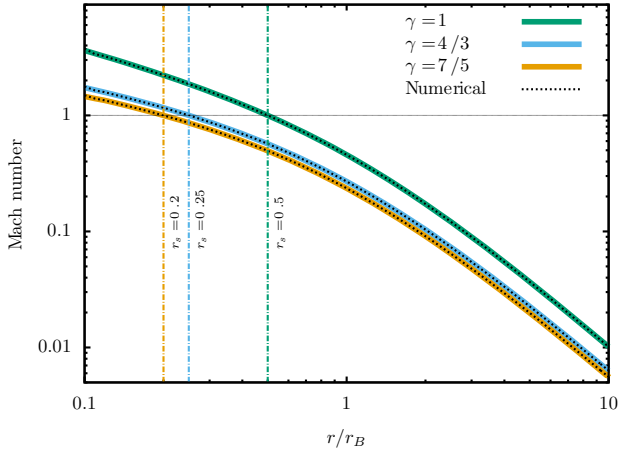


Figure 3. Comparison of the spherically symmetric numerical simulations performed with *aztekas* and the Bondi accretion solution corresponding to the adiabatic indices $\gamma = 1$, $4/3$, and $7/5$. The figure shows the Mach number versus radius for the three cases. The solid, coloured lines correspond to the Bondi solution while the dashed, black lines correspond to the numerical results. The vertical dashed lines indicate the position of the sonic radius for each γ .

Table 1. Simulations summary. In this table, we give the accretion, injection, and ejection rates in units of the corresponding Bondi rates (equation 7), ratio between ejection and injection, the position of the stagnation point along the vertical axis, as well as the ratio of the maximum ejection velocity to the local escape velocity and to the local speed of sound a .

$\gamma = 1$							
δ (%)	$\frac{\dot{M}}{\dot{M}_B}$	$\frac{\dot{M}_{in}}{\dot{M}_B}$	$\frac{\dot{M}_{ej}}{\dot{M}_B}$	$\frac{\dot{M}_{ej}}{\dot{M}_{in}}$	$\frac{S}{r_B}$	$\frac{v_{max}}{v_{esc}}$	$\frac{v_{max}}{a}$
0.0	0.99	0.99	0	0	–	–	–
0.1	0.99	1.95	0.94	0.48	5.10	0.130	0.057
1.0	1.02	4.18	3.16	0.75	3.35	0.373	0.164
10.0	1.05	9.99	8.94	0.89	2.55	1.182	0.520
$\gamma = 4/3$							
δ (%)	$\frac{\dot{M}}{\dot{M}_B}$	$\frac{\dot{M}_{in}}{\dot{M}_B}$	$\frac{\dot{M}_{ej}}{\dot{M}_B}$	$\frac{\dot{M}_{ej}}{\dot{M}_{in}}$	$\frac{S}{r_B}$	$\frac{v_{max}}{v_{esc}}$	$\frac{v_{max}}{a}$
0.0	1.00	1.00	0	0	–	–	–
0.1	1.00	2.55	1.55	0.61	4.50	0.130	0.057
1.0	1.01	5.60	4.59	0.82	3.29	0.376	0.166
10.0	1.04	15.44	14.40	0.93	2.16	1.186	0.522
$\gamma = 7/5$							
δ (%)	$\frac{\dot{M}}{\dot{M}_B}$	$\frac{\dot{M}_{in}}{\dot{M}_B}$	$\frac{\dot{M}_{ej}}{\dot{M}_B}$	$\frac{\dot{M}_{ej}}{\dot{M}_{in}}$	$\frac{S}{r_B}$	$\frac{v_{max}}{v_{esc}}$	$\frac{v_{max}}{a}$
0.0	0.99	0.99	0	0	–	–	–
0.1	1.00	2.76	1.76	0.63	4.34	0.130	0.057
1.0	1.01	6.23	5.22	0.83	3.17	0.376	0.166
10.0	1.04	17.41	16.37	0.94	2.05	1.188	0.523

against other analytic solutions and astrophysical problems can be found in Aguayo-Ortiz et al. (2018) and Tejada & Aguayo-Ortiz (2019).

The treatment of the inner boundary is crucial for solving numerically the spherical accretion problem. One important point being whether the sonic surface is well resolved in the numerical

domain or not. In the Bondi problem, the sonic surface appears at

$$r_s = \frac{5 - 3\gamma}{4} r_B. \quad (22)$$

As mentioned above, in all the simulations we placed the inner boundary at $\mathcal{R}_{acc} = 0.1 r_B$ and, thus, the sonic surface is well resolved for all values of γ .

Note that we have not included the commonly used adiabatic index for a monoatomic gas $\gamma = 5/3$, as in this case the sonic radius vanishes altogether. This makes a simulation that does not include artificial viscosity unstable to numerical fluctuations appearing at the inner boundary. We prefer not to include any such artificial effects so as to retain confidence in that the results obtained are a robust consequence of the physics being modelled.

3.3 Results

We now present the results for numerical simulations where the assumption of spherical symmetry for the infalling flow is relaxed, and parametrized through the density contrast δ as in equation (15).

To explore the relation between total infall and total outflow in the resulting steady-state configurations, for each simulation we compute the mass accretion rate using equation (5). We apply this formula at each radial grid point and then take the average rate for all the domain. Likewise, we measure the injected and ejected mass rates across \mathcal{R} using equations (9) and (10).

A summary of all of the simulations is shown in Table 1 where, for the various adiabatic indices and equatorial-to-polar density contrasts probed, we report the different accretion, injection, and ejection rates, the ratio between ejection and injection, together with the location of the stagnation point and the maximum velocity attained by the outflowing material.

In order to validate these results, we performed a self-convergence test of the numerical solutions by increasing by a factor of 1.5 the resolution in both radial and angular coordinates. We obtained a second-order convergence as expected for a stationary shockless solution with an HRSC method (Lora-Clavijo & Guzmán 2013).

In Fig. 4, we show the resulting flow configurations for $\gamma = 1$ and the four density contrasts. The figure shows the streamlines of the fluid together with isocontours of the density field. Figs 5 and 6 give the results for $\gamma = 4/3$ and $7/5$, respectively. In these figures, clear semicircles in the inner region of the numerical domain show the locations of the sonic surfaces in the Bondi solution, which can be seen to be resolved in all cases, as our domains start at $0.1 r_B$ in all the cases.

In Fig. 7, we show a close-up of the inner region in the case of $\delta = 10$ per cent. Here we show the analytic value of the sonic radius (equation 22), as well as the one extracted from our simulations. As can be seen, there is a very good agreement between both surfaces, even though the numerical ones do not correspond to a spherically symmetric accretion flow. This illustrates the strong convergence of the solutions found towards the Bondi solution for small radii.

Moreover, we have analysed the distribution of the entropy and of the values of the Bernoulli constant among different streamlines. As expected for a perfect fluid in the absence of shocks, and due to our choice of the boundary conditions, the entropy remains constant throughout the entire numerical domain. On the other hand, for the Bernoulli constant, although it has a small variation from streamline to streamline, the mean value remains within 1 part in 10^4 to the corresponding Bondi one, which agrees with the fact that $\dot{M} \approx \dot{M}_B$.

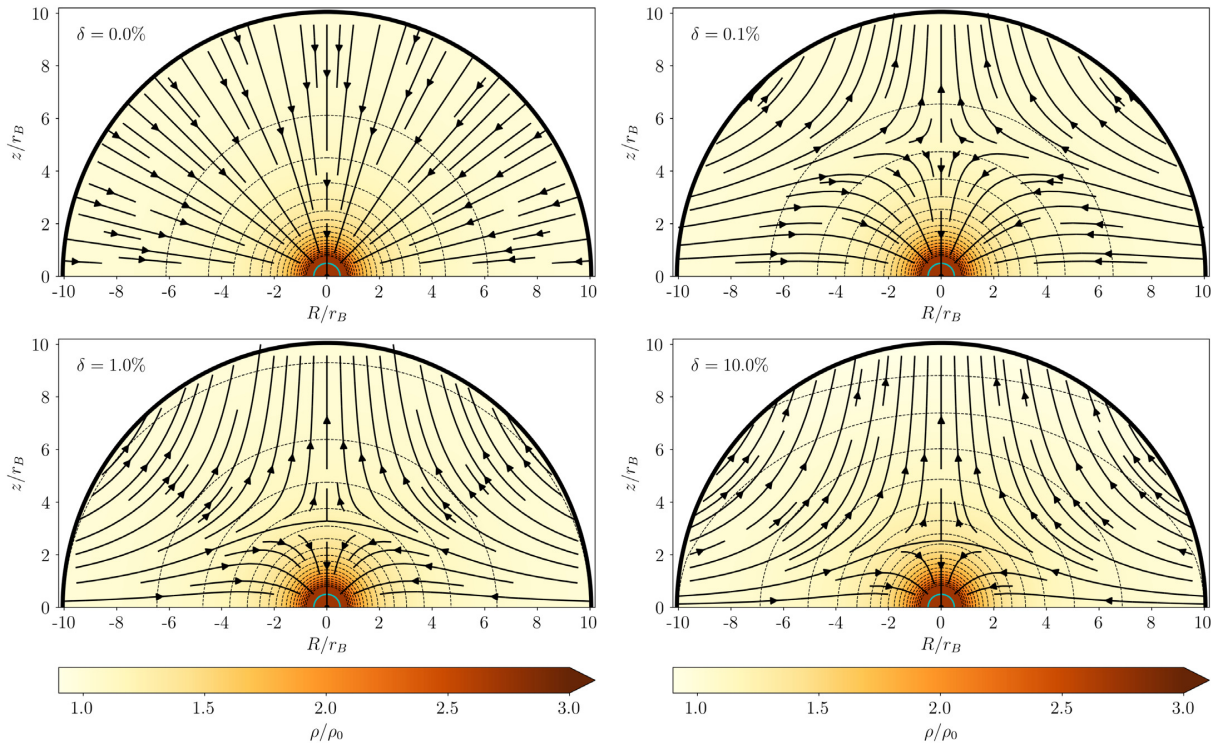


Figure 4. Resulting steady-state flow configurations for the numerical simulations for a fluid with equation of state $\gamma = 1$ accreting on to a point mass. The different values of the density contrast δ used in each case are indicated on the top-left corner of each panel. The first panel gives the spherically symmetric case, which, as expected, recovers the Bondi solution. As soon as $\delta \neq 0$, we see a qualitative change in the flow morphology, with even marginal departures from sphericity resulting in polar outflows. As the density contrast increases, the stagnation point reaches deeper into the accretion flow while the outflow region expands towards the equator. Streamlines are shown as black solid arrows. The grey scale gives the density profile, with some isodensity curves shown as black dashed lines (colour version online). The axes correspond to the usual cylindrical coordinates $R = r \sin \theta$, $z = r \cos \theta$. The clear semicircles at small radii identify the position of the Bondi sonic surface, in all cases located within the numerical domain, which begins at $0.1 r_B$.

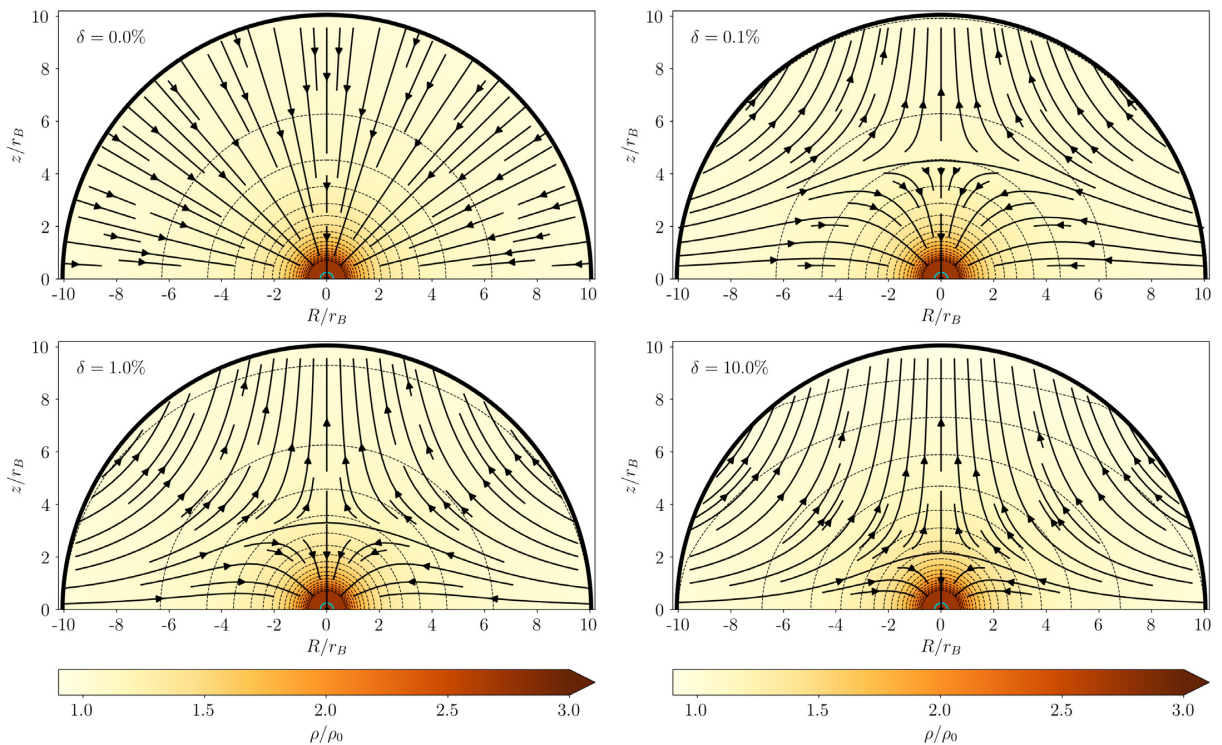


Figure 5. Resulting steady-state flow configurations for the numerical simulations with $\gamma = 4/3$. The meaning of the different lines is the same as in Fig. 4.

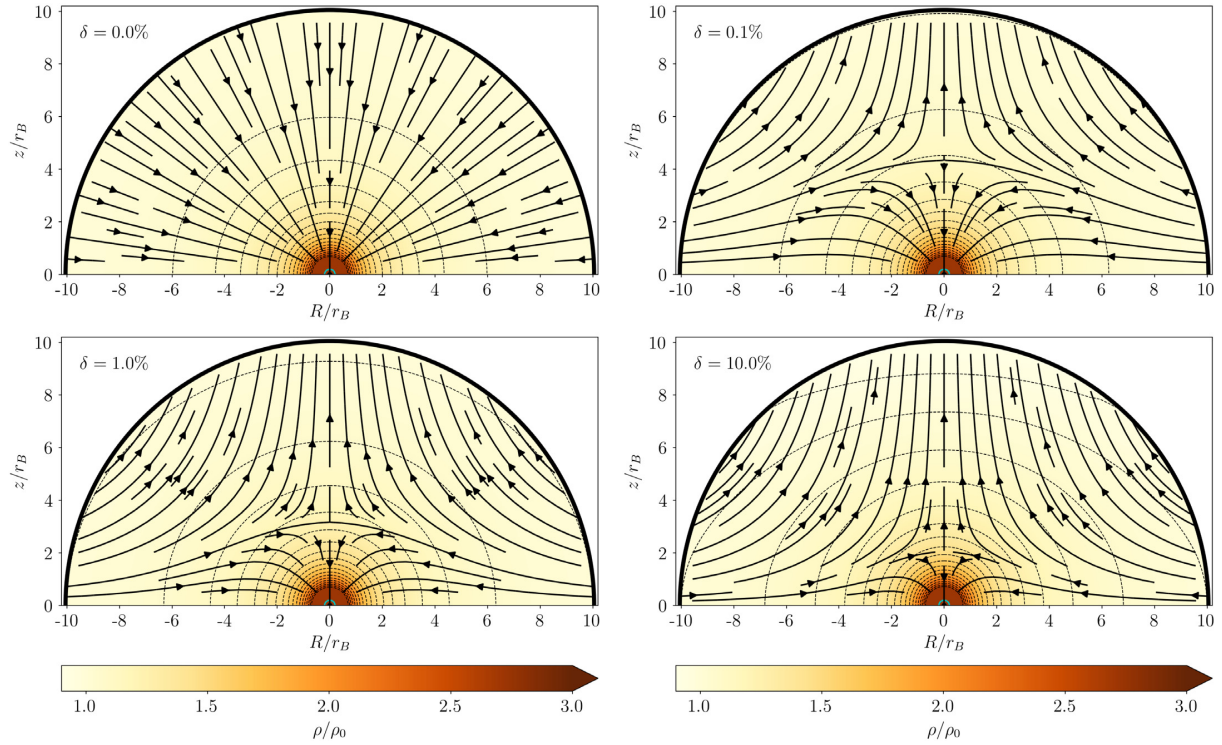


Figure 6. Resulting steady-state flow configurations for the numerical simulations with $\gamma = 7/5$. The meaning of the different lines is the same as in Fig. 4.

4 DISCUSSION

Based on the hydrodynamical numerical simulations presented in the previous section, we have explored the consequences of breaking spherical symmetry by imposing an axisymmetric, polar density contrast δ in the accretion flow. Naturally, when $\delta = 0$, the spherically symmetric Bondi solution is recovered, as can be seen from Fig. 3 and the top-left panel in Figs 4–6. However, as soon as there is a non-zero density contrast between the equatorial plane and the polar regions, the flow morphology changes qualitatively into an inflow/outflow configuration. The onset of even a quite marginal density contrast of $\delta = 0.1$ per cent results in the appearance of flow patterns highly resembling the analytic toy model discussed in Section 2 as well as the inflow/outflow configurations of the perturbative results of Hernandez et al. (2014) for an isothermal model.

As can be seen from the results reported in Table 1, as we take progressively larger values for the density contrast, the magnitude of the ejection velocities increases, and the position of the stagnation point moves towards smaller radii as the outflow region expands to occupy a larger fraction of the simulation domain. Note from Figs 4–6 that for $\delta = 10$ per cent, the density contours appear slightly oblate, with the departure from spherical symmetry becoming more apparent. Moreover, for this same density contrast, we obtain ejection velocities larger than the local escape velocity, while, at the same time, the ratio of mass ejection and mass injection rates reaches values as high as 94 per cent.

We have presented simulation results for three different values of the adiabatic index: $\gamma = 1, 4/3$, and $7/5$. Although we also explored intermediate values of γ , we do not include any further results, as they are all very similar and show a continuous progression between the cases presented. Indeed, we see that the three cases already considered are qualitatively very similar, as could have

been anticipated from the qualitative similarities of the analytic solution of the highly simplified incompressible model presented in Section 2 and the slightly more realistic streamlines of the isothermal perturbative solutions of Hernandez et al. (2014). It is clear that breaking spherical symmetry with a polar density gradient in hydrodynamical accretion models leads to the same qualitative solutions with a morphology as shown in Figs 4–6.

In Fig. 8, we show, for all of the simulations reported in this work, the ratio of the ejected and injected mass rates ($\dot{M}_{\text{ej}}/\dot{M}_{\text{in}}$) versus the injected mass rate in units of the corresponding Bondi value ($\dot{M}_{\text{in}}/\dot{M}_{\text{B}}$). The solid line represents the points where the injection and ejection of material are such that the total mass accretion rate equals the Bondi value, i.e.

$$\dot{M} = \dot{M}_{\text{in}} - \dot{M}_{\text{ej}} \equiv \dot{M}_{\text{B}}. \quad (23)$$

From this figure, we see that for $\dot{M}_{\text{in}}/\dot{M}_{\text{B}} = 1$, the ejected mass is zero, while as $\dot{M}_{\text{in}}/\dot{M}_{\text{B}}$ increases, the ratio $\dot{M}_{\text{ej}}/\dot{M}_{\text{in}}$ tends to unity. It is remarkable that this dependence between injection and accretion holds quite accurately across the adiabatic index range sampled. Differences between \dot{M} and \dot{M}_{B} remain beyond numerical resolution, but in all cases below a 5 per cent level. Thus, regardless of how large the injected mass rate is at the outer boundary, the central object only accretes at a maximum critical rate, closely corresponding to the Bondi mass accretion rate. This justifies our choice in equation (7) for the mass accretion rate of the analytic model of choked accretion.

The bipolar boundary density distribution adopted in equation (14) is not intended as a physical model corresponding to any specific situation, but rather as a convenient first-order parametrization of departure from spherical symmetry. However, infall processes originating from accretion disc phenomena will quite probably be characterized by axisymmetric density profiles denser towards the equator than the poles. The details of the flow patterns

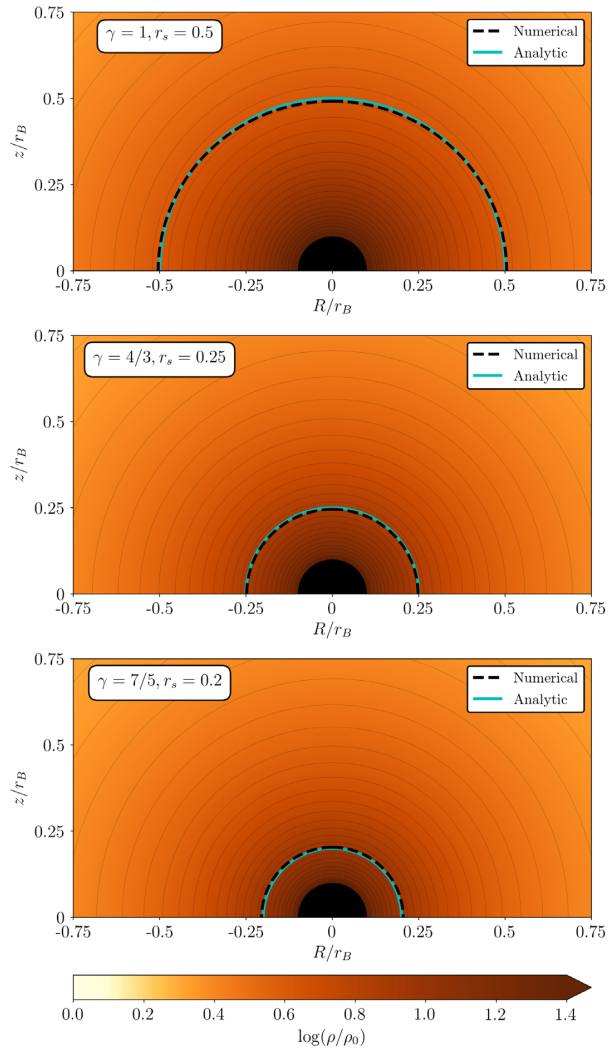


Figure 7. A close-up of the inner region of the simulations with $\delta = 10$ per cent for the three values of γ . In the three panels, we show the location of the sonic surface as extracted from the numerical simulations (dashed lines) together with the one corresponding to the Bondi solution (solid line).

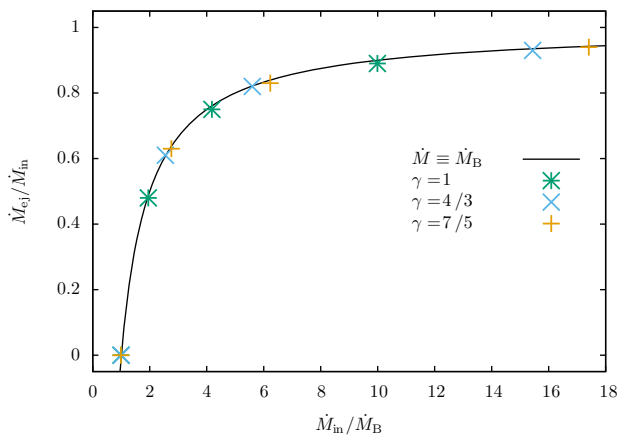


Figure 8. Ratio between the ejected and injected mass rates versus the injected mass rate in units of \dot{M}_B (see equation 7) for all of the simulations reported in this work. The solid line represents the case where the accretion rate on to the central object \dot{M} is equal to the Bondi mass accretion rate.

resulting from particular situations will surely differ from the results presented here, although the clear convergence towards spherical accretion seen at small radii implies robustness in our conclusions with respect to this point. Indeed, the overall flow patterns obtained persist even when changing the particular parametrization used. Other similar density profiles were explored, obtaining consistent results, although very distinct boundary conditions may very well lead to substantially different solutions.

Although the imposed geometry of the inflow boundary conditions necessarily leads to final configurations sharing the same symmetry, the resulting inflow/outflow morphology is by no means the only configuration sharing this symmetry, e.g. a pure inflow configuration with oblate isodensity contours would have also satisfied the symmetry conditions alone. Further, the resulting limit on the accretion rate saturating close to the Bondi value is in no way evident simply from the assumption of a polar density gradient on the boundary conditions.

Let us explore now the viability of the choked accretion model to contribute towards the launching of a jet in different astrophysical settings. For this model, we have neglected the effects of fluid rotation, which is a valid approximation just for the innermost part of an accretion disc where, through viscous transport mechanisms (e.g. Balbus & Hawley 1991), the disc material has lost most of its angular momentum. It is then natural to ask for the whole choked accretion machinery to fit within the inner walls of the disc. In other words, we require \mathcal{S} , the characteristic length-scale of the choked accretion model, to be comparable to the physical size of this inner region.

Our simulation results show that \mathcal{S} sinks deeper into the central region as we consider both larger density contrasts δ and larger adiabatic indices γ . We note, however, that for the parameters explored in this work \mathcal{S} is always larger than the Bondi radius $r_B = GM/a_\infty^2$. Assuming that this result holds in general, and considering an ideal gas composed of monoatomic hydrogen, we can write

$$a_\infty = \sqrt{\frac{\gamma k_B T_\infty}{m_H}} \simeq 3 \times 10^5 \left(\frac{T}{10^3 \text{ K}} \right)^{1/2} \text{ cm s}^{-1}, \quad (24)$$

and, consequently, we have

$$\mathcal{S} \gtrsim 100 \left(\frac{M}{M_\odot} \right) \left(\frac{T}{10^3 \text{ K}} \right)^{-1} \text{ au}, \quad (25)$$

or, in units of the gravitational radius $r_g = GM/c^2$

$$\mathcal{S} \gtrsim 5 \times 10^6 \left(\frac{T}{10^6 \text{ K}} \right)^{-1} r_g. \quad (26)$$

These expressions should be considered as upper limits for \mathcal{S} . Additional physical ingredients that have been left out from this simple model can contribute to reduce this characteristic length-scale. For example, we have neglected the necessary presence of radiation and magnetic fields in the system, both of which will result in an enhanced effective temperature, which will in turn result in smaller values of \mathcal{S} .

Let us consider the accretion discs behind X-ray binaries or AGNs. For these systems, the inner border of the disc is expected to have a radius of the order of $1\text{--}10 r_g$ and a temperature of around $T \sim 10^6 \text{ K}$ (Czerny et al. 2003; Kaaret, Feng & Roberts 2017). From equation (26), we have $\mathcal{S} \gtrsim 10^6 r_g$ and we can then conclude that these systems are too cold for choked accretion on its own to be responsible for the ejection.

On the other hand, for a Keplerian protoplanetary disc around a YSO, we have inner radii of the order of 0.1–1.0 au and temperatures that can reach up to 10^3 K (Mori, Bai & Okuzumi 2019). In this case from equation (25) we obtain $\mathcal{S} \gtrsim 100$ au, which is two to three orders of magnitude larger than the presumed physical size of the system. Nevertheless, choked accretion might contribute to the ejection of molecular outflows associated with YSOs (Bachiller 1996), as these outflows are driven by infalling matter and originate from regions farther than several 100 au from the central accretor.

Lastly, if we consider the central progenitors of long GRBs within the so-called collapsar scenario (Woosley & Bloom 2006), we have again inner radii of the order of 1–10 r_g but temperatures that can now reach up to 10^{11} K. From equation (26) for this temperature we obtain $\mathcal{S} \gtrsim 50 r_g$, which is now within the expected order of magnitude for the mechanism presented to become relevant.

From these examples, it might seem that the length-scale \mathcal{S} on which the choked accretion mechanism operates is too large to contribute towards the ejection mechanism behind most astrophysical jets. It is important to keep in mind, however, that relaxing some of the simplifying assumptions behind the present model will necessarily lead to smaller values of \mathcal{S} . In addition to the already mentioned role played by radiation and magnetic fields, we have also seen a clear trend for diminishing values of \mathcal{S} as the equatorial-to-polar density contrast increases. Hence, we can expect the applicability of the choked accretion mechanism to increase once larger density contrasts are considered.

In connection to the previous point, a non-zero angular momentum will naturally contribute to increase the density contrast between the material in the disc with respect to the polar regions (see e.g. Mendoza, Tejada & Nagel 2009). We were not able to explore this regime in this work since from our numerical experiments we have found that taking larger values of δ or outer boundaries smaller than r_B leads to rather unstable, highly dynamic accretion flows that do not seem to relax to steady-state configurations. We plan, however, to study both the effect of rotation and the dynamic regime resulting from steeper density gradients in future work.

There are additional physical processes, particularly non-adiabatic effects such as radiative cooling, heat transfer, and shock formation, that can in principle modify our results. However, it is not clear a priori whether the inclusion of these effects will enhance or hamper the applicability of the choked accretion mechanism. We leave addressing these important points as the focus of future investigations, whereas the current simple model can be seen as presenting an underlying phenomenon that might be an important factor within a more general scheme.

5 CONCLUSIONS

Through simple analytic considerations for an idealized incompressible fluid, and axisymmetric numerical simulations for hydrodynamical accretion in a central Newtonian potential spanning a range of adiabatic indices, we have shown that large-scale, small-amplitude departures from spherical symmetry, where the polar regions are underdense with respect to the equatorial plane, result in substantial qualitative and quantitative modifications in the resulting flow morphology.

Although the details depend on the particular choice of physical parameters, for the continuous bipolar boundary conditions explored, the resulting flow patterns are no longer the classical radial accretion ones, but have a consistent morphology comprising

a central quasi-spherical accretion region, and an outer zone of equatorial infall and polar outflows.

We have seen that as the density contrast increases, a larger fraction of the mass injection rate is reversed and expelled along a bipolar outflow. Moreover, the maximum velocity attained by this ejected material can reach values larger than the local escape velocity.

As the accretion flow tends towards spherical symmetry at small radii, we find the interesting result that the total mass accretion rate is limited at a few per cent above the Bondi value of the corresponding spherically symmetric case. Thus, hydrodynamical accretion towards central objects appears to choke at a maximum value, with any extra input material fuelling the bipolar outflow.

In conclusion, we have presented compelling evidence for the existence of a choked accretion phenomenon in hydrodynamical flows on to gravitating objects. Furthermore, we have shown that choked accretion works as a hydrodynamical mechanism for ejecting axisymmetric outflows, thus constituting a transition bridge between purely radial accretion flows and jet-generating systems.

ACKNOWLEDGEMENTS

We thank Sergio Mendoza, John Miller, Olivier Sarbach, Francisco Guzmán, Diego López-Cámara, Fabio de Colle, and Jorge Cantó for useful discussions and comments on the manuscript. The authors also acknowledge the constructive criticism from an anonymous referee. This work was supported by DGAPA-UNAM (IN112616 and IN112019) and CONACyT (CB-2014-01 No. 240512; No. 290941; No. 291113) grants. AAO and ET acknowledge financial support from CONACyT (788898 and 673583). XH acknowledges support from DGAPA-UNAM PAPIIT IN104517 and CONACyT.

REFERENCES

- Aguayo-Ortiz A., Mendoza S., Olvera D., 2018, *PLoS ONE*, 13, e0195494
 Awe T. J., Adams C. S., Davis J. S., Hanna D. S., Hsu S. C., Cassibry J. T., 2011, *Phys. Plasmas*, 18, 072705
 Bachiller R., 1996, *ARA&A*, 34, 111
 Balbus S. A., Hawley J. F., 1991, *ApJ*, 376, 214
 Blandford R. D., 1976, *MNRAS*, 176, 465
 Blandford R. D., Payne D. G., 1982, *MNRAS*, 199, 883
 Blandford R. D., Rees M. J., 1974, *MNRAS*, 169, 395
 Blandford R. D., Znajek R. L., 1977, *MNRAS*, 179, 433
 Bondi H., 1952, *MNRAS*, 112, 195
 Canto J., Rodríguez L. F., 1980, *ApJ*, 239, 982
 Casse F., Keppens R., 2002, *ApJ*, 581, 988
 Currie I. G., 2003, *Fundamental Mechanics of Fluids*, 3rd edn. Marcel Dekker, New York
 Czerny B., Nikořajuk M., Róźańska A., Dumont A. M., Loska Z., Zycki P. T., 2003, *A&A*, 412, 317
 Del Zanna L., Velli M., Londrillo P., 1998, *A&A*, 330, L13
 Harten A., Lax P. D., Leer B., 1983, *SIAM Rev.*, 25, 35
 Hawley J. F., Fendt C., Hardcastle M., Nokhrina E., Tchekhovskoy A., 2015, *Space Sci. Rev.*, 191, 441
 Hernandez X., Rendón P. L., Rodríguez-Mota R. G., Capella A., 2014, *Rev. Mex. Astron. Astrofis.*, 50, 23
 Jafari A., 2019, preprint ([arXiv:1904.09677](https://arxiv.org/abs/1904.09677))
 Kaaret P., Feng H., Roberts T. P., 2017, *ARA&A*, 55, 303
 Lery T., Henriksen R. N., Fiege J. D., Ray T. P., Frank A., Bacciotti F., 2002, *A&A*, 387, 187
 Liska M., Tchekhovskoy A., Ingram A., van der Klis M., 2019, *MNRAS*, 487, 550
 Lora-Clavijo F. D., Guzmán F. S., 2013, *MNRAS*, 429, 3144

- Lovelace R. V. E., 1976, *Nature*, 262, 649
- Mendoza S., Tejada E., Nagel E., 2009, *MNRAS*, 393, 579
- Michel F. C., 1972, *Ap&SS*, 15, 153
- Mirabel I. F., Rodríguez L. F., 1994, *Nature*, 371, 46
- Mori S., Bai X.-N., Okuzumi S., 2019, *ApJ*, 872, 98
- Olvera D., Mendoza S., 2008, in Oscoz A., Mediavilla E., Serra-Ricart M., eds, *A GPL Relativistic Hydrodynamical Code*, Vol. 30. EAS Publ. Ser., p. 399
- Petrich L. I., Shapiro S. L., Teukolsky S. A., 1988, *Phys. Rev. Lett.*, 60, 1781
- Pudritz R. E., Ouyed R., Fendt C., Brandenburg A., 2007, in Reipurth B., Jewitt D., Keil K., eds, *Protostars and Planets V*. Univ. Arizona Press, Tucson, Arizona, USA, p. 277
- Qian Q., Fendt C., Vourellis C., 2018, *ApJ*, 859, 28
- Romero G. E., Boettcher M., Markoff S., Tavecchio F., 2017, *Space Sci. Rev.*, 207, 5
- Semenov V., Dyadechkin S., Punsly B., 2004, *Science*, 305, 978
- Shakura N. I., Sunyaev R. A., 1973, *A&A*, 24, 337
- Sheikhnezami S., Fendt C., 2018, *ApJ*, 861, 11
- Shu C.-W., Osher S., 1988, *J. Comput. Phys.*, 77, 439
- Tchekhovskoy A., 2015, in Contopoulos I., MGabuzda D., Kylafis N., eds, *Astrophysics and Space Science Library*, Vol. 414, *The Formation and Disruption of Black Hole Jets*. Springer-Verlag, Berlin. p. 45
- Tejada E., 2018, *Rev. Mex. Astron. Astrofis.*, 54, 171
- Tejada E., Aguayo-Ortiz A., 2019, *MNRAS*, 487, 3607
- Tejada E., Aguayo-Ortiz A., Hernandez X., 2019, preprint ([arXiv:1909.01527](https://arxiv.org/abs/1909.01527))
- Velli M., 1994, *ApJ*, 432, L55
- Woosley S. E., Bloom J. S., 2006, *ARA&A*, 44, 507

This paper has been typeset from a $\text{\TeX}/\text{\LaTeX}$ file prepared by the author.

Choked accretion onto a Schwarzschild black hole: a hydrodynamical jet-launching mechanism

In this chapter, we present the relativistic extension of the *choked accretion* model. We consider the same choked accretion setup as in Chapter 5, in which we assume that the spherical symmetry is broken by considering a large amplitude, small scale density gradient where the accreted material is more concentrated at the equator than in the polar regions. In this case, the central massive object corresponds to a Schwarzschild black hole.

As discussed in Chapter 5, the first part of the work focuses on the development of an analytic model of the choked accretion mechanism. For this solution we use the ultra-relativistic stiff equation of state for modelling a fluid that is accreted by a Schwarzschild black hole. With this kind of description for the gas, we are able to obtain a hydrodynamic analytic solution, with the restriction that the sound speed is constant everywhere and equal to the speed of light. By assuming an irrotational condition, we obtain the relativistic extension of the incompressible-Newtonian potential fluid description, from which we obtain not only the velocity field, but also the density field and the mass accretion rate. This analytic model provides a more general understanding of the physics behind in the choked accretion mechanism.

In the next part of the paper, we extend the relativistic version of the choked accretion mechanism by relaxing the assumption of the equation of state, and considering an ideal gas following a polytropic relation. We perform this by running a set of full-hydrodynamic simulations with the AZTEKAS code. In this case, taking advantage of the fact that our analytic model represents a full-hydrodynamic solution, we use it as a benchmark test to validate our simulations. The numerical experiments regard the exploration of different parameters: density contrast of the density profile




at the boundary, adiabatic index and speed of sound of the fluid. The steady state solutions allow us to compute the ejected and injected mass, as well as the total mass accretion rate, showing the viability of the choked accretion model to preserve its flux-limited accretion regime in the relativistic regime.

The study presented in this chapter was published in ApJ in 2020. The details of the paper are:

Tejeda E., Aguayo-Ortiz A., Hernandez X., 2020, ApJ, 893, 81. [doi:10.3847/1538-4357/ab7ffe](https://doi.org/10.3847/1538-4357/ab7ffe)



Choked Accretion onto a Schwarzschild Black Hole: A Hydrodynamical Jet-launching Mechanism

Emilio Tejada¹ , Alejandro Aguayo-Ortiz² , and X. Hernandez² ¹ Cátedras Conacyt—Instituto de Física y Matemáticas, Universidad Michoacana de San Nicolás de Hidalgo, Edificio C-3, Ciudad Universitaria, 58040 Morelia, Michoacán, Mexico; emilio.tejada@conacyt.mx² Instituto de Astronomía, Universidad Nacional Autónoma de México, AP 70-264, 04510 Ciudad de México, Mexico; aaguayo@astro.unam.mx, xavier@astro.unam.mx

Received 2019 October 22; revised 2020 March 11; accepted 2020 March 13; published 2020 April 17

Abstract

We present a novel, relativistic accretion model for accretion onto a Schwarzschild black hole. This consists of a purely hydrodynamical mechanism in which, by breaking spherical symmetry, a radially accreting flow transitions into an inflow-outflow configuration. The spherical symmetry is broken by considering that the accreted material is more concentrated on an equatorial belt, leaving the polar regions relatively under-dense. What we have found is a flux-limited accretion regime in which, for a sufficiently large accretion rate, the incoming material *chokes* at a gravitational bottleneck and the excess flux is redirected by the density gradient as a bipolar outflow. The threshold value at which the accreting material chokes is of the order of the mass-accretion rate found in the spherically symmetric case studied by Bondi and Michel. We describe the choked accretion mechanism first in terms of a general relativistic, analytic toy model based on the assumption of an ultrarelativistic stiff fluid. We then relax this approximation and, by means of numerical simulations, show that this mechanism can operate also for general polytropic fluids. Interestingly, the qualitative inflow-outflow morphology obtained appears as a generic result of the proposed symmetry break, across analytic and numeric results covering both the Newtonian and relativistic regimes. The qualitative change in the resulting steady-state flow configuration appears even for a very small equatorial-to-polar-density contrast ($\sim 0.1\%$) in the accretion profile. Finally, we discuss the applicability of this model as a jet-launching mechanism in different astrophysical settings.

Unified Astronomy Thesaurus concepts: [Black hole physics \(159\)](#); [Astrophysical black holes \(98\)](#); [Accretion \(14\)](#); [Bondi accretion \(174\)](#); [Hydrodynamical simulations \(767\)](#); [Analytical mathematics \(38\)](#); [Relativistic fluid dynamics \(1389\)](#); [General relativity \(641\)](#); [Jets \(870\)](#)

1. Introduction

Astrophysical jets are found in vastly different scenarios: from the parsec scales of the H-H objects associated with young stellar systems (Hartigan 2009), to the megaparsec scales of the radio lobes that accompany some radio galaxies and other active galactic nuclei (AGNs; Beckmann & Shrader 2012). They are also inferred in connection with high-energy phenomena such as long gamma ray bursts (GRBs) following the collapse of a massive star (Woosley & Bloom 2006), jetted emission associated with microquasars in some X-ray binaries (Mirabel & Rodríguez 1994), X-ray flares after a stellar tidal disruption event (Burrows et al. 2011), and short GRBs accompanying the kilonova explosion after the merger of two neutron stars (Abbott et al. 2017).

In recent decades, substantial progress has been made in understanding different aspects of astrophysical jets, particularly in relation to their acceleration and collimation (see, e.g., Qian et al. 2018; Liska et al. 2019). However, open questions remain concerning the process of launching the jet in the first place, as well as the details connecting the accreted and ejected flows (Romero et al. 2017).

Several mechanisms have been proposed to address these issues. The most widely accepted ones are the mechanisms introduced by Blandford & Payne (1982, hereafter BP) and Blandford & Znajek (1977, hereafter BZ). The BP mechanism consists of the extraction of energy and angular momentum from an accretion disk via a magneto-centrifugal process. The main ingredient is a global, poloidal magnetic field threading

an accretion disk that rotates with Keplerian velocity. This mechanism is mostly used to explain the origin of jets in AGNs (e.g., Hawley et al. 2015; Blandford et al. 2019) and in young stellar objects (YSOs; e.g., Ouyed et al. 2003; Pudritz et al. 2007; Fendt 2018). On the other hand, the BZ mechanism shows an efficient way of extracting rotational energy from the spin of a Kerr black hole, provided a sufficiently strong magnetic field threads its event horizon. This mechanism has been used to explain the jets associated with GRBs (Lloyd-Ronning et al. 2019; Zhong et al. 2019) and radio jets in AGNs (Komissarov et al. 2007). Both mechanisms have been successfully tested under broad physical conditions using general relativistic, magneto-hydrodynamic simulations (e.g., Semenov et al. 2004; McKinney 2006; Qian et al. 2018; Liska et al. 2019).

On the other hand, a purely hydrodynamical mechanism has been proposed by Hernandez et al. (2014) in which an axisymmetric, polar-density gradient is responsible for deflecting part of the material accreting from an equatorially over-dense inflow and redirecting it along a bipolar outflow. The main advantage of this jet-launching mechanism is that for it to work, one does not need to invoke the presence of magnetic fields that might lack the necessary strength or geometry in some systems (Hawley et al. 2015), or processes taking place in the vicinity of a rotating event horizon and that, thus, can only account for jets associated with systems having a Kerr black hole as central accretor.

In this work, we revisit the jet-launching model of Hernandez et al. (2014) and study it in the general relativistic

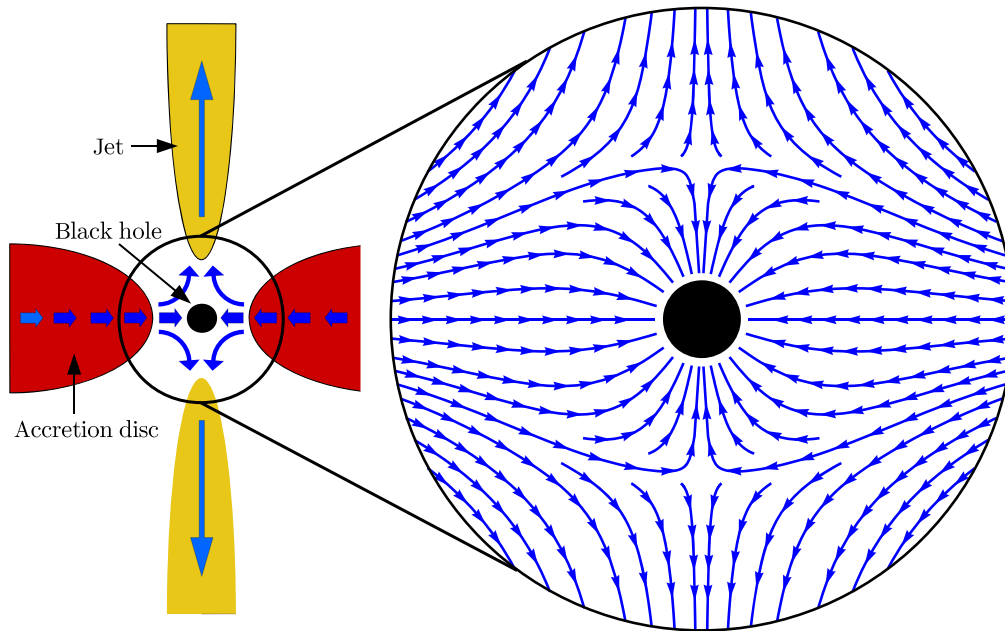


Figure 1. Schematic representation of the astrophysical setting under study: the inner region of an accretion disk–jet system around a central black hole. The analytic solution presented in this work constitutes a toy model of the inner engine behind a jet-launching process in which, through the action of hydrodynamical forces only, an accretion flow can be transformed into an inflow-outflow bipolar structure. Subsequent numerical simulations relaxing the assumptions included in the analytic solution validate and extend the qualitative aspects of the solution found to more general cases. The blue arrows show, schematically, the streamlines of the resulting flow.

regime of an accreting, nonrotating black hole (Schwarzschild spacetime). Based on the general solution derived by Petrich et al. (1988) for a relativistic potential flow with a stiff equation of state, we construct an analytic model corresponding to an inflow-outflow configuration around a Schwarzschild black hole. We propose that this analytic solution can be used as a toy model for the inner engine of a jet-launching system.

The physical setting of this model is shown schematically in Figure 1 and consists of the innermost region of an accretion disk–jet system around a central black hole. Specifically, we will confine our study to a finite, spherical region of radius \mathcal{R} with the black hole at its center. We will refer to the surface of this domain as the injection sphere and consider it as the outer boundary of this system. Moreover, for the analytic model presented, in addition to considering a perfect fluid described by a stiff equation of state, we will assume stationarity, axisymmetry, and an irrotational flow, i.e., we consider that the gas entering the injection sphere from the inner edge of an accretion disk has lost all of its angular momentum through some kind of viscous dissipation mechanism (e.g. Shakura & Sunyaev 1973; Balbus & Hawley 1991).

Even though for constructing the present model we did not explicitly include fluid rotation, it is important to remark that we have accounted for it indirectly by assuming that the flow configuration has a well-defined symmetry axis, possibly as an inherited property of a rotation axis at larger scales. Furthermore, our assumption of a density anisotropy with the equatorial region having a higher density than the poles is a natural consequence of fluid rotation.

On the other hand, demanding a regular solution across the black-hole event horizon implies that, for the present model with an ultrarelativistic stiff fluid, the total mass-accretion rate onto the central black hole is fixed at a specific value (Petrich et al. 1988). This value corresponds closely to that found in the spherically symmetric case discussed by Michel (1972) for a

Schwarzschild spacetime and by Bondi (1952) in the nonrelativistic regime.

This important characteristic of the analytic model implies that the mass flux onto the central black hole is limited by a fixed value and that any additional mass flux crossing the injection sphere has to be redirected and ejected from the system. In the present case, we show that the assumed anisotropic density field at the injection sphere translates into the bipolar outflow shown in Figure 1. Given that the incoming mass-accretion rate is *choking* at a fixed value, we refer to this ejection mechanism as *choked accretion*.

With the aim of studying this accretion scenario under more general conditions, we also present the results of numerical simulations performed with the free GNU General Public License hydrodynamics code *aztekas*³ (Olvera & Mendoza 2008; Aguayo-Ortiz et al. 2018; and Tejeda & Aguayo-Ortiz 2019). By means of this numerical exploration, we are able to show that the choked accretion mechanism can operate for more realistic equations of state.

The basic idea behind the choked accretion model relies on a purely hydrodynamical mechanism and, thus, is not restricted to a relativistic regime. We presented the nonrelativistic limit of the choked accretion model in Aguayo-Ortiz et al. (2019). In that work, we also introduced the Newtonian counterpart of the ultrarelativistic stiff fluid studied by Petrich et al. (1988) that, as discussed in Tejeda (2018), corresponds to the incompressible flow approximation.

With the present model, we intend to draw attention to a potentially relevant phenomenon in which an accretion flow can become choked at a gravitational bottleneck, with the excess material being launched from the central region by a pure hydrodynamical mechanism. The present model is not intended as a substitute for other well-established jet-launching

³ The code can be downloaded from github.com/aztekas-code/aztekas-main.

mechanisms, but rather as a further process based on simple physics that can operate alongside them.

The rest of this article is organized as follows. In Section 2, we present the analytic toy model of choked accretion. In Section 3, we explore numerically the feasibility of this model for fluids described by more realistic equations of state, where the constraint of potential flow imposed on the analytical model is dropped. There we find that the qualitative results of the analytic model also apply. We discuss possible astrophysical applications of the choked accretion model in Section 4. Finally, in Section 5, we summarize our results. Throughout this work, we adopt geometrized units for which $G = c = 1$. Greek indices denote spacetime components, and we adopt the Einstein summation convention over repeated indices.

2. Analytic Model

In this section, we present an analytic model of an inflow-outflow configuration around a Schwarzschild black hole. The model is based on the assumptions of a stationary, axisymmetric, and irrotational flow. Moreover, we shall assume that the accreted gas corresponds to an ultrarelativistic gas described by a stiff equation of state of the form

$$P = K\rho^2, \quad (1)$$

where $K = \text{const.}$, P is the pressure, and ρ is the rest-mass density.⁴

With the possible exception of the dense interior of a neutron star, the assumed stiff equation of state has a rather limited applicability in astrophysics (Lattimer & Prakash 2007). We have adopted this equation of state, however, as it allows us to carry out a full analytic treatment of the problem. The general relativistic solution obtained in this way, gives us a direct insight into the physics behind the proposed mechanism as well as the possibility to analyze in detail the dependence of the solution on the different model parameters. It is important to stress that this limiting assumption is relaxed in Section 3 where, by means of full-hydrodynamic simulations, we show that very similar results are obtained as steady-state solutions for a more general equation of state and, thus, that the model here presented has a wider applicability in astrophysics.

For an ultrarelativistic gas, one has that its internal energy u is much larger than its rest-mass energy, i.e., $u \gg 1$. This allows us to approximate the corresponding specific enthalpy as $h = 1 + u + P/\rho \simeq u + P/\rho$. From the first law of thermodynamics together with the equation of state in Equation (1), it follows that $u = P/\rho$ and, hence,

$$h = 2K\rho. \quad (2)$$

From Equation (2) it follows that, in the case of a stiff fluid, the sound speed a is constant everywhere and equal to the speed of light, i.e.,⁵

$$a \equiv \sqrt{\left(\frac{\partial \ln h}{\partial \ln \rho}\right)}_{\text{s}} = 1. \quad (3)$$

⁴ In relativistic hydrodynamics, it is customary to use the baryon number density n instead of the rest-mass density ρ . Introducing an average baryonic rest mass m , n and ρ are simply related as $\rho = mn$.

⁵ Note that this definition of the sound speed is equivalent to the more common expression $a = \sqrt{\partial P / \partial e}$, where $e = \rho(1 + u)$ is the relativistic energy density.

This result implies that the corresponding flow will be subsonic at every point and that shock fronts cannot develop.

2.1. Potential Flow

The evolution of a perfect fluid in general relativity is dictated by local conservation equations, namely, the conservation of rest mass as expressed by the continuity equation

$$(\rho U^\mu)_{;\mu} = 0 \quad (4)$$

and local conservation of energy–momentum

$$(T^\mu_{\nu})_{;\mu} = (\rho h U^\mu U_\nu + P \delta^\mu_{\nu})_{;\mu} = 0, \quad (5)$$

where $U^\mu = dx^\mu/d\tau$ is the fluid four-velocity, $T^{\mu\nu}$ is the stress-energy tensor of a perfect fluid, δ^μ_{ν} is the Kronecker delta, and the semicolon stands for covariant differentiation. Since, for a perfect fluid $dh = dP/\rho$, together with the continuity equation, Equation (5) can be rewritten as

$$U^\mu (h U_\nu)_{;\mu} + h_{,\nu} = 0. \quad (6)$$

An irrotational flow is characterized by zero vorticity. In general relativity, vorticity is defined in terms of the tensor (Moncrief 1980)

$$\omega_{\mu\nu} = P^\alpha_\mu P^\beta_\nu [(h U_\alpha)_{;\beta} - (h U_\beta)_{;\alpha}], \quad (7)$$

where $P^\mu_\nu = U^\mu U_\nu + \delta^\mu_\nu$ is the projection tensor onto the hypersurface orthogonal to U^μ .

Expanding Equation (7) and using Equation (6) to simplify the resulting expression, we arrive at

$$\omega_{\mu\nu} = (h U_\mu)_{;\nu} - (h U_\nu)_{;\mu}. \quad (8)$$

From Equation (8), we can see that a vanishing vorticity implies that $h U_\mu$ can be written as the gradient of a scalar velocity potential Φ , i.e.,

$$h U_\mu = \Phi_{;\mu}. \quad (9)$$

Substituting Equation (9) into Equation (4) leads to

$$(\rho/h \Phi^{;\mu})_{;\mu} = 0. \quad (10)$$

In general, we will have that ρ is related to h through an equation of state while, from the normalization condition of U^μ , h is related to Φ as $h = \sqrt{-\Phi_{;\mu} \Phi^{;\mu}}$. It is clear then that, in general, Equation (10) will be a nonlinear differential equation in Φ (see, e.g., Beskin & Pidoprygora 1995). Nevertheless, by taking an ultrarelativistic fluid with a stiff equation of state (see Equation (2)), Equation (10) reduces to the simple wave equation

$$\Phi^{;\mu}{}_{;\mu} = 0. \quad (11)$$

In the case of Schwarzschild spacetime with spherical coordinates (t, r, θ, ϕ) , Equation (11) has as general solution (Petrich et al. 1988)

$$\Phi = -e t + \sum_{l,m} [A_{lm} P_l(\xi) + B_{lm} Q_l(\xi)] Y_{lm}(\theta, \phi), \quad (12)$$

where Y_{lm} are spherical harmonics, P_{lm} , Q_{lm} are Legendre functions on $\xi = r/M - 1$, and e is a constant related to the boundary conditions as we will show later on. Petrich et al. (1988) showed that requiring a regular solution across the black horizon necessarily implies that all B_{lm} vanish identically except for B_{00} , which is in turn fixed as $B_{00} = 4Me$.

On the other hand, the coefficients A_{lm} can be freely specified in order to match some given boundary conditions. In the present case, the assumption of axisymmetry leads us to consider only the $m = 0$ modes, while demanding reflection symmetry with respect to the equatorial plane, leaves us only with even- l multipoles different from zero. The lowest-order model featuring both inflow and outflow regions can then be obtained from a velocity potential as in Equation (12) with all $A_{lm} = 0$ except for A_{20} , i.e.,

$$\Phi = -e \left[t + 2M \ln \left(1 - \frac{2M}{r} \right) - A(3r^2 - 6Mr + 2M^2)(3 \cos^2 \theta - 1) \right], \quad (13)$$

where $A = 4\sqrt{\pi/5} A_{20}/e$.

Note that a different choice of the coefficients A_{lm} will result in quite different flow configurations. For instance, Petrich et al. (1988) and Tejeda (2018) adopt the dipole $l = 1$ to study the scenario of wind accretion.

With the velocity potential as given in Equation (13), we have specified the dependence of the fluid properties on the polar angle θ at the outer boundary, i.e., at the injection sphere $r = \mathcal{R}$. Nonetheless, we are still free to specify the overall magnitude (scale) of the fluid properties at this boundary. In order to do this, we can specify values for the fluid velocity, density, and pressure (or any other pair of thermodynamical variables) at a reference point on the injection sphere. For this work, we shall take as reference the point ($r = \mathcal{R}$, $\theta = \pi/2$), i.e., the equator of the injection sphere. Let us call ρ_0 and P_0 the values of the density and pressure at this point as measured by a co-moving observer. Clearly, from these reference values, we can write $K = P_0/\rho_0^2$ and $h_0 = 2P_0/\rho_0$. On the other hand, we parameterize the fluid velocity at this point using V_0 , defined as the magnitude of the three-velocity vector measured by a local Eulerian observer (LEO).⁶ In terms of V_0 , the four-velocity of the fluid at the equator of the injection sphere is given by

$$U^\mu = \Gamma_0(1/\alpha_0, -\alpha_0 V_0, 0, 0), \quad (14)$$

with $\alpha_0 = \alpha(\mathcal{R})$, where

$$\alpha = \sqrt{1 - \frac{2M}{r}} \quad (15)$$

is the lapse function associated with the $3 + 1$ decomposition of the four-metric and

$$\Gamma_0 = (1 - V_0^2)^{-1/2} \quad (16)$$

is the Lorentz factor between the fluid element and the LEO. As V_0 corresponds to the magnitude of a physical three-velocity vector, it is naturally bounded as $V_0 < 1$. Also note that in Equation (14), we have explicitly considered that the radial velocity is negative at the reference point as we are interested in a scenario with equatorial inflow. The velocity potential in Equation (13) should also be useful to describe a very different scenario with polar inflow and equatorial outflow (akin to a

wall jet) by allowing for a positive radial velocity at the reference point. We shall only focus on the former case for the remainder of this work.

It is worth noticing at this point that the present analytic model is scale-free with respect to the specific values of M , ρ_0 , and P_0 . On the other hand, as we shall see below, the parameters dictating the overall morphology of the resulting accretion flow are V_0 and \mathcal{R}/M .

2.2. Velocity Field

Substituting the velocity potential Φ given in Equation (13) into Equation (9) leads to the velocity field

$$\frac{h}{e} \frac{dt}{d\tau} = \left(1 - \frac{2M}{r} \right)^{-1}, \quad (17)$$

$$\frac{h}{e} \frac{dr}{d\tau} = -\frac{4M^2}{r^2} + \frac{6A}{r}(r-M)(r-2M)(3 \cos^2 \theta - 1), \quad (18)$$

$$\frac{h}{e} \frac{d\theta}{d\tau} = -\frac{6A}{r^2}(3r^2 - 6Mr + 2M^2) \sin \theta \cos \theta. \quad (19)$$

By evaluating Equations (17) and (18) at the reference point ($r = \mathcal{R}$, $\theta = \pi/2$) and comparing the result with Equation (14), we arrive at the following expressions for the constants e and A in terms of the boundary conditions:

$$e = \alpha_0 h_0 \Gamma_0, \quad (20)$$

$$A = \frac{V_0 \mathcal{R}^2 - 4M^2}{6\mathcal{R}(\mathcal{R} - M)(\mathcal{R} - 2M)}. \quad (21)$$

Note that, since we have assumed inflow across the equatorial region, the velocity field described by Equations (18) and (19) is characterized by the existence of a pair of stagnation points (points at which the spatial components of the velocity field vanish) located along the polar axis ($\theta = 0, \pi$) at mirror points with respect to the origin. Calling \mathcal{S} their radial distance to the origin, from Equation (18), we obtain the following relationship between V_0 , \mathcal{R} , and \mathcal{S}

$$V_0 = \frac{2M^2}{\mathcal{R}^2} \left[2 + \frac{\mathcal{R}(\mathcal{R} - M)(\mathcal{R} - 2M)}{\mathcal{S}(\mathcal{S} - M)(\mathcal{S} - 2M)} \right]. \quad (22)$$

Alternatively, Equation (22) can be inverted to express \mathcal{S} as a function of V_0 and \mathcal{R}

$$\frac{\mathcal{S}}{M} = 1 + \left(\xi + \sqrt{\xi^2 - \frac{1}{27}} \right)^{1/3} + \left(\xi - \sqrt{\xi^2 - \frac{1}{27}} \right)^{1/3}, \quad (23)$$

where

$$\xi = \frac{\mathcal{R}(\mathcal{R} - M)(\mathcal{R} - 2M)}{M(V_0 \mathcal{R}^2 - 4M^2)}. \quad (24)$$

Note that we can also use \mathcal{S} to rewrite the coefficient A as

$$A = \frac{M^2}{3\mathcal{S}(\mathcal{S} - M)(\mathcal{S} - 2M)}. \quad (25)$$

Using Equation (25), together with Equation (17) to get rid of the dependence on h , we can rewrite the spatial components

⁶ These are static observers carrying a local tetrad with respect to which they can perform local measurements, thus describing physical properties of the fluid. This family of observers can be introduced in a covariant (coordinate-independent) way by noticing that their four-velocity corresponds to the time isometry of Schwarzschild spacetime as encoded by the time-like Killing vector $t^\mu = \delta^\mu_t$.

of the velocity with respect to the coordinate time t as

$$\frac{dr}{dt} = -\frac{2M^2}{r^2} \left(1 - \frac{2M}{r}\right) \times \left[2 - \frac{r(r-M)(r-2M)}{\mathcal{S}(\mathcal{S}-M)(\mathcal{S}-2M)}(3\cos^2\theta - 1)\right], \quad (26)$$

$$\frac{d\theta}{dt} = -\frac{2M^2}{r^2} \left(1 - \frac{2M}{r}\right) \frac{3r^2 - 6Mr + 2M^2}{\mathcal{S}(\mathcal{S}-M)(\mathcal{S}-2M)} \sin\theta \cos\theta. \quad (27)$$

Furthermore, we can also express the velocity field in terms of the physical, locally measured components of the three-velocity defined by LEOs and given by

$$V^r = \left(1 - \frac{2M}{r}\right)^{-1/2} \frac{dr}{dt}, \quad (28)$$

$$V^\theta = \left(1 - \frac{2M}{r}\right)^{-1/2} \frac{d\theta}{dt}, \quad (29)$$

as well as its corresponding (squared) magnitude

$$\begin{aligned} V^2 &= \left(1 - \frac{2M}{r}\right)^{-2} \left(\frac{dr}{dt}\right)^2 + \left(1 - \frac{2M}{r}\right)^{-1} r^2 \left(\frac{d\theta}{dt}\right)^2 \\ &= \frac{4M^4}{r^4} \left[4 - \frac{4r(r-M)(r-2M)}{\mathcal{S}(\mathcal{S}-M)(\mathcal{S}-2M)}(3\cos^2\theta - 1) \right. \\ &\quad + \frac{r^2(r-M)^2(r-2M)^2}{\mathcal{S}^2(\mathcal{S}-M)^2(\mathcal{S}-2M)^2}(3\cos^2\theta - 1)^2 \\ &\quad \left. + \frac{r(r-2M)(3r^2 - 6Mr + 2M^2)^2}{\mathcal{S}^2(\mathcal{S}-M)^2(\mathcal{S}-2M)^2} \sin^2\theta \cos^2\theta\right]. \end{aligned} \quad (30)$$

Note that for a sufficiently large radius r , the physical three-velocity magnitude V as given in Equation (30) will grow like $V \propto r$, eventually becoming superluminal.⁷ To prevent this from happening, we need to consider the preset model as a local solution that is only properly defined within a finite spatial domain. For simplicity, we will restrict this work to the spherical domain $r \leq \mathcal{R}$, where \mathcal{R} is the radius of the injection sphere.

By examining Equation (30), we can see that, for a radius $\mathcal{R} > \mathcal{S}$, V reaches its maximum at the polar axis, which is given by

$$\begin{aligned} V(\mathcal{R}, 0) &= \frac{4M^2}{\mathcal{R}^2} \left| \frac{\mathcal{R}(\mathcal{R}-M)(\mathcal{R}-2M)}{\mathcal{S}(\mathcal{S}-M)(\mathcal{S}-2M)} - 1 \right| \\ &= \left| 2V_0 - \frac{12M^2}{\mathcal{R}^2} \right|, \end{aligned} \quad (31)$$

where we have used Equation (22) to arrive at the last equal sign. From this last expression, we obtain the following upper bound on V_0 in order to guarantee V to be subluminal within

the domain⁸ $2M < r \leq \mathcal{R}$

$$V_0 < \frac{1}{2} + 6\frac{M^2}{\mathcal{R}^2}. \quad (32)$$

Based on Equation (31) and taking into account the sign of the radial velocity in Equation (26), we define the ejection velocity at the poles of the shell $r = \mathcal{R}$ as

$$V_{\text{ej}} \equiv 2V_0 - \frac{12M^2}{\mathcal{R}^2}. \quad (33)$$

From this expression, we note that, in order to actually have polar outflow at $r = \mathcal{R}$ (i.e., $V_{\text{ej}} > 0$), we require

$$V_0 > 6\frac{M^2}{\mathcal{R}^2}. \quad (34)$$

Moreover, note that when $0 < V_0 < 6\frac{M^2}{\mathcal{R}^2}$, the stagnation point lies outside the injection sphere ($\mathcal{S} > \mathcal{R}$) and the flow is everywhere radially inwards although not spherically symmetric.

Summarizing the previous results, only for values of V_0 within the range

$$6\frac{M^2}{\mathcal{R}^2} < V_0 < \frac{1}{2} + 6\frac{M^2}{\mathcal{R}^2}, \quad (35)$$

we find flow configurations characterized by equatorial inflow and bipolar outflows within the domain of interest $2M < r \leq \mathcal{R}$.

See Figure 2 for three examples of the streamlines resulting from the velocity field in Equations (26) and (27) for $\mathcal{R} = 10M$. In the left and right panels, $V_0 = 0.06, 0.56$, which correspond to the lower and upper bounds of the interval in Equation (35). For the central panel, we have taken $V_0 = 0.1$ as a representative middle value for V_0 .

In the top panel of Figure 3, we show the magnitude of the three-velocity V as function of the polar angle θ evaluated at the injection sphere for the particular case $\mathcal{R} = 10M$ and several values of V_0 .

2.3. Density Field

We can now recover the density field by substituting Equations (17)–(19) into the normalization condition of the four-velocity $U_\mu U^\mu = -1$ and then using Equation (20); the result is

$$\frac{\rho}{\rho_0} = \frac{\alpha_0 \Gamma_0}{\alpha \Gamma} = \sqrt{\frac{r(\mathcal{R}-2M)(1-V^2)}{\mathcal{R}(r-2M)(1-V_0^2)}}, \quad (36)$$

with $V^2(r, \theta)$ as given in Equation (30).

Recalling that the local density measured by an LEO is given by $D = \Gamma\rho$, from Equation (36), we obtain the interesting result that the density field as described by LEOs is spherically symmetric, i.e., D is only a function of r .

Note that the same criterion introduced in Equation (32) in order to guarantee a subluminal three-velocity within $2M < r \leq \mathcal{R}$ also guarantees that the density field, as expressed in Equation (36), is a well-defined, real quantity within the same spatial domain.

⁷ In terms of the velocity potential Φ , this translates into the gradient $\Phi_{,\mu}$ transitioning from being time-like to space-like.

⁸ Note that at the event horizon $V(2M) = 1$, although, this is only due to the fact the Eulerian observers become ill-defined at this radius. The fluid velocity as described by U^μ is completely regular across the horizon.

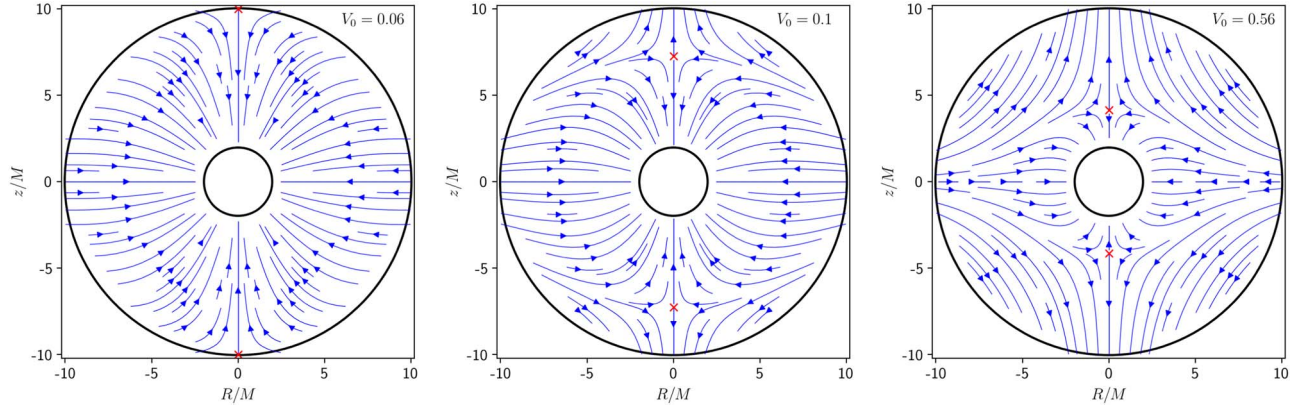


Figure 2. Streamlines of the accretion flow resulting from the velocity field in Equations (26) and (27). We have taken $\mathcal{R} = 10M$ as radius of the injection sphere while, from left to right, $V_0 = 0.06, 0.1, 0.56$. Note that the first and third values of V_0 correspond to the lower and upper limits in Equation (35), respectively. The stagnation points in each case are shown as red crosses. The outer boundary of the model ($r = \mathcal{R}$) as well as the event horizon of the central black hole ($r = 2M$) are shown as circles drawn with thick, solid lines. The axes correspond to the usual cylindrical coordinates $R = r \sin \theta$, $z = r \cos \theta$.

From Equation (36), we obtain the following simple relation for the ratio between the density at the pole and the equator of the injection sphere:

$$\begin{aligned} \frac{\rho(\mathcal{R}, 0)}{\rho(\mathcal{R}, \pi/2)} &= \frac{\rho(\mathcal{R}, 0)}{\rho_0} = \sqrt{\frac{1 - V_{\text{ej}}^2}{1 - V_0^2}} \\ &= \sqrt{\frac{\mathcal{R}^4 - 4V_0^2\mathcal{R}^4 + 48V_0\mathcal{R}^2M^2 - 144M^4}{\mathcal{R}^4 - V_0^2\mathcal{R}^4}}. \end{aligned} \quad (37)$$

In the following, we shall use the contrast δ between the polar and equatorial densities at the injection sphere defined as

$$\delta = 1 - \frac{\rho(\mathcal{R}, 0)}{\rho_0}. \quad (38)$$

From Equations (37) and (38), we can see that an arbitrarily small density contrast suffices not only to produce the inflow-outflow configuration shown in the central and right panels of Figure 2 but also to guarantee that $V_{\text{ej}} > V_0$. Furthermore, notice that, as the density contrast approaches unity, the ejection velocity approaches the speed of light. Indeed, for the present case of an ultrarelativistic stiff fluid, as $\delta \rightarrow 1$, we can obtain arbitrarily large Lorentz factors for the ejected flow.

Complementary to the top panel of Figure 3, where we see that the magnitude of the velocity field at the injection sphere increases as V_0 increases, in the bottom panel of this figure, we show the angular density profile $\rho(\theta)$ evaluated at the injection sphere. From this figure, we see that, as V_0 increases, the polar to equatorial density contrast increases. Moreover, we can also see that as the velocity at the poles becomes luminal for $V_0 = 1/2 + 6M^2/\mathcal{R}^2$, the corresponding value of the density field becomes zero.

2.4. Equation for the Streamlines

An equation for the streamlines can be found by combining Equations (26) and (27) to obtain

$$\frac{dr}{d\theta} = \frac{2 - \frac{r(r-M)(r-2M)}{\mathcal{S}(\mathcal{S}-M)(\mathcal{S}-2M)}(3\cos^2\theta - 1)}{\frac{3r^2 - 6Mr + 2M^2}{\mathcal{S}(\mathcal{S}-M)(\mathcal{S}-2M)}\sin\theta\cos\theta}, \quad (39)$$

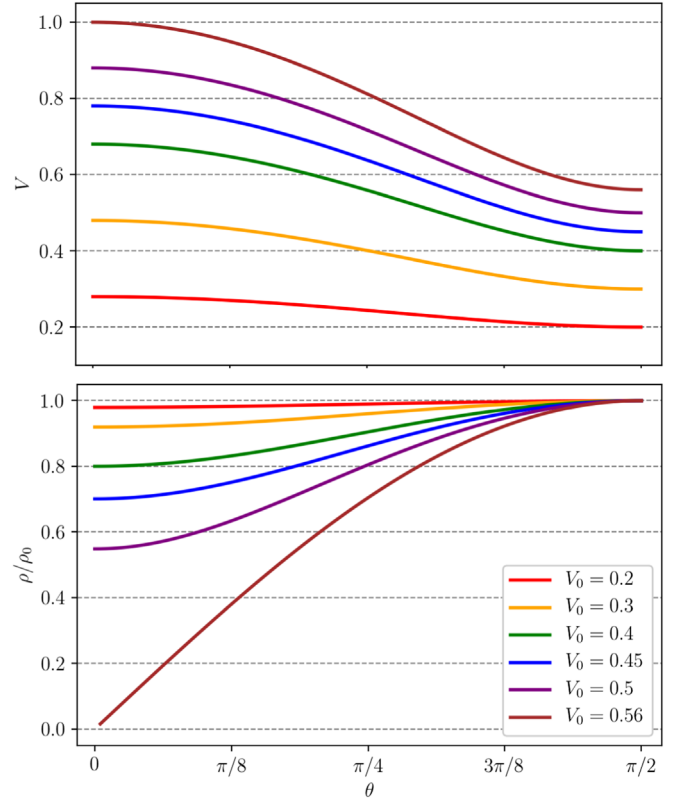


Figure 3. Magnitude of the three-velocity V (Equation (30)) and density ρ (Equation (36)) of the analytic model for an ultrarelativistic stiff fluid. Both quantities are shown as functions of the polar angle θ evaluated at the injection sphere for the particular case $\mathcal{R} = 10M$ and six different values of the velocity V_0 . In this case, from Equation (32), we have that V_0 is limited as $V_0 < 0.56$ in order to guarantee that the whole solution is well defined within the spatial domain $r \leq \mathcal{R}$. Note that for $V_0 = 0.56$, $V_{\text{ej}} = 1$ while the corresponding value of ρ goes to zero.

which, in turn, can be integrated as

$$\Psi = \cos\theta \left[1 + \frac{r(r-M)(r-2M)}{\mathcal{S}(\mathcal{S}-M)(\mathcal{S}-2M)} \frac{\sin^2\theta}{2} \right], \quad (40)$$

where Ψ is an integration constant. Equation (40) constitutes an implicit equation for the streamlines, where, for every constant value of Ψ , one has a different streamline. Note, in particular,

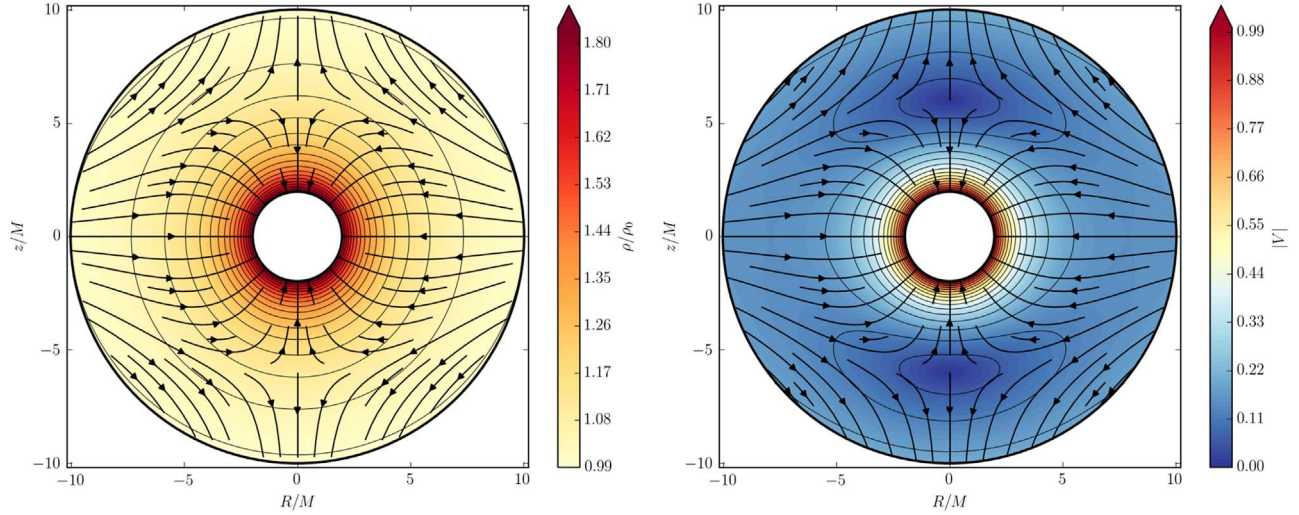


Figure 4. Example of the analytic model of choked accretion for the values $\mathcal{R} = 10M$ and $V_0 = 0.16$. The figure shows isocontours of the fluid's density as given by Equation (36) (left panel) as well as the magnitude of the three-velocity as given by Equation (30) (right panel). Note that the stagnation points are located at $\mathcal{S} = 6M$. Fluid streamlines are indicated by thick, solid lines with an arrow. The axes correspond to the usual cylindrical coordinates $R = r \sin \theta$, $z = r \cos \theta$.

that $\Psi = \pm 1$ corresponds to the streamlines reaching the stagnation points located at $(r = \mathcal{S}, \theta = 0)$ for the plus sign and $(r = \mathcal{S}, \theta = \pi)$ for the minus sign. Streamlines with $|\Psi| < 1$ end up accreting onto the central black hole, while those with $|\Psi| > 1$ escape along the bipolar outflow.

In Figure 4, we show the resulting density, velocity, and streamlines of the analytic model of choked accretion for the particular values of $\mathcal{R} = 10M$, $V_0 = 0.16$. For this choice of boundary conditions, the stagnation points are located at $\mathcal{S} = 6M$.

2.5. Mass-accretion, Injection, and Ejection Rates

The total mass-accretion rate onto the central black hole can be calculated as the flux of mass density integrated over any closed surface σ enclosing it, i.e.,

$$\dot{M} = - \int_{\sigma} \rho U^{\mu} \sqrt{-g} dS_{\mu}, \quad (41)$$

where $\sqrt{-g} = r^2 \sin \theta$ and dS_{μ} is a differential area element orthogonal to the surface σ . Taking any sphere of radius r as the integration surface, together with the conditions of axisymmetry and stationarity, we obtain

$$\begin{aligned} \dot{M} &= -2\pi \int_0^{\pi} \rho U^r r^2 \sin \theta d\theta \\ &= 16\pi M^2 \alpha_0 \rho_0 \Gamma_0. \end{aligned} \quad (42)$$

The result of Equation (42) holds even if higher multipoles are considered in the velocity potential (see Equation (12)): by virtue of the orthogonality of the spherical harmonics, the contribution of any multipole (l, m) to the integral in Equation (42) identically vanishes except for the spherically symmetric monopole $l = 0$, $m = 0$. Note however that, in the spherically symmetric case, V_0 is not a free parameter. In accordance with Equation (30), in this case, $V_0 = 4M^2/\mathcal{R}^2$. Therefore, in the spherically symmetric case, the mass-accretion rate as given by Equation (42) can

be written as

$$\dot{M}_M = 16\pi M^2 \alpha_0 \rho_0 \left(1 - 16 \frac{M^4}{\mathcal{R}^4}\right)^{-1/2}. \quad (43)$$

This value corresponds to the Michel (1972) solution as applied to a stiff equation of state, as shown by Chaverra & Sarbach (2015). See Appendix A for a brief overview of the Michel (1972) model in the case of a general polytrope.

We can express the general result for the mass-accretion rate as given in Equation (42) in units of \dot{M}_M as

$$\dot{M} = \eta \dot{M}_M, \quad (44)$$

where

$$\eta = \left(\frac{1 - 16M^4/\mathcal{R}^4}{1 - V_0^2} \right)^{1/2}. \quad (45)$$

Note that, in most cases of interest, $\eta \gtrsim 1$. For instance, taking $\mathcal{R} = 10M$, from the allowed range of velocities in Equation (35), we obtain $1 < \eta \lesssim 1.2$, while for $\mathcal{R} \gg M$, we have $1 < \eta \lesssim 1.15$.

On the other hand, we can also define the mass-injection rate \dot{M}_{in} as the inward flux of mass across the injection sphere of radius \mathcal{R} , i.e., by considering an integration analogous to the one in Equation (42) but in which we consider only the fluid elements with a negative radial velocity U^r . From Equation (18), we obtain that $U^r(\mathcal{R}, \theta) < 0$ for $\theta_c < \theta < \pi - \theta_c$, where θ_c is such that $U^r(\mathcal{R}, \theta_c) = 0$ and is given by

$$\begin{aligned} \cos \theta_c &= \sqrt{\frac{1}{3} + \frac{2}{3} \frac{\mathcal{S}(\mathcal{S} - M)(\mathcal{S} - 2M)}{\mathcal{R}(\mathcal{R} - M)(\mathcal{R} - 2M)}} \\ &= \sqrt{\frac{V_0 \mathcal{R}^2}{3(V_0 \mathcal{R}^2 - 4M^2)}}. \end{aligned} \quad (46)$$

We can thus calculate \dot{M}_{in} as

$$\dot{M}_{\text{in}} = -4\pi \int_{\theta_c}^{\pi/2} \rho U^r r^2 \sin \theta d\theta = \Lambda \dot{M}, \quad (47)$$

with

$$\begin{aligned}\Lambda &= \frac{1}{6\sqrt{3}} \frac{V_0 \mathcal{R}^2}{M^2} \left(1 - \frac{4M^2}{V_0 \mathcal{R}^2}\right)^{-1/2} \\ &\simeq \frac{1}{6\sqrt{3}} \left(\frac{V_0 \mathcal{R}^2}{M^2} + 2\right) + \mathcal{O}\left(\frac{M^2}{V_0 \mathcal{R}^2}\right),\end{aligned}\quad (48)$$

where, for the second step, we have used the Taylor series expansion assuming $M^2 \ll V_0 \mathcal{R}^2$.

From Equation (46), we have that when $V_0 = 6M^2/\mathcal{R}^2$ (or, equivalently $\mathcal{S} = \mathcal{R}$) then $\theta_c = 0$ and, hence, $\dot{M}_{\text{in}} = \dot{M}$. On the other hand, when $V_0 < 6M^2/\mathcal{R}^2$, we have that $U^r < 0$ for all θ and again $\dot{M}_{\text{in}} = \dot{M}$. We can then write

$$\dot{M}_{\text{in}} = \begin{cases} \dot{M}, & \text{if } V_0 \leq 6M^2/\mathcal{R}^2, \\ \Lambda \dot{M}, & \text{if } V_0 > 6M^2/\mathcal{R}^2. \end{cases}\quad (49)$$

Similarly, we define the mass-ejection rate \dot{M}_{ej} as the outward flux of mass across the sphere of radius $r = \mathcal{R}$. Clearly,

$$\dot{M}_{\text{ej}} = \begin{cases} 0, & \text{if } V_0 \leq 6M^2/\mathcal{R}^2, \\ (\Lambda - 1)\dot{M}, & \text{if } V_0 > 6M^2/\mathcal{R}^2. \end{cases}\quad (50)$$

Note that for a fixed injection radius \mathcal{R} , it can be shown that the upper bound for V_0 found in Equation (32) implies the following upper bound for the mass-injection rate:

$$\dot{M}_{\text{in}} < 8\pi \rho_0 \sqrt{\frac{(\mathcal{R} - 2M)\mathcal{R}^3(\mathcal{R}^2 + 12M^2)^3}{3(\mathcal{R}^2 + 4M^2)[4\mathcal{R}^4 - (\mathcal{R}^2 + 12M^2)^2]}}.\quad (51)$$

The Equations (49) and (50) encapsulate the concept of choked accretion described in the introduction: the central black hole accretes at an essentially fixed rate $\dot{M} \simeq \dot{M}_{\text{M}}$. Whenever the mass-injection rate surpasses this limit, the excess flux is ejected from the system as a bipolar outflow at the rate \dot{M}_{ej} . Note, in particular, that from Equation (50), we can write

$$\frac{\dot{M}_{\text{ej}}}{\dot{M}_{\text{in}}} = 1 - \frac{\dot{M}}{\dot{M}_{\text{in}}} = 1 - \frac{1}{\Lambda}.\quad (52)$$

This simple functional dependence of the ratio of ejected-to-injected-mass fluxes on the injection-mass rate is shown in Figure 14 to compare the analytic model against the results of hydrodynamic numerical simulations.

Finally, it is interesting to explore the behavior of the analytic model as a function of the parameters \mathcal{R} and $\dot{M}_{\text{in}}/\dot{M}_{\text{M}} = \eta \Lambda$. Note that, as shown in Equation (48), $\eta \Lambda$ is essentially a linear re-parameterization of V_0 for most of the domain of interest. In Figure 5, we show the dependence on these parameters of the location of the stagnation point \mathcal{S} (see Equation (23)), the maximum velocity attained by the ejected material V_{ej} (see Equation (33)), and the contrast δ between the polar and equatorial densities at the injection sphere (see Equation (38)).

From this figure, we see that as $\dot{M}_{\text{in}}/\dot{M}_{\text{M}}$ increases, the stagnation point sinks closer to the central accretor, while at the same time, the velocity of the ejected material approaches the speed of light and the density contrast increases. From Equation (52) and Figure 14, it is also clear that as the injection rate increases, more and more material is expelled from the system as a bipolar outflow. Moreover, the restrictions on the model parameters, as established in Equations (32) and (51),

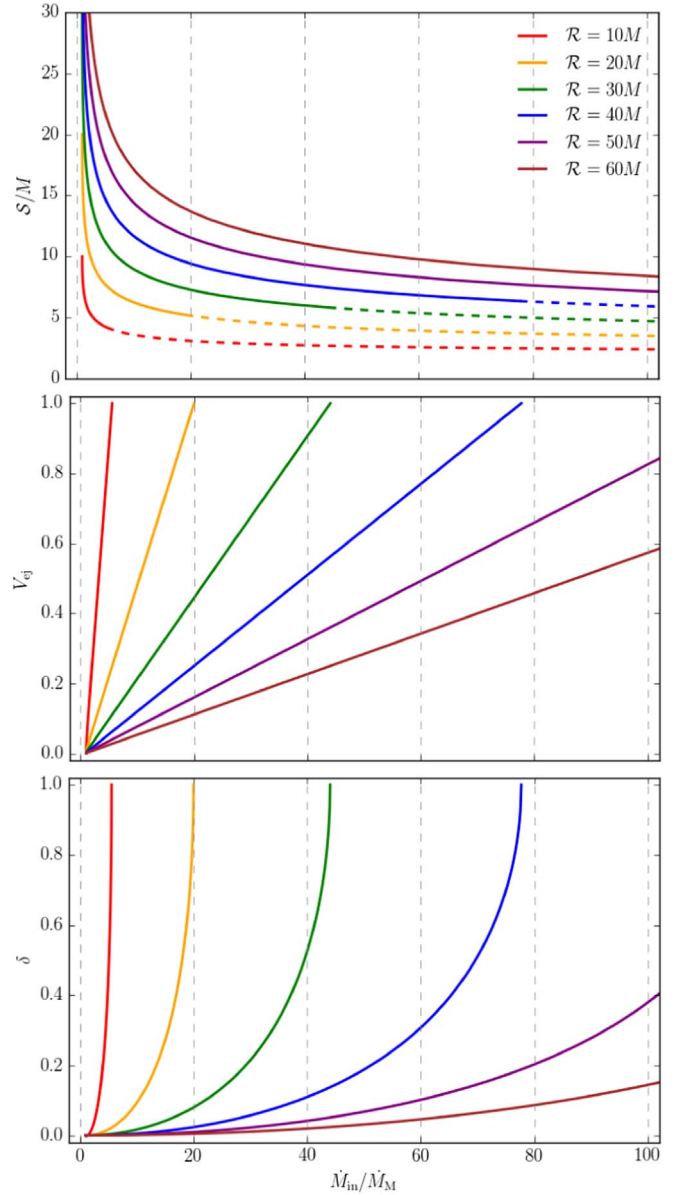


Figure 5. Dependence of different properties of the analytic model of choked accretion on the parameters \mathcal{R}/M and $\dot{M}_{\text{in}}/\dot{M}_{\text{M}}$. From top to bottom, each panel shows: the location of the stagnation point \mathcal{S} , the maximum velocity attained by the ejected material V_{ej} (Equation (31)), and the density contrast between the pole and the equator of the injection sphere δ (Equation (38)). The dashed lines in the top panel indicate regions in the parameter space for which the model is not well defined within the whole domain $r < \mathcal{R}$ (see discussion in the main text).

are also apparent in Figure 5: as soon as these limits are exceeded, the model ceases to be well-defined within the whole domain $r < \mathcal{R}$.

The nonrelativistic limit of an ultrarelativistic, stiff fluid corresponds to an incompressible fluid (Tejeda 2018). This Newtonian counterpart of the present analytic model is discussed in Aguayo-Ortiz et al. (2019). Indeed, it is simple to verify that, in the limit in which $V_0 \ll 1$ and $\mathcal{R} \gg M$, all of the equations derived in this section for the velocity field, the streamlines, and the different mass fluxes reduce to the expressions presented in Aguayo-Ortiz et al. (2019).

The analytic model that we have presented allows for a transparent understanding of the physics involved in the

choked accretion mechanism. However, generalizing this model to accommodate a more realistic equation of state becomes analytically intractable. We explore this generalization in the next section by means of numerical simulations.

3. Numerical Simulations

The main limitation of the analytic model for choked accretion discussed in the previous section is that it is based on the assumption of an ultrarelativistic gas with a stiff equation of state, an assumption with a rather restricted applicability in astrophysics. In this section, we want to explore whether the phenomenon of choked accretion might also arise when considering more general equations of state, thus relaxing the associated assumption of a potential flow. This exploration will be based on full-hydrodynamic, numerical simulations performed with the open-source code *aztekas*.

The general relativistic hydrodynamic equations are solved numerically with *aztekas* by recasting them in a conservative form using the Valencia formulation (Banyuls et al. 1997). The *aztekas* code uses a grid-based finite volume scheme, a High-Resolution Shock Capturing method with an approximate Riemann solver for the flux calculation, and a monotonically centered second-order reconstructor at cell interfaces. The code adopts a second-order total variation diminishing Runge–Kutta method (Shu & Osher 1988) for the time integration. See Tejeda & Aguayo-Ortiz (2019) for further details about the discretization used in *aztekas*. Code validation through comparisons to standard analytical solutions in the Newtonian and relativistic regimes can be found in Aguayo-Ortiz et al. (2018, 2019) and Tejeda & Aguayo-Ortiz (2019), while a number of standard shock tube tests successfully reproduced by the code are included in Appendix B.

The simulations presented in this section were performed for a perfect fluid evolving in a fixed, background metric corresponding to a Schwarzschild black hole of mass M . We adopt horizon-penetrating, Kerr–Schild coordinates and, imposing axisymmetry, we consider only 2D spatial domains with spherical coordinates r and θ .

Furthermore, by assuming symmetry with respect to the equatorial plane located at $\theta = \pi/2$ (north–south symmetry), we restrict the numerical domain as $(r, \theta) \in [\mathcal{R}_{\text{acc}}, \mathcal{R}] \times [0, \pi/2]$, where \mathcal{R}_{acc} is the radius of the inner boundary at which we adopt a free outflow condition (i.e., free inflow onto the central black hole) and \mathcal{R} is the radius of the injection sphere at which we impose a given profile for the physical parameters of the injected fluid. At both polar boundaries $\theta = 0, \pi/2$, we adopt reflection conditions.

As initial conditions, we populate the whole numerical domain with the same values as those used at the outer boundary \mathcal{R} . For the code, we adopt geometrized units and take $M = 1$ as unit of length and time.

3.1. Stiff Fluid

An analytic model can be useful as a benchmark solution for testing the ability of a numerical code to recover certain behavior under appropriate conditions. Here, we use the exact analytic solution presented in the previous section as a benchmark test for *aztekas*. Specifically, we will consider the values of $\mathcal{R} = 10M$ for the radius of the injection sphere and

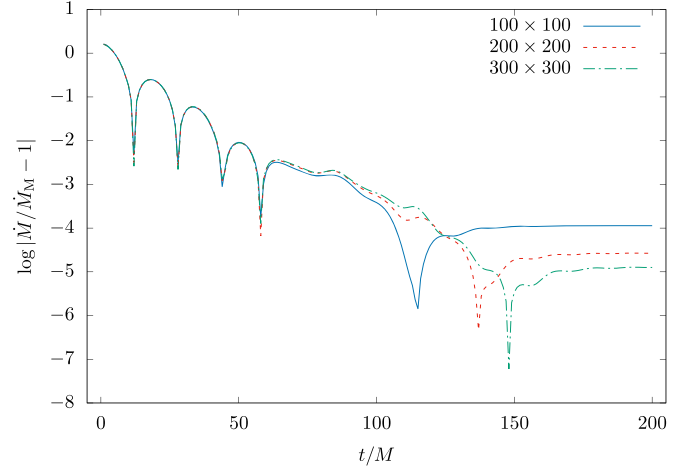


Figure 6. Benchmark test of *aztekas* with the analytic model of choked accretion described in Section 2. In this case, we took $\mathcal{R} = 10M$ as radius of the injection sphere and $V_0 = 0.16$ at the equator. The figure shows the time evolution of the relative error between the numerically calculated accretion rate \dot{M} and the exact value of $\dot{M}_M = 16\pi M^2 \alpha_0 \rho_0 \Gamma_0$ for three resolutions (grid points) 100×100 , 200×200 , and 300×300 . Note that the sharp falls observed in this figure correspond to changes in sign of the relative error being plotted. Moreover, the apparent periodicity observed at the beginning of the curve corresponds to an initial transient mode reflecting back and forth throughout the numerical domain at the speed of sound (in this case, the sound crossing time is $t \sim 10M$).

$V_0 = 0.16$ for the magnitude of the three-velocity at the equator of the injection sphere.

For this test, we take as radial boundaries $\mathcal{R}_{\text{acc}} = M$ and $\mathcal{R} = 10M$ and use three different resolutions (grid points) 100×100 , 200×200 , and 300×300 for the radial and polar ranges. We adopt the approximation of an ultrarelativistic gas with a stiff equation of state as described in Section 2. At the injection sphere, we impose the analytic value for the density as given in Equation (36) and the velocity components corresponding to the transformation from Schwarzschild coordinates to Kerr–Schild coordinates.⁹

We let the simulations run until a steady-state condition is reached. This is monitored by calculating the mass-accretion rate \dot{M} across \mathcal{R}_{acc} . In Figure 6, we show the time evolution of the numerically calculated \dot{M} as compared to the analytically expected value of $\dot{M}_M = 16\pi M^2 \alpha_0 \rho_0 \Gamma_0$ for the three adopted resolutions. As can be seen from this figure, the value of \dot{M} rapidly stabilizes to a constant value that agrees with \dot{M}_M to within 0.001% for the largest resolution considered.

In Figure 7, we show the density and velocity fields of the *aztekas* simulation at $t = 650M$. The stagnation point in the numerical simulation is located at $S = 6.0175M$, which is consistent with the analytically exact value of $S = 6M$, taking into account the radial grid size of $\Delta r = 0.045M$.

⁹ The transformation between Schwarzschild (t, r, θ, ϕ) and Kerr–Schild coordinates (T, r, θ, ϕ) is given by

$$dT = dt + \frac{2M}{r - 2M} dr,$$

while the spatial components remain unchanged. The radial and polar components of the four-velocity in Kerr–Schild coordinates are then given by Equations (18) and (19), whereas the time component is now given by

$$\frac{h}{e} \frac{dT}{d\tau} = \left(1 - \frac{2M}{r}\right)^{-1} \left(1 + \frac{2M}{r} \frac{h}{e} \frac{dr}{d\tau}\right).$$

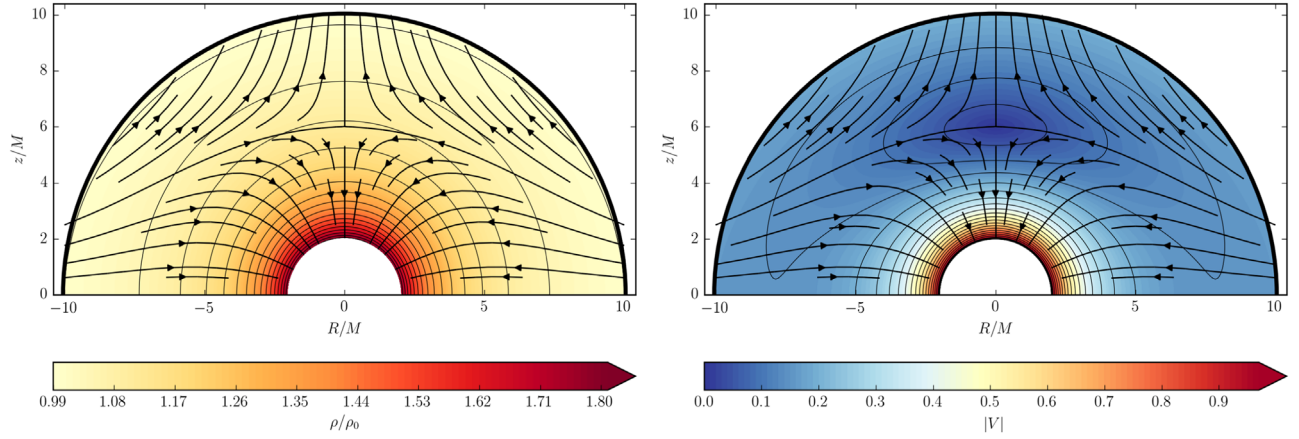


Figure 7. Benchmark test of *aztekas* with the analytic model of choked accretion described in Section 2. In this case, we took $\mathcal{R} = 10M$ as radius of the injection sphere and $V_0 = 0.16$ at the equator. The left panel shows isocontour levels of the density field with the scale indicated by the color bar. The right panel shows isocontour levels of the magnitude of the three-velocity. Fluid streamlines are indicated by thick, solid lines with an arrow. The simulation time is $t = 650M$. An excellent agreement is found between this figure and its analytic counterpart in Figure 4.

We have also tried this benchmark test with different values of \mathcal{R} and V_0 , and we consistently found that the numerical results recover the analytic solution in this limit case of a stiff equation of state, thus validating our numerical setup.

3.2. Polytropic Fluids

In this section, we relax the stiff-fluid condition and consider perfect fluids described by a polytropic equation of state of the form

$$P = K \rho^\gamma, \quad (53)$$

with ρ the rest-mass density, γ the adiabatic index, and $K = \text{const.}$ From Equation (3), the sound speed corresponding to this equation of state is given by

$$a^2 = \frac{\gamma P}{h \rho}, \quad (54)$$

where h is the relativistic specific enthalpy. For a perfect fluid described by Equation (53), h is related to the other thermodynamical variables through

$$h = 1 + \frac{\gamma P}{\gamma - 1 \rho}, \quad (55)$$

or, by combining Equations (54) and (55), we can also write

$$h = \frac{1}{1 - a^2/(\gamma - 1)}. \quad (56)$$

The expected requirement for the appearance of choked accretion is that there should exist a small contrast between the density at the equator and that at the poles of the injection sphere. Here, we impose this density contrast by adopting the following density profile as a boundary condition at the injection radius \mathcal{R}

$$\rho(\theta) = \rho_0(1 - \delta \cos^2 \theta), \quad (57)$$

where ρ_0 is the value of the density at the equator of the injection sphere, i.e., $\rho_0 = \rho(\pi/2)$, and δ is the same density contrast between the equator and the poles as defined in Equation (38).

The specific functional form of the boundary condition in Equation (57) was chosen as a convenient first-order

parameterization of a bipolar deviation from spherical symmetry. This profile is qualitatively similar to the one of the analytic model presented above (see bottom panel of Figure 4). We have explored with other similar boundary profiles and obtained consistent results.

For the simulations reported in this work, we have taken $\rho_0 = 10^{-10}$, although we have found that taking any other value of ρ_0 results in the same flow structure but with the density re-scaled by this new factor. In other words, the value of ρ_0 can be set arbitrarily, thus defining a unit scale for the density and related thermodynamical quantities, provided the fluid considered remains a negligible perturbation on the background metric. On the other hand, the resulting steady-state solution depends strongly on the value of the sound speed a_0 imposed at the equator of the injection sphere. Note, in particular, that, from Equation (56) and for a fixed adiabatic index γ , a_0 is limited as

$$0 < a_0 < \sqrt{\gamma - 1}. \quad (58)$$

Once we have adopted a given γ , setup values for ρ_0 and a_0 at the equator of the injection sphere, and a density contrast δ , we use the equation of state in Equation (53) to find the corresponding pressure profile at the injection boundary as

$$P(\theta) = \frac{1}{\gamma} \left[\frac{a_0^2}{1 - a_0^2/(\gamma - 1)} \right] \frac{\rho(\theta)^\gamma}{\rho_0^{\gamma-1}}. \quad (59)$$

Since we do not know the structure of the accretion flow beforehand (on which no a priori restrictions are imposed), we cannot prescribe specific values for the velocity components at the injection radius. For this reason, we adopt free-boundary conditions for the radial and polar components of the velocity field and let the simulation evolve starting off from an initial state at rest (zero initial velocities), until an equilibrium state is reached throughout the numerical domain. Note that this means that we cannot use the same parameterization that we had adopted for the analytic model of Section 2 (i.e., \mathcal{R}/M , ρ_0 , P_0 , and V_0), but instead, now we shall replace V_0 by the density contrast δ .

3.2.1. Dependence on the Density Contrast δ

Based on the analytic results of Section 2, we expect ejection rates and velocities to strongly correlate with the density

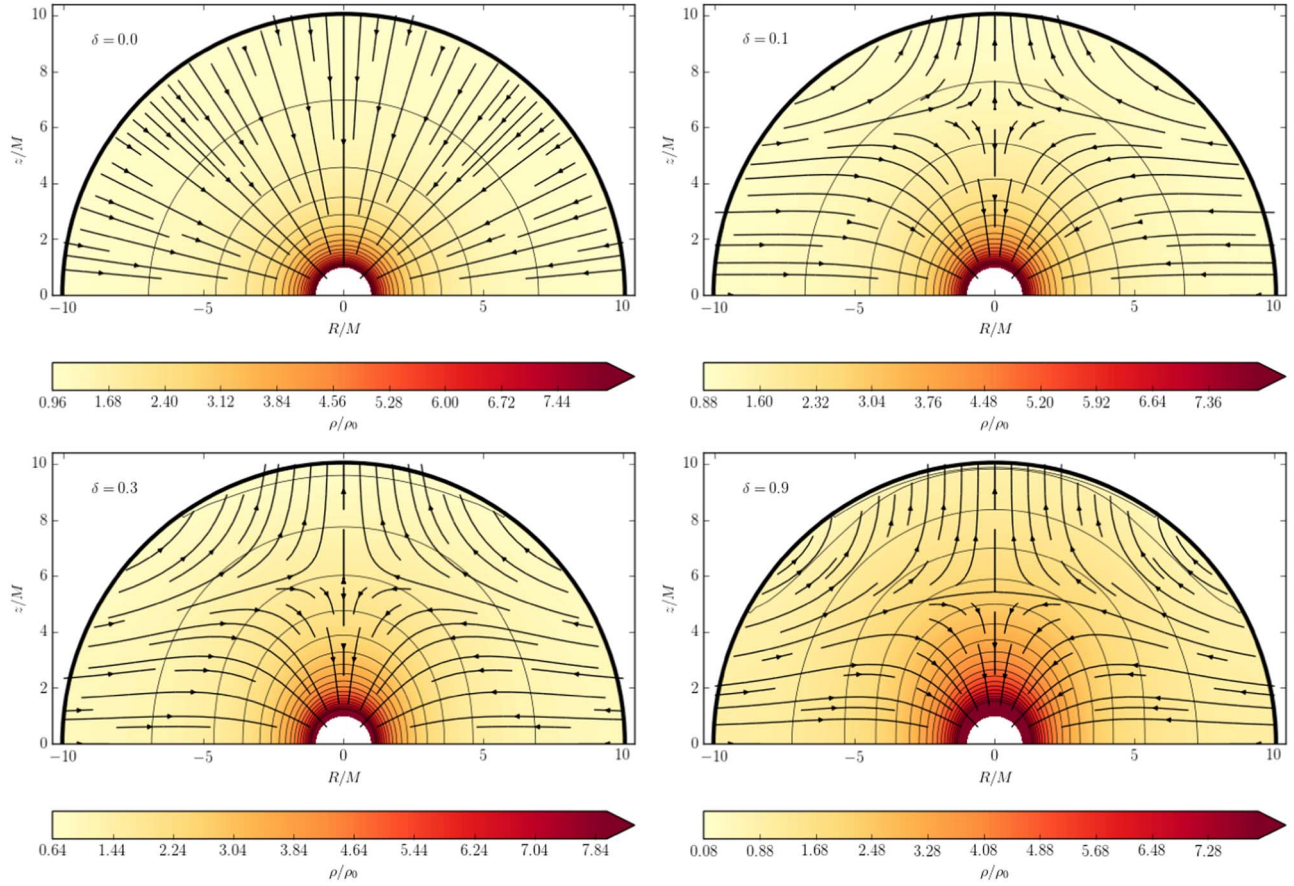


Figure 8. Resulting steady-state-flow configuration for the numerical simulations for a polytropic fluid with $\gamma = 4/3$ accreting onto a Schwarzschild black hole. The value of the density contrast δ used in each case is indicated on the top-left corner of each panel and increases gradually from $\delta = 0$ in the first panel (isotropic case where the Michel solution is recovered) to the highly anisotropic $\delta = 0.9$ case in the fourth panel.

contrast at the injection surface. Here, we study the role of the density contrast as parameterized by δ in Equation (57). In Figure 8, we show the steady-state results for four numerical simulations with $\gamma = 4/3$, $a_0 = 0.5$, $\mathcal{R} = 10M$, and density contrasts $\delta = 0, 0.1, 0.3$, and 0.9 . The results of these four simulations, also including the $\delta = 0.5$ case, are reported in Table 1. We can see that, as soon as the equatorial region becomes over-dense with respect to the polar regions, i.e., $\delta > 0$, a strong qualitative change ensues with an inflow-outflow configuration appearing across the numerical domain. The resulting streamlines closely resemble the flow morphology of the analytic model presented in the previous section.¹⁰

We can also see that as the density contrast increases, both \dot{M} and \dot{M}_{in} increase. Note however, that \dot{M}_{in} increases faster than \dot{M} , with the net result that the ratio between ejection and injection also increases with increasing δ .

As a further positive test of our numerical scheme, when $\delta = 0$, the simulation recovers the analytic solution of spherically symmetric accretion discussed by Michel (1972).

¹⁰ We note that since the posting of the initial version of this paper, a couple of relevant independent results have appeared: Waters et al. (2020) present a numerical scheme using the ATHENA++ code simulating accretion onto a black hole, modeled using a pseudo-Newtonian potential, which yields very similar results to what we obtain, for the same angular accretion density profile that we present. Zahra Zeraatgari et al. (2020) explore a similar scenario through an approximate semi-analytic approach, including the additional physical ingredients of rotation, viscosity, and radiation pressure, to again obtain flow patterns highly resembling our results, provided an equatorial-to-polar-accretion-density profile is present.

Table 1
Dependence on the Density Contrast δ

δ	\dot{M}	\dot{M}_{in}	\dot{M}_{ej}	$\frac{\dot{M}_{\text{ej}}}{\dot{M}_{\text{in}}}$	$\frac{\dot{M}}{\dot{M}_{\text{M}}}$	\mathcal{S}	V_{ej}
0.0	9.08	9.08	0.0	0.0	1.0
0.1	9.55	11.16	1.61	0.14	1.05	6.63	0.25
0.3	10.35	14.10	3.75	0.27	1.14	5.91	0.43
0.5	11.14	16.24	5.10	0.31	1.23	5.64	0.46
0.9	12.81	19.77	6.96	0.35	1.41	5.46	0.47

Note. The simulation parameters are fixed as $\mathcal{R} = 10M$, $\gamma = 4/3$, and $a_0 = 0.5$. All of the accretion rates are expressed in units of $\dot{M}_0 = M^2\rho_0$, and the stagnation point in units of M . The velocity V_{ej} is defined as the magnitude of the three-velocity at the poles of the injection sphere. According to Equation (A15), the Michel mass-accretion rate in this case is given by $\dot{M}_{\text{M}} = 9.08\dot{M}_0$.

The sixth column in Table 1 reports the ratio $\dot{M}/\dot{M}_{\text{M}}$, i.e., the numerically found mass-accretion rate in units of the mass-accretion rate of Michel’s solution \dot{M}_{M} (an analytic expression for \dot{M}_{M} is derived in Appendix A). Note that, as also occurs in the analytic model discussed in the previous section, this ratio does not remain strictly equal to one as δ increases; although, the mass-accretion rate remains of the order of \dot{M}_{M} .

This first exploration confirms that the basic principle behind the choked accretion model presented in Section 2 also works for fluids described by more general equations of state, where the resulting flow pattern is no longer assumed to be a potential flow.

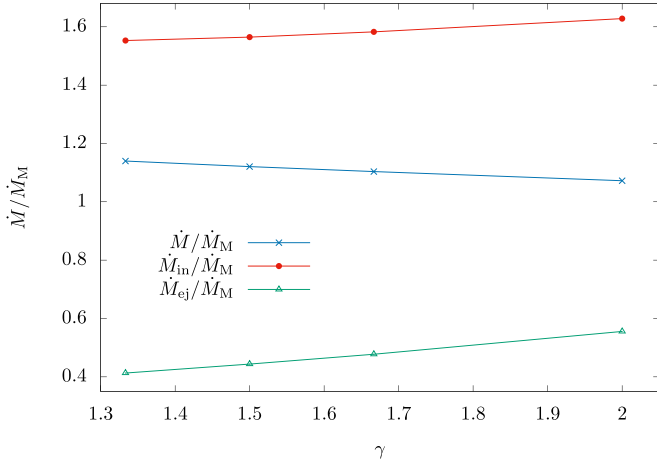


Figure 9. Dependence of the different mass flux rates (in units of the corresponding Michel value \dot{M}_M) on the polytropic index γ .

3.2.2. Dependence on the Adiabatic Index γ

Here, we examine the behavior of the steady-state, numerical solution as a function of the adiabatic index γ . We keep as fixed parameters $\mathcal{R} = 10M$, $\delta = 0.3$, and $a_0 = 0.5$ while considering four different values of $\gamma = 4/3, 3/2, 5/3$, and 2. In Table 2, we summarize the results of these simulations, while in Figure 9, we plot the ratios \dot{M}/\dot{M}_M , \dot{M}_{in}/\dot{M}_M , and \dot{M}_{ej}/\dot{M}_M as functions of γ . The resulting density field and fluid streamlines for these four simulations are qualitatively similar to those shown in the bottom left panel of Figure 8.

From these results, we see a weak dependence on the adiabatic index γ . As we consider increasing values of γ , the values of \dot{M} , \dot{M}_{in} , \mathcal{S} , and V_{ej} slightly decrease while both \dot{M}_{ej} and the ratio $\dot{M}_{ej}/\dot{M}_{in}$ increase.

3.2.3. Dependence on the Sound Speed a_0

Now, we turn our attention to the role played by the sound speed as defined at the equator of the injection sphere, a_0 . We will also consider a larger injection radius than in the previous sections in order to probe a different regime with smaller density contrasts and larger mass-injection rates. Specifically, we take $\mathcal{R} = 100M$, $\gamma = 5/3$, four density contrasts: $\delta = 0.1\%$, 0.5% , 1.0% , and 5.0% , and four different values for the sound speed: $a_0 = 0.2, 0.4, 0.6$, and 0.8 . Note that, from Equation (58) for $\gamma = 5/3$, the maximum possible value for this parameter is $a_0 = 0.816$.

In Tables 3–6, we present a summary of the results obtained in this case. In Figure 10, we show the dependence of the ratio \dot{M}_{in}/\dot{M}_M on a_0 for the four values of the density contrast δ . Figure 11 shows the dependence of the location of the stagnation point \mathcal{S} on a_0 , while Figure 12 shows the dependence of the maximum velocity of the ejected material V_{ej} on a_0 .

It is interesting to notice from Figure 11 that, at least for the parameter space explored for this figure, \mathcal{S} follows a dependence on a_0 similar to the one followed by the critical radius r_c as defined in Appendix A for the accretion flow in the spherically symmetric case.

In Figure 13, we show the resulting steady-state-flow configurations for the four values of a_0 in Tables 3–6 and $\delta = 0.5\%$. The corresponding configurations for the other

Table 2
Dependence on the Adiabatic Index γ

γ	\dot{M}	\dot{M}_{in}	\dot{M}_{ej}	$\frac{\dot{M}_{ej}}{\dot{M}_{in}}$	$\frac{\dot{M}}{\dot{M}_M}$	\mathcal{S}	V_{ej}
4/3	10.35	14.10	3.75	0.27	1.14	5.91	0.43
3/2	9.75	13.61	3.86	0.28	1.12	5.82	0.42
5/3	9.15	13.12	3.96	0.30	1.10	5.73	0.41
2	8.01	12.16	4.15	0.34	1.07	5.55	0.40

Note. The simulation parameters are $\mathcal{R} = 10M$, $a_0 = 0.5$, and $\delta = 0.3$. From top to bottom, the values of \dot{M}_M/\dot{M}_0 are 9.08, 8.70, 8.28, and 7.47.

Table 3
Dependence on the Density Contrast δ for $a_0 = 0.2$

δ (%)	\dot{M}	\dot{M}_{in}	\dot{M}_{ej}	$\frac{\dot{M}_{ej}}{\dot{M}_{in}}$	$\frac{\dot{M}}{\dot{M}_M}$	\mathcal{S}	V_{ej}
0.1	63.12	70.50	7.37	0.10	0.98	66.28	0.014
0.5	63.93	89.90	25.97	0.29	0.99	56.78	0.025
1.0	64.13	97.61	33.49	0.34	1.00	51.08	0.031
5.0	64.78	159.93	95.15	0.59	1.01	39.68	0.071

Note. The sound speed a_0 is given at the equator of the injection sphere. The simulation parameters are $\mathcal{R} = 100M$ and $\gamma = 5/3$. In this case, $\dot{M}_M = 64.39\dot{M}_0$.

Table 4
Dependence on the Density Contrast δ for $a_0 = 0.4$

δ (%)	\dot{M}	\dot{M}_{in}	\dot{M}_{ej}	$\frac{\dot{M}_{ej}}{\dot{M}_{in}}$	$\frac{\dot{M}}{\dot{M}_M}$	\mathcal{S}	V_{ej}
0.1	17.49	43.25	25.76	0.60	1.10	42.53	0.019
0.5	17.14	79.47	62.33	0.78	1.08	33.03	0.043
1.0	16.49	106.08	89.60	0.84	1.04	29.23	0.061
5.0	17.74	222.67	204.93	0.92	1.11	22.58	0.136

Note. The sound speed a_0 is given at the equator of the injection sphere. The simulation parameters are $\mathcal{R} = 100M$ and $\gamma = 5/3$. In this case, $\dot{M}_M = 15.93\dot{M}_0$.

Table 5
Dependence on the Density Contrast δ for $a_0 = 0.6$

δ (%)	\dot{M}	\dot{M}_{in}	\dot{M}_{ej}	$\frac{\dot{M}_{ej}}{\dot{M}_{in}}$	$\frac{\dot{M}}{\dot{M}_M}$	\mathcal{S}	V_{ej}
0.1	10.82	52.63	41.81	0.79	1.32	33.03	0.029
0.5	11.35	108.20	96.85	0.90	1.39	25.43	0.064
1.0	10.37	147.74	137.37	0.93	1.27	22.58	0.091
5.0	10.76	318.85	308.09	0.97	1.32	17.83	0.202

Note. The sound speed a_0 is given at the equator of the injection sphere. The simulation parameters are $\mathcal{R} = 100M$ and $\gamma = 5/3$. In this case, $\dot{M}_M = 8.17\dot{M}_0$.

values of δ are qualitatively similar to the ones presented in this figure.

From these results, we see that the final steady-state configuration depends strongly on the value of the sound speed a_0 . In general, we see that as a_0 increases, the stagnation point \mathcal{S} sinks deeper into the accretion flow, as more material is expelled from the system along the bipolar outflow at increasingly larger speeds V_{ej} . Moreover, we also see that as the influx asymmetry increases, even for a small 5% density contrast, the ejection velocities become larger, reaching values of $V_{ej} > 0.25$ for the sound speed values probed.

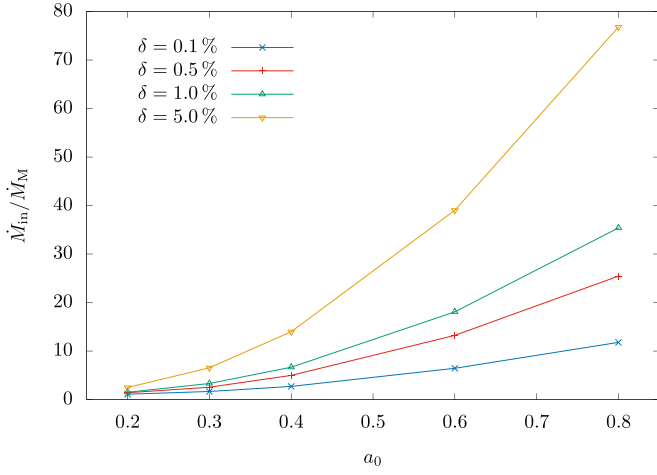


Figure 10. Dependence of the ratio \dot{M}_{in}/\dot{M}_M on the sound speed a_0 as given at the equator of the injection sphere. Clearly, this ratio is a monotonically increasing function of a_0 with a steeper growth with increasing δ .

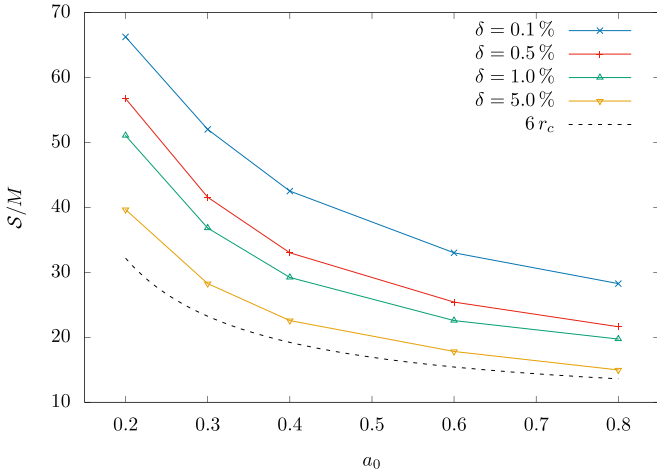


Figure 11. Dependence of the location of the stagnation point \mathcal{S} on a_0 . Here, we see that \mathcal{S} is inversely proportional to both a_0 and δ . Note that \mathcal{S} shows a dependence on a_0 that resembles the one followed by the critical radius r_c on this same parameter.

4. Discussion

4.1. Comparison between the Numerical Simulations and the Analytic Model

Even though the physics of the analytic model of Section 2 differs from the one included in the simulations of Section 3, it is illustrative to compare the results of these two sections. For this comparison, we will consider only the case of the $\gamma = 5/3$ polytrope and injection radius $\mathcal{R} = 100M$ presented in Tables 3–6, as this large injection radius allowed us to explore a broader range of mass-injection rates.

In Figure 14, we show the ratio of ejected over injected-mass rates $\dot{M}_{ej}/\dot{M}_{in}$ as a function of the mass-injection rate. From this figure, we find a very good agreement between the numerical data and the analytic model. This agreement is remarkable if we take into account that the latter is based on the assumption of an ultrarelativistic stiff fluid, $\gamma = 2$, while the former involves a more realistic $\gamma = 5/3$ polytrope. We have also found this same agreement for different polytropic indices in the nonrelativistic regime, as can be seen in Figure 7 of Aguayo-Ortiz et al. (2019).

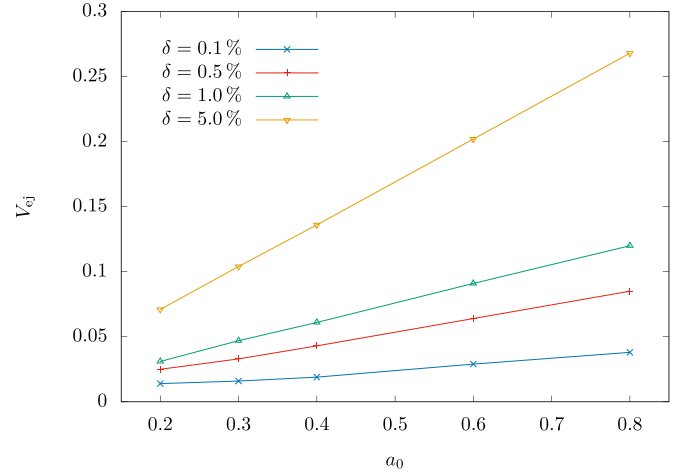


Figure 12. Dependence of the maximum velocity of the ejected material V_{ej} on a_0 . Here, we see that V_{ej} grows more or less linearly with a_0 .

Table 6
Dependence on the Density Contrast δ for $a_0 = 0.8$

δ (%)	\dot{M}	\dot{M}_{in}	\dot{M}_{ej}	$\frac{\dot{M}_{ej}}{\dot{M}_{in}}$	$\frac{\dot{M}}{\dot{M}_M}$	\mathcal{S}	V_{ej}
0.1	7.77	64.80	57.04	0.88	1.41	28.28	0.038
0.5	9.20	139.98	130.78	0.93	1.67	21.63	0.085
1.0	9.20	194.61	185.40	0.95	1.67	19.73	0.120
5.0	8.14	422.31	414.17	0.98	1.48	14.98	0.268

Note. The sound speed a_0 is given at the equator of the injection sphere. The simulation parameters are $\mathcal{R} = 100M$ and $\gamma = 5/3$. In this case, $\dot{M}_M = 5.50\dot{M}_0$.

In Figure 15, we show the location of the stagnation point \mathcal{S} as a function of the injection-mass rate \dot{M}_{in}/\dot{M}_M . Note that as \dot{M}_{in} increases, \mathcal{S} descends toward the central accretor, just as occurred for the analytic model (see Figure 5). We find, again, a good agreement between the numerical data and the analytic model.

In Figure 16, we show the maximum velocity attained by the ejected material V_{ej} as a function of the injection-mass rate \dot{M}_{in}/\dot{M}_M . We compare the numerical results against the analytic value for V_{ej} given in Equation (31). In contrast to what happens for the two parameters discussed above, here, we find a large difference among the numerical results for each value of the sound speed a_0 , as well as between these results and the analytic model. Note, however, that for each value of a_0 , the numerically obtained values of V_{ej} follow a linear dependence on \dot{M}_{in}/\dot{M}_M with a slope inversely proportional to a_0 . Also, as a_0 increases, the numerical data approaches the analytic model, for which $a = 1$ everywhere in the fluid.

4.2. Applicability in Astrophysics

We discuss now the viability of the choked accretion phenomenon presented here for operating as the inner engine behind a given jet-launching astrophysical system. Given that the characteristic length scale of this mechanism is given by \mathcal{S} , we can expect the physical size of the inner accretion disk (that we have associated with \mathcal{R}) to be larger than \mathcal{S} . In general, for an accretion disk around a black hole, we will have $\mathcal{R} = 1 - 10M$ (the actual value will be a function of both the disk model and the black-hole spin). On the other hand,

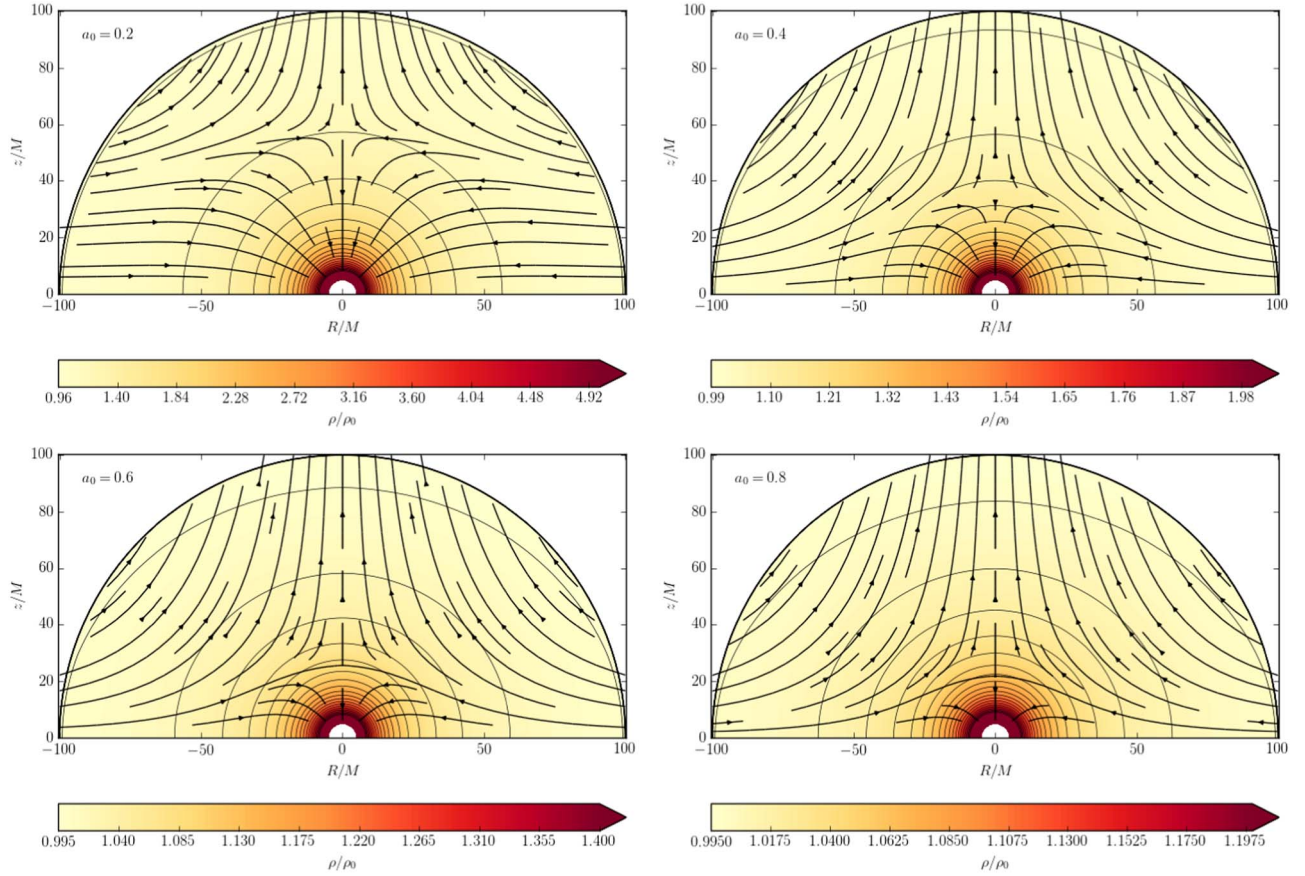


Figure 13. Resulting steady-state configurations for a polytropic fluid with $\gamma = 5/3$ and $\delta = 0.5\%$. The value of the sound speed a_0 used in each case is indicated on the top-left corner of each panel.

from all of the simulations presented in this work, as well as those in Aguayo-Ortiz et al. (2019) for the nonrelativistic case, we see that a robust lower limit for \mathcal{S} is given by the corresponding Bondi radius $r_B = M/a_\infty^2$. Moreover, provided that $\mathcal{R} > r_B$, we have $a_0 \simeq a_\infty$, and then we can write

$$\mathcal{S} > M/a_0^2. \quad (60)$$

At this point, it is useful to recall that, assuming an ideal gas, we can relate the sound speed a and the fluid temperature T by

$$\frac{T}{T_i} = \left(\frac{\gamma - 1}{\gamma} \right) \left(\frac{a^2}{\gamma - 1 - a^2} \right), \quad (61)$$

where $T_i = m_i/k_B$ is the temperature corresponding to the rest-mass energy of the average gas particle of mass m_i . For a gas composed of ionized hydrogen, we have $T_H = 1.08 \times 10^{13}$ K, while for an electron–positron plasma $T_e = 5.93 \times 10^9$ K.

Then, from Equations (60) and (61), we have

$$\frac{\mathcal{S}}{M} > \frac{1}{\gamma} \frac{T_i}{T} + \frac{1}{\gamma - 1}. \quad (62)$$

A regular plasma dominated by radiation pressure and consisting of protons and electrons can be modeled, in a first approximation, as a $\gamma = 4/3$ polytrope with an average particle mass $m_i \simeq m_H$ and, thus, $T_i \simeq T_H$. As discussed in Aguayo-Ortiz et al. (2019), taking $T = 10^7$ K as the temperature at the inner edge of the disk in an X-ray binary (Kaaret et al. 2017), from Equation (62), we have $\mathcal{S} > 10^5 M$. In the case of an AGN, instead of taking the gas in the inner disk (at a temperature of

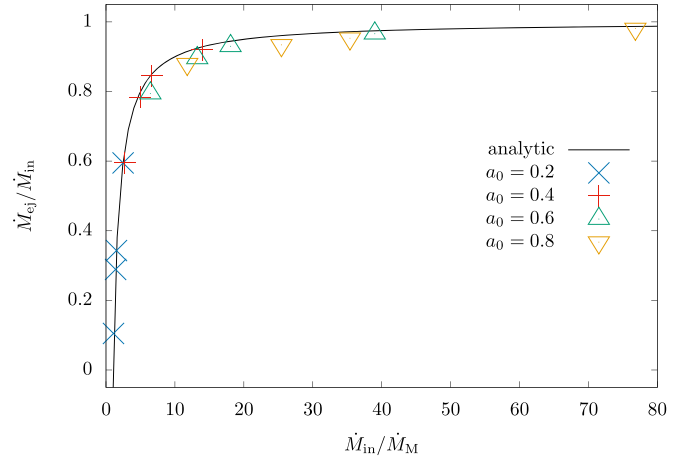


Figure 14. Ratio of ejected- to injected-mass rates $\dot{M}_{ej}/\dot{M}_{in}$ as a function of the injection-mass rate in units of the Michel value \dot{M}_M . The injection radius is $\mathcal{R} = 100M$. The different symbols correspond to the numerical results reported in Tables 3–6 for $\gamma = 5/3$ and sound speeds as labeled. The solid line corresponds to the analytic model of an ultrarelativistic $\gamma = 2$ stiff fluid presented in Section 2 (see Equation (52)).

around $T = 10^5$ K), we can consider the ionized plasma in the hot corona above the disk with a temperature of up to $T = 10^9$ K (Czerny et al. 2003). Nevertheless, even for this large temperature, from Equation (62), we obtain $\mathcal{S} > 10^3 M$. Even in the case of the accretion disk associated with a long GRB, where the gas temperature can reach up to 10^{11} K (Woosley 1993), from

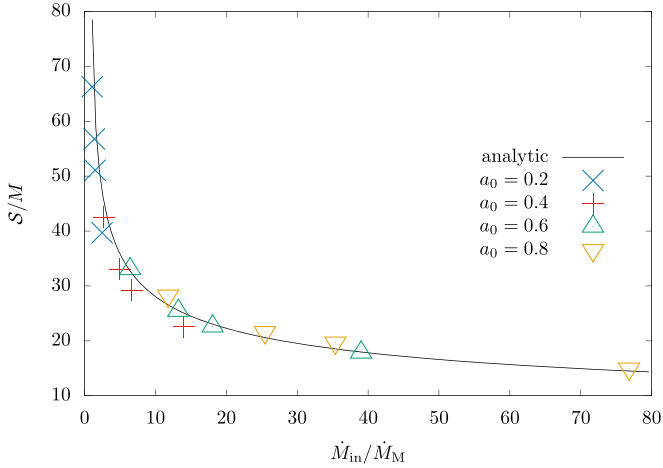


Figure 15. Location of the stagnation point \mathcal{S} as a function of the injection-mass rate. The injection radius is $\mathcal{R} = 100M$. The different symbols correspond to the numerical results reported in Tables 3–6 for $\gamma = 5/3$ and sound speeds as labeled. The solid line corresponds to the analytic model of an ultrarelativistic $\gamma = 2$ stiff fluid presented in Section 2.

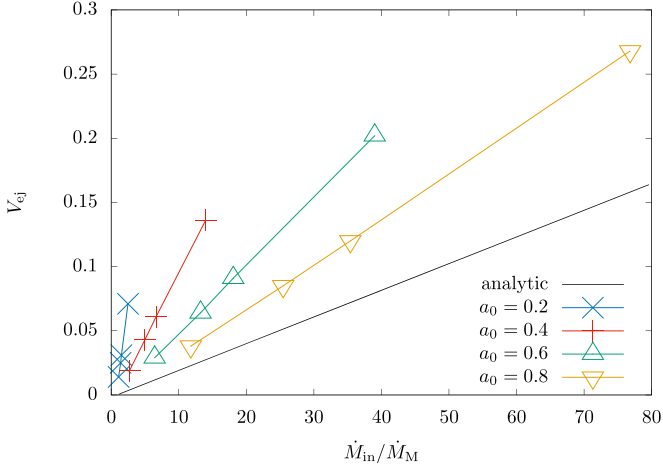


Figure 16. Maximum velocity attained by the ejected material V_{ej} as a function of the injection-mass rate. The injection radius is $\mathcal{R} = 100M$. The different symbols correspond to the numerical results reported in Tables 3–6 for $\gamma = 5/3$ and sound speeds as labeled. The solid line corresponds to the analytic model of an ultrarelativistic $\gamma = 2$ stiff fluid presented in Section 2.

Equation (62), we have $\mathcal{S} > 80M$, which is still a factor of 10 larger than the expected size of the inner engine.

The above analysis implies that, for the choked accretion mechanism to work for a regular plasma, the temperature of the infalling gas is required to be substantially higher than that of the inferred values at the inner edge of the disk (or disk corona). These higher temperatures could result from highly localized heating processes such as magnetic reconnection, shock heating, or viscous friction at the point of transition between the disk and the radial-infall domains.

On the other hand, the extreme conditions at the innermost parts of these systems give rise to a different kind of plasma composed of relativistic electron–positron pairs (Wardle et al. 1998; Beloborodov 1999; Siegert et al. 2016). Considering that at least a fraction of this plasma has a thermal component, the pair production mechanism implies temperatures in excess of 10^{11} K. If we consider this gas as the accreted material, then for this temperature and substituting $T_i = T_e$ in Equation (62), we

get $\mathcal{S} > M$. We obtain then that, under these circumstances, the choked accretion mechanism might become relevant for the ejection of this pair plasma.

Contrary to the analytic model presented in Section 2, we do not have direct control on the mass-injection rate crossing the outer boundary of our numerical simulations, as it is indirectly determined by the values of \mathcal{R} , a_0 , and δ . Nevertheless, it is clear that in an astrophysical scenario, this mass rate will be imposed by external, possibly time-varying conditions. For example, in the context of low-mass X-ray binaries, stellar oscillations or orbital variations can modulate the total mass transfer across the Roche lobe from the regular star to the compact companion (Tauris & van den Heuvel 2006). More dramatic time-varying conditions will be found for jets launched during a common-envelope phase as studied by López-Cámara et al. (2019), or for long GRBs as studied by, e.g., López-Cámara et al. (2010) and Taylor et al. (2011).

The strong dependence that we have found between the ratio of ejected-to-injected material and the incoming mass-accretion rate, leads us to suggest that the choked accretion mechanism could offer a compelling, simple connection between the external mass flux feeding an accretion disk and the jet activity. Whenever the mass-injection rate surpasses the threshold value \dot{M}_M , the excess flux is prone to being ejected from the system as a bipolar outflow. This could be of relevance for studying the time variability of the jet emission.

Once a tight connection appears between accretion rates and geometry on the one hand, and ejection rates and velocities on the other, we have the potential to correlate the time variability in the mass flux across the accretion disk to the resulting ejection rates and velocities. This, in turn, naturally leads to the appearance of internal shocks in the ensuing jets, such as those typically assumed to be associated with the GRB phenomenology.

As already implied by the above discussion, a proper exploration of the role played by choked accretion in launching relativistic jets, demands accounting for additional physics, such as the effect of rotation, magnetic fields, and radiative transport. Indeed, these factors are considered as crucial for the acceleration and collimation of the resulting jets (Semenov et al. 2004; McKinney 2006). Moreover, as discussed in Aguayo-Ortiz et al. (2019), some of these ingredients might actually improve the applicability of choked accretion by increasing both the effective temperature and the polar-density contrast, thus, bringing \mathcal{S} closer to the central accretor. It should also be interesting to study the possible interplay of choked accretion with the well-established Blandford & Znajek (1977) mechanism. We intend to address these points in future work.

5. Summary

We have presented the choked accretion phenomenon as a purely hydrodynamical outflow-generating mechanism. Choked accretion operates under two basic premises: a sufficiently large mass flux accreting onto a central object, and an anisotropic density field in which an equatorial belt has a higher density than the polar regions. These two ingredients are plausibly met in several jet-launching astrophysical scenarios involving accretion disks around massive objects. We suggest that choked accretion constitutes a relevant ingredient for studying some of these systems.

Moreover, we have shown that breaking spherical symmetry by imposing a polar-density gradient in the accretion flow onto

a central object qualitatively changes the resulting steady-state configurations from the purely radial accretion models (Bondi 1952; Michel 1972) to the infall-outflow morphology that characterizes the choked accretion model. Thus, choked accretion provides a natural transition between spherical accretion and systems characterized by bipolar outflows.

We have studied this phenomenon by introducing first a general relativistic analytic model of choked accretion onto a Schwarzschild black hole. This model is based on the approximations of steady-state, axisymmetry, and irrotational flow and assumes an ultrarelativistic stiff fluid. We then relaxed this last assumption, together with the associated potential flow condition, and studied more general fluids by means of full-hydrodynamic simulations performed with the numerical code *aztekas*.

Both for an ultrarelativistic stiff fluid as for a regular polytrope, the limiting value for the total mass-accretion rate corresponds quite closely to the one found in the spherically symmetric case (Michel 1972). We have thus found that, within the assumptions underlying this work, hydrodynamical accretion flows onto massive objects choke at this threshold value and any extra infalling material is deflected into a bipolar outflow.

The analytic solution presented here allowed us to study in detail the basic physical principle behind the choked accretion phenomenon. Moreover, we have also demonstrated the usefulness of this exact analytic solution as a benchmark test for validating numerical hydrodynamic codes in general. The nonrelativistic limit of this analytic solution is presented in Aguayo-Ortiz et al. (2019).

Considering together: (i) the perturbative Newtonian solutions for isothermal fluids of Hernandez et al. (2014); (ii) the exact Newtonian solution for incompressible fluids and the numerical Newtonian experiments for polytropic equations of state in Aguayo-Ortiz et al. (2019); and (iii) the present exact analytic relativistic model for a stiff fluid and the numerical experiments presented for polytropic fluids; we can conclude that the inflow-outflow steady-state configurations presented here are an extremely general and robust consequence of breaking spherical symmetry with a polar-density gradient in an accretion flow onto a central object. Similarly, we see that the choked accretion character of these configurations extends across the Newtonian and relativistic regimes.

We thank Olivier Sarbach and John Miller for insightful discussions and critical comments on the manuscript. We also thank Fabio de Colle and Diego López-Cámara for useful comments and suggestions. This work was supported by DGAPA-UNAM (IN112616 and IN112019) and CONACyT (CB-2014-01 No. 240512; No. 290941; No. 291113) grants. A. A.O. and E.T. acknowledge economic support from CONACyT (788898, 673583). X.H. acknowledges support from DGAPA-UNAM PAPIIT IN104517 and CONACyT.

Appendix A

Relativistic, Spherically Symmetric Accretion Flow

In this Appendix Section, we give a brief overview of Michel's (1972) analytic model of a spherically symmetric accretion flow onto a Schwarzschild black hole. In particular, we derive an analytic expression for the resulting mass-accretion rate in a form that is useful for the present work (see Beskin & Pidoprygora 1995, for an alternative derivation).

Here, we will consider only the case of a perfect fluid described by a polytropic equation of state as in Equation (53). See Chaverra & Sarbach (2015) for a recent extension of Michel's (1972) model to a general class of static, spherically symmetric background metrics, as well as for more general equations of state.

Under the assumptions of stationary state and spherical symmetry, the equations governing the accretion flow are the continuity equation and the radial component of the relativistic Euler equation (Equations (4) and 5, respectively), i.e.,

$$\frac{d}{dr}(r^2 \rho U^r) = 0, \quad (\text{A1})$$

$$\frac{d}{dr}(r^2 T_t^r) = 0, \quad (\text{A2})$$

where $v = U^r = dr/d\tau$ and $T_t^r = \rho h U_t U^r$. Direct integration of these two equations gives

$$4\pi r^2 \rho v = \dot{M}_M = 4\pi \lambda = \text{const.}, \quad (\text{A3})$$

$$\rho h U_t v r^2 = \mu = \text{const.} \quad (\text{A4})$$

We can simplify Equation (A4) by dividing it by Equation (A3) and taking its square; the result is

$$h^2 \left(1 - \frac{2M}{r} + v^2\right) = \left(\frac{\mu}{\lambda}\right)^2 = h_\infty^2. \quad (\text{A5})$$

Following Michel (1972), we can combine Equations (A1) and (A2) into the following differential equation

$$\left[1 - \frac{a^2}{v^2} \left(1 - \frac{2M}{r} + v^2\right)\right] v \frac{dv}{dr} = -\frac{M}{r^2} + 2 \frac{a^2}{r} \left(1 - \frac{2M}{r} + v^2\right). \quad (\text{A6})$$

From Equation (A6), we obtain that the condition of having a critical point, i.e., a radius $r = r_c$ at which both sides of this equation vanish simultaneously, translates into

$$v_c^2 = \frac{1}{2} \frac{M}{r_c}, \quad (\text{A7})$$

and

$$a_c^2 = \frac{v_c^2}{1 - 3v_c^2}. \quad (\text{A8})$$

Substituting Equations (A7) and (A8) into Equation (A5) results in

$$n h_c^3 - h_\infty^2 [(n+3)h_c - 3] = 0, \quad (\text{A9})$$

where $n = 1/(\gamma - 1)$. This polynomial has three real roots for h_c , but only one satisfies $h_c > 1$ and, thus, has physical meaning. This root is given by

$$h_c = 2 h_\infty \sqrt{\frac{n+3}{3n}} \sin\left(\Psi + \frac{\pi}{6}\right), \quad (\text{A10})$$

where

$$\cos(3\Psi) = \frac{3}{2n h_\infty} \left(\frac{n+3}{3n}\right)^{-3/2}. \quad (\text{A11})$$

We can now find an expression for the accretion rate in terms of M , the equation of state of the fluid, and its asymptotic

conditions (expressed in terms of ρ_∞ and h_∞). Let us start by substituting Equation (A7) into the continuity Equation (A3), which results in

$$\lambda = r_c^2 \rho_c v_c = \frac{1}{4} M^2 \rho_c v_c^{-3}. \quad (\text{A12})$$

Now, using Equations (53) and (55), we can rewrite the equation of state as

$$\rho_c = \rho_\infty \left(\frac{h_c - 1}{h_\infty - 1} \right)^n, \quad (\text{A13})$$

on the other hand, by combining Equations (56), (A8), and (A10) we obtain

$$v_c^2 = \frac{h_c - 1}{(n + 3)h_c - 3} = \frac{h_\infty^2 (h_c - 1)}{n h_c^3}. \quad (\text{A14})$$

Then, substituting Equations (A13) and (A14) into Equation (A12), we obtain

$$\dot{M}_M = 4\pi \lambda = \pi \left[\frac{n^3 h_c^9 (h_c - 1)^{2n-3}}{h_\infty^6 (h_\infty - 1)^{2n}} \right]^{1/2} M^2 \rho_\infty. \quad (\text{A15})$$

Note that \dot{M}_M as expressed in Equation (A15) is given in terms of thermodynamical quantities measured asymptotically far away from the central object (ρ_∞ and either a_∞ or h_∞). In order to compare the results presented in Section 2 with Michel's solution, one needs first to find the asymptotic values ρ_∞ and a_∞ resulting in a solution such that $\rho|_{\mathcal{R}} = \rho_0$ and $a|_{\mathcal{R}} = a_0$.

Appendix B Validation of the Numerical Code

In this Appendix Section, we present a series of standard tests in order to validate the results using *aztekas*. This section is complementary to the test already presented in Section 3.1 as well as the Appendix presented in Tejeda & Aguayo-Ortiz (2019), where the code is tested using the relativistic spherical accretion problem (Michel 1972).

B.1. One-dimensional Shock Tube Tests

The one-dimensional shock tube test (Sod 1978) is a standard problem to solve for code validation, as it is easy to implement, and the exact solution can be computed. It consists of a perfect fluid at two different initial states with parameters (ρ_L, P_L, v_L) and (ρ_R, P_R, v_R) (where subscripts *L* and *R* refer to the left and right sides, respectively) separated by an interface at $x = x_0$. At $t = 0$, the interface is removed, and the two states are left to interact with each other. The evolution of this configuration depends only on the initial values and on the equation of state. Here, we present a set of four one-dimensional shock tube tests, along with a two-dimensional version of the problem. For the former case, we compare the results with the analytic solution.

We reproduce four of the shock tube tests presented by Lora-Clavijo et al. (2015). The tests were performed in a Cartesian 1D domain $x \in [0, 1]$ with a resolution $N = 800$ and a Courant number of 0.5. The initial conditions of each test are presented in Table B1. Test 1 and Test 2 correspond to a mild and strong relativistic blast-wave explosion, respectively. The initial conditions for Test 3 produce a highly relativistic symmetric head-on stream collision, with a Lorentz factor $\Gamma = 1000$.

Table B1

Initial Conditions for the Left (*L*) and Right (*R*) States of the Set of One-dimensional Shock Tube Tests

	Test 1	Test 2	Test 3	Test 4
ρ_L	10	1	1	1
P_L	13.33	1000	0.001	1
v_L	0	0	0.999999995	0.9
ρ_R	1	1	1	1
P_R	10^{-8}	0.001	0.001	10
v_R	0	0	-0.999999995	0
γ	5/3	5/3	4/3	4/3

Finally, Test 4 follows the evolution of a shock traveling at $v = 0.9$, as seen from the rest frame of the shock front.

In Figure B1, we show the evolution of all four tests at $t = 0.35$ and the comparison between the numerical simulations performed with *aztekas* and the analytic solution. The latter was computed using a code written by Martí & Müller (1999). In the first two tests, a contact discontinuity and a rarefaction wave are formed. In Test 1, where the Lorentz factor is $\Gamma \approx 1$, the analytic solution is well resolved. In Test 2, where the Lorentz factor is $\Gamma \approx 6$, we obtain an overall satisfactory result, although a higher resolution should lead to a better defined contact discontinuity. Test 3 shows the evolution of a strong head-on collision between two shock waves. A stationary high-density, high-pressure shell is formed, and we see, again, a good match with the analytic solution. Finally, in Test 4, we can see the formation of a stationary contact discontinuity. In this case, small oscillations are developed right behind the shock. These oscillations are damped with higher resolution. All of the results presented here agree with previous works that use similar schemes (e.g., Lucas-Serrano et al. 2004; De Colle et al. 2012; Lora-Clavijo et al. 2015).

B.2. Two-dimensional Riemann Problem

For this test, we follow closely the initial setup proposed by Del Zanna & Bucciantini (2002) for the two-dimensional Riemann problem, which is the relativistic extension of the case presented by Lax & Liu (1998). The problem consists of a square domain subdivided into four regions with different initial states

$$(\rho, P, v_x, v_y) = \begin{cases} (0.1, 0.01, 0, 0) & \text{if } x > 0.5, y > 0. \\ (0.1, 1, 0.99, 0) & \text{if } x \leq 0.5, y > 0. \\ (0.5, 1, 0, 0) & \text{if } x > 0.5, y \leq 0. \\ (0.1, 1, 0, 0.99) & \text{if } x \leq 0.5, y \leq 0. \end{cases} \quad (\text{B1})$$

The test was performed in a 2D Cartesian domain $(x, y) \in [0, 1] \times [0, 1]$ with a 400×400 resolution and a Courant number of 0.25. In Figure B2, we show the evolution of the solution shows a stationary high-density contact discontinuity along the diagonal of the domain and a jet-like structure propagating into the initially over-dense region. These results are qualitatively similar to the ones obtained by Del Zanna & Bucciantini (2002), De Colle et al. (2012), and Lora-Clavijo et al. (2015).

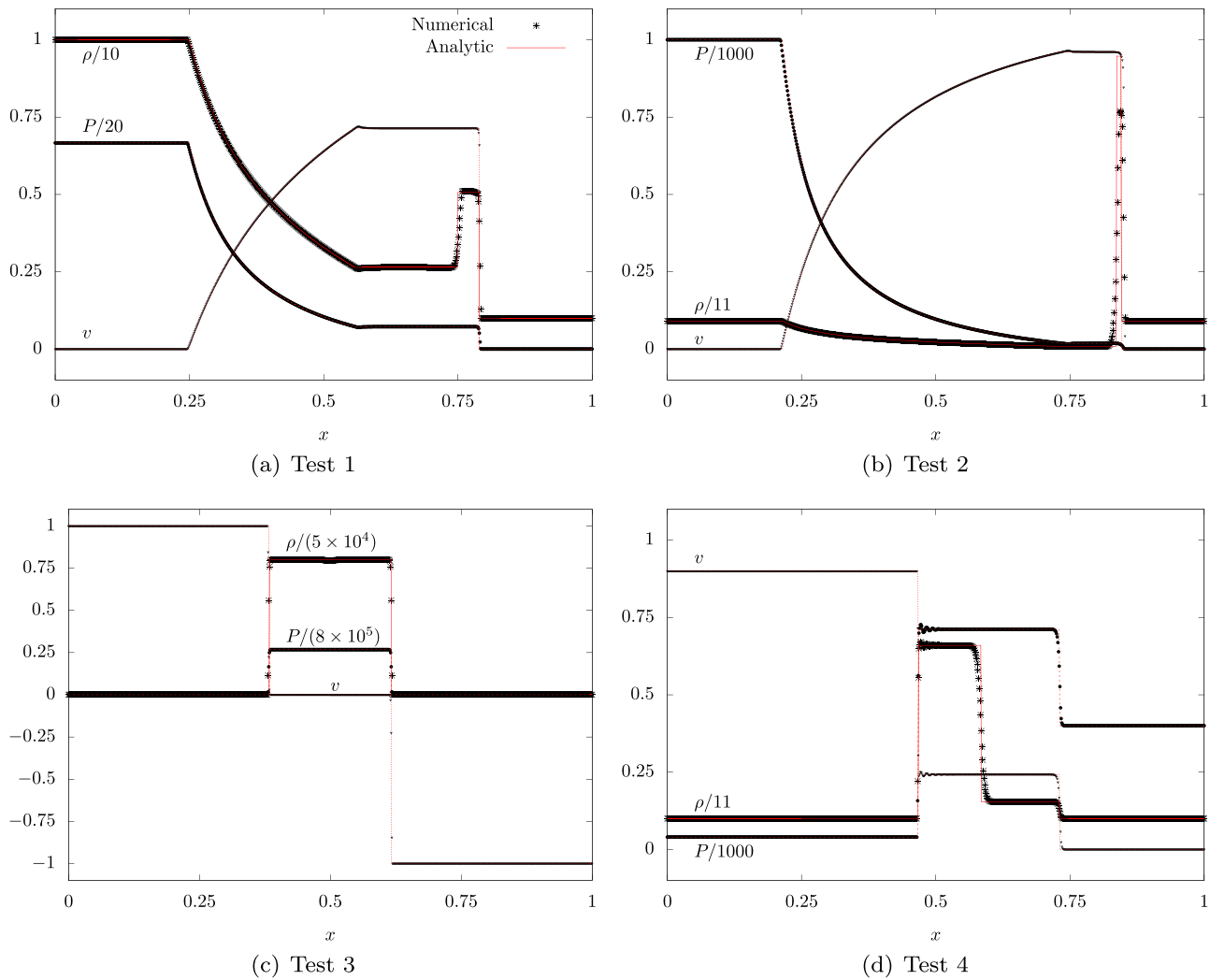


Figure B1. Evolution at a time $t = 0.35$ of the density ρ , pressure P , and velocity v for the four tests presented in Table B1. All tests were performed using a resolution $N = 800$ with a Courant factor of 0.5.

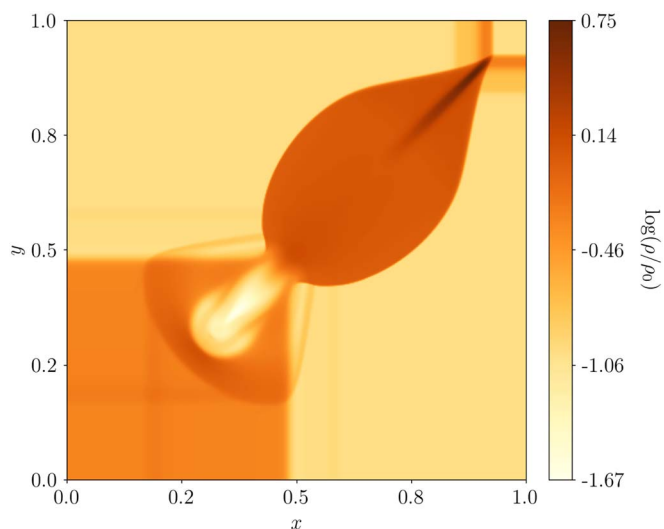


Figure B2. Logarithmic rest-mass density color map of the two-dimensional Riemann problem at a time $t = 0.4$. The simulation was performed using a 400×400 resolution and a Courant factor of 0.25.

ORCID iDs

Emilio Tejeda <https://orcid.org/0000-0001-9936-6165>

Alejandro Aguayo-Ortiz <https://orcid.org/0000-0001-5729-7958>

X. Hernandez <https://orcid.org/0000-0002-7778-6457>

References

- Abbott, B. P., Abbott, R., Abbott, T. D., et al. 2017, *PhRvL*, **119**, 161101
Aguayo-Ortiz, A., Mendoza, S., & Olvera, D. 2018, *PLoS*, **13**, e0195494
Aguayo-Ortiz, A., Tejeda, E., & Hernandez, X. 2019, *MNRAS*, **490**, 5078
Balbus, S. A., & Hawley, J. F. 1991, *ApJ*, **376**, 214
Banyuls, F., Font, J. A., Ibáñez, J. M., Martí, J. M., & Miralles, J. A. 1997, *ApJ*, **476**, 221
Beckmann, V., & Shrader, C. R. 2012, *Active Galactic Nuclei* (Weinheim: Wiley)
Beloborodov, A. M. 1999, *MNRAS*, **305**, 181
Beskin, V. S., & Pidoprygora, Y. N. 1995, *JETP*, **80**, 575
Blandford, R., Meier, D., & Readhead, A. 2019, *ARA&A*, **57**, 467
Blandford, R. D., & Payne, D. G. 1982, *MNRAS*, **199**, 883
Blandford, R. D., & Znajek, R. L. 1977, *MNRAS*, **179**, 433
Bondi, H. 1952, *MNRAS*, **112**, 195

- Burrows, D. N., Kennea, J. A., Ghisellini, G., et al. 2011, *Natur*, **476**, 421
- Chaverra, E., & Sarbach, O. 2015, *CQGra*, **32**, 155006
- Czerny, B., Nikolajuk, M., Rózańska, A., et al. 2003, *A&A*, **412**, 317
- De Colle, F., Granot, J., López-Cámara, D., & Ramirez-Ruiz, E. 2012, *ApJ*, **746**, 122
- Del Zanna, L., & Bucciantini, N. 2002, *A&A*, **390**, 1177
- Fendt, C. 2018, *CoSka*, **48**, 40
- Hartigan, P. 2009, *ASSP*, **13**, 317
- Hawley, J. F., Fendt, C., Hardcastle, M., Nokhrina, E., & Tchekhovskoy, A. 2015, *SSRv*, **191**, 441
- Hernandez, X., Rendón, P. L., Rodríguez-Mota, R. G., & Capella, A. 2014, *RMxAA*, **50**, 23
- Kaaret, P., Feng, H., & Roberts, T. P. 2017, *ARA&A*, **55**, 303
- Komissarov, S. S., Barkov, M. V., Vlahakis, N., & Königl, A. 2007, *MNRAS*, **380**, 51
- Lattimer, J. M., & Prakash, M. 2007, *PhR*, **442**, 109
- Lax, P. D., & Liu, X.-D. 1998, *SIAM Journal on Scientific Computing*, **19**, 319
- Liska, M., Tchekhovskoy, A., Ingram, A., & van der Klis, M. 2019, *MNRAS*, **487**, 550
- Lloyd-Ronning, N. M., Fryer, C., Miller, J. M., et al. 2019, *MNRAS*, **485**, 203
- López-Cámara, D., De Colle, F., & Moreno Méndez, E. 2019, *MNRAS*, **482**, 3646
- López-Cámara, D., Lee, W. H., & Ramirez-Ruiz, E. 2010, *ApJ*, **716**, 1308
- Lora-Clavijo, F. D., Cruz-Osorio, A., & Guzmán, F. S. 2015, *ApJS*, **218**, 24
- Lucas-Serrano, A., Font, J. A., Ibáñez, J. M., & Martí, J. M. 2004, *A&A*, **428**, 703
- Martí, J. M., & Müller, E. 1999, *LRR*, **2**, 3
- McKinney, J. C. 2006, *MNRAS*, **368**, 1561
- Michel, F. C. 1972, *Ap&SS*, **15**, 153
- Mirabel, I. F., & Rodríguez, L. F. 1994, *Natur*, **371**, 46
- Moncrief, V. 1980, *ApJ*, **235**, 1038
- Olvera, D., & Mendoza, S. 2008, in *EAS Publications Series*, Vol. 30, ed. A. Oscoz, E. Mediavilla, & M. Serra-Ricart (Les Ulis: EDP Sciences), 399
- Ouyed, R., Clarke, D. A., & Pudritz, R. E. 2003, *ApJ*, **582**, 292
- Petrich, L. I., Shapiro, S. L., & Teukolsky, S. A. 1988, *PhRvL*, **60**, 1781
- Pudritz, R. E., Ouyed, R., Fendt, C., & Brandenburg, A. 2007, in *Protostars and Planets V*, ed. B. Reipurth, D. Jewitt, & K. Keil (2nd ed.; Tucson, AZ: Univ. Arizona Press), 277
- Qian, Q., Fendt, C., & Vourellis, C. 2018, *ApJ*, **859**, 28
- Romero, G. E., Boettcher, M., Markoff, S., & Tavecchio, F. 2017, *SSRv*, **207**, 5
- Semenov, V., Dyadechkin, S., & Punsly, B. 2004, *Sci*, **305**, 978
- Shakura, N. I., & Sunyaev, R. A. 1973, *A&A*, **24**, 337
- Shu, C.-W., & Osher, S. 1988, *JCoPh*, **77**, 439
- Siegert, T., Diehl, R., Greiner, J., et al. 2016, *Natur*, **531**, 341
- Sod, G. A. 1978, *JCoPh*, **27**, 1
- Tauris, T. M., & van den Heuvel, E. P. J. 2006, in *Formation and Evolution of Compact Stellar X-ray Sources*, 39, ed. W. Lewin & M. van der Klis (Cambridge: Cambridge Univ. Press), 623
- Taylor, P. A., Miller, J. C., & Podsiadlowski, P. 2011, *MNRAS*, **410**, 2385
- Tejeda, E. 2018, *RMxAA*, **54**, 171
- Tejeda, E., & Aguayo-Ortiz, A. 2019, *MNRAS*, **487**, 3607
- Wardle, J. F. C., Homan, D. C., Ojha, R., & Roberts, D. H. 1998, *Natur*, **395**, 457
- Waters, T., Aykotalp, A., Proga, D., et al. 2020, *MNRAS*, **491**, L76
- Woosley, S. E. 1993, *BAAS*, **25**, 894
- Woosley, S. E., & Bloom, J. S. 2006, *ARA&A*, **44**, 507
- Zahra Zeraatgari, F., Mosallanezhad, A., Yuan, Y.-F., Bu, D.-F., & Mei, L. 2020, *ApJ*, **888**, 86
- Zhong, S.-Q., Dai, Z.-G., & Deng, C.-M. 2019, *ApJL*, **883**, L19

Choked accretion onto a Kerr black hole

Continuing the extension of the choked accretion model, in this chapter we explore the behaviour of the choked accretion mechanism in the case when the central object is a rotating black hole. This study generalizes the previous articles by including an extra parameter to analyse, which is the spin of the black hole.

In this paper, we extend our steady-state, irrotational analytic solution of an ultra-relativistic, perfect fluid for the case when the metric describes a rotating Kerr black hole. By assuming a stiff equation of state, we derive the general potential fluid solution using horizon-penetrating coordinates, from which we derive the expressions for the density and velocity fields. From this solution, we focus on the axisymmetric quadrupolar flow solution, which contains the physics related to the choked accretion mechanism. We find that, not only a bipolar outflow solution is obtained, but also an equatorial outflow one, in which the fluid escapes from the equatorial region and is accreted through the poles. Likewise, we analyse the case when the bipolar outflow is not align with the spin of the black hole.

As in the previous papers, we extend our analytic model by relaxing the assumption on the equation of state and performing general relativistic hydrodynamic numerical simulations of the choked accretion model for an ideal gas accreted by a Kerr black hole. We use the AZTEKAS code for these numerical experiments, for which we develop the algorithms and methods necessary for the program to allow more general metrics and coordinates, as the Kerr-Schild one. Moreover, we use our analytic solution as a benchmark test for validating our numerical results. Our simulations use a numerical setup similar to the one used in our previous works, but now we focus on the dependence of the solution on the spin parameter, finding that the overall solution and properties of the choked accretion model persists largely unaffected by the rotation of the black hole.

The study presented in this chapter was published in PhRvD in 2021. The details of the paper are:

Aguayo-Ortiz A., Sarbach O., Tejeda E., 2021, PhRvD, 103, 023003.

[doi:10.1103/PhysRevD.103.023003](https://doi.org/10.1103/PhysRevD.103.023003)

Choked accretion onto a Kerr black holeAlejandro Aguayo-Ortiz^{1,*}, Olivier Sarbach², and Emilio Tejada³¹*Instituto de Astronomía, Universidad Nacional Autónoma de México,
AP 70-264, 04510 Ciudad de México, México*²*Instituto de Física y Matemáticas, Universidad Michoacana de San Nicolás de Hidalgo,
Edificio C-3, Ciudad Universitaria, 58040 Morelia, Michoacán, México*³*Cátedras Conacyt—Instituto de Física y Matemáticas,
Universidad Michoacana de San Nicolás de Hidalgo,
Edificio C-3, Ciudad Universitaria, 58040 Morelia, Michoacán, México* (Received 17 September 2020; accepted 10 December 2020; published 5 January 2021)

The choked accretion model consists of a purely hydrodynamical mechanism in which, by setting an equatorial to polar density contrast, a spherically symmetric accretion flow transitions to an inflow-outflow configuration. This scenario has been studied in the case of a (nonrotating) Schwarzschild black hole as central accretor, as well as in the nonrelativistic limit. In this article, we generalize these previous works by studying the accretion of a perfect fluid onto a (rotating) Kerr black hole. We first describe the mechanism by using a steady-state, irrotational analytic solution of an ultrarelativistic perfect fluid, obeying a stiff equation of state. We then use hydrodynamical numerical simulations in order to explore a more general equation of state. Analyzing the effects of the black hole's rotation on the flow, we find in particular that the choked accretion inflow-outflow morphology prevails for all possible values of the black hole's spin parameter, showing the robustness of the model.

DOI: [10.1103/PhysRevD.103.023003](https://doi.org/10.1103/PhysRevD.103.023003)**I. INTRODUCTION**

Black hole accretion theory has been an important building-block of our current understanding of high-energy astrophysical phenomena such as x-ray binaries, gamma ray bursts, and active galactic nuclei [1]. In recent years, this field of knowledge has gone through a revolution led by the observational breakthrough of gravitational wave astronomy, that has allowed a systematic analysis of close to fifty binary black hole mergers to date [2,3], as well as the extreme-resolution imaging of the immediate environment of astrophysical black holes achieved by the Event Horizon Telescope [4].

Since the pioneering work of Bondi [5], the introduction of exact, analytic solutions for modeling different astrophysical scenarios has been instrumental in the continuous development of accretion theory. Analytic models, by transparently highlighting the role played by different physical ingredients, are key in cementing our understanding and building our intuition around the studied phenomena. Moreover, analytic solutions are crucial tools as benchmark tests for numerical codes [6].

Within the regime of Newtonian gravity, the Bondi solution describes the stationary flow of a spherically symmetric gas cloud accreting onto a gravitational object.

This solution was extended by Michel [7] to a relativistic regime by considering a Schwarzschild black hole as central accretor. On the other hand, analytic solutions to the so-called wind accretion scenario have been introduced by Bondi and Hoyle [8] and Hoyle and Littleton [9] in the Newtonian context as well as by Tejada and Aguayo-Ortiz [10] in the relativistic context of a Schwarzschild black hole.¹ Several analytic and numerical investigations have further extended the study of spherical accretion, e.g., [14–24], as well as of wind accretion, e.g., [25–30].

It is important to note, however, that although astrophysical black holes are expected to rotate in general, very few analytic solutions exist for rotating black holes as described by the Kerr metric. A notable exception is the analytic solution introduced by Petrich, Shapiro and Teukolsky [31] that describes, under the assumptions of steady-state and irrotational flow, an ultrarelativistic stiff fluid accreting onto a Kerr black hole.

Based on the general solution presented in [31], and following on the work of [32,33], Tejada, Aguayo-Ortiz and Hernandez [34] presented a simple, hydrodynamical mechanism for launching bipolar outflows from a choked accretion flow onto a Schwarzschild black hole. This model starts from a spherically symmetric accretion flow onto a central massive object and introduces a deviation

*Corresponding author.
aaguayo@astro.unam.mx

¹Also see [11–13] for a related, analytic model of a rotating dust cloud accreting onto a rotating or a nonrotating black hole.

away from spherical symmetry by considering a small-amplitude, large-scale density gradient in such a way that the equatorial region of the accreting material is over dense as compared to the polar regions. This anisotropic density field translates into a pressure-driven force that, provided a sufficiently large mass accretion rate, can deflect a fraction of the originally radial accretion flow onto a bipolar outflow. The threshold value for the accretion rate determining whether the inflow chokes and the launching mechanism is successful or not is found to be of the order of the mass accretion rate corresponding to the spherically symmetric cases discussed by Bondi and Michel.

Even though the approximation of a stiff fluid has a rather limited applicability in astrophysics, the mechanism presented in [34] was shown to be valid for more general equations of state by means of full hydrodynamic numerical simulations. Moreover, as discussed in [33], this mechanism is also valid in the context of Newtonian gravity.

In this work, we present an extension of the choked accretion model introduced in [33,34] to the case of a rotating central black hole as described by the Kerr metric. We study this problem using both an analytic solution for an ultrarelativistic stiff fluid as well as full hydrodynamic numerical simulations for fluids described by more general equations of state. In addition to demonstrating that the choked accretion mechanism can successfully operate with a central rotating black hole, we also analyze the effects of the black hole rotation on the accretion flow.

We focus mostly on the case in which the axis of the bipolar outflow is aligned with the black hole's rotation axis, although we also briefly discuss the case of a possible misalignment between these two. Considering that the infalling gas might come from the inner edge of an accretion disk, we believe that the restriction of alignment is well justified in view of the Bardeen-Petterson effect [35,36], which foresees that the inner part of an accretion disk around a rotating black hole will be aligned with the equatorial plane of the central black hole.

The choked accretion mechanism introduced in [33,34] can be considered as a hydrodynamic toy model of the central engine in astrophysical scenarios involving both equatorial accretion flows and bipolar outflows. These scenarios can range from the jets and winds associated with some young stellar objects to the accretion disk-jet systems associated with stellar mass black holes (such as x-ray binaries and gamma-ray bursts) as well as with supermassive black holes (such as radio loud galaxies and other active galactic nuclei).

Even though the choked accretion model does not account directly for fluid rotation, the assumption of an anisotropic density field is motivated precisely as a way to introduce indirectly one of the effects of fluid rotation and angular momentum conservation, namely, the existence of a well-defined symmetry axis (the rotation axis) and the accompanying flattening of the accreting fluid that results in an equator-to-poles density gradient (see, e.g., [37,38]).

Several works in the literature have studied before different accretion scenarios featuring both equatorial inflows and bipolar outflows, particularly within the regime of hot accretion flows [39,40], that correspond to geometrically thick, optically thin, and radiatively inefficient accretion flows. These studies have been both analytic, with models such as advection dominated accretion flows (ADAF) [41,42] or adiabatic inflow-outflow solutions (ADIOS) [43–45], as well as based on numerical simulations [46–51]. From the point of view of the incorporated physical ingredients, these models are more realistic than the choked accretion scenario discussed here as they account for effects such as fluid rotation, viscous dissipation of energy and transport of angular momentum, interaction with a radiation field, magnetic fields, among others. Nevertheless, we believe that, given its simplicity and reliance on pure hydrodynamics, the choked accretion mechanism might be already at work in some of those systems, acting alongside more complex processes.

Also note that the choked accretion model shares some broad, qualitative features with some versions of hot accretion flows [40], namely, an accreting, quasispherical gas distribution, with sub-Keplerian rotation, and with such a large internal energy that parcels of it become gravitationally unbound from the central object and can be ejected as bipolar outflows.

The paper is organized as follows. Based on the approximations of steady-state and irrotational flow, in Sec. II we present the general solution of an ultrarelativistic stiff fluid in Kerr spacetime. In contrast to [31], who adopted the Boyer-Lindquist coordinates for this derivation, we shall employ horizon-penetrating coordinates which are regular across the black hole's event horizon and allow for a clearer and, in fact, simpler derivation of the solution. In Sec. III we restrict our discussion on the axisymmetric, quadrupolar solution and discuss its most salient properties. Based on this solution, in Sec. IV we introduce and discuss the analytic model describing choked accretion in a Kerr spacetime. In Sec. V we complement this study by means of hydrodynamic simulations for a more general equation of state. Finally, in Sec. VI, we present a summary of the model and give our conclusions. Technical details regarding the region of validity of the analytic solution, a nonaxisymmetric exact solution, and convergence tests of our numerical results are discussed in three appendixes. Throughout this article we use the signature convention $(-, +, +, +)$ for the spacetime metric and work in geometrized units for which $G = c = 1$.

II. STEADY-STATE, IRROTATIONAL SOLUTIONS FOR AN ULTRARELATIVISTIC STIFF EQUATION OF STATE ON A KERR BACKGROUND SPACETIME

In this section, we review the analytic approach of [31] for obtaining exact, irrotational, steady-state solutions of the relativistic Euler equations on a Kerr black hole background with an ultrarelativistic stiff equation of state.

We start in Sec. II A with the derivation of the Petrich-Shapiro-Teukolsky solution [31] in horizon-penetrating coordinates. Next, in Sec. II B we compute the components of the three-velocity of the fluid with respect to the reference frame associated with zero angular momentum observers (ZAMOs), which are naturally adapted to the Killing symmetries of the Kerr geometry and reduce to the usual static observers in the non-rotating limit. Finally, in Sec. II C we discuss the conserved quantities obeyed by the fluid field, such as the (rest) mass and energy accretion rates which are important for the physical interpretation of our model, as well as the angular momentum accretion rate.

An ultrarelativistic stiff equation of state is characterized by the fluid's pressure $P = K\rho^2$ being proportional to the square of the rest-mass density ρ and the internal energy dominating the rest mass energy. For a perfect fluid in local thermodynamical equilibrium obeying the first law $dh = dP/\rho$, this implies that its specific enthalpy $h = 2K\rho$ is proportional to ρ . Together with the irrotational condition such a fluid can be described by a scalar potential Φ satisfying the linear wave equation

$$\nabla^\mu \nabla_\mu \Phi = \frac{1}{\sqrt{-g}} \partial_\mu (\sqrt{-g} g^{\mu\nu} \partial_\nu \Phi) = 0. \quad (1)$$

The potential Φ determines the fluid's specific enthalpy and four-velocity U^μ according to

$$h = \sqrt{-(\nabla^\mu \Phi)(\nabla_\mu \Phi)}, \quad U^\mu = \frac{1}{h} \nabla^\mu \Phi, \quad (2)$$

from which the rest-mass density and the pressure can also be obtained. An important point to notice is that not every solution of the wave equation (1) yields a valid solution for the fluid; indeed, for h to be well-defined the gradient $\nabla^\mu \Phi$ of Φ needs to be timelike.

The key observation in [31] is that for a steady-state configuration on a Kerr background, Eq. (1) can be decoupled into standard spherical harmonics (even though the Kerr spacetime is not spherically symmetric), leading to a general solution which can be expressed in terms of well-known special functions. In the following, we briefly repeat the arguments leading to this expression. However, unlike the Boyer-Lindquist coordinates used in [31], we base our calculations on the Kerr-type coordinates² (t, ϕ, r, θ) . This

²These coordinates are related to the Kerr coordinates (v, ϕ, r, θ) found in standard textbooks [52,53] by the transformation $v = t + r$, and they are related to the standard Boyer-Lindquist coordinates $(t_{\text{BL}}, \phi_{\text{BL}}, r_{\text{BL}}, \theta_{\text{BL}})$ through the transformation $r = r_{\text{BL}}$, $\theta = \theta_{\text{BL}}$, while

$$t = t_{\text{BL}} + \frac{2M}{r_+ - r_-} \left[r_+ \ln \left(\frac{r - r_+}{r_+} \right) - r_- \ln \left(\frac{r - r_-}{r_-} \right) \right], \quad (3a)$$

$$\phi = \phi_{\text{BL}} + \frac{a}{r_+ - r_-} \ln \left(\frac{r - r_+}{r - r_-} \right). \quad (3b)$$

has at least two advantages. First, as we will see, the derivation and final expression for the analytic solution of Eq. (1) is clearer and simpler in terms of these coordinates. Second, and most importantly, it greatly facilitates the understanding of the properties of the flow at the horizon, since these coordinates cover the (future) event horizon $r = r_+$ in addition to the outside region $r > r_+$ (whereas the Boyer-Lindquist coordinates are ill-defined at the horizon).

A. Derivation of the Petrich-Shapiro-Teukolsky solution in the Kerr-type coordinates

In terms of the coordinates (t, ϕ, r, θ) , the Kerr metric components have determinant $g := \det(g_{\mu\nu}) = -\varrho^4 \sin^2 \theta$ and the components of the inverse metric are

$$(g^{\mu\nu}) = \frac{1}{\varrho^2} \begin{pmatrix} -(q^2 + 2Mr) & 0 & 2Mr & 0 \\ 0 & \frac{1}{\sin^2 \theta} & a & 0 \\ 2Mr & a & \Delta & 0 \\ 0 & 0 & 0 & 1 \end{pmatrix}, \quad (4)$$

where we use the standard abbreviations³

$$q^2 = r^2 + a^2 \cos^2 \theta, \quad \Delta = r^2 - 2Mr + a^2.$$

Here, M and a are the mass and rotation parameter of the Kerr spacetime, and we assume that $a^2 < M^2$ such that this spacetime describes a nonextremal black hole with angular momentum $J = aM$.

With these coordinates, the wave equation (1) assumes the following explicit form:

$$(q^2 + 2Mr)\Phi_{,tt} - 2Mr\Phi_{,tr} - (2Mr\Phi_{,t})_{,r} - 2a\Phi_{,r\phi} - (\Delta\Phi_{,r})_{,r} - \frac{1}{\sin \theta} (\sin \theta \Phi_{,\theta})_{,\theta} - \frac{1}{\sin^2 \theta} \Phi_{,\phi\phi} = 0, \quad (5)$$

where, here and in what follows, subindices following a coma refer to partial derivatives; for instance $\Phi_{,tr} = \partial_r \partial_t \Phi$.

For a stationary solution (such that h and U^μ are independent of t), the scalar potential has the form

$$\Phi = e[-t + \psi(r, \theta, \phi)], \quad (6)$$

with a new function ψ which does not depend on t , and where the positive constant e corresponds to the Bernoulli constant (per unit mass), defined as

$$e = -hU_\mu K^\mu = -hU_t = -\Phi_{,t}, \quad (7)$$

where $K = \partial_t$ is the Killing vector field associated with the time symmetry of Kerr spacetime.

³We warn the reader that throughout this work we follow the convention of Ref. [1] where the similar-looking symbols ρ and q denote the rest-mass density and the metric coefficient $q = \sqrt{r^2 + a^2 \cos^2 \theta}$, respectively.

Introducing the ansatz (6) into Eq. (5) yields

$$(\Delta\psi_{,r})_{,r} + \frac{1}{\sin\theta}(\sin\theta\psi_{,\theta})_{,\theta} + \frac{1}{\sin^2\theta}\psi_{,\phi\phi} + 2a\psi_{,r\phi} = 2M. \quad (8)$$

Despite of the presence of the rotation parameter a , this equation can be separated into radial and angular parts by means of a decomposition in terms of the standard spherical harmonics $Y^{\ell m}(\theta, \phi)$:

$$\psi(r, \theta, \phi) = \sum_{\ell m} R_{\ell m}(r) Y^{\ell m}(\theta, \phi), \quad (9)$$

with the functions $R_{\ell m}$ to be determined. Introduced into Eq. (8) this gives⁴

$$\frac{d}{dr} \left(\Delta \frac{dR_{00}}{dr} \right) = 2M, \quad (10)$$

for $\ell = 0$, and

$$\frac{d}{dr} \left(\Delta \frac{dR_{\ell m}}{dr} \right) + 2im a \frac{dR_{\ell m}}{dr} - \ell(\ell + 1)R_{\ell m} = 0, \quad (11)$$

for $\ell \geq 1$. Integrating Eq. (10) once gives

$$\frac{dR_{00}}{dr} = \frac{2Mr + c_0}{(r - r_+)(r - r_-)},$$

for some constant c_0 , where $r_{\pm} = M \pm \sqrt{M^2 - a^2}$ denote the roots of Δ . In order for R_{00} to be regular at the event horizon $r = r_+$, one needs to choose $c_0 = -2Mr_+$, such that the factor $r - r_+$ in the denominator is canceled. This yields

$$R_{00} = 2M \ln \left(\frac{r - r_-}{r - r_+} \right) \quad (12)$$

plus a constant which is irrelevant since the flow only depends on the gradient of Φ . Note that R_{00} is regular for all $r > r_-$, but diverges at the Cauchy horizon $r = r_-$.⁵ Therefore, the ‘‘spherical’’ ($\ell = 0$) piece of ψ is fixed to the specific function (12) by the requirement of regularity at the horizon.

Equation (11) describes the ‘‘nonspherical’’ ($\ell \geq 1$) contributions to ψ and can be brought into the hypergeometric differential equation by introducing the dimensionless coordinate

$$x := \frac{r - r_+}{r_+ - r_-}, \quad (13)$$

which ranges from -1 to ∞ as r varies from r_- to ∞ and is zero at the event horizon $r = r_+$. In terms of this, Eq. (11) reads

$$x(1+x) \frac{d^2 R_{\ell m}}{dx^2} + \left(1 + 2x + \frac{2im a}{r_+ - r_-} \right) \frac{dR_{\ell m}}{dx} - \ell(\ell + 1)R_{\ell m} = 0, \quad (14)$$

which, after the further substitution $x = -y$, yields the standard form of the hypergeometric differential equation (see, for example [54], Sec. 15). The solutions which are regular at the event horizon $x = 0$ can be written in terms of Gauss’ hypergeometric function F (as defined in [54], Sec. 15):

$$R_{\ell m}(r) = A_{\ell m} F(-\ell, \ell + 1; 1 + im\alpha; -x), \quad (15)$$

where $A_{\ell m}$ is a free (complex) constant and where we have introduced the dimensionless quantity

$$\alpha := \frac{2a}{r_+ - r_-} = \frac{a}{\sqrt{M^2 - a^2}}.$$

Note that Eq. (15) is actually a polynomial in r of order ℓ ,⁶ since for any complex number $c \neq 0, -1, -2, \dots$,

$$F(-\ell, \ell + 1; c; -x) = \sum_{n=0}^{\ell} \frac{(\ell + n)!}{(\ell - n)!} \frac{1}{(c)_n} \frac{x^n}{n!}, \quad (16)$$

with $(c)_n := c(c+1)(c+2)\dots(c+n-1)$ for $n \geq 1$ and $(c)_0 := 1$. A few examples relevant for this article are

[$\ell = 0$]: $F(0, 1; c; -x) = 1$ (‘‘spherical’’ Bondi-Michel-type accretion which will be discussed in a future work)

[$\ell = 1$]: $F(-1, 2; c; -x) = 1 + \frac{2x}{c}$ (wind accretion discussed in [31,55,56])

[$\ell = 2$]: $F(-2, 3; c; -x) = 1 + \frac{6x}{c} + \frac{12x^2}{c(c+1)}$ (choked accretion, discussed in the Schwarzschild limit in [34], and in the present paper for arbitrary rotation)

Summarizing, the general solution describing a steady-state, irrotational flow on a Kerr background which is regular at the horizon and which has an ultrarelativistic stiff equation of state is characterized by the potential

$$\Phi = e[-t + 2M \ln(1+x) + \mathcal{F}(r, \theta, \phi)], \quad (17)$$

with

⁴For simplicity, we assume that $Y^{00} = 1$ while for $\ell > 0$ the spherical harmonics $Y^{\ell m}$ are defined with the usual normalization.

⁵Note also that R_{00} and its gradient diverge at the horizon in the extremal case $a = \pm M$, when $r_+ = r_- = M$.

⁶These polynomials are related to the associated Legendre functions of the first kind, see [31,54]. For the special case $c = 1$ these polynomials are also related to the shifted Legendre polynomials.

$$\mathcal{F}(r, \theta, \phi) := \sum_{\ell=1}^{\infty} \sum_{m=-\ell}^{\ell} A_{\ell m} F(-\ell, \ell+1; c; -x) Y^{\ell m}(\theta, \phi), \quad (18)$$

where we recall that $A_{\ell m} \in \mathbb{C}$, $x = (r - r_+)/ (r_+ - r_-)$, $c = 1 + im\alpha$, and $\alpha = 2a / (r_+ - r_-)$.

Except for the addition of an irrelevant constant, the expression for the potential in Eq. (17) agrees with Eq. (30) in [31], taking into account the relations (3a), (3b) between the Kerr-type coordinates and the Boyer-Lindquist coordinates used in that reference.

For Φ as given in Eq. (17) to be real, the coefficients $A_{\ell m}$ need to satisfy the reality conditions

$$A_{\ell-m} = (-1)^m A_{\ell m}^*, \quad (19)$$

so that there are $2\ell + 1$ independent real constants for each ℓ . Note also that $F(-\ell, \ell+1; 1 + im\alpha; 0) = 1$ on the event horizon; hence the coefficients $A_{\ell m}$ describe the ℓm contributions of the fluid potential Φ when evaluated on the horizon cross section.

The specific enthalpy and four-velocity are obtained from substituting Eq. (17) into Eq. (2), which yields

$$\begin{aligned} \frac{h^2}{e^2} = & 1 + \frac{2Mr(r+r_+) + 2Mr_+}{q^2} \frac{1}{r-r_-} \\ & + \frac{4M}{q^2} \left(r_+ \mathcal{F}_{,r} - \frac{a}{r-r_-} \mathcal{F}_{,\phi} \right) \\ & - \frac{1}{q^2} \left(\Delta \mathcal{F}_{,r}^2 + 2a \mathcal{F}_{,r} \mathcal{F}_{,\phi} + \mathcal{F}_{,\theta}^2 + \frac{\mathcal{F}_{,\phi}^2}{\sin^2 \theta} \right), \quad (20) \end{aligned}$$

and

$$\frac{h}{e} U^t = 1 + \frac{2Mr}{q^2} \frac{r+r_+}{r-r_-} + \frac{2Mr}{q^2} \mathcal{F}_{,r}, \quad (21a)$$

$$\frac{h}{e} U^r = \frac{1}{q^2} (-2Mr_+ + \Delta \mathcal{F}_{,r} + a \mathcal{F}_{,\phi}), \quad (21b)$$

$$\frac{h}{e} U^\theta = \frac{1}{q^2} \mathcal{F}_{,\theta}, \quad (21c)$$

$$\frac{h}{e} U^\phi = \frac{1}{q^2} \left(\frac{2Ma}{r-r_-} + a \mathcal{F}_{,r} + \frac{1}{\sin^2 \theta} \mathcal{F}_{,\phi} \right). \quad (21d)$$

Recall that the gradient of Φ needs to be timelike for the solution to be well-defined, which is equivalent to the requirement that the right-hand side of Eq. (20) be positive. In general, this condition cannot be satisfied everywhere outside the horizon. Since $F(-\ell, \ell+1; 1 + im\alpha; -x)$ grows like r^ℓ at large distances, the right-hand side of Eq. (20) is dominated by the term $-\Delta \mathcal{F}_{,r}^2 / q^2 \sim -r^{2\ell-2}$ for a solution containing multipoles up to a given ℓ and hence

will eventually become negative, for a sufficiently large radius, if $\ell \geq 2$. However, since $h^2/e^2 > 1$ when $\mathcal{F} = 0$, one can always choose the coefficients $A_{\ell m}$ small enough such that the right-hand side of Eq. (20) is positive (and hence h well-defined) within a finite spherical shell of the form $r_+ \leq r \leq \mathcal{R}$ containing the horizon.

A further restriction comes from the requirement that the fluid should fall into the black hole at the horizon, such that the four-velocity satisfies the inequality

$$U^\mu \nabla_\mu r = U^r = \frac{e}{h} \frac{1}{q^2} [-2Mr_+ + a \mathcal{F}_{,\phi}] < 0 \quad (22)$$

at the horizon $r = r_+$, which is equivalent to the bound $a \mathcal{F}_{,\phi} < 2Mr_+$ at $r = r_+$. We will show shortly that this is, as expected, a consequence of the requirement for $\nabla^\mu \Phi$ to be future-directed timelike.

B. ZAMO frame and three-velocity

For the results and calculations that follow, it is convenient to express the four-velocity in terms of an orthonormal frame instead of local coordinates. A very convenient frame in the Kerr exterior spacetime is the one associated with ZAMOs [57,58], that is, observers whose world lines are tangent to a linear combination of the Killing vector fields,

$$\frac{\partial}{\partial t} + \Omega \frac{\partial}{\partial \phi}, \quad \text{with} \quad \Omega = \frac{2Mar}{\Sigma}, \quad (23)$$

and

$$\Sigma = (r^2 + a^2)^2 - a^2 \Delta \sin^2 \theta = \Delta q^2 + 2Mr(r^2 + a^2). \quad (24)$$

The ZAMO's angular velocity Ω is singled out by the requirement of zero angular momentum. These observers' tangent vectors are also orthogonal to the $t_{\text{BL}} = \text{const.}$ Boyer-Lindquist time slices, and in this sense they generalize the ‘‘local Eulerian observers’’ used in [34] to discuss the quadrupolar flow in a Schwarzschild background.

A natural orthonormal frame associated with the ZAMOs is given by the following basis vectors (see [57,58])⁷:

$$e_{\hat{t}} = \frac{1}{q} \sqrt{\frac{\Sigma}{\Delta}} \left(\frac{\partial}{\partial t} + \Omega \frac{\partial}{\partial \phi} \right), \quad (25a)$$

$$e_{\hat{r}} = \frac{\sqrt{\Delta}}{q} \left(\frac{\partial}{\partial r} + \frac{2Mr}{\Delta} \frac{\partial}{\partial t} + \frac{a}{\Delta} \frac{\partial}{\partial \phi} \right), \quad (25b)$$

⁷Here and in the following, hatted indices refer to labels for this orthonormal frame.

$$e_{\hat{\theta}} = \frac{1}{\varrho} \frac{\partial}{\partial \theta}, \quad (25c)$$

$$e_{\hat{\phi}} = \frac{\varrho}{\sqrt{\Sigma} \sin \theta} \frac{\partial}{\partial \phi}. \quad (25d)$$

The orthonormal components of the four-velocity are given by

$$\frac{h}{e} U^{\hat{t}} = \frac{1}{\varrho} \sqrt{\frac{\Sigma}{\Delta}} (1 - \Omega \mathcal{F}_{,\phi}), \quad (26a)$$

$$\frac{h}{e} U^{\hat{r}} = \frac{1}{\varrho \sqrt{\Delta}} (-2Mr_+ + \Delta \mathcal{F}_{,r} + a \mathcal{F}_{,\phi}), \quad (26b)$$

$$\frac{h}{e} U^{\hat{\theta}} = \frac{1}{\varrho} \mathcal{F}_{,\theta}, \quad (26c)$$

$$\frac{h}{e} U^{\hat{\phi}} = \frac{\varrho}{\sqrt{\Sigma} \sin \theta} \mathcal{F}_{,\phi}. \quad (26d)$$

On the other hand, the components of the three-velocity are defined as

$$V^{\hat{r}} = \frac{U^{\hat{r}}}{U^{\hat{t}}} = \frac{-2Mr_+ + \Delta \mathcal{F}_{,r} + a \mathcal{F}_{,\phi}}{\sqrt{\Sigma} (1 - \Omega \mathcal{F}_{,\phi})}, \quad (27a)$$

$$V^{\hat{\theta}} = \frac{U^{\hat{\theta}}}{U^{\hat{t}}} = \sqrt{\frac{\Delta}{\Sigma}} \frac{\mathcal{F}_{,\theta}}{1 - \Omega \mathcal{F}_{,\phi}}, \quad (27b)$$

$$V^{\hat{\phi}} = \frac{U^{\hat{\phi}}}{U^{\hat{t}}} = \frac{\varrho^2 \sqrt{\Delta}}{\Sigma \sin \theta} \frac{\mathcal{F}_{,\phi}}{1 - \Omega \mathcal{F}_{,\phi}}, \quad (27c)$$

with the corresponding Lorentz factor

$$\Gamma = U^{\hat{t}} = \frac{1}{\sqrt{1 - V^2}}, \quad (28)$$

where

$$V = \sqrt{(V^{\hat{r}})^2 + (V^{\hat{\theta}})^2 + (V^{\hat{\phi}})^2}. \quad (29)$$

A number of interesting conclusions can be drawn from these representations of the four- and three-velocities. First, the four-velocity vector is future-directed timelike outside the horizon if and only if $U^{\hat{t}} > 0$ and if the magnitude of the three-velocity V is smaller than one. This is equivalent to the two conditions

$$\Omega \mathcal{F}_{,\phi} < 1 \quad (30)$$

and

$$V^2 = \frac{1}{\Sigma (1 - \Omega \mathcal{F}_{,\phi})^2} \left[(-2Mr_+ + \Delta \mathcal{F}_{,r} + a \mathcal{F}_{,\phi})^2 + \Delta \left(\mathcal{F}_{,\theta}^2 + \frac{\varrho^4}{\Sigma \sin^2 \theta} \mathcal{F}_{,\phi}^2 \right) \right] < 1. \quad (31)$$

In the axisymmetric case, when $\mathcal{F}_{,\phi} = 0$, the first inequality is automatically satisfied and the second one simplifies considerably:

$$V^2 = \frac{(2Mr_+ - \Delta \mathcal{F}_{,r})^2 + \Delta \mathcal{F}_{,\theta}^2}{\Sigma} < 1. \quad (32)$$

Since $\Sigma \geq (2Mr_+)^2 + \Delta \varrho^2$ for $r \geq r_+$, one can always satisfy this inequality for small enough values of the gradient of \mathcal{F} . The restrictions implied by the inequalities (30,31) for a quadrupolar solution ($\ell = 2$) will be analyzed in more detail in the next two sections.

The next property that can be inferred from Eqs. (30) and (31) is obtained by taking the limit $r \rightarrow r_+$. In this limit, the inequality (30) yields $\Omega_+ \mathcal{F}_{,\phi}|_{r=r_+} \leq 1$, where $\Omega_+ = a/(2Mr_+)$ is the angular velocity of the event horizon. This provides a bound for the value of $\mathcal{F}_{,\phi}$ at the horizon, and comparison with Eq. (22) reveals the meaning of this bound: the fluid cannot flow out of the black hole, a property that is, of course, expected on physical grounds. By requiring that the four-velocity U^μ is everywhere timelike on the horizon, one can further eliminate the possibility that $\Omega_+ \mathcal{F}_{,\phi} = 1$ somewhere on the horizon; otherwise Eq. (22) would imply that U^μ is tangent to the horizon and thus cannot be timelike. Summarizing, the requirement for U^μ to be future-directed timelike at the horizon yields the strict inequality,

$$\Omega_+ \mathcal{F}_{,\phi}|_{r=r_+} < 1 \quad (33)$$

which implies that the flow can only cross inwards the event horizon.

Another point to notice from the expressions for the three-velocity of the fluid in Eqs. (27a)–(27c) is that the fluid is at rest with respect to a ZAMO if and only if the function \mathcal{F} satisfies

$$\Delta \mathcal{F}_{,r} + a \mathcal{F}_{,\phi} = 2Mr_+, \quad \mathcal{F}_{,\theta} = \mathcal{F}_{,\phi} = 0. \quad (34)$$

Finally, we note that, even though the ZAMO frame is very useful in many situations, this frame is not well defined at the event horizon nor in the region inside the black hole between the two horizons r_- and r_+ , where $\Delta \leq 0$. In case one is interested in analyzing the flow at or inside the horizon, one may use instead the orthonormal frame adapted to local Eulerian observers relative to the $t = \text{const.}$ Kerr-type coordinates.

C. Conserved quantities

Due to the presence of the Killing vector fields $K = \partial_t$ and $L = \partial_\phi$ of the Kerr spacetime, the following four-currents are divergence-free:

$$J^\mu = \rho U^\mu, \quad (35a)$$

$$J^\mu_{\mathcal{E}} = -T^\mu{}_\nu K^\nu, \quad (35b)$$

$$J^\mu_{\mathcal{L}} = T^\mu{}_\nu L^\nu, \quad (35c)$$

corresponding to the rest-mass, energy, and angular momentum current densities, respectively.

For an ultrarelativistic stiff fluid, the specific enthalpy $h = 2K\rho$ is proportional to the particle density and $P = \rho h/2$, such that

$$J^\mu = \rho U^\mu = \frac{\rho}{h} \nabla^\mu \Phi, \quad (36a)$$

$$\begin{aligned} T^\mu{}_\nu &= \rho h U^\mu U_\nu + P \delta^\mu{}_\nu \\ &= \frac{\rho}{h} \left[(\nabla^\mu \Phi)(\nabla_\nu \Phi) - \frac{1}{2} \delta^\mu{}_\nu (\nabla^\alpha \Phi)(\nabla_\alpha \Phi) \right]. \end{aligned} \quad (36b)$$

In particular, using Eqs. (17) and (21b) we find

$$J^r = \frac{\rho e}{h} \frac{1}{Q^2} [-2Mr_+ + \Delta \mathcal{F}_{,r} + a \mathcal{F}_{,\phi}], \quad (37a)$$

$$J^\mu_{\mathcal{E}} = e J^\mu, \quad (37b)$$

$$J^\mu_{\mathcal{L}} = e \mathcal{F}_{,\phi} J^\mu. \quad (37c)$$

Since the flow is stationary, the equation $\nabla_\mu J^\mu = 0$ gives

$$(Q^2 \sin \theta J^r)_{,r} + (Q^2 \sin \theta J^\theta)_{,\theta} + (Q^2 \sin \theta J^\phi)_{,\phi} = 0. \quad (38)$$

Therefore, the mass accretion rate (current flux) associated with J through a two-surface S is given by

$$\dot{M} = - \int_S (J^r N_r + J^\theta N_\theta + J^\phi N_\phi) Q^2 \sin \theta dS, \quad (39)$$

with (N_r, N_θ, N_ϕ) the unit outward normal field and dS a differential area element of S . If S is closed, then \dot{M} is independent of any deformations of S , since J^μ is conserved. For example, if S is a constant- r surface, then

$$\dot{M} = - \int_S J^r Q^2 \sin \theta d\theta d\phi, \quad (40)$$

which is independent of r . Using now the orthogonality relations of the spherical harmonics we can integrate Eq. (40) as

$$\dot{M} = 8\pi M r_+ \frac{\rho e}{h} = 4\pi (r_+^2 + a^2) \frac{\rho e}{h}, \quad (41)$$

which is constant since $\rho/h = 1/(2K)$.

Similarly, for the energy accretion rate we have

$$\dot{\mathcal{E}} = - \int_S J^\mu_{\mathcal{E}} Q^2 \sin \theta d\theta d\phi = 4\pi (r_+^2 + a^2) \frac{\rho e^2}{h} = e \dot{M}, \quad (42)$$

while, for the angular momentum accretion rate

$$\begin{aligned} \dot{J} &= - \int_S J^\mu_{\mathcal{L}} Q^2 \sin \theta d\theta d\phi \\ &= -a \frac{\rho e^2}{h} \int_{r=r_+} \mathcal{F}^2_{,\phi} \sin \theta d\theta d\phi \\ &= -a \frac{\rho e^2}{h} \sum_{\ell=1}^{\infty} \sum_{m=-\ell}^{\ell} m^2 |A_{\ell m}|^2. \end{aligned} \quad (43)$$

Notice that the mass and energy accretion rates are uniquely determined by the $\ell = 0$ part of the solution (they are independent of the coefficients $A_{\ell m}$), which in turn was determined by the regularity requirement at the event horizon. In contrast to this, the angular momentum accretion rate is solely determined by the $\ell > 0$ part of the solution. Interestingly, the sign of \dot{J} indicates that the accreted material always slows down the spin of the black hole (unless the flow is perfectly axisymmetric in which case $\dot{J} = 0$). Therefore, the accretion flow described by (17) always drives the Kerr black hole away from extremality ($|J|$ decreases, M increases, such that J/M^2 decreases).

III. THE AXISYMMETRIC QUADRUPOLEAR FLOW

In this section we shall focus on the axisymmetric quadrupolar solution, i.e., the velocity potential Φ in Eq. (17) for which all of the coefficients $A_{\ell m}$ vanish except for the $(\ell, m) = (2, 0)$ contribution, which results in

$$\Phi = e \left[-t + 2M \ln \left(\frac{r - r_-}{r_+ - r_-} \right) + AF(r, \theta, \phi) \right], \quad (44)$$

with

$$F(r, \theta, \phi) = (3r^2 - 6Mr + 2M^2 + a^2)(3 \cos^2 \theta - 1), \quad (45)$$

where, as we shall see below, e can be identified as a scaling factor for the gas' thermodynamic state while A determines the overall flow morphology.

We can now exploit all of the results derived in the previous section. In particular, from Eqs. (27a)–(27c), we obtain the following expressions for the spatial components of the three-velocity as described by the ZAMOs

$$V^{\hat{r}} = \frac{-2Mr_+ + A\Delta F_{,r}}{\sqrt{\Sigma}}, \quad (46a)$$

$$V^{\hat{\theta}} = \sqrt{\frac{\Delta}{\Sigma}} AF_{,\theta}, \quad (46b)$$

$$V^{\hat{\phi}} = 0, \quad (46c)$$

where

$$F_{,r} = 6(r - M)(3\cos^2\theta - 1), \quad (47a)$$

$$F_{,\theta} = -6(3r^2 - 6Mr + 2M^2 + a^2) \cos\theta \sin\theta. \quad (47b)$$

The value for the constant e can be set by specifying a reference point at which the fluid state is known. Calling h_0 the specific enthalpy and V_0 the magnitude of the three-velocity at this reference point, from Eq. (26), we have

$$e = \Gamma_0 h_0 q_0 \sqrt{\frac{\Delta_0}{\Sigma_0}}, \quad (48)$$

where $\Gamma_0 = 1/\sqrt{1 - V_0^2}$.

Using Eqs. (20) and (26a) we find that the specific enthalpy in this case is given by

$$\begin{aligned} \frac{h^2}{e^2} &= \frac{\Sigma(1 - V^2)}{\Delta q^2} \\ &= 1 + \frac{2Mr}{q^2} + \frac{4M^2 r + r_+}{q^2 r - r_-} \\ &\quad + \frac{4Mr_+}{q^2} AF_{,r} - \frac{A^2}{q^2} (\Delta F_{,r}^2 + F_{,\theta}^2). \end{aligned} \quad (49)$$

On the other hand, denoting by ρ_0 the rest-mass density at the reference point, from the equation of state we have $\rho/\rho_0 = h/h_0$. Using this, and substituting Eq. (48) back into Eq. (26), we obtain

$$\frac{\rho}{\rho_0} = \frac{h}{h_0} = \frac{\Gamma_0 q_0}{\Gamma q} \sqrt{\frac{\Sigma \Delta_0}{\Sigma_0 \Delta}}. \quad (50)$$

From Eq. (50), we note that the following combination of variables

$$\rho \Gamma q \sqrt{\frac{\Delta}{\Sigma}} = \text{const.} \quad (51)$$

yields a global constant that characterizes the resulting flow. Indeed, as follows from Eqs. (41) and (26a), this constant is proportional to the total mass accretion rate. Also note that, from Eq. (49), it is clear that both h and ρ are completely regular (finite) quantities at the event horizon

($r = r_+$),⁸ although they do become infinite at the Cauchy horizon ($r = r_-$).

Provided that $A \neq 0$, the flow structure described by Eqs. (46a)–(46c) consists of an inflow-outflow morphology. We can characterize this morphology in terms of the location of the stagnation points, i.e., points at which the three-velocity vanishes. From Eqs. (46b), (47b) we see that $V^{\hat{\theta}}$ vanishes only at points along the polar axis ($\theta = 0, \pi$) and on the equatorial plane ($\theta = \pi/2$). Now it only remains examining the points at which $V^{\hat{r}} = 0$ restricted to either $\theta = 0, \pi$ or $\theta = \pi/2$. From Eqs. (46a), (47a) we can distinguish two qualitatively different cases:

Case 1: When $A > 0$, the resulting structure consists of inflow across an equatorial region and outflow confined to the polar regions (bipolar outflow). In this case, $V^{\hat{r}}$ vanishes at two points along the polar axis symmetrically located with respect to the origin at a coordinate distance $r = \mathcal{S}$ that satisfies

$$A = \frac{Mr_+}{6(\mathcal{S} - r_-)(\mathcal{S} - r_+)(\mathcal{S} - M)}. \quad (52)$$

See Fig. 1 for an example of the resulting flow for $AM = 0.01$ (which corresponds to $\mathcal{S} \simeq 4.24M$) and a Kerr black hole with $a = 0.5M$.

Case 2: When $A < 0$, the scenario is reversed and one has two bipolar inflow regions and outflow across the equatorial region. In this case, we have that $V^{\hat{r}}$ vanishes now at an infinite number of points located on an equatorial ring of radius $r = \mathcal{S}$ satisfying

$$A = -\frac{Mr_+}{3(\mathcal{S} - r_-)(\mathcal{S} - r_+)(\mathcal{S} - M)}. \quad (53)$$

In Fig. 2, we show an example of the resulting flow for $AM = -0.01$ (which corresponds to $\mathcal{S} \simeq 5M$) and a Kerr black hole with $a = 0.5M$.

In both examples shown in Figs. 1 and 2, it is apparent that V becomes luminal at two surfaces. From Eqs. (46a)–(46c), and as discussed in the previous section, it is simple to see that one such surface is the black hole's event horizon located at $r = r_+$. This behavior is, however, a coordinate effect related to the fact that the ZAMOs become ill defined at this radius. Indeed, using Eqs. (21a)–(21b), it can be seen that the fluid's four-velocity is completely regular across the event horizon.

On the other hand, the outer surface at which $V = 1$ signals an unavoidable characteristic of the quadrupolar solution. This surface, that in what follows we shall refer to as \mathcal{E} , marks the transition of the gradient $\Phi_{,\mu}$ from being timelike (for points inner to \mathcal{E}) to becoming spacelike (for

⁸Provided that $|A|$ remains sufficiently small. See the discussion below Eq. (56) for conditions on A that guarantee that $h^2/e^2 > 0$ near the horizon.

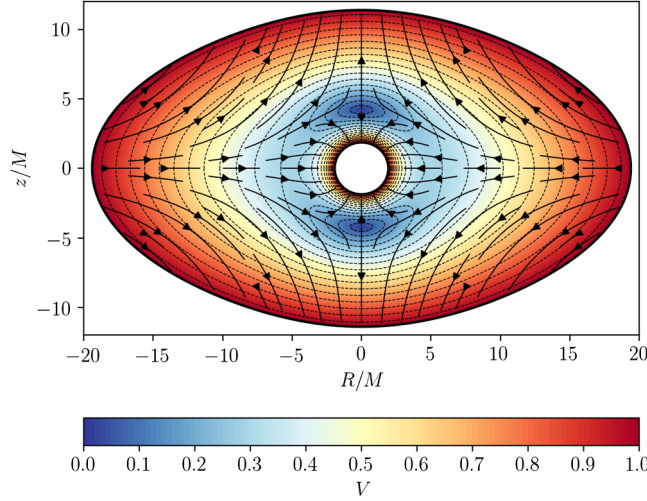


FIG. 1. Example of the axisymmetric quadrupolar flow with $AM = 0.01$ and a central Kerr black hole with $a = 0.5$. The stagnation points in this case are located along the polar axis at a coordinate distance $r = S \simeq 4.2M$. The figure shows isocontours of the three-velocity's magnitude V . Note that V becomes luminal at the event horizon ($r = r_+$) and at the outer ellipsoid indicated by a black, thick line. Fluid streamlines are indicated by thick, solid lines with an arrow. The axes correspond to the cylindrical-like coordinates $R = \sqrt{r^2 + a^2} \sin \theta$, $z = r \cos \theta$.

points outside \mathcal{E}). Moreover, from Eq. (50) we see that, at this surface, the density ρ becomes zero and, for points outside \mathcal{E} , ρ ceases to be a real quantity. For these reasons, we have to consider \mathcal{E} as the outermost boundary delimiting the spatial domain of applicability of the quadrupolar solution.

An expression for \mathcal{E} can be obtained by combining Eqs. (49) and (50), and rewrite the condition $V^2 = 1$ as the following second order polynomial in $\cos^2 \theta$:

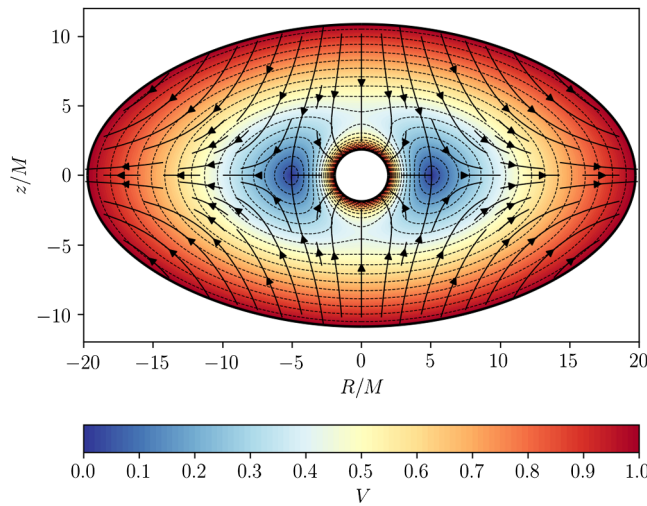


FIG. 2. Same as in Fig. 1, except that $AM = -0.01$ is negative. The stagnation points in this case are located on an equatorial ring at a coordinate distance $r = S \simeq 5M$.

$$c_2(r)\cos^4\theta + c_1(r)\cos^2\theta + c_0(r) = 0, \quad (54)$$

where

$$c_0(r) = r^2 + 2Mr + 4M^2 \left(\frac{r+r_+}{r-r_-} \right) - 24AMr_+(r-M) - 36A^2\Delta(r-M)^2, \quad (55a)$$

$$c_1(r) = a^2 + 72A(r-M)Mr_+ - 36A^2[(3r^2 - 6Mr + 2M^2 + a^2) - 6(r-M)^2\Delta], \quad (55b)$$

$$c_2(r) = 36A^2(M^2 - a^2)(3r^2 - 6Mr + 4M^2 - a^2). \quad (55c)$$

From Eq. (54), one can show that, in the limit $AM \ll 1$ (which necessarily implies $S \gg M$ and $r \gg M$), \mathcal{E} reduces to the simple ellipsoid of revolution described by

$$r^2(1 + 3\cos^2\theta) = x^2 + y^2 + 4z^2 = \frac{1}{(6A)^2}, \quad (56)$$

where, within this same limit, from Eq. (52) in Case 1 we have $A = M^2/(3S^3)$ while, from Eq. (53) in Case 2 it follows that $A = -2M^2/(3S^3)$.

On the other hand, by examining Eq. (54), it becomes apparent that, for a sufficiently large value of $|A|$, the surface \mathcal{E} actually pierces through the event horizon. When $A > 0$, \mathcal{E} first touches the horizon at $\theta = \pi/2$ while, when $A < 0$, \mathcal{E} starts merging with the horizon at $\theta = 0$. This means that the coefficient $|A|$ cannot be arbitrarily large or, in other words, that there is a minimum possible value S_{\min} for S such that $S_{\min} > r_+$. In order to find the maximum value A_{\max} , let us first substitute $\theta = \pi/2$ in Eq. (54) and then evaluate the result at $r = r_+$. Doing this gives the condition $c_0(r_+) = 0$, which can be solved explicitly for A as

$$A_{\max} = \frac{5M^2 - a^2 + 3M\sqrt{M^2 - a^2}}{24M(M^2 - a^2)}. \quad (57)$$

Similarly, for finding the minimum value A_{\min} , we substitute $\theta = 0$ in Eq. (54) and then evaluate the result at $r = r_+$. This results in the condition $c_2(r_+) + c_1(r_+) + c_0(r_+) = 0$ which can be solved for A as

$$A_{\min} = -\frac{M^2 + M\sqrt{M^2 - a^2}}{12M(M^2 - a^2)}. \quad (58)$$

For a Schwarzschild black hole, $A_{\max} = 1/3$ ($S \simeq 2.32M$) and $A_{\min} = -1/6$ ($S \simeq 2.80M$). On the other hand, for a Kerr black hole with $a = 0.5M$, we have $A_{\max} \simeq 0.41$ ($S \simeq 2.18M$) and $A_{\min} = -0.21$ ($S \simeq 2.61M$). Finally, note that in the extremal limit $a \rightarrow M$, A actually becomes unbounded, i.e., $(A_{\min}, A_{\max}) \rightarrow (-\infty, \infty)$. In Fig. 3 we

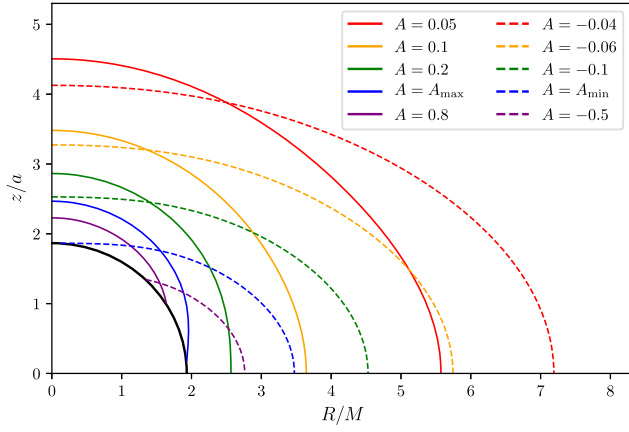


FIG. 3. Outermost boundary \mathcal{E} of the axisymmetric, quadrupolar flow for several values of the coefficient A . Solid, colored lines represent cases with $A > 0$, while dashed colored lines correspond to $A < 0$. The central black hole has a spin parameter $a = 0.5M$. The event horizon is indicated by a solid black line. Note that the curves \mathcal{E} corresponding to $A = A_{\max} \simeq 0.41$ and $A = A_{\min} \simeq -0.21$ touch the event horizon at the equator and pole, respectively. Curves with $A > A_{\max}$ or $A < A_{\min}$ actually pierce through the horizon. The axes correspond to the cylindrical-like coordinates $R = \sqrt{r^2 + a^2} \sin \theta$, $z = r \cos \theta$.

show examples of the boundary \mathcal{E} for different values of A for a Kerr black hole with $a = 0.5M$.

We conclude this section with some words regarding the case in which there is a misalignment between the accretion flow morphology and the black hole spin axis. As we show in further detail in the Appendix A, this case still allows for the

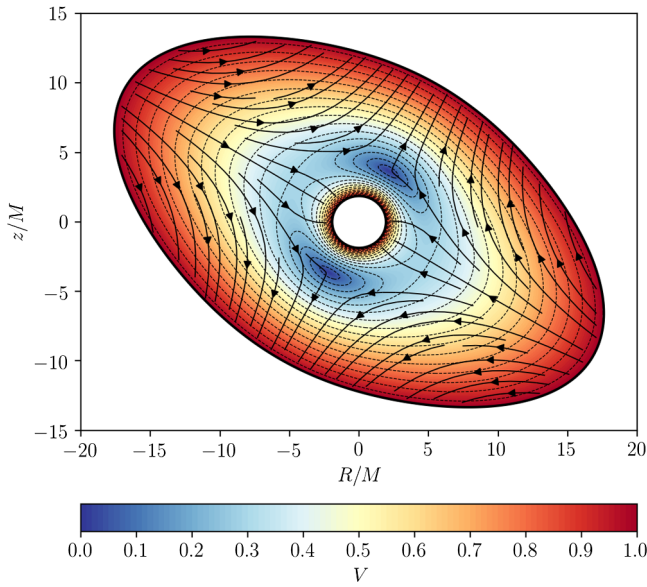


FIG. 4. Same as in Fig. 1, except that now we consider an inclination angle $\theta_0 = 30^\circ$. In order to show the stagnation points, the plot corresponds to the plane $\phi = \phi(\epsilon) = -0.15882$ (see Table II and accompanying discussion).

same kind of inflow-outflow solutions. However, the resulting expressions become more involved as lack of axisymmetry forces us to consider, in addition to the $(\ell, m) = (2, 0)$ mode, the contributions from the $m = -2, -1, 1, 2$ modes. As an example of the resulting accretion flow, in Fig. 4 we show the result of considering a misalignment angle of $\theta_0 = 30^\circ$ for the same flow parameters as in Fig. 1.

IV. CHOKED ACCRETION

Here we apply the results obtained in the previous section to the choked accretion scenario discussed in [34] for a Schwarzschild spacetime. The idea is the following: a gas flow is injected radially inwards from points lying close to the equator of a sphere of certain coordinate radius $r = \mathcal{R} > r_+$ (the “injection sphere”) toward the black hole. Part of this flow will be accreted by the black hole and disappears through the event horizon. However, when the injection rate is sufficiently large, it has been shown in [34] that (due to an anisotropic density field) part of the flow is diverted and ejected toward the poles. Under these conditions, the resulting flow is characterized by an inflow region originating from an equatorial belt in the injection sphere and a bipolar outflow region (Case 1 discussed in the previous section).

For the reasons mentioned in the introduction, we shall limit the rest of this work to the case in which the black hole’s angular momentum is perpendicular to the injection plane, that is, the equator of the injection sphere lies inside the equatorial plane $\theta = \pi/2$ of the Kerr spacetime.

For given values of the black hole parameters (M, a) , we characterize the resulting flow by specifying the fluid properties at the equator of the injection sphere, i.e., at $r = \mathcal{R}$, $\theta = \pi/2$. At this reference point, we prescribe the thermodynamic variables $\rho_0 = \rho(\mathcal{R}, \pi/2)$, $h_0 = h(\mathcal{R}, \pi/2)$, and the magnitude of the fluid’s three-velocity V_0 as measured by a ZAMO at this location. See Fig. 5 for a schematic representation of the setup.

By imposing these boundary conditions in Eqs. (46a) and (48), it follows that

$$e = \Gamma_0 h_0 \mathcal{R} \sqrt{\frac{\Delta_0}{\Sigma_0}}, \quad (59a)$$

$$A = \frac{\sqrt{\Sigma_0} V_0 - 2M r_+}{6(\mathcal{R} - M) \Delta_0}, \quad (59b)$$

where

$$\Delta_0 = (\mathcal{R} - r_-)(\mathcal{R} - r_+), \quad (60a)$$

$$\Sigma_0 = (\mathcal{R}^2 + a^2)\mathcal{R}^2 + 2M\mathcal{R}a^2, \quad (60b)$$

$$\Gamma_0 = (1 - V_0^2)^{-1/2}. \quad (60c)$$

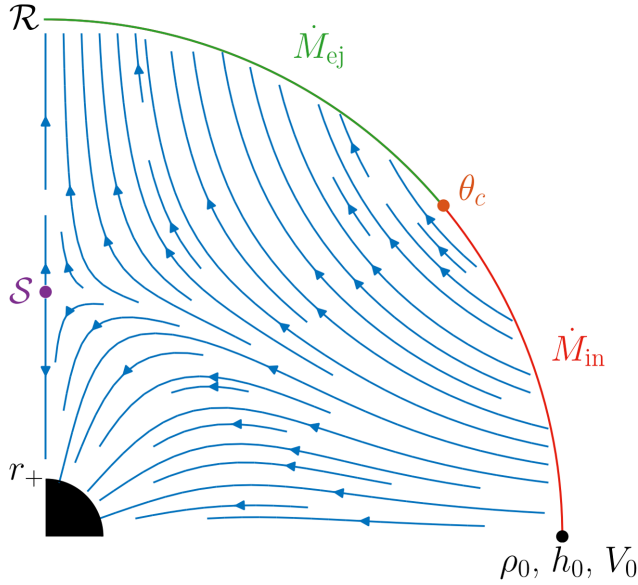


FIG. 5. Schematic representation of the choked accretion model in the polar plane. Shown are the black hole region ($r < r_+$), the location of the injection sphere ($r = \mathcal{R}$), the location of the reference point ($r = \mathcal{R}, \theta = \pi/2$) where the data (ρ_0, h_0, V_0) characterizing the solution are specified, the location of the stagnation point at $r = \mathcal{S}$ and the critical angle θ_c which separates the inflow from the outflow regions on the injection sphere.

With the values for the model parameters in Eqs. (59a) and (59b), all of the results derived in the previous section can be directly adopted. In particular, the velocity field of the corresponding solution is given by Eqs. (46a)–(46c), the fluid enthalpy by Eq. (49), and the density field by Eq. (50). Also note that the location of the stagnation points in this case follows by combining Eq. (52) and Eq. (59b), which results in

$$\frac{\sqrt{\Sigma_0} V_0}{M r_+} - 2 = \frac{(\mathcal{R} - r_-)(\mathcal{R} - r_+)(\mathcal{R} - M)}{(\mathcal{S} - r_-)(\mathcal{S} - r_+)(\mathcal{S} - M)}. \quad (61)$$

This equation can be explicitly solved for \mathcal{S} as

$$\begin{aligned} \mathcal{S} = M + & \left(\xi + \sqrt{\xi^2 - \frac{(M^2 - a^2)^3}{27}} \right)^{1/3} \\ & + \left(\xi - \sqrt{\xi^2 - \frac{(M^2 - a^2)^3}{27}} \right)^{1/3}, \end{aligned} \quad (62)$$

where

$$\xi = \frac{(\mathcal{R} - r_-)(\mathcal{R} - r_+)(\mathcal{R} - M) M r_+}{2(\sqrt{\Sigma_0} V_0 - 2 M r_+)}. \quad (63)$$

Finally note that, following a procedure analogous to that described in [34], one can obtain an expression for the projection of a streamline onto the $r - \theta$ plane given by

$$\Psi = \cos \theta \left[1 + \frac{(r - r_-)(r - r_+)(r - M)}{(\mathcal{S} - r_-)(\mathcal{S} - r_+)(\mathcal{S} - M)} \frac{\sin^2 \theta}{2} \right], \quad (64)$$

where Ψ is an integration constant. Streamlines with $|\Psi| < 1$ accrete onto the central black hole, those with $|\Psi| > 1$ escape along the bipolar outflow, while those with $\Psi = 1$ ($\Psi = -1$) are connected to the stagnation point at $\theta = 0$ ($\theta = \pi$).

A. Parameter range

The solution described by Eq. (44) with e and A as given in Eqs. (59a)–(59b) is characterized by six parameters: M and a describing the black hole, and \mathcal{R} , ρ_0 , h_0 and V_0 specifying the boundary conditions at the injection sphere. As discussed in [34], the obtained solution is actually scale-free with respect to the model parameters M (that sets the overall length scale), ρ_0 , and h_0 (that set the thermodynamic state of the fluid).

Once a Kerr background metric has been fixed with M and a (satisfying $|a| < M$), our next goal is to determine the range for the parameters \mathcal{R} and V_0 leading to solutions that:

- (1) Are well-defined within the domain $r \in [r_+, \mathcal{R}]$.
- (2) Present the inflow-outflow morphology of the choked accretion mechanism.

To this end, it is convenient to examine the ejection velocity defined as

$$V_{\text{ej}} \equiv V^{\hat{r}}(\mathcal{R}, 0) = \frac{2V_0\sqrt{\Sigma_0} - 6Mr_+}{\mathcal{R}^2 + a^2}, \quad (65)$$

where we have used Eqs. (46a) and (59b).

Condition 1 is satisfied by requiring that the gradient of the potential function remains timelike within the domain of interest, which is equivalent to the condition that the right-hand side of Eq. (49) is positive for all $r \in [r_+, \mathcal{R}]$ and all $\theta \in [0, \pi]$. In Appendix B we prove that this can be guaranteed by requiring

$$\mathcal{R} \geq 3M + r_+ \quad (66)$$

and demanding that $V_{\text{ej}} < 1$. From Eq. (65), this last condition in turn is equivalent to

$$V_0 < \frac{\mathcal{R}^2 + a^2 + 6Mr_+}{2\sqrt{\Sigma_0}}. \quad (67)$$

On the other hand, since we have already assumed inflow across the equator of the injection sphere, condition 2 is satisfied by requiring $V_{\text{ej}} > 0$. Again, from Eq. (65), this condition translates as

$$V_0 > \frac{3Mr_+}{\sqrt{\Sigma_0}}. \quad (68)$$

Therefore, the injection velocity parameter is restricted as

$$V_0 \in (V_{\text{min}}, V_{\text{max}}), \quad (69)$$

with

$$V_{\min} = \frac{3Mr_+}{\sqrt{\Sigma_0}}, \quad V_{\max} = \frac{\mathcal{R}^2 + a^2}{2\sqrt{\Sigma_0}} + V_{\min}. \quad (70)$$

B. Mass accretion, injection, and ejection rates

The accretion rate follows by substituting Eq. (59a) into Eq. (41), which results in

$$\dot{M} = 8\pi Mr_+ \frac{\rho e}{h} = 8\pi Mr_+ \Gamma_0 \rho_0 \mathcal{R} \sqrt{\frac{\Delta_0}{\Sigma_0}}. \quad (71)$$

By considering the flux of mass across the injection sphere, we can distinguish between the inflow and outflow fluxes, \dot{M}_{in} and \dot{M}_{ej} , respectively, defined in such a way that

$$\dot{M}_{\text{in}} - \dot{M}_{\text{ej}} = \dot{M}. \quad (72)$$

We can calculate both fluxes explicitly by examining the radial component of the fluid velocity at the injection sphere. From Eq. (46a), it follows the existence of a critical angle θ_c given by

$$\theta_c = \arccos \left[3 \left(1 - \frac{2Mr_+}{\sqrt{\Sigma_0} V_0} \right) \right]^{-1/2}, \quad (73)$$

such that there is inflow ($V^{\hat{r}} < 0$) for the equatorial belt defined by $\theta \in (\theta_c, \pi - \theta_c)$ and outflow ($V^{\hat{r}} > 0$) for the polar regions $\theta \in (0, \theta_c)$ and $\theta \in (\pi - \theta_c, \pi)$.

We can thus calculate \dot{M}_{in} in terms of θ_c as

$$\dot{M}_{\text{in}} = -4\pi \int_{\theta_c}^{\pi/2} \rho U^r \varrho^2 \sin \theta d\theta = \Lambda \dot{M} \quad (74)$$

where

$$\Lambda = \frac{2\cos^3 \theta_c}{3\cos^2 \theta_c - 1} = \frac{\sqrt{\Sigma_0} V_0}{3\sqrt{3}Mr_+} \left(1 - \frac{2Mr_+}{\sqrt{\Sigma_0} V_0} \right)^{-1/2}. \quad (75)$$

Clearly, in view of Eq. (72), it follows that

$$\dot{M}_{\text{ej}} = (\Lambda - 1)\dot{M}. \quad (76)$$

In Fig. 6 we show the isocontour levels of the rest-mass density field, as well as the magnitude of the three-velocity V , and the resulting fluid streamlines (black solid arrows) for a representative case with model parameters $a = 0.99M$, $\mathcal{R} = 10M$, and $V_0 = 0.2$.

In Fig. 7 we represent the regions in the parameter space (a, V_0) that lead to the choked accretion solution as discussed in Sec. IV A. The plotted isocontours correspond to the mass accretion rate \dot{M} expressed in units of $\dot{M}_0 = 8\pi M^2 \rho_0$. Each panel corresponds to a different value of the injection radius \mathcal{R} , from top to bottom $\mathcal{R}/M = 4, 8, 100$. The boundary lines delimiting each region correspond to the V_{\min} and V_{\max} limits given in Eq. (70). From this figure we can see a general trend for increasing values of \dot{M} as the value of V_0 increases, while \dot{M} decreases as the spin parameter a/M grows from zero to 1. Also note that the dependence on a of the limits V_{\min} and V_{\max} becomes less noticeable as increasingly larger values of \mathcal{R} are considered.

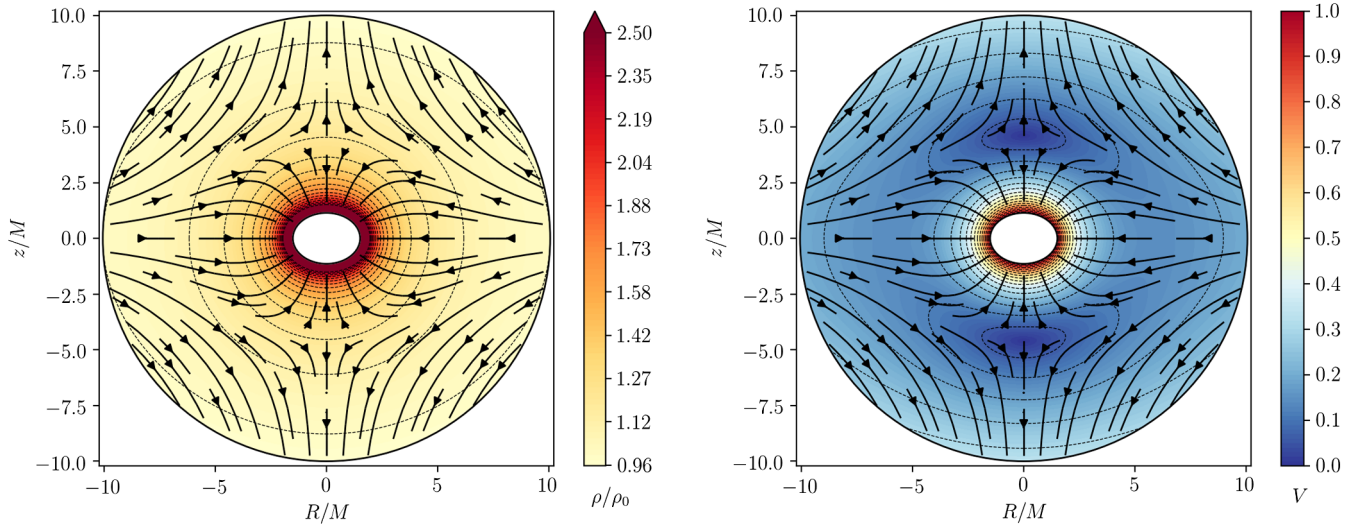


FIG. 6. Analytic model of choked accretion for a Kerr black hole with $a = 0.99M$ and flow parameters $\mathcal{R} = 10M$ and $V_0 = 0.2$. The figure shows isocontours of the fluid's normalized rest-mass density (left panel) as well as the magnitude of the three-velocity (right panel). The stagnation points are located on the symmetry axis with radius $S \simeq 4.6011M$. Fluid streamlines are indicated by thick, solid lines with an arrow. The axes correspond to the cylindrical-like coordinates $R = \sqrt{r^2 + a^2} \sin \theta$ and $z = r \cos \theta$.

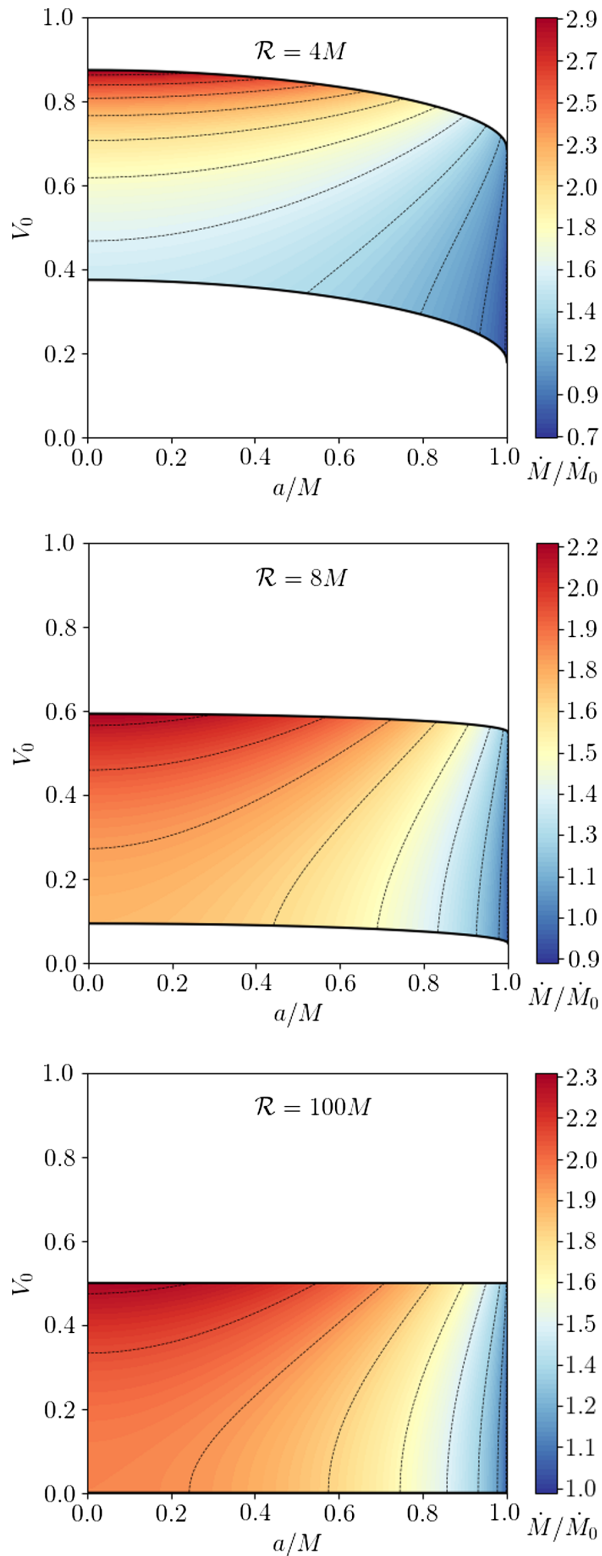


FIG. 7. Mass accretion rate as a function of the model parameters (a, V_0) in units of $\dot{M}_0 = 8\pi M^2 \rho_0$. The value of the injection radius \mathcal{R} in each case is indicated by a central label on each panel. The solid, black lines in each panel indicate the range of validity of the model parameters according to $V_0 \in (V_{\min}, V_{\max})$, with the lower boundary corresponding to V_{\min} and the upper one to V_{\max} .

In Fig. 8 we show three different properties of the choked accretion model as a function of the spin parameter a/M , for an injection sphere at $\mathcal{R} = 10M$. Each color line represents a different value of the injection velocity. The quantities correspond to: the mass accretion rate \dot{M} (in units of \dot{M}_0) in the top panel, the location of the stagnation points \mathcal{S} in the middle panel, and the ejection-to-injection mass rate ratio $\eta = \dot{M}_{\text{ej}}/\dot{M}_{\text{in}}$ in the bottom panel. For comparison, in the top

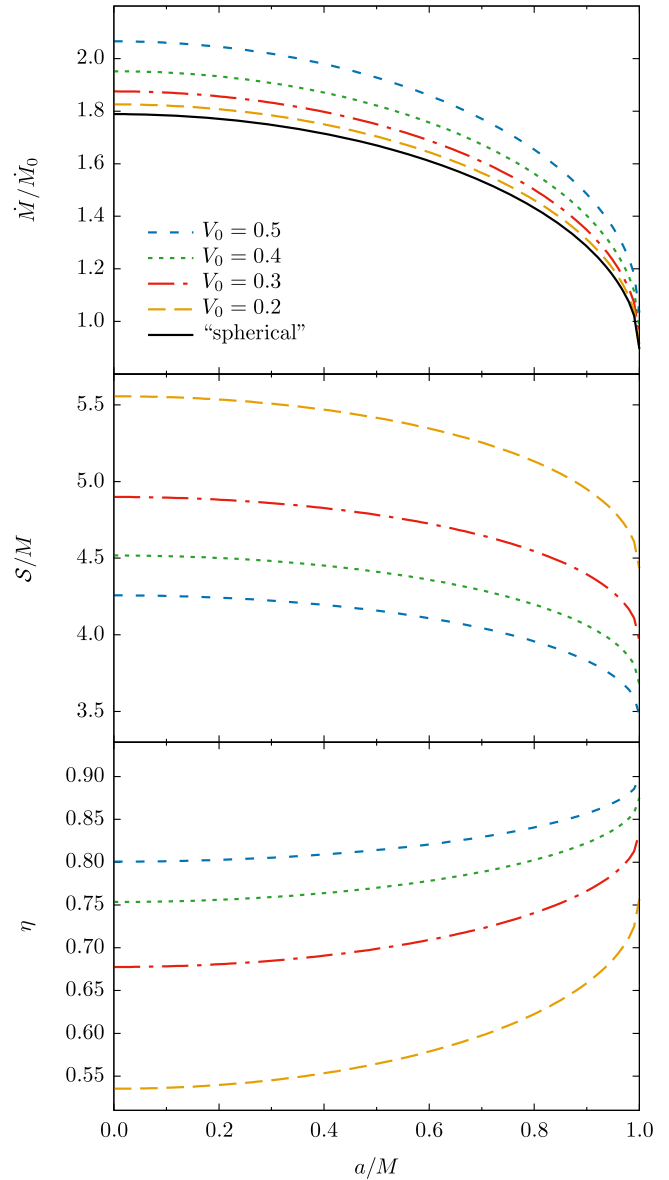


FIG. 8. Dependence of different properties of the choked accretion model on the spin parameter a/M and the injection velocity V_0 , for an injection sphere at $\mathcal{R} = 10M$. From top to bottom, each panel shows: the mass accretion rate \dot{M} in units of $\dot{M}_0 = 8\pi M^2 \rho_0$, the location of the stagnation points \mathcal{S}/M , and the ejection-to-injection mass rate ratio $\eta = \dot{M}_{\text{ej}}/\dot{M}_{\text{in}}$. The black line in the first panel corresponds to the “spherical” case $(\ell, m) = (0, 0)$, for which $V_0 = 2Mr_+/\sqrt{\Sigma_0} \simeq 0.0003$.

panel we also show, in a black solid line, the accretion rate for the “spherically symmetric” case $(\ell, m) = (0, 0)$ corresponding to $A = 0$ and $V_0 = 2Mr_+/\sqrt{\Sigma_0}$ (note that there is no ejection for V_0 in the range between this value and V_{\min}).

From the previous discussion we note that, as the injection velocity grows from V_{\min} to V_{\max} , we have:

- (i) The radii of the stagnation points decrease from $\mathcal{S} = \mathcal{R}$ to \mathcal{S}_{\min} .
- (ii) The critical angle increases from $\theta_c = 0$ to

$$\theta_{\max} = \arccos \left[3 \left(\frac{\mathcal{R}^2 + a^2 + 2Mr_+}{\mathcal{R}^2 + a^2 + 6Mr_+} \right) \right]^{-1/2}, \quad (77)$$

that, in the limit $\mathcal{R} \gg M$, converges to $\theta_{\max} = \arccos(1/\sqrt{3}) \simeq 54.7^\circ$.

- (iii) The mass injection rate increases from $\dot{M}_{\text{in}} = \dot{M}$ to

$$\dot{M}_{\text{in}} = \frac{\left[\frac{1}{3} \left(1 + \frac{4Mr_+}{(\mathcal{R}-r_+)(\mathcal{R}-r_-)} \right) \right]^{3/2}}{\frac{2Mr_+}{(\mathcal{R}-r_+)(\mathcal{R}-r_-)}} \dot{M}. \quad (78)$$

On the other hand, from Figs. 7 and 8, we note that, as the spin parameter a/M increases from zero to 1, the mass accretion rate onto the central black hole decreases down to $\sim 50\%$, the location of the stagnation point \mathcal{S} decreases by a factor of $\sim 10\%$, while the ejection-to-injection mass rate ratio η increases by up to $\sim 30\%$.

The analytic model studied in the previous sections allows us to explore in detail the effect of the black holes’s rotation on the choked accretion mechanism. Unfortunately, this model cannot easily be extended to perform a more general study including a more realistic equation of state. Keeping the irrotational assumption one can still formulate the problem in terms of a scalar potential; however, this potential satisfies a wave equation which is nonlinear for a realistic equation of state. Clearly, this makes it much harder to find an analytic treatment. For this reason, in the next section, we extend our study to the case of a general polytropic fluid by performing numerical simulations of the choked accretion scenario.

V. NUMERICAL SIMULATIONS

The general solution presented by Petrich, Shapiro and Teukolsky [31] revisited in Sec. II and, in particular, the choked accretion scenario discussed in Sec. IV, are limited by the assumption of an ultrarelativistic gas with a stiff equation of state, which leads to an unphysical speed of sound. In this section we show, by means of full hydrodynamic numerical simulations, that the main features of the choked accretion model are maintained when the adopted equation of state is extended to consider a general polytropic gas. Moreover, we make use of the analytical solution presented above as a 2D benchmark test for the validation of the code.

We perform full hydrodynamic numerical simulations with the open source code AZTEKAS⁹ [10,60], which solves the general relativistic hydrodynamic equations using a grid based finite volume scheme, with a high resolution shock capturing (HRSC) method.¹⁰ The set of equations are written in a conservative form using a variation of the “3 + 1 Valencia formulation” [61] for time independent, fixed metrics [62]. The time integration is achieved by adopting a second order total variation diminishing Runge-Kutta method [63]. The fluid evolution is performed in a fixed background metric corresponding to a Kerr black hole using the same (horizon-penetrating) Kerr-type coordinates adopted in Sec. II. The code uses as primitive variables the rest-mass density, pressure and the locally measured three-velocity vector (ρ, P, v_i) , where $v_i = \gamma_{ij}v^j$ and

$$v^i = \frac{U^i}{\alpha U^t} + \frac{\beta^i}{\alpha}, \quad i = r, \theta, \phi, \quad (79)$$

with α , β^i and γ_{ij} the lapse, shift vector and three-metric of the 3 + 1 formalism [64], written in these coordinates. See [10,33,34,60], for more details about the characteristics, test suite, and discretization method of AZTEKAS.

For all the simulations presented in this section, we adopt an axisymmetric 2D numerical domain $(r, \theta) \in [\mathcal{R}_{\text{acc}}, \mathcal{R}] \times [0, \pi/2]$, with a uniform polar grid and an exponential radial grid (see [33] for details), where \mathcal{R} is the radius of the outer boundary at which we implement a free outflow condition for the velocities and a fixed profile for the density and pressure. The inner boundary, set at $\mathcal{R}_{\text{acc}} = 1.1M$, for which we impose free outflow in all the variables, is chosen such that $r_- < \mathcal{R}_{\text{acc}} < r_+$ for all the explored values of a . We fix reflection conditions at both polar boundaries. A dissipative, second-order piecewise linear reconstruction for the primitive variables is used in order to avoid spurious oscillations due to these fixed boundary conditions.

In all the simulations, we evolve the equations from an initial state consisting of a constant density and pressure gas cloud, with zero initial three-velocity $v_i = 0$. The convergence to a steady-state is monitored by computing the mean mass accretion rate \dot{M} all over the domain, until its variation drops below 1 part in 10^4 .

A. Benchmark test

Taking advantage of the exact analytic description presented in the previous sections, we use the solution in Eq. (44) as a benchmark test to prove the convergence and stability of the AZTEKAS code for this type of problems. Moreover, this test is important in order to validate the

⁹The code can be downloaded from Ref. [59].

¹⁰Note that, even though we may expect smooth steady state solutions based on the analytical results, we are exploring an *a priori* unknown scenario in which shock fronts might develop during the evolution, or even persist in the stationary state.

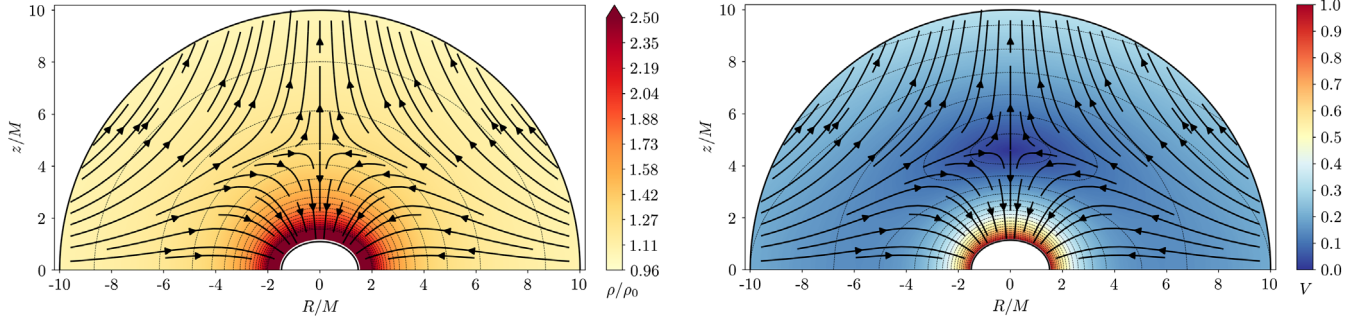


FIG. 9. Validation test of the AZTEKAS code. In this figure we show the steady state of numerical simulation for the benchmark test, which corresponds to the analytic solution presented in Sec. IV, with parameters $\mathcal{R} = 10M$, $V_0 = 0.2$, and $a = 0.99M$ (compare with Fig 6). The figure shows the isocontour levels of the normalized rest-mass density ρ/ρ_0 (left panel) and the magnitude of the three-velocity V , as measured by a ZAMO at this location. The fluid streamlines are indicated with black solid arrows. The simulation reached the stationary state at $t = 180M$, showing a good agreement with the analytic solution.

subsequent simulations discussed in this article. For these tests we implement the ultrarelativistic stiff equation of state in the numerical code.

We reproduce the analytic solution corresponding to the choked accretion model with $\mathcal{R} = 10M$, $V_0 = 0.2$ and a black hole spin $a = 0.99M$. We run the simulations in units such that $M = 1$ and set the value $\rho_0 = 1$ for the density at the reference point, although we remark here that, just as in the analytic case, the resulting steady-state solution is scale-free with respect to this specific value of ρ_0 . We perform four tests varying the spatial resolution by a factor of 2 each time (with number of grid points in the radial and polar directions 64×64 , 128×128 , 256×256 , 512×512 , respectively). The values for (ρ, P, v_i) from the analytic solution are imposed at the injection sphere as the boundary condition, and these values are extended into the whole numerical domain as the initial condition.

In Fig. 9 we show the isocontour levels of the density field and of the magnitude of the three-velocity V (as measured by a ZAMO) of the AZTEKAS simulations when the steady-state is reached at $t = 180M$. Likewise, the streamlines of the stationary flow are shown in both figures. From these simulations we obtain the stagnation point at $\mathcal{S} \simeq 4.6015M$ which coincides with the analytical value within the resolution uncertainty (see Fig. 6).

In Fig. 10 we show the evolution in time of the relative error between the numerical mass accretion rate \dot{M} and the analytic value \dot{M}_A , for all of the resolutions considered here. As expected, the relative error decreases for larger resolutions. Indeed, as further shown in Appendix C, from this benchmark test we confirm a second order convergence rate, as expected from the adopted numerical scheme.

B. Polytropic fluid

In order to explore the behavior of the choked accretion mechanism for a gas with a less restrictive equation of state, we perform numerical simulations of an ideal gas with a polytropic relation $P = K\rho^\gamma$, where γ is the adiabatic index.

We run experiments using a 256×256 grid resolution, for a wide range of values of the spin parameter $a/M \in [0, 1)$ and two different values of the adiabatic index $\gamma \in \{4/3, 5/3\}$.

The main feature of the choked accretion mechanism relies on the existence of a density contrast at the external boundary. Following closely the boundary treatment of [33,34], we fix the gas rest-mass density at the outer boundary as

$$\rho_b(\theta) = \rho_0(1 - \delta \cos^2 \theta), \quad (80)$$

where ρ_0 is the rest-mass density at the reference point $(\mathcal{R}, \pi/2)$ and δ is the density contrast defined as

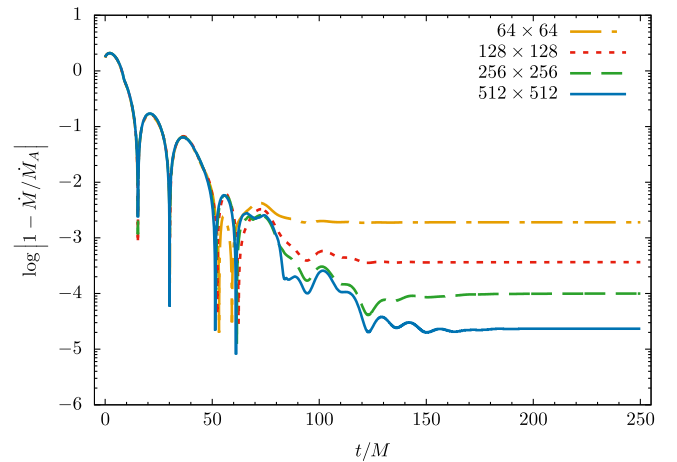


FIG. 10. Validation test for the AZTEKAS code. In this figure we show the evolution in time of the relative error between the numerical mass accretion rate \dot{M} and analytic value \dot{M}_A for the solution with parameters $\mathcal{R} = 10M$, $V_0 = 0.2$, and $a = 0.99M$. The four different resolutions used for this benchmark test are represented with different dashed lines, showing a diminishing of the error as the resolution increases which, as shown in Appendix C, is consistent with second order convergence.

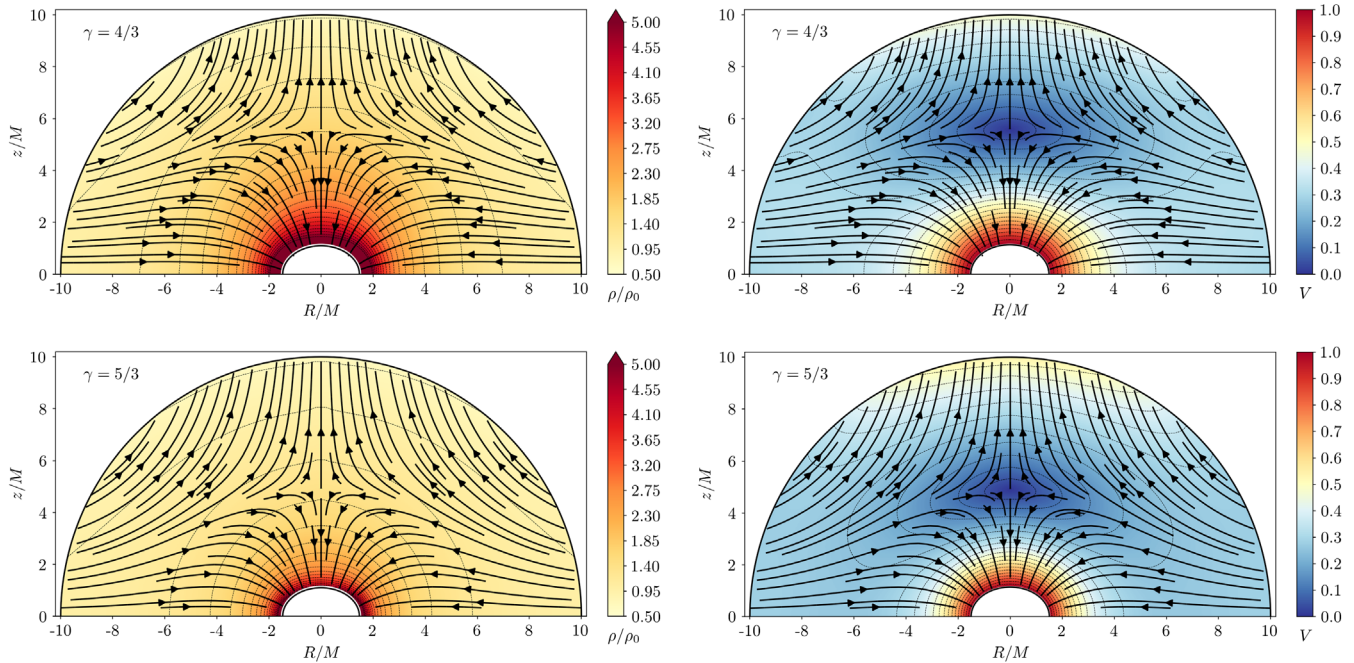


FIG. 11. Stationary state of the numerical simulations of the choked accretion mechanism for a rotating black hole with $a = 0.99M$, an injection radius of $\mathcal{R} = 10M$, a dimensionless temperature of $\Theta_0 = 1$ at the equator of the injection sphere, and a polytropic fluid with $\gamma = 4/3$ (top panels) and $5/3$ (bottom panels). On the left panels of this figure we show the isocontour levels of the normalized rest-mass density ρ/ρ_0 while, on the right panels, the magnitude of the three-velocity V as measured by the ZAMO. The fluid streamlines are indicated with black solid arrows, while a white solid line shows the location of the event horizon r_+ .

$$\delta = 1 - \frac{\rho_b(0)}{\rho_0}. \quad (81)$$

As mentioned in Sec. I, this density profile is motivated as a way to introduce the axisymmetric anisotropy associated with fluid rotation. In particular, it has been shown that low angular momentum fluids accreting onto a central massive object give rise to a quasispherical, oblate density distribution, as long as the angular momentum is sufficiently low as to avoid encountering the centrifugal barrier [37,38].

The pressure at this boundary is then determined by the polytropic relation $P = K\rho^\gamma$, where K is computed as [10]

$$K = \frac{1}{\rho_0^{\gamma-1}} \left[\frac{c_0^2(\gamma-1)}{\gamma(\gamma-1) - c_0^2} \right] \quad (82)$$

with c_0 the speed of sound at the reference point.

An extensive exploration of the choked accretion mechanism's dependence on \mathcal{R} , δ and c_0 can be found in [33] for the nonrelativistic regime and in [34] for the case of a Schwarzschild black hole. We performed a quick exploration of these three parameters, for a rotating black hole with $a = 0.99M$, and found essentially the same results as reported in those previous works. Moreover, we noticed that it is more intuitive, in order to compare with possible astrophysical settings, to use the dimensionless

temperature¹¹ $\Theta_0 = P_0/\rho_0$ rather than specifying c_0 . For this reason, in what follows, we shall take as representative values $\mathcal{R} = 10M$ for the domain size, $\delta = 0.5$ for the density contrast and $\Theta_0 = 1$ for the temperature of the gas at the reference point. This value of the dimensionless temperature corresponds to $c_0 \approx 0.52$ and $c_0 \approx 0.69$, for $\gamma = 4/3$ and $5/3$, respectively. Furthermore, in order to have an appropriate baseline reference for each combination of the γ and a parameters, we also run simulations corresponding to “spherical” accretion in each case (i.e., same values for γ and a but a $\delta = 0$ density contrast).

We evolve all the simulations until the stationary state has been reached (within the previously mentioned limit of accuracy in which variations in the mean accretion rate drop below 1 part in 10^4). The relaxation time depends on γ , as well as on the value of a , but in all cases it is found to conform to $500M < t < 1500M$. We also perform a self-convergence test which is presented in Appendix C.

In Fig. 11 we show the resulting steady-state, rest-mass density field and magnitude of the three-velocity V for the $a = 0.99M$ case. The top panels show the results

¹¹Note that our definition of the dimensionless temperature is only valid for an ideal gas equation of state. In terms of natural units, the general definition of the dimensionless temperature [1] is $\Theta = k_B T/m_b c^2$, with T the fluid temperature, c the speed of light, k_B Boltzmann's constant, and m_b the average baryonic mass.

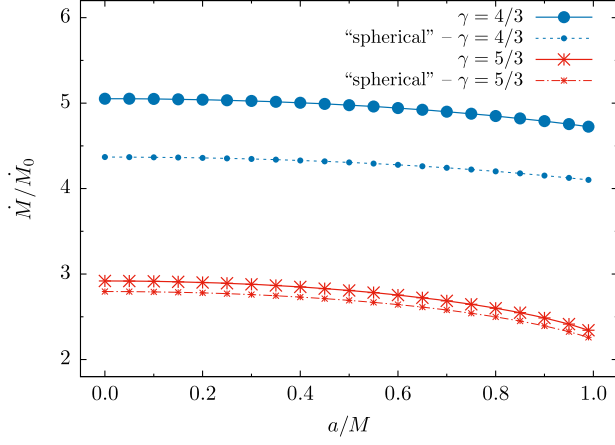


FIG. 12. Mass accretion rate as a function of the spin parameter. The blue and red dotted lines correspond to $\gamma = 4/3$ and $5/3$, respectively. The black dashed lines represent their respective “spherical” accretion values, i.e., $\delta = 0$.

corresponding to $\gamma = 4/3$ while the bottom panels those for $\gamma = 5/3$. The black solid arrows represent the fluid streamlines and the solid white line the location of the outer horizon r_+ . As we can see from these figures, there is not a strong qualitative difference in the flow morphology for different values of γ , neither for the one presented in the nonrotating black hole case [34]. Moreover, although the streamlines configuration are similar to the analytical case, the ejection velocity at the polar region is larger for the polytropic fluid (see Fig. 6).

In Fig. 12 we show the dependence of the mean mass accretion rate \dot{M} on the spin parameter a , for all the simulations performed in this study. The blue dots correspond to $\gamma = 4/3$, while the red crosses to $\gamma = 5/3$. The points joined by the dashed lines represent the corresponding “spherical” accretion case ($\delta = 0$). It is interesting to notice from this figure that, for each value of γ , the dependence on a remains the same regardless of the value of δ (except for a re-scaling factor that depends on γ). This suggests that the change in the mass accretion rate with the spin parameter is an intrinsic characteristic of the accretion

TABLE I. Results for our simulations with parameters $\mathcal{R} = 10M$, $\delta = 0.5$ and $\Theta_0 = 1$.

a/M	$\gamma = 4/3$				$\gamma = 5/3$			
	S/M	\dot{M}	\dot{M}_{ej}	\dot{M}_{in}	S/M	\dot{M}	\dot{M}_{ej}	\dot{M}_{in}
0.0	5.781	5.052	2.195	7.246	5.247	2.919	2.768	5.687
0.25	5.770	5.033	2.201	7.234	5.231	2.892	2.777	5.670
0.5	5.734	4.977	2.220	7.197	5.179	2.808	2.805	5.614
0.75	5.672	4.876	2.256	7.132	5.083	2.647	2.857	5.504
0.99	5.581	4.725	2.308	7.032	4.905	2.343	2.947	5.289

NOTE—The quantities \dot{M} , \dot{M}_{in} and \dot{M}_{ej} are given in units of $\dot{M}_0 = 8\pi M^2 \rho_0$.

onto a Kerr black hole, and not of the choked accretion mechanism. A more complete study of the “spherical” accretion case onto a rotating black hole will be explored elsewhere.

In addition to the mass accretion rate, we compute the mass injection rate \dot{M}_{in} and the mass ejection rate \dot{M}_{ej} at the injection sphere (as defined in Sec. IV B). We also extract

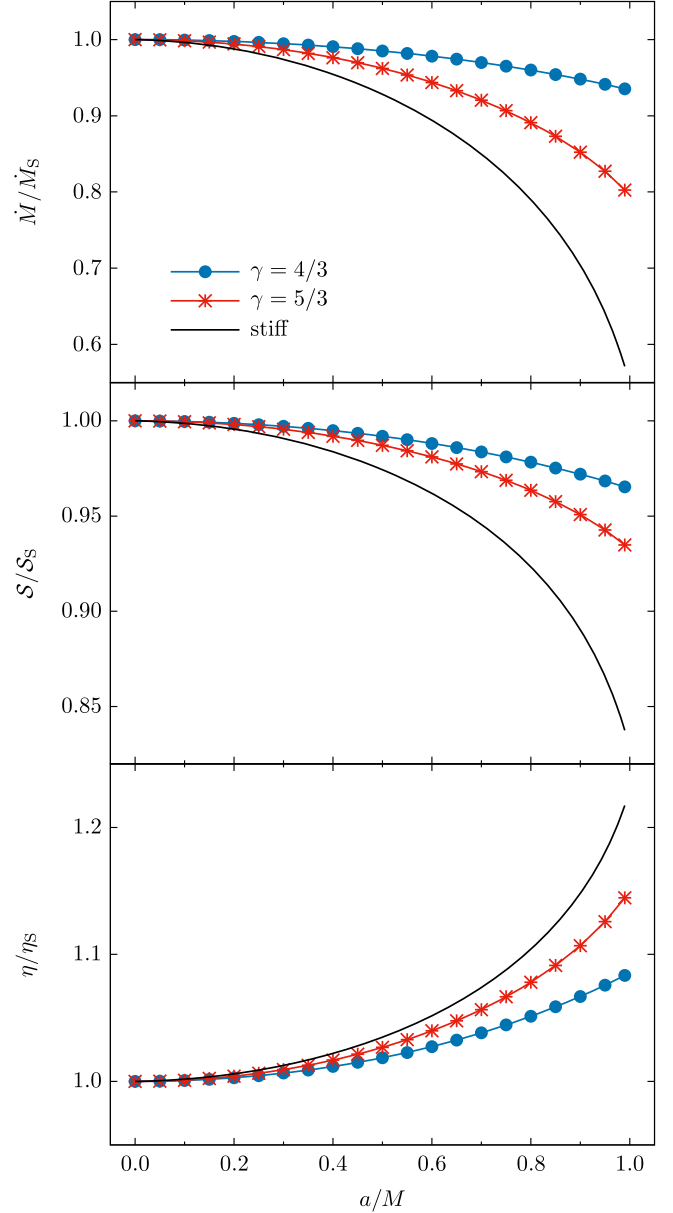


FIG. 13. Dependence of different properties of the choked accretion simulations on the spin parameter a/M and γ . From top to bottom, each panel shows: the mass accretion rate \dot{M} , the location of the stagnation point S/M , and the ejection-to-injection mass rate ratio $\eta = \dot{M}_{\text{ej}}/\dot{M}_{\text{in}}$. Each panel is normalized by its corresponding nonrotating case value, which is denoted with the subscript S . The black solid line represents the analytic solution presented in Sec. IV for an ultrarelativistic stiff fluid.

from the simulation's results the location of the stagnation point \mathcal{S} . In Table I we present a summary of these results for a representative set of the performed simulations. We also measure the magnitude of the three-velocity at the equator V_0 and at the pole V_{ej} , which do not present a significant dependence on the spin parameter, maintaining a value around $V_0 = 0.30$ and $V_{\text{ej}} = 0.54$, for $\gamma = 4/3$; and $V_0 = 0.29$ and $V_{\text{ej}} = 0.48$, for $\gamma = 5/3$.

In Fig. 13 we show the dependence on a for the mass accretion rate \dot{M} (top panel), the location of the stagnation point \mathcal{S} (middle panel), and the ejection-to-injection mass rate η (bottom panel), for both values of γ . In order to clearly see the change with a for these quantities, we normalize them by \dot{M}_S , \mathcal{S}_S and η_S , respectively, which correspond to the values obtained in the non-rotating case ($a = 0$). Moreover, we also include the stiff analytic solution obtained in Sec. IV, using as the V_0 parameter the value found for $\gamma = 5/3$.

As we can see from Fig. 13, the mass accretion rate decreases with the spin parameter down to a factor of $\sim 10\%$ (20%) for the $\gamma = 4/3$ ($\gamma = 5/3$) case as the spin parameter increases to its maximum value. On the other hand, the location of the stagnation point only decreases down to a factor of $\sim 5\%$ for both values of γ . In contrast, the ejection-to-injection mass rate (η) increases up to a factor of 10 to 15% as $a \rightarrow M$.

Even though it is not possible to make a direct comparison of the numerical simulations with the analytic model of an ultrarelativistic stiff fluid, since in each case we are using different equations of state and the boundary conditions are not exactly the same, there are still some observations that can be drawn from Fig. 13. First of all, there is a shared, qualitatively consistent dependence of the different quantities shown in this figure on the spin parameter a , both for the polytropic gas and the stiff fluid. Moreover, it is also clear that there is a stronger response from the stiff fluid to the black hole rotation. Indeed, from this figure we see that the analytic solution presented in Sec. IV can be used as a lower limit for the mass accretion rate and for the location of the stagnation point that would follow for a polytropic gas, whereas it can be used as an upper limit for the ejection-to-injection mass rate ratio. Finally, we note that there is a clear trend for a stronger dependence on the spin parameter a as the fluid stiffens ($\gamma \rightarrow 2$).

VI. SUMMARY AND CONCLUSIONS

The choked accretion model is a purely hydrodynamical mechanism with which it is possible to obtain a bipolar outflow by perturbing an originally radial inflow. The necessary conditions for this mechanism to operate consist of a sufficiently large mass accretion rate onto a central massive object (as compared to the Bondi accretion rate), and an anisotropic density field in which the equatorial

region is at a higher density than at the poles. Potential astrophysical applications of this model for outflow-generating phenomena are mentioned in the introduction and have been discussed in further detail in [33,34].

In this article we have presented a generalization of the choked accretion mechanism for the case of a rotating Kerr black hole, extending the perturbative study initiated by Hernandez *et al.* [32] and the subsequent analytical and numerical studies at the nonrelativistic level [33] and in the Schwarzschild case [34]. Here we have shown, using both analytic solutions and numerical simulations, that the choked accretion's main features are recovered in the presence of a rotating black hole, regardless of the value of the spin parameter.

Our analytic model is based on the steady-state, irrotational solution for an ultrarelativistic stiff fluid presented by Petrich, Shapiro and Teukolsky [31]. We have derived the general equations of the model using horizon-penetrating Kerr-type coordinates and then mostly focused on the axisymmetric quadrupolar case, studying the dependence of the flow morphology on the unique parameter A that remains free (we have also briefly discussed the misaligned quadrupolar case at the end of Sec. III and in Appendix A). Depending on the sign of this parameter, the flow describes an equatorial inflow-bipolar outflow solution ($A > 0$) or an equatorial outflow-polar inflow solution ($A < 0$). Given that it has a wider applicability in an astrophysical context and corresponds to the choked accretion scenario discussed in this article, we have mainly focused on the case $A > 0$ and discussed the physical properties of the choked accretion model, including its mass accretion rate, location of the stagnation points and ejection-to-injection mass rate ratio. We have also extended the present study to a perfect fluid obeying a polytropic relation with adiabatic index $\gamma = 4/3$ and $5/3$, by performing full hydrodynamic, relativistic numerical simulations of an ideal gas in a Kerr background metric.

In previous works, it was found that the total mass accretion rate in the choked accretion model has a threshold value close to the one found in the spherical accretion scenario. In this study, based on both analytic and numerical analysis, we have extended this result to the case of a rotating black hole and shown that the accretion rate obtained from the ‘‘spherically symmetric’’ case, in which the density contrast is set to zero at the injection sphere, still yields a lower limit for the threshold value for the choking mechanism to work (see Figs. 8 and 12). Note, however, that in the case of the Kerr spacetime there is no analytic equivalent to Michel's solution in the Schwarzschild case. Therefore, this problem has to be studied by numerical means as we have briefly discussed here and will further address in a future work.

Most of the configurations analyzed in this article have focused on the aligned case, in which the axis of the bipolar outflow coincides with the rotation axis of the black hole, in

which case the fluid elements have zero angular momentum and hence would not affect the black hole's spin during their accretion. However, in Appendix A we have also analyzed a misaligned configuration, and it is interesting to note that such an accretion flow would slow down the black hole's rotation, as the results in Sec. II C show.

This work continues a series of analytic and numerical studies of the choked accretion model as a purely hydrodynamical mechanism for generating axisymmetric outflows. In future work we intend to expand the ingredients involved in this model, by including additional physics such as fluid angular momentum, viscous transport, and magnetic fields, in order to explore the applicability of the model in outflow-generating astrophysical systems.

ACKNOWLEDGMENTS

It is a pleasure to thank Diego López-Cámara and Xavier Hernández for fruitful discussions and useful comments on a previous version of this article. We also thank the anonymous referee for helpful suggestions and remarks. This work was supported in part by CONACyT (CVUs 788898, 673583) and by a CIC Grant to Universidad Michoacana.

APPENDIX A: THE MISALIGNED QUADRUPOLEAR FLOW

In Sec. III we discussed the axisymmetric quadrupolar flow solution and some important properties regarding its morphology, and in Sec. IV this solution was applied to the choked accretion scenario. This flow has the property of being reflection-symmetric about the equatorial plane of the Kerr black hole, such that the bipolar outflow regions are aligned with the symmetry axis. In this appendix, we discuss an example in which the flow discussed in Secs. III and IV is “rotated” by an angle θ_0 about an axis within the plane $\theta = \pi/2$ (in a sense made precise below).

When the black hole is nonrotating, the aforementioned rotation can be carried out exactly and is simply a rigid rotation of the (spherically symmetric) Schwarzschild geometry the Kerr metric reduces to in the limit $a = 0$. We may construct this rotated solution explicitly by writing the angular dependency in the axisymmetric quadrupolar flow solution (45) in the form

$$3 \cos^2 \theta - 1 = 2P_2(\cos \theta) = 2P_2(\mathbf{x}' \cdot \mathbf{x}), \quad (\text{A1})$$

with P_2 denoting the Legendre polynomial P_ℓ with $\ell = 2$ and $\mathbf{x} = (\sin \theta \cos \phi, \sin \theta \sin \phi, \cos \theta)$ and $\mathbf{x}' := (0, 0, 1)$. Applying a rotation by the angle θ_0 about the y axis is equivalent to replacing the vector $\mathbf{x}' = (0, 0, 1)$ with the vector $\mathbf{x}' = (\sin \theta_0, 0, \cos \theta_0)$ in the right-hand side of Eq. (A1). Recalling the addition theorem for spherical harmonics (see, for instance, chapter 3.6 in Ref. [65])

$$P_\ell(\mathbf{x}' \cdot \mathbf{x}) = \frac{4\pi}{2\ell + 1} \sum_{m=-\ell}^{\ell} (Y^{\ell m})^*(\theta', \phi') Y^{\ell m}(\theta, \phi), \quad (\text{A2})$$

we can write the rotated quadrupolar flow solution on a Schwarzschild background as in Eq. (44) with $a = 0$ and $F(r, \theta, \phi)$ given by

$$F(r, \theta, \phi) = \frac{8\pi}{5} (3r^2 - 6Mr + 2M^2) \sum_{m=-\ell}^{\ell} d_m Y^{\ell m}(\theta, \phi) \quad (\text{A3})$$

with the coefficients $d_m := (Y^{\ell m})^*(\theta_0, 0)$. This has again the form of the general solution in Eq. (17) when $a = 0$, and hence it describes a solution of the potential flow equation (1). However, it bears exactly the same physical content as the original axisymmetric quadrupolar flow solution discussed in Secs. III and IV, since it is obtained from it by an isometry.

When $a \neq 0$, the method we have just described cannot be performed, since merely replacing $\mathbf{x}' = (0, 0, 1) \mapsto \mathbf{x}' = (\sin \theta_0, 0, \cos \theta_0)$ in the right-hand side of Eq. (A1) would not yield a solution of Eq. (1). This is due to the m -dependency in the radial functions appearing in the expansion (18) which, in turn, arises because of the lack of spherical symmetry of the Kerr metric when $a \neq 0$. On the other hand, we still have the freedom of choosing the five complex constants A_{2m} in Eq. (18), as long as they satisfy the reality conditions (19). In particular, we can choose these coefficients such that the function $F(r, \theta, \phi)$ has the same weights d_m as in Eq. (A3) on *some particular constant r surface*. This is equivalent to applying the rotation $\mathbf{x}' = (0, 0, 1) \mapsto \mathbf{x}' = (\sin \theta_0, 0, \cos \theta_0)$ on this particular surface only, which yields

$$F(r, \theta, \phi) = \frac{4\pi}{5} (r_+ - r_-)^2 F(-2, 3; 1, -x_*) \times \sum_{m=-2}^2 \frac{F(-2, 3; 1 + i m \alpha, -x_*)}{F(-2, 3; 1 + i m \alpha, -x_*)} d_m Y^{2m}(\theta, \phi), \quad (\text{A4})$$

where we recall that $\alpha = 2a/(r_+ - r_-)$ and $x = (r - r_+)/ (r_+ - r_-)$ and x_* is the value of x corresponding to the location of the surface where the rotation is applied. Note that for $x = x_*$ the weight functions are the same as in Eq. (A3), as required. Notice also that when $\theta_0 = 0$ (in which case only the $m = 0$ mode contributes and $(Y^{20})^*(0, 0) Y^{20}(\theta, \phi) = 5P_2(\cos \theta)/(4\pi)$), the function F in Eq. (A4) reduces to the function F in Eq. (45) in the aligned case.

To determine uniquely the solution it remains to choose the value for x_* . One possibility is to choose it such that it corresponds to the radius of the injection sphere $r = \mathcal{R}$.

However, note that for finite r , the two-surfaces $(t, r) = \text{const}$ are not strict metric spheres in the Kerr geometry, so we argue that only in the asymptotic limit $r \rightarrow \infty$ does it make sense to apply the rotation in a sensible way. Hence, even though the flow is only well defined inside a finite region, we exploit the fact that the potential Φ itself is well defined for all $r > r_-$ and thus we take the limit $x_* \rightarrow \infty$ in Eq. (A4). This finally yields

$$F(r, \theta, \phi) = \frac{4\pi}{5} \sum_{m=-2}^2 [6r^2 - 6(2M - im a)r + 4M^2 + 2a^2 - 2m^2 a^2 - 6im aM] d_m Y^{2m}(\theta, \phi). \quad (\text{A5})$$

Using the explicit representation of the spherical harmonics one can write the result in the form

$$F(r, \theta, \phi) = \frac{1}{4} a_0(r) (3\cos^2\theta_0 - 1)(3\cos^2\theta - 1) + 3[a_1(r) \cos\phi + b_1(r) \sin\phi] \times \cos\theta_0 \sin\theta_0 \cos\theta \sin\theta + \frac{3}{4} [a_2(r) \cos(2\phi) + b_2(r) \sin(2\phi)] \sin^2\theta_0 \sin^2\theta, \quad (\text{A6})$$

with the radial functions

$$a_m(r) = 6r^2 - 12Mr + 4M^2 + 2(1 - m^2)a^2, \quad (\text{A7})$$

$$b_m(r) = -6ma(r - M). \quad (\text{A8})$$

Another useful representation of the solution is obtained by writing it in terms of the ‘‘rotated’’ Cartesian coordinates $(r\xi, r\eta, r\zeta)$, where

$$\begin{pmatrix} \xi \\ \eta \\ \zeta \end{pmatrix} = \begin{pmatrix} \cos\theta_0 & 0 & -\sin\theta_0 \\ 0 & 1 & 0 \\ \sin\theta_0 & 0 & \cos\theta_0 \end{pmatrix} \begin{pmatrix} \sin\theta \cos\phi \\ \sin\theta \sin\phi \\ \cos\theta \end{pmatrix}. \quad (\text{A9})$$

This gives

$$F(r, \theta, \phi) = 2(3r^2 - 6Mr + 2M^2 + a^2)P_2(\zeta) - 6\epsilon[3(r - M)\eta + a \cos\theta_0 \xi] \zeta + 6\epsilon^2(\eta^2 - \zeta^2), \quad (\text{A10})$$

with $\epsilon := a \sin\theta_0$. Note that for $\epsilon = 0$ (which is the case if the black hole is nonrotating or the inclination angle θ_0 vanishes), the second line in Eq. (A10) vanishes and one recovers the axisymmetric quadrupolar flow solution (45) with the rotated symmetry axis $r\zeta$.

We conclude this appendix by showing that for small values of $|\epsilon|$ the solution Eq. (44) with $A > 0$ and F as in Eq. (A10) still has two stagnation points whose location can be determined by a perturbative method. To this

purpose we introduce the vector-valued function $H(\epsilon; w)$ with $w = (r, \xi, \eta)$, defined as

$$H(\epsilon; w) := \left(\Delta \frac{\partial F}{\partial r} - \frac{2Mr_+}{A}, \frac{\partial F}{\partial \xi}, \frac{\partial F}{\partial \eta} \right), \quad (\text{A11})$$

where the constraint $\zeta^2 = 1 - \xi^2 - \eta^2$ should be taken into account (since the function F is symmetric with respect to $(\xi, \eta, \zeta) \mapsto -(\xi, \eta, \zeta)$ it is sufficient to perform the analysis for the case $\zeta > 0$). The location of the stagnation points (for a given value of ϵ) is characterized by a zero of the function $H(\epsilon; \cdot)$, see Eq. (34). For $\epsilon = 0$ one can check that the zero lies at

$$w = w_0 = (r_0, 0, 0), \quad (\text{A12})$$

with $r_0 = S$ as in Eq. (52). To determine the location $w(\epsilon)$ of the zero for small values of $|\epsilon|$ one can differentiate both sides of the equation $H(\epsilon; w(\epsilon)) = 0$ with respect to ϵ , which gives

$$DH(\epsilon; w(\epsilon)) \frac{dw}{d\epsilon}(\epsilon) + \frac{\partial H}{\partial \epsilon}(\epsilon; w(\epsilon)) = 0, \quad (\text{A13})$$

where DH refers to the Jacobi matrix of H with respect to w . Evaluating at $\epsilon = 0$ yields

$$DH(0; w_0)w_1 = -\frac{\partial H}{\partial \epsilon}(0; w_0), \quad w_1 := \frac{dw}{d\epsilon}(0). \quad (\text{A14})$$

Since $DH(0; w_0) = 6K \text{diag}(2, -1, -1)$ with $K := 3r_0^2 - 6Mr_0 + 2M^2 + a^2 > 0$, the first-order correction w_1 is uniquely determined by this equation (and according to the implicit function theorem, the function $H(\epsilon; \cdot)$ has a unique zero for small enough values of $|\epsilon|$). By further differentiation of Eq. (A13) one can compute the higher-order corrections of $w(\epsilon)$. Up to terms of order ϵ^3 this gives

$$r(\epsilon) = r_0 + \frac{Mr_+}{4AK^2} (3M^2 - 2a^2)\epsilon^2 + \mathcal{O}(\epsilon^3), \quad (\text{A15})$$

$$\xi(\epsilon) = -\frac{a}{K}\epsilon + \mathcal{O}(\epsilon^3), \quad (\text{A16})$$

$$\eta(\epsilon) = -\frac{3(r_0 - M)}{K}\epsilon + \mathcal{O}(\epsilon^3). \quad (\text{A17})$$

A few numerical examples for the case $AM = 0.01$ and $a/M = 0.5$ are given in Table II. The particular entry corresponding to $\theta_0 = 30^\circ$ corresponds to the flow shown in Fig. 4.

Finally, we point out that the characterization of the stagnation point we have used so far, based on the vanishing of the ZAMO’s three-velocity, might not be the most adequate definition from a conceptual point of view when $\epsilon \neq 0$. This is due to the fact that a ZAMO

TABLE II. Location of the stagnation point for the parameter values $AM = 0.01$ and $a/M = 0.5$. Five significant figures are shown. The perturbative calculation refers to the expansion (A15)–(A17), truncating the $\mathcal{O}(\varepsilon^3)$ terms and translated back to the angle coordinates $\theta(\varepsilon)$ and $\phi(\varepsilon)$ by means of Eq. (A9). The numerical calculation is based on the `fsolve` routine in MAPLE, using 15 digits of precision and the seed values provided by the perturbative calculation. As can be appreciated from the table, the values provided by the quadratic expansion (A15)–(A17) give a very good approximation [less than 1% relative error in the quantities $(r(\varepsilon), \theta(\varepsilon), \phi(\varepsilon))$].

θ_0	Perturbative calculation			Numerical calculation		
	$r(\varepsilon)/M$	$\theta(\varepsilon) - \theta_0$	$\phi(\varepsilon)$	$r(\varepsilon)/M$	$\theta(\varepsilon) - \theta_0$	$\phi(\varepsilon)$
0°	4.2242	0.0	(undefined)	4.2242	0.0	(undefined)
10°	4.2243	0.00073719	-0.15890	4.2243	0.00075882	-0.15886
20°	4.2244	0.0012597	-0.15902	4.2244	0.0014289	-0.15884
30°	4.2245	0.0013812	-0.15919	4.2245	0.0019307	-0.15882
40°	4.2247	0.00096893	-0.15939	4.2247	0.0022033	-0.15879
50°	4.2249	-0.000035935	-0.15959	4.2249	0.0022116	-0.15875
60°	4.2250	-0.0016067	-0.15972	4.2251	0.0019516	-0.15872
70°	4.2252	-0.0036296	-0.15979	4.2253	0.0014526	-0.15870
80°	4.2253	-0.0059139	-0.15974	4.2254	0.00077429	-0.15868

rotates around the black hole with angular frequency Ω [see Eq. (23)], and hence such an observer which is located at $r = r(\varepsilon)$ and $\theta = \theta(\varepsilon)$ only sees the fluid at rest in its frame at the moments it crosses the plane $\phi = \phi(\varepsilon)$. In other words, the world line of the stagnation point defined in this way does not agree with the one of the ZAMO. An alternative definition of the stagnation point which does not suffer from this problem can be given by requiring the fluid's three-velocity of a static observer (as opposed to a ZAMO) to vanish. The location of this point can be determined perturbatively by the same method as the one we have just described; however we adopt the former definition in view of the compatibility with Fig. 4 in which the ZAMO's three-velocity is shown.

APPENDIX B: BOUNDS ON THE PARAMETER A

In this appendix we prove that for sufficiently large radii \mathcal{R} of the injection sphere, the maximum range $A_-(\mathcal{R}) < A < A_+(\mathcal{R})$ for the parameter A in the axisymmetric quadrupolar potential Φ in Eq. (44) to yield a well-defined flow on the domain $r_+ \leq r \leq \mathcal{R}$ is determined by the requirement for the magnitude of the three-velocity V to be subluminal at the poles of the injection sphere. That is, we show that for any large enough value of \mathcal{R} , $V < 1$ at the poles of the sphere $r = \mathcal{R}$ guarantees that the gradient of Φ is everywhere timelike on the domain $r_+ \leq r \leq \mathcal{R}$.

To prove this claim, we go back to the investigation toward the end of Sec. III, from which it follows that the gradient $\nabla_\mu \Phi$ is timelike if and only if

$$q^2 \frac{h^2}{e^2} = c_2(r) \cos^4 \theta + c_1(r) \cos^2 \theta + c_0(r) > 0. \quad (\text{B1})$$

In the limit $AM \ll 1$ it was shown that the outer boundary of the region for which (B1) holds describes a large ellipsoid of revolution with semi-axes equal to $1/(6|A|)$, $1/(6|A|)$, $1/(12|A|)$ in the x , y , z -directions, respectively. It

is then clear that for \mathcal{R} large enough, the outer boundary first intersects the sphere $r = \mathcal{R}$ at the poles $\theta = 0, \pi$. The corresponding values for A can be determined by evaluating the condition $c_2(\mathcal{R}) + c_1(\mathcal{R}) + c_0(\mathcal{R}) = 0$, which yields

$$A_\pm(\mathcal{R}) = \pm \frac{1}{12(\mathcal{R} - M)} \left[1 + \frac{2M(\mathcal{R} \pm r_+)}{(\mathcal{R} - r_+)(\mathcal{R} - r_-)} \right], \quad (\text{B2})$$

and hence for large \mathcal{R} the gradient $\nabla_\mu \Phi$ is timelike on the sphere $r = \mathcal{R}$ if $A_-(\mathcal{R}) < A < A_+(\mathcal{R})$. We now prove the following statements, which show that these conditions are also sufficient for the flow to be everywhere well defined in the shell delimited by the event horizon and the injection sphere.

Theorem 1

- Suppose $\mathcal{R} > r_+$ is large enough such that $12r_+A_+(\mathcal{R}) \leq 1$, and let $0 \leq A < A_+(\mathcal{R})$. Then the right-hand side of Eq. (B1) is strictly positive for all $r_+ \leq r \leq \mathcal{R}$ and all $0 \leq \theta \leq \pi$.
- Suppose $\mathcal{R} > r_+$ and $A_-(\mathcal{R}) < A \leq 0$. Then the right-hand side of Eq. (B1) is strictly positive for all $r_+ \leq r \leq \mathcal{R}$ and all $0 \leq \theta \leq \pi$.

Proof. For the proof it is convenient to rewrite the right-hand side of Eq. (B1) in the following form:

$$E_A(r, \xi) := d_2(r)\xi^2 + d_1(r)\xi + d_0(r), \quad (\text{B3})$$

where $\xi := \sin^2 \theta$ and the coefficients $d_0(r) := c_0(r) + c_1(r) + c_2(r)$, $d_1(r) := -c_1(r) - 2c_2(r)$ and $d_2(r) := c_2(r)$ are explicitly given by

$$d_0(r) = -144A^2\Delta(\Delta + b^2) + 48AMr_+(r - M) + \Delta + 4Mr + 4M^2 \frac{r + r_+}{r - r_-}, \quad (\text{B4a})$$

$$d_1(r) = 36A^2(3\Delta^2 - 4b^4) - 72AMr_+(r - M) - a^2, \quad (\text{B4b})$$

$$d_2(r) = 36A^2b^2(3\Delta + 4b^2). \quad (\text{B4c})$$

In order to shorten the notation we have also introduced the quantity $b := \sqrt{M^2 - a^2} > 0$ (remember that we are excluding the extremal case from our analysis).

It is simple to verify that $E_A(r, \xi) > 0$ for all $r \geq r_+$ and all $0 \leq \xi \leq 1$ when $A = 0$. Therefore, in the following we assume $A \neq 0$ which implies $d_2(r) > 0$ for all $r \geq r_+$. The strategy of the proof is to provide a positive lower bound for the quantity

$$f_A(r) := \min_{0 \leq \xi \leq 1} E_A(r, \xi) \quad (\text{B5})$$

for each $r_+ \leq r \leq \mathcal{R}$. For this, we distinguish between the following three cases:

Case A: $d_1(r) \geq 0$: In this case the minimum (B5) occurs at the poles $\xi = 0$:

$$f_A(r) = E_A(r, 0) = d_0(r). \quad (\text{B6})$$

Case B: $-2d_2(r) < d_1(r) < 0$: The minimum occurs at $\xi = \xi_* = -d_1(r)/(2d_2(r))$; hence

$$f_A(r) = E_A(r, \xi_*) = d_0(r) - \frac{d_1(r)^2}{4d_2(r)}. \quad (\text{B7})$$

Case C: $d_1(r) \leq -2d_2(r)$: The minimum occurs at the equator $\xi = 1$; thus

$$f_A(r) = E_A(r, 1) = d_0(r) + d_1(r) + d_2(r). \quad (\text{B8})$$

We start with case A, for which $E_A(r, \xi) \geq d_0(r)$. Denoting by $A_{\pm}(r)$ the same function as the one defined in Eq. (B2) with \mathcal{R} replaced with r , one has

$$d_0(r) = 144\Delta(r - M)^2[A_+(r) - A][A - A_-(r)]. \quad (\text{B9})$$

As one can easily verify, $A_-(r)$ is an increasing function of r while $A_+(r)$ is a decreasing function of r . Therefore, $A_-(r) \leq A_-(\mathcal{R}) < A < A_+(\mathcal{R}) \leq A_+(r)$ for all $r_+ \leq r \leq \mathcal{R}$, which implies that $d_0(r) > 0$ for all $r_+ < r \leq \mathcal{R}$. At the horizon,

$$d_0(r_+) = 48AMr_+b + 4Mr_+ + 8M^2\frac{r_+}{b}, \quad (\text{B10})$$

which is obviously positive when $A > 0$. When $A < 0$ we use the fact that

$$|A_-(\mathcal{R})| \leq |A_-(r_+)| = \frac{1}{12b} \left(1 + \frac{M}{b}\right) \quad (\text{B11})$$

to conclude that $d_0(r_+) \geq 4M^2r_+/b > 0$.

Next, we analyze case B for which $0 < -d_1(r) < 2d_2(r)$. This allows us to estimate

$$\begin{aligned} f_A(r) &= d_0(r) + \frac{d_1(r)(-d_1(r))}{2 \cdot 2d_2(r)} \\ &\geq d_0(r) + \frac{1}{2}d_1(r) \geq d_0(r) + \frac{4}{3}d_1(r). \end{aligned} \quad (\text{B12})$$

Explicitly, this yields

$$\begin{aligned} f_A(r) &\geq -144A^2b^2 \left(\Delta + \frac{4}{3}b^2 \right) - 48AMr_+(r - M) \\ &\quad + \Delta + 4Mr + 4M^2 \frac{r + r_+}{r - r_-} - \frac{4}{3}a^2. \end{aligned} \quad (\text{B13})$$

For positive A we have the bounds $12A \leq 1/r_+ \leq 1/b$ which yields the estimate

$$\begin{aligned} f_A(r) &\geq -\Delta - \frac{4}{3}b^2 - 4M(r - M) + \Delta + 4Mr \\ &\quad + 4M^2 - \frac{4}{3}a^2 = \frac{16}{3}M^2 > 0. \end{aligned} \quad (\text{B14})$$

This bound still holds for negative A , provided $12|A_-(\mathcal{R})|b \leq 1$ which is the case if $\mathcal{R} \geq M + \sqrt{b(b + 2M)}$. If $r_+ < \mathcal{R} \leq M + \sqrt{b(b + 2M)}$ we use instead the bound (B11) and the fact that $r_+ \leq r \leq \mathcal{R}$ implies $\Delta \leq 2Mb$ to conclude

$$\begin{aligned} f_A(r) &\geq -\left(1 + \frac{M}{b}\right) \left(\Delta + \frac{4}{3}b^2 \right) + \Delta + 4Mr \\ &\quad + 4M^2 \frac{r + r_+}{r - r_-} - \frac{4}{3}a^2 \\ &\geq -\frac{M}{b}\Delta + 4Mr + \frac{4}{3}M^2 - \frac{4}{3}Mb \\ &\geq 2M(2r - M) > 0. \end{aligned}$$

Finally, in case C the condition $2d_2(r) + d_1(r) \leq 0$ yields

$$\begin{aligned} 108A^2\Delta(\Delta + b^2) &\leq 108A^2 \left[(\Delta + b^2)^2 + \frac{1}{3}b^4 \right] \\ &\leq 72AMr_+(r - M) + a^2. \end{aligned} \quad (\text{B15})$$

Therefore,

$$\begin{aligned}
 f_A(r) &= d_0(r) + d_1(r) + d_2(r) \\
 &= -36A^2\Delta(\Delta + b^2) - 24AMr_+(r - M) + r^2 \\
 &\quad + 2Mr + 4M^2\frac{r + r_+}{r - r_-} \\
 &\geq -48AMr_+(r - M) - \frac{a^2}{3} + r^2 + 2Mr \\
 &\quad + 4M^2\frac{r + r_+}{r - r_-},
 \end{aligned}$$

which is clearly positive when $A < 0$. For $A > 0$ we use the bound $12Ar_+ \leq 1$ and obtain for all $r \geq r_+$

$$\begin{aligned}
 f_A(r) &\geq -4M(r - M) - \frac{a^2}{3} + r^2 + 2Mr + 4M^2 \\
 &= \Delta + 8M^2 - \frac{4}{3}a^2 > 0.
 \end{aligned} \tag{B16}$$

This concludes the proof of the theorem. \blacksquare

One can verify that the required hypothesis $12r_+A_+(\mathcal{R}) \leq 1$ is always satisfied for $\mathcal{R} \geq 3M + r_+ = 4M + b$. Although this bound is not optimal, the condition $A < A_+(\mathcal{R})$ ceases to be sufficient for small $\mathcal{R} - r_+$, as can be understood from the plots in Fig. 3 which show that in this case, the upper bound on A comes from the equator (case C in the proof) instead of the poles.

APPENDIX C: NUMERICAL CONVERGENCE TESTS

In this appendix we present the convergence and self-convergence tests that are necessary to validate our numerical results.

For the benchmark test presented in Sec. VA we compute, for each resolution studied, the relative error between the numerical and analytic values of the mass accretion rate, once the steady state has been reached. In Fig. 14 we present the results of these values as a function of the radial resolution N_r , from which we obtain second order convergence, as expected for smooth solutions considering the numerical methods used in AZTEKAS.

On the other hand, in order to validate the numerical results of the polytropic fluid simulations reported in Sec. VB, we perform a series of self-convergence tests in which, using three different consecutive resolutions, we compute the convergence rate of the solution. We carry out the simulations using resolutions $R_1 = 64 \times 64$, $R_2 = 128 \times 128$, and $R_3 = 256 \times 256$, for each studied value of the adiabatic index γ and three different values of the spin parameter $a/M = 0, 0.5, 0.99$.

In Fig. 15 we show the evolution in time of the convergence rate Q , which is computed as

$$2Q = \frac{|\dot{M}_1 - \dot{M}_2|}{|\dot{M}_2 - \dot{M}_3|}, \tag{C1}$$

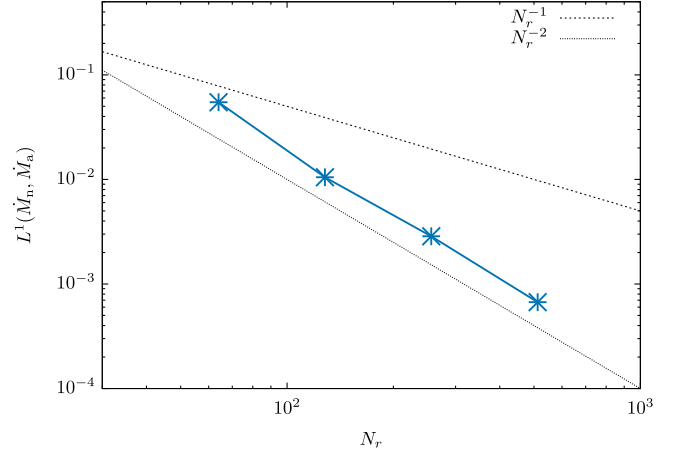


FIG. 14. L^1 -norm of the error in the mass accretion rate, for the benchmark test presented in Sec. VA. The test is performed using the radial resolutions $N_r = 64, 128, 256, 512$. The black dashed lines represent the expected tendency for a first (top) and second order (bottom) convergence.

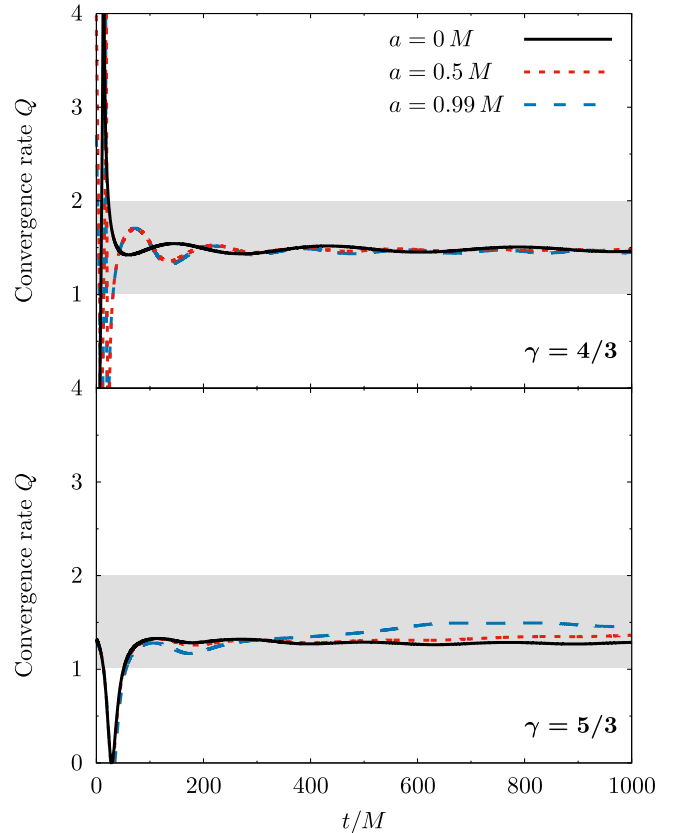


FIG. 15. Self-convergence tests of the polytropic fluid simulations, for both values of γ : $4/3$ (top panel) and $5/3$ (bottom panel). In this figure we show the evolution in time of the convergence rate Q for three different values of the spin parameter a . The gray stripe shows the expected convergence zone (given the numerical methods used in AZTEKAS).

where \dot{M}_1 , \dot{M}_2 , and \dot{M}_3 are the values of the mass accretion rate as obtained from resolutions R_1 , R_2 , and R_3 , respectively. As can be seen from this figure, the time evolution of the simulations' convergence rate rapidly becomes confined within the gray stripe. Note that in this case, since we have set free-outflow boundary

conditions for the velocity field, the simulations develop sharp global oscillations throughout the domain during their evolution, causing the convergence rate to be less than second order, which would have been otherwise expected since we obtain a smooth final steady state solution.

-
- [1] M. A. Abramowicz and P. C. Fragile, Foundations of black hole accretion disk theory, *Living Rev. Relativity* **16**, 1 (2013).
- [2] B. P. Abbott, R. Abbott, T. D. Abbott *et al.*, GWTC-1: A Gravitational-Wave Transient Catalog of Compact Binary Mergers Observed by LIGO and Virgo during the First and Second Observing Runs, *Phys. Rev. X* **9**, 031040 (2019).
- [3] R. Abbott, T. D. Abbott, S. Abraham, F. Acernese, K. Ackley, A. Adams, C. Adams, R. X. Adhikari *et al.* (The LIGO Scientific and the Virgo Collaborations), Population properties of compact objects from the second LIGO-Virgo gravitational-wave transient catalog, [arXiv:2010.14533](https://arxiv.org/abs/2010.14533).
- [4] Event Horizon Telescope Collaboration, First M87 Event Horizon Telescope Results. I. The shadow of the supermassive black hole, *Astrophys. J. Lett.* **875**, L1 (2019).
- [5] H. Bondi, On spherically symmetrical accretion, *Mon. Not. R. Astron. Soc.* **112**, 195 (1952).
- [6] L. Rezzolla and O. Zanotti, *Relativistic Hydrodynamics* (Oxford University Press, Oxford, 2013).
- [7] F. C. Michel, Accretion of matter by condensed objects, *Astrophys. Space Sci.* **15**, 153 (1972).
- [8] H. Bondi and F. Hoyle, On the mechanism of accretion by stars, *Mon. Not. R. Astron. Soc.* **104**, 273 (1944).
- [9] F. Hoyle and A. Lyttleton, The effect of interstellar matter on climatic variation, *Math. Proc. Cambridge Philos. Soc.* **35**, 405 (1939).
- [10] E. Tejeda and A. Aguayo-Ortiz, Relativistic wind accretion on to a Schwarzschild black hole, *Mon. Not. R. Astron. Soc.* **487**, 3607 (2019).
- [11] S. Mendoza, E. Tejeda, and E. Nagel, Analytic solutions to the accretion of a rotating finite cloud towards a central object—I. Newtonian approach, *Mon. Not. R. Astron. Soc.* **393**, 579 (2009).
- [12] E. Tejeda, S. Mendoza, and J. C. Miller, Analytic solutions to the accretion of a rotating finite cloud towards a central object—II. Schwarzschild space-time, *Mon. Not. R. Astron. Soc.* **419**, 1431 (2012).
- [13] E. Tejeda, P. A. Taylor, and J. C. Miller, An analytic toy model for relativistic accretion in Kerr space-time, *Mon. Not. R. Astron. Soc.* **429**, 925 (2013).
- [14] L. Nobili, R. Turolla, and L. Zampieri, Spherical accretion onto black holes: A complete analysis of stationary solutions, *Astrophys. J.* **383**, 250 (1991).
- [15] J. Karkowski, B. Kinasiewicz, P. Mach, E. Malec, and Z. Świerczyński, Universality and backreaction in a general-relativistic accretion of steady fluids, *Phys. Rev. D* **73**, 021503 (2006).
- [16] P. Mach and E. Malec, Stability of self-gravitating accreting flows, *Phys. Rev. D* **78**, 124016 (2008).
- [17] P. C. Fragile, A. Gillespie, T. Monahan, M. Rodriguez, and P. Anninos, Numerical simulations of optically thick accretion onto a black hole. I. Spherical case, *Astrophys. J. Suppl. Ser.* **201**, 9 (2012).
- [18] C. Roedig, O. Zanotti, and D. Alic, General relativistic radiation hydrodynamics of accretion flows—II. Treating stiff source terms and exploring physical limitations, *Mon. Not. R. Astron. Soc.* **426**, 1613 (2012).
- [19] A. Sadowski, R. Narayan, A. Tchekhovskoy, and Y. Zhu, Semi-implicit scheme for treating radiation under M1 closure in general relativistic conservative fluid dynamics codes, *Mon. Not. R. Astron. Soc.* **429**, 3533 (2013).
- [20] J. C. McKinney, A. Tchekhovskoy, A. Sadowski, and R. Narayan, Three-dimensional general relativistic radiation magnetohydrodynamical simulation of super-Eddington accretion, using a new code HARMRAD with M1 closure, *Mon. Not. R. Astron. Soc.* **441**, 3177 (2014).
- [21] F. D. Lora-Clavijo, M. Gracia-Linares, and F. S. Guzmán, Horizon growth of supermassive black hole seeds fed with collisional dark matter, *Mon. Not. R. Astron. Soc.* **443**, 2242 (2014).
- [22] E. Chaverra and O. Sarbach, Radial accretion flows on static, spherically symmetric black holes, *Classical Quantum Gravity* **32**, 155006 (2015).
- [23] E. Chaverra, M. D. Morales, and O. Sarbach, Quasi-normal acoustic oscillations in the Michel flow, *Phys. Rev. D* **91**, 104012 (2015).
- [24] L. R. Weih, H. Olivares, and L. Rezzolla, Two-moment scheme for general-relativistic radiation hydrodynamics: A systematic description and new applications, *Mon. Not. R. Astron. Soc.* **495**, 2285 (2020).
- [25] R. Hunt, A fluid dynamical study of the accretion process, *Mon. Not. R. Astron. Soc.* **154**, 141 (1971).
- [26] E. Shima, T. Matsuda, H. Takeda, and K. Sawada, Hydrodynamic calculations of axisymmetric accretion flow, *Mon. Not. R. Astron. Soc.* **217**, 367 (1985).
- [27] J. A. Font and J. M. Ibáñez, Non-axisymmetric relativistic Bondi-Hoyle accretion on to a Schwarzschild black hole, *Mon. Not. R. Astron. Soc.* **298**, 835 (1998).
- [28] M. Ruffert, Three-dimensional hydrodynamic Bondi-Hoyle accretion. I. Code validation and stationary accretors, *Astrophys. J.* **427**, 342 (1994).
- [29] J. A. Font, J. M. Ibáñez, and P. Papadopoulos, Non-axisymmetric relativistic Bondi-Hoyle accretion on to a Kerr black hole, *Mon. Not. R. Astron. Soc.* **305**, 920 (1999).

- [30] F. D. Lora-Clavijo and F. S. Guzmán, Axisymmetric Bondi-Hoyle accretion on to a Schwarzschild black hole: Shock cone vibrations, *Mon. Not. R. Astron. Soc.* **429**, 3144 (2013).
- [31] L. I. Petrich, S. Shapiro, and S. A. Teukolsky, Accretion Onto a Moving Black Hole: An Exact Solution, *Phys. Rev. Lett.* **60**, 1781 (1988).
- [32] X. Hernandez, P. L. Rendón, R. G. Rodríguez-Mota, and A. Capella, A hydrodynamical mechanism for generating astrophysical jets, [arXiv:1103.0250](https://arxiv.org/abs/1103.0250).
- [33] A. Aguayo-Ortiz, E. Tejada, and X. Hernandez, Choked accretion: From radial infall to bipolar outflows by breaking spherical symmetry, *Mon. Not. R. Astron. Soc.* **490**, 5078 (2019).
- [34] E. Tejada, A. Aguayo-Ortiz, and X. Hernandez, Choked accretion onto a Schwarzschild black hole: A hydrodynamical jet-launching mechanism, *Astrophys. J.* **893**, 81 (2020).
- [35] J. M. Bardeen and J. A. Petterson, The Lense-Thirring effect and accretion disks around Kerr black holes, *Astrophys. J. Lett.* **195**, L65 (1975).
- [36] M. Liska, A. Tchekhovskoy, A. Ingram, and M. van der Klis, Bardeen-Petterson alignment, jets, and magnetic truncation in GRMHD simulations of tilted thin accretion discs, *Mon. Not. R. Astron. Soc.* **487**, 550 (2019).
- [37] D. Proga and M. C. Begelman, Accretion of low angular momentum material onto black holes: Two-dimensional hydrodynamical inviscid case, *Astrophys. J.* **582**, 69 (2003).
- [38] P. Mach, M. Piróg, and J. A. Font, Relativistic low angular momentum accretion: Long time evolution of hydrodynamical inviscid flows, *Classical Quantum Gravity* **35**, 095005 (2018).
- [39] S. L. Shapiro, A. P. Lightman, and D. M. Eardley, A two-temperature accretion disk model for Cygnus X-1: Structure and spectrum, *Astrophys. J.* **204**, 187 (1976).
- [40] F. Yuan and R. Narayan, Hot accretion flows around black holes, *Annu. Rev. Astron. Astrophys.* **52**, 529 (2014).
- [41] R. Narayan and I. Yi, Advection-dominated accretion: A self-similar solution, *Astrophys. J. Lett.* **428**, L13 (1994).
- [42] R. Narayan and I. Yi, Advection-dominated accretion: Underfed black holes and neutron stars, *Astrophys. J.* **452**, 710 (1995).
- [43] R. D. Blandford and M. C. Begelman, On the fate of gas accreting at a low rate on to a black hole, *Mon. Not. R. Astron. Soc.* **303**, L1 (1999).
- [44] R. D. Blandford and M. C. Begelman, Two-dimensional adiabatic flows on to a black hole—I. Fluid accretion, *Mon. Not. R. Astron. Soc.* **349**, 68 (2004).
- [45] M. C. Begelman, Radiatively inefficient accretion: Breezes, winds and hyperaccretion, *Mon. Not. R. Astron. Soc.* **420**, 2912 (2012).
- [46] I. V. Igumenshchev, R. Narayan, and M. A. Abramowicz, Three-dimensional magnetohydrodynamic simulations of radiatively inefficient accretion flows, *Astrophys. J.* **592**, 1042 (2003).
- [47] J. F. Hawley and J. H. Krolik, Magnetically driven jets in the Kerr metric, *Astrophys. J.* **641**, 103 (2006).
- [48] D. Proga, Dynamics of accretion flows irradiated by a quasar, *Astrophys. J.* **661**, 693 (2007).
- [49] A. Tchekhovskoy, R. Narayan, and J. C. McKinney, Efficient generation of jets from magnetically arrested accretion on a rapidly spinning black hole, *Mon. Not. R. Astron. Soc.* **418**, L79 (2011).
- [50] R. Narayan, A. Sadowski, R. F. Penna, and A. K. Kulkarni, GRMHD simulations of magnetized advection-dominated accretion on a non-spinning black hole: Role of outflows, *Mon. Not. R. Astron. Soc.* **426**, 3241 (2012).
- [51] T. Waters, A. Aykutalp, D. Proga, J. Johnson, H. Li, and J. Smidt, Outflows from inflows: The nature of Bondi-like accretion, *Mon. Not. R. Astron. Soc.* **491**, L76 (2020).
- [52] C. W. Misner, K. S. Thorne, and J. A. Wheeler, *Gravitation* (W. H. Freeman, San Francisco, 1973).
- [53] S. W. Hawking and G. F. R. Ellis, *The Large Scale Structure of Space Time* (Cambridge University Press, Cambridge, England, 1973).
- [54] Digital library of mathematical functions, <http://dlmf.nist.gov/>.
- [55] V. Karas and R. Mucha, Accretion onto a rotating compact object in general relativity, *Am. J. Phys.* **61**, 825 (1993).
- [56] E. Tejada, Incompressible wind accretion, [arXiv:1705.07093](https://arxiv.org/abs/1705.07093).
- [57] J. M. Bardeen, A variational principle for rotating stars in general relativity, *Astrophys. J.* **162**, 71 (1970).
- [58] J. M. Bardeen, Timelike and null geodesics in the Kerr metric, edited by C. DeWitt and B. S. DeWitt, in *Black Holes, Les Astres Occlus* (Gordon and Breach Science Publishers, Inc, New York, 1973), pp. 215–239.
- [59] <https://github.com/aztekas-code/aztekas-main>.
- [60] A. Aguayo-Ortiz, S. Mendoza, and D. Olvera, A direct primitive variable recovery scheme for hyperbolic conservative equations: The case of relativistic hydrodynamics, *PLoS One* **13**, e0195494 (2018).
- [61] F. Banyuls, J. A. Font, J. M. Ibáñez, J. M. Martí, and J. A. Miralles, Numerical 3 + 1 general relativistic hydrodynamics: A local characteristic approach, *Astrophys. J.* **476**, 221 (1997).
- [62] L. Del Zanna, O. Zanotti, N. Bucciantini, and P. Londrillo, ECHO: A Eulerian conservative high-order scheme for general relativistic magnetohydrodynamics and magnetodynamics, *Astron. Astrophys.* **473**, 11 (2007).
- [63] C.-W. Shu and S. Osher, Efficient implementation of essentially non-oscillatory shock-capturing schemes, *J. Comput. Phys.* **77**, 439 (1988).
- [64] M. Alcubierre, *Introduction to 3+1 Numerical Relativity* (Oxford Univ. Press, Oxford, 2008).
- [65] J. D. Jackson, *Classical Electrodynamics* (John Wiley & Sons, New York, 1975).

Conclusions

In this work, we studied different accretion problems in astrophysics, extending two classical solutions into the general relativistic regime, and presenting an inflow-outflow hydrodynamic solution, the *choked accretion* mechanism. Moreover, we presented AZTEKAS, the code used for the numerical studies presented in this thesis.

In Chapter 2, we presented the algorithms and validation tests of AZTEKAS, a general relativistic hydrodynamic numerical code. We showed the specific numerical methods used to solve a general system of hyperbolic, partial differential equations in conservative form, and applied them to solve the inviscid-Euler hydrodynamic equations in both non-relativistic and relativistic regimes. For the non-relativistic case, we presented the set of equations in a three-dimensional covariant form, which facilitates their implementation in a numerical code. On the other hand, for the relativistic case, we wrote the set of equations in full covariant form following a variation of the “Valencia” formulation, using the 3+1 formalism. For both cases, we presented different numerical problems used to test and validate our code, either comparing with analytic solutions and models, and with simulations reported previously in the literature.

In Chapters 3 and 4, we presented the extension into the general relativistic regime of two gas accretion analytic models: Bondi spherical accretion and Bondi-Hoyle-Lyttleton wind accretion. These two studies complemented the main study of this thesis, allowing not only to extend two classical solutions to their relativistic counterparts, but also to prepare and validate the AZTEKAS code.

In the first study (Chapter 3), we revisited, from the non-relativistic to the ultra-relativistic regimes, the spherically symmetric gas accretion problem presented by Bondi (1952) and Michel (1972). We performed a detailed comparison between these two models, studying their differences for ultra-relativistic values of the temperature, and showing how both solutions match each other in the non-relativistic regime. We also extended the relativistic Michel solution by considering an equation of state corresponding to a relativistic, monoatomic gas. Then, we extended the spherical accretion problem to the case of a rotating Kerr black hole, by means of

general relativistic hydrodynamic simulations performed with AZTEKAS. We studied the influence of the spin parameter on the flow morphology, sonic surface and mass accretion rate, finding that its effect is more significant for larger values of the black hole rotation.

In the second study (Chapter 4), we presented the relativistic extension of the Bondi-Hoyle-Lyttleton (Hoyle & Lyttleton, 1939; Bondi & Hoyle, 1944) wind accretion problem, by considering the accretion onto a Schwarzschild black hole. We used the ballistic motion approximation for the gas description, allowing us to obtain the wind streamlines, the density field and its corresponding mass accretion rate. We compared this solution with the classical BHL problem, finding that the mass accretion rate is greater in our model, when the wind velocity approaches the speed of light. We completed this study by comparing the analytic model with full hydrodynamic simulations performed with the AZTEKAS code, finding a good agreement between both solutions.

In Chapters 5, 6 and 7 we presented three studies regarding *choked accretion*: an inflow-outflow hydrodynamical mechanism. These show the behaviour and characteristics of this accretion mechanism in the non-relativistic, Schwarzschild black hole and Kerr black hole cases, respectively. The main features of the *choked accretion* model are summarized next:

- Steady-state, two-dimensional solution that results from breaking the spherical symmetry in the density profile of Bondi's accretion solution.
- The model considers an axisymmetric, large-scale, small-amplitude deviation in the density field in which the equatorial belt is denser than the polar regions.
- This equatorial-to-polar density contrast is assumed to come from the rotation of the fluid, either from the inner part of an accretion disk or by the flattening of a rotating spherical gas cloud.
- This model is studied by means of both analytic solutions and numerical simulations. The analytic models consider a potential fluid solution which in the non-relativistic regime leads to an incompressible fluid description, whereas in the relativistic regimes corresponds to an ultra-relativistic stiff fluid.
- The numerical experiments allow us to study the behaviour of the choked accretion mechanism with a perfect fluid that follows a polytropic process. By means of numerical simulations performed with the AZTEKAS code, we analyse the model dependence on different variables such as adiabatic index γ , spin parameter a and speed of sound \mathcal{C} .
- The steady-state flow configurations show an inflow coming from the equatorial region and a bipolar outflow expelled through the less dense poles. This morphology is due to a flux-limited accretion regime in which the incoming

material chokes at a certain mass accretion rate threshold, forcing the exceeding non-accreted material to escape through the poles. The threshold value at which the accreting material chokes is of the order of the value found for the spherically symmetric classical solutions.

- We find a strong dependence between the ratio of ejected to injected material and the injected mass accretion rate, suggesting that this mechanism gives a simple connection between accretion and ejection phenomena.
- The *choked accretion* mechanism shows the same qualitative behaviour and features in all the regimes, from the non-relativistic to the ultra-relativistic cases, either around non-rotating or rotating black holes.
- Regarding the astrophysical applicability of our model, we find that in order for the choked accretion mechanism to work at length scales close to the black hole horizon, it requires high temperature values ($\sim 10^{11}$ K), which suggests that this solution could be related with the hot accretion flows discussed in Chapter 1. In particular, in the ADAFs solutions, the gas is unstable against convection which could be triggered in the *choked accretion* mechanism by the density contrast δ at the boundary, explaining why the bipolar outflow configuration is found even for small values of δ .

Even though the choked accretion mechanism requires high temperature values to work, the density contrast, which is one of the main characteristic of the model, seems to be a reasonable feature to be found in different astrophysical phenomena; particularly in those with gas rotation along the equator. Different authors have reported the existence of winds and outflows in rotating systems such as supergiants stars (Curé et al., 2005) or in fast-rising blue optical transients (Coppejans et al., 2020). In this kind of scenarios, the choked accretion model could be useful to explain the relation between the ejected and the accreted gas, as well as the nature of the central engine which gives rise to the bipolar outflow configuration.

On the other hand, the applicability of the choked accretion model might be improved by including some additional physical ingredients that could reduce the effective temperature and increase the polar density contrast. Some of these ingredients can be: the inclusion of fluid rotation, which might give raise to a natural equatorial-to-polar density gradient; radiative transfer, which could reduce the effective temperature that give raise to an inflow-outflow configuration; magnetic fields, which could give rise, along with the fluid rotation, to a possible interplay between our model and the well-established magneto-centrifugal launching mechanisms.

Bibliography

- Abramowicz, M. A., Chen, X., Kato, S., Lasota, J.-P., & Regev, O. (1995, January). Thermal Equilibria of Accretion Disks. *Astrophysical Journal Letters*, *438*, L37. Retrieved from <https://ui.adsabs.harvard.edu/abs/1995ApJ...438L..37A> doi: 10.1086/187709
- Acuña-Cárdenas, R. O., Gabarrete, C., & Sarbach, O. (2022, March). An introduction to the relativistic kinetic theory on curved spacetimes. *General Relativity and Gravitation*, *54*(3), 23. doi: 10.1007/s10714-022-02908-5
- Aguayo-Ortiz, A., Sarbach, O., & Tejada, E. (2021, January). Choked accretion onto a Kerr black hole. *Physical Review D*, *103*(2), 023003. Retrieved from <https://ui.adsabs.harvard.edu/abs/2021PhRvD.103b3003A> doi: 10.1103/PhysRevD.103.023003
- Aguayo-Ortiz, A., Tejada, E., & Hernandez, X. (2019, December). Choked accretion: from radial infall to bipolar outflows by breaking spherical symmetry. *Monthly Notices of the Royal Astronomical Society*, *490*(4), 5078-5087. Retrieved from <https://ui.adsabs.harvard.edu/abs/2019MNRAS.490.5078A> doi: 10.1093/mnras/stz2989
- Aguayo-Ortiz, A., Tejada, E., Sarbach, O., & López-Cámara, D. (2021, July). Spherical accretion: Bondi, Michel, and rotating black holes. *Monthly Notices of the Royal Astronomical Society*, *504*(4), 5039-5053. Retrieved from <https://ui.adsabs.harvard.edu/abs/2021MNRAS.504.5039A> doi: 10.1093/mnras/stab1127
- Aguayo-Ortiz, A., Mendoza, S., & Olvera, D. (2018, 04). A direct primitive variable recovery scheme for hyperbolic conservative equations: The case of relativistic hydrodynamics. *PLOS ONE*, *13*(4), 1-21. Retrieved from <https://doi.org/10.1371/journal.pone.0195494> doi: 10.1371/journal.pone.0195494
- Alcubierre, M. (2008). *Introduction to 3+1 numerical relativity*. Oxford: Oxford Univ. Press. Retrieved from <https://cds.cern.ch/record/1138167> doi: 10.1093/acprof:oso/9780199205677.001.0001

- Anglada, G., Rodríguez, L. F., & Carrasco-González, C. (2018, June). Radio jets from young stellar objects. *Astronomy and Astrophysics Reviews*, *26*(1), 3. Retrieved from <https://ui.adsabs.harvard.edu/abs/2018A&ARv..26....3A> doi: 10.1007/s00159-018-0107-z
- Arnowitt, R., Deser, S., & Misner, C. W. (1962, September). Republication of: The dynamics of general relativity. *General Relativity and Gravitation*, *40*(9), 1997-2027. Retrieved from <https://ui.adsabs.harvard.edu/abs/2008GRGr..40.1997A> doi: 10.1007/s10714-008-0661-1
- Balbus, S. A., & Hawley, J. F. (1991, Jul). A Powerful Local Shear Instability in Weakly Magnetized Disks. I. Linear Analysis. *Astrophysical Journal*, *376*, 214. Retrieved from <https://ui.adsabs.harvard.edu/abs/1991ApJ...376..214B> doi: 10.1086/170270
- Banyuls, F., Font, J. A., Ibanez, J. M., Martí, J. M., & Miralles, J. A. (1997, feb). Numerical $\{3 + 1\}$ general relativistic hydrodynamics: A local characteristic approach. *The Astrophysical Journal*, *476*(1), 221–231. Retrieved from <https://doi.org/10.1086%2F303604> doi: 10.1086/303604
- Begelman, M. C., Armitage, P. J., & Reynolds, C. S. (2015, August). Accretion Disk Dynamo as the Trigger for X-Ray Binary State Transitions. *Astrophysical Journal*, *809*(2), 118. Retrieved from <https://ui.adsabs.harvard.edu/abs/2015ApJ...809..118B> doi: 10.1088/0004-637X/809/2/118
- Bicak, J., Semerak, O., & Hadrava, P. (1993, August). Collimation Effects of the Kerr Field. *Monthly Notices of the Royal Astronomical Society*, *263*, 545. Retrieved from <http://cdsads.u-strasbg.fr/abs/1993MNRAS.263..545B> doi: 10.1093/mnras/263.3.545
- Bjerkeli, P., van der Wiel, M. H. D., Harsono, D., Ramsey, J. P., & Jørgensen, J. K. (2016, December). Resolved images of a protostellar outflow driven by an extended disk wind. *Nature*, *540*(7633), 406-409. Retrieved from <https://ui.adsabs.harvard.edu/abs/2016Natur.540..406B> doi: 10.1038/nature20600
- Blandford, R., Meier, D., & Readhead, A. (2019, August). Relativistic Jets from Active Galactic Nuclei. *Ann. Rev. Ast. & Ast.*, *57*, 467-509. Retrieved from <https://ui.adsabs.harvard.edu/abs/2019ARA&A..57..467B> doi: 10.1146/annurev-astro-081817-051948
- Blandford, R. D., & Begelman, M. C. (1999, February). On the fate of gas accreting at a low rate on to a black hole. *Monthly Notices of the Royal Astronomical Society*, *303*(1), L1-L5. Retrieved from <https://ui.adsabs.harvard.edu/abs/1999MNRAS.303L...1B> doi: 10.1046/j.1365-8711.1999.02358.x

- Blandford, R. D., & Payne, D. G. (1982, June). Hydromagnetic flows from accretion discs and the production of radio jets. *Monthly Notices of the Royal Astronomical Society*, *199*, 883-903. Retrieved from <http://adsabs.harvard.edu/abs/1982MNRAS.199..883B> doi: 10.1093/mnras/199.4.883
- Blandford, R. D., & Znajek, R. L. (1977, May). Electromagnetic extraction of energy from Kerr black holes. *Monthly Notices of the Royal Astronomical Society*, *179*, 433-456. Retrieved from <http://adsabs.harvard.edu/abs/1977MNRAS.179..433B> doi: 10.1093/mnras/179.3.433
- Bondi, H. (1952, January). On spherically symmetrical accretion. *Monthly Notices of the Royal Astronomical Society*, *112*, 195. Retrieved from <https://ui.adsabs.harvard.edu/abs/1952MNRAS.112..195B> doi: 10.1093/mnras/112.2.195
- Bondi, H., & Hoyle, F. (1944). On the mechanism of accretion by stars. *Monthly Notices of the Royal Astronomical Society*, *104*, 273. Retrieved from <http://adsabs.harvard.edu/abs/1944MNRAS.104..273B> doi: 10.1093/mnras/104.5.273
- Braito, V., Reeves, J. N., Matzeu, G. A., Severgnini, P., Ballo, L., Caccianiga, A., . . . Turner, T. J. (2018, September). A new powerful and highly variable disc wind in an AGN-star-forming galaxy, the case of MCG-03-58-007. *Monthly Notices of the Royal Astronomical Society*, *479*(3), 3592-3603. Retrieved from <https://ui.adsabs.harvard.edu/abs/2018MNRAS.479.3592B> doi: 10.1093/mnras/sty1697
- Bronzwaer, T., Davelaar, J., Younsi, Z., Mościbrodzka, M., Falcke, H., Kramer, M., & Rezzolla, L. (2018, May). RAPTOR. I. Time-dependent radiative transfer in arbitrary spacetimes. *Astronomy and Astrophysics*, *613*, A2. Retrieved from <https://ui.adsabs.harvard.edu/abs/2018A&A...613A...2B> doi: 10.1051/0004-6361/201732149
- Cawthorne, T. V., & Cobb, W. K. (1990, Feb). Linear Polarization of Radiation from Oblique and Conical Shocks. *Astrophysical Journal*, *350*, 536. Retrieved from <https://ui.adsabs.harvard.edu/#abs/1990ApJ...350..536C> doi: 10.1086/168409
- Chandrasekhar, S. (1981). *Hydrodynamic and hydromagnetic stability*. Dover Publications. Retrieved from https://books.google.com.mx/books?id=oU_-6ikmidoC
- Comerford, T. A. F., Izzard, R. G., Booth, R. A., & Rosotti, G. (2019, December). Bondi-Hoyle-Lyttleton accretion by binary stars. *Monthly Notices of the Royal Astronomical Society*, *490*(4), 5196-5209. Retrieved from <https://ui.adsabs.harvard.edu/abs/2019MNRAS.490.5196C> doi: 10.1093/mnras/stz2977
- Coppejans, D. L., Margutti, R., Terreran, G., Nayana, A. J., Coughlin, E. R., Laskar, T., . . . Zhang, B. (2020, May). A Mildly Relativistic Outflow from the Energetic,

- Fast-rising Blue Optical Transient CSS161010 in a Dwarf Galaxy. *Astrophysical Journal Letters*, 895(1), L23. Retrieved from <https://ui.adsabs.harvard.edu/abs/2020ApJ...895L..23C> doi: 10.3847/2041-8213/ab8cc7
- Courant, R., Friedrichs, K., & Lewy, H. (1928). Über die partiellen Differenzengleichungen der mathematischen Physik. *Mathematische Annalen*, 100, 32-74. Retrieved from <http://adsabs.harvard.edu/abs/1928MatAn.100...32C> doi: 10.1007/BF01448839
- Cruz-Orsorio, A., & Rezzolla, L. (2020, May). Common-envelope Dynamics of a Stellar-mass Black Hole: General Relativistic Simulations. *Astrophysical Journal*, 894(2), 147. Retrieved from <https://ui.adsabs.harvard.edu/abs/2020ApJ...894..147C> doi: 10.3847/1538-4357/ab89aa
- Curé, M., Rial, D. F., & Cidale, L. (2005, July). Outflowing disk formation in B[e] supergiants due to rotation and bi-stability in radiation driven winds. *Astronomy and Astrophysics*, 437(3), 929-933. doi: 10.1051/0004-6361:20052686
- Davelaar, J., Olivares, H., Porth, O., Bronzwaer, T., Janssen, M., Roelofs, F., ... Rezzolla, L. (2019, December). Modeling non-thermal emission from the jet-launching region of M 87 with adaptive mesh refinement. *Astronomy and Astrophysics*, 632, A2. Retrieved from <https://ui.adsabs.harvard.edu/abs/2019A&A...632A...2D> doi: 10.1051/0004-6361/201936150
- De Colle, F., Granot, J., López-Cámara, D., & Ramirez-Ruiz, E. (2012, February). Gamma-Ray Burst Dynamics and Afterglow Radiation from Adaptive Mesh Refinement, Special Relativistic Hydrodynamic Simulations. *Astrophysical Journal*, 746(2), 122. doi: 10.1088/0004-637X/746/2/122
- Del Zanna, L., & Bucciantini, N. (2002, August). An efficient shock-capturing central-type scheme for multidimensional relativistic flows. I. Hydrodynamics. *Astronomy and Astrophysics*, 390, 1177-1186. Retrieved from <http://adsabs.harvard.edu/abs/2002A%26A...390.1177D> doi: 10.1051/0004-6361:20020776
- Del Zanna, L., Zanotti, O., Bucciantini, N., & Londrillo, P. (2007, October). ECHO: a Eulerian conservative high-order scheme for general relativistic magnetohydrodynamics and magnetodynamics. *Astronomy and Astrophysics*, 473(1), 11-30. Retrieved from <https://ui.adsabs.harvard.edu/abs/2007A&A...473...11D> doi: 10.1051/0004-6361:20077093
- Dexter, J., Scepi, N., & Begelman, M. C. (2021, October). Radiation GRMHD Simulations of the Hard State of Black Hole X-Ray Binaries and the Collapse of a Hot Accretion Flow. *Astrophysical Journal Letters*, 919(2), L20. Retrieved from <https://ui.adsabs.harvard.edu/abs/2021ApJ...919L..20D> doi: 10.3847/2041-8213/ac2608

- Dihingia, I. K., Vaidya, B., & Fendt, C. (2021, August). Jets, disc-winds, and oscillations in general relativistic, magnetically driven flows around black hole. *Monthly Notices of the Royal Astronomical Society*, 505(3), 3596-3615. Retrieved from <https://ui.adsabs.harvard.edu/abs/2021MNRAS.505.3596D> doi: 10.1093/mnras/stab1512
- Duffell, P., & Kasen, D. (2016, Feb). Synchrotron Magnetic Fields from Rayleigh-Taylor Instability in Supernovae. *arXiv e-prints*, arXiv:1602.07692. Retrieved from <https://ui.adsabs.harvard.edu/#abs/2016arXiv160207692D>
- Eddington, A. S. (1925, March). A limiting case in the theory of radiative equilibrium. *Monthly Notices of the Royal Astronomical Society*, 85, 408. Retrieved from <https://ui.adsabs.harvard.edu/abs/1925MNRAS..85..408E> doi: 10.1093/mnras/85.5.408
- Edgar, R. (2004, September). A review of Bondi-Hoyle-Lyttleton accretion. *New Astronomy Reviews*, 48(10), 843-859. Retrieved from <https://ui.adsabs.harvard.edu/abs/2004NewAR..48..843E> doi: 10.1016/j.newar.2004.06.001
- Einfeldt, B. (1988). On godunov-type methods for gas dynamics. *SIAM Journal on Numerical Analysis*, 25(2), 294-318. Retrieved from <https://doi.org/10.1137/0725021> doi: 10.1137/0725021
- Espinasse, M., Corbel, S., Kaaret, P., Tremou, E., Migliori, G., Plotkin, R. M., ... Motta, S. (2020, June). Relativistic X-Ray Jets from the Black Hole X-Ray Binary MAXI J1820+070. *Astrophysical Journal Letters*, 895(2), L31. Retrieved from <https://ui.adsabs.harvard.edu/abs/2020ApJ...895L..31E> doi: 10.3847/2041-8213/ab88b6
- Esquivel, A., Raga, A. C., Cantó, J., & Rodríguez-González, A. (2009, November). The interaction of an O star wind with a Herbig-Haro jet. *Astronomy and Astrophysics*, 507(2), 855-860. doi: 10.1051/0004-6361/200912825
- Fishbone, L. G., & Moncrief, V. (1976, Aug). Relativistic fluid disks in orbit around Kerr black holes. *Astrophysical Journal*, 207, 962-976. Retrieved from <https://ui.adsabs.harvard.edu/abs/1976ApJ...207..962F> doi: 10.1086/154565
- Font, J. A., Ibáñez, J. M., & Papadopoulos, P. (1999, May). Non-axisymmetric relativistic Bondi-Hoyle accretion on to a Kerr black hole. *Monthly Notices of the Royal Astronomical Society*, 305(4), 920-936. Retrieved from <https://ui.adsabs.harvard.edu/abs/1999MNRAS.305..920F> doi: 10.1046/j.1365-8711.1999.02459.x
- Fraschetti, F., Teyssier, R., Ballet, J., & Decourchelle, A. (2010, Jun). Simulation of the growth of the 3D Rayleigh-Taylor instability in supernova remnants using an expanding reference frame. *Astronomy and Astrophysics*, 515, A104.

- Retrieved from <https://ui.adsabs.harvard.edu/#abs/2010A&A...515A.104F>
doi: 10.1051/0004-6361/200912692
- Fryxell, B., Olson, K., Ricker, P., Timmes, F. X., Zingale, M., Lamb, D. Q., ... Tufo, H. (2000, November). FLASH: An Adaptive Mesh Hydrodynamics Code for Modeling Astrophysical Thermonuclear Flashes. *Astrophysical Journal Supplements*, 131(1), 273-334. Retrieved from <https://ui.adsabs.harvard.edu/abs/2000ApJS..131..273F> doi: 10.1086/317361
- Gammie, C. F., McKinney, J. C., & Tóth, G. (2003, May). HARM: A Numerical Scheme for General Relativistic Magnetohydrodynamics. *Astrophysical Journal*, 589(1), 444-457. Retrieved from <https://ui.adsabs.harvard.edu/abs/2003ApJ...589..444G> doi: 10.1086/374594
- Gariel, J., MacCallum, M. A. H., Marilhacy, G., & Santos, N. O. (2010, June). Kerr geodesics, the Penrose process and jet collimation by a black hole. *Astronomy and Astrophysics*, 515, A15. Retrieved from <http://adsabs.harvard.edu/abs/2010A%26A...515A..15G> doi: 10.1051/0004-6361/200913678
- Godunov, S. K. (1959). *A Difference Scheme for Numerical Solution of Discontinuous Solution of Hydrodynamic Equation* (Vol. 47). Mat. Sb. (N.S.).
- Gourgoulhon, E. (2007, March). 3+1 Formalism and Bases of Numerical Relativity. *arXiv e-prints*, gr-qc/0703035. Retrieved from <https://ui.adsabs.harvard.edu/abs/2007gr.qc.....3035G>
- Harten, A., Lax, P. D., & Leer, B. (1983, 04). On Upstream Differencing and Godunov-Type Conservation Laws. *SIAM Review*, 25. Retrieved from <http://gen.lib.rus.ec/scimag/index.php?s=10.2307/2030019> doi: 10.2307/2030019
- Hartigan, P. (2009). Measurement of Magnetic Fields in Stellar Jets. *Astrophysics and Space Science Proceedings*, 13, 317-327. Retrieved from <http://adsabs.harvard.edu/abs/2009ASSP...13..317H> doi: 10.1007/978-3-642-00576-3_38
- Hawley, J. F., Fendt, C., Hardcastle, M., Nokhrina, E., & Tchekhovskoy, A. (2015, October). Disks and Jets. Gravity, Rotation and Magnetic Fields. *Space Science Reviews*, 191, 441-469. Retrieved from <http://adsabs.harvard.edu/abs/2015SSRv..191..441H> doi: 10.1007/s11214-015-0174-7
- Hernández, X., Rendón, P. L., Rodríguez-Mota, R. G., & Capella, A. (2014, April). A Hydrodynamical Mechanism for Generating Astrophysical Jets. *Revista Mexicana de Astronomía y Astrofísica*, 50, 23-35. Retrieved from <http://adsabs.harvard.edu/abs/2014RMxAA..50...23H>
- Hoyle, F., & Lyttleton, R. A. (1939, January). The effect of interstellar matter on climatic variation. *Proceedings of the Cambridge Philosophical Society*,

- 35(3), 405. Retrieved from <https://ui.adsabs.harvard.edu/abs/1939PCPS..35..405H> doi: 10.1017/S0305004100021150
- Ichimaru, S. (1977, June). Bimodal behavior of accretion disks: theory and application to Cygnus X-1 transitions. *Astrophysical Journal*, 214, 840-855. Retrieved from <https://ui.adsabs.harvard.edu/abs/1977ApJ...214..840I> doi: 10.1086/155314
- Igumenshchev, I. V., & Narayan, R. (2002, February). Three-dimensional Magnetohydrodynamic Simulations of Spherical Accretion. *Astrophysical Journal*, 566(1), 137-147. Retrieved from <https://ui.adsabs.harvard.edu/abs/2002ApJ...566..137I> doi: 10.1086/338077
- Jeffrey, N. L. S., Fletcher, L., Labrosse, N., & Simões, P. J. A. (2018, Dec). The development of lower-atmosphere turbulence early in a solar flare. *Science Advances*, 4, 2794. Retrieved from <https://ui.adsabs.harvard.edu/#abs/2018SciA....4.2794J> doi: 10.1126/sciadv.aav2794
- Kaaz, N., Antoni, A., & Ramirez-Ruiz, E. (2019, May). Bondi-Hoyle-Lyttleton Accretion onto Star Clusters. *Astrophysical Journal*, 876(2), 142. Retrieved from <https://ui.adsabs.harvard.edu/abs/2019ApJ...876..142K> doi: 10.3847/1538-4357/ab158b
- Kamm, J. (2000). *Evaluation of the Sedov-von Neumann-Taylor blast wave solution* (Tech. Rep. No. LA-UR-00-6055). <https://www.bibsonomy.org/bibtex/27fb1fca43a523e294f724c47c64f3f1b/surferdwa>: Los Alamos National Laboratory. Retrieved from <https://www.bibsonomy.org/bibtex/27fb1fca43a523e294f724c47c64f3f1b/surferdwa>
- Kaye, C., Cawthorne, T., & Hughes, P. (2018, May). Hydrodynamical Simulations of Recollimation Shocks within Relativistic Astrophysical Jets. *Galaxies*, 6, 53. Retrieved from <https://ui.adsabs.harvard.edu/#abs/2018Galax...6...53K> doi: 10.3390/galaxies6020053
- Kemm, F. (2015, July). Heuristical and numerical considerations for the carbuncle phenomenon. *arXiv e-prints*, arXiv:1507.00666. Retrieved from <https://ui.adsabs.harvard.edu/abs/2015arXiv150700666K>
- King, A. (2010, May). Accretion and Outflow in Active Galaxies. In B. M. Peterson, R. S. Somerville, & T. Storchi-Bergmann (Eds.), *Co-evolution of central black holes and galaxies* (Vol. 267, p. 273-282). Retrieved from <https://ui.adsabs.harvard.edu/abs/2010IAUS..267..273K> doi: 10.1017/S1743921310006484
- Kwitter, K. B., & Henry, R. B. C. (2021, October). Planetary Nebulae: Sources of Enlightenment. *arXiv e-prints*, arXiv:2110.13993. Retrieved from <https://ui.adsabs.harvard.edu/abs/2021arXiv211013993K>

- Landau, E. M., Lifshitz, L. D. & Lifshitz. (1987). *Fluid mechanics* (2nd ed. ed., Vol. 6). London: Pergamon Books.
- Laney, C. (1998). *Computational gasdynamics*. Cambridge University Press. Retrieved from <https://books.google.com.mx/books?id=r-bYw-JjKGAC>
- Lee, H. K., Wijers, R. A. M. J., & Brown, G. E. (2000, Jan). The Blandford-Znajek process as a central engine for a gamma-ray burst. *Physics Reports*, 325(3), 83-114. Retrieved from <https://ui.adsabs.harvard.edu/abs/2000PhR...325...83L> doi: 10.1016/S0370-1573(99)00084-8
- Leng, M., & Giannios, D. (2014, Nov). Testing the neutrino annihilation model for launching GRB jets. *Monthly Notices of the Royal Astronomical Society*, 445, L1-L5. Retrieved from <https://ui.adsabs.harvard.edu/abs/2014MNRAS.445L...1L> doi: 10.1093/mnras/slu122
- LeVeque, R. J. (2002). *Finite volume methods for hyperbolic problems*. Cambridge University Press. Retrieved from <https://doi.org/10.1017/CBO9780511791253> doi: 10.1017/CBO9780511791253
- Li, Y.-P., Dempsey, A. M., Li, H., Li, S., & Li, J. (2021, December). Hot Circumsingle Disks Drive Binary Black Hole Mergers in Active Galactic Nucleus Disks. *arXiv e-prints*, arXiv:2112.11057. Retrieved from <https://ui.adsabs.harvard.edu/abs/2021arXiv211211057L>
- Liska, M., Hesp, C., Tchekhovskoy, A., Ingram, A., van der Klis, M., Markoff, S. B., & Van Moer, M. (2021, October). Disc tearing and Bardeen-Petterson alignment in GRMHD simulations of highly tilted thin accretion discs. *Monthly Notices of the Royal Astronomical Society*, 507(1), 983-990. Retrieved from <https://ui.adsabs.harvard.edu/abs/2021MNRAS.507...983L> doi: 10.1093/mnras/staa099
- Livio, M. (1997). The Formation Of Astrophysical Jets. In D. T. Wickramasinghe, G. V. Bicknell, & L. Ferrario (Eds.), *Iau colloq. 163: Accretion phenomena and related outflows* (Vol. 121, p. 845). Retrieved from <http://adsabs.harvard.edu/abs/1997ASPC..121..845L>
- López-Cámara, D., De Colle, F., & Moreno Méndez, E. (2019, January). Self-regulating jets during the common-envelope phase. *Monthly Notices of the Royal Astronomical Society*, 482(3), 3646-3655. Retrieved from <https://ui.adsabs.harvard.edu/abs/2019MNRAS.482.3646L> doi: 10.1093/mnras/sty2959
- Lora-Clavijo, F. D., Cruz-Osorio, A., & Guzmán, F. S. (2015, June). CAFE: A New Relativistic MHD Code. *Astrophysical Journal Supplements*, 218, 24. Retrieved from <http://adsabs.harvard.edu/abs/2015ApJS..218...24L> doi: 10.1088/0067-0049/218/2/24

- Lora-Clavijo, F. D., Cruz-Perez, J. P., Guzman, F. S., & Gonzalez, J. A. (2013, March). Exact solution of the 1D Riemann problem in Newtonian and relativistic hydrodynamics. *arXiv e-prints*, arXiv:1303.3999. Retrieved from <https://ui.adsabs.harvard.edu/abs/2013arXiv1303.3999L>
- Malik, K. A., & Matravers, D. R. (2003, Jul). The Kelvin-Helmholtz instability in an expanding universe and its effect on dark matter. *Astronomy and Astrophysics*, *406*, 37-41. Retrieved from <https://ui.adsabs.harvard.edu/#abs/2003A&A...406...37M> doi: 10.1051/0004-6361:20030778
- Marquina, A. (1994). Local piecewise hyperbolic reconstruction of numerical fluxes for n nonlinear scalar conservation laws. *SIAM Journal on Scientific Computing*, *15*(4), 892-915. Retrieved from <https://doi.org/10.1137/0915054> doi: 10.1137/0915054
- Marti, J. M., & Muller, E. (1994, January). Analytical solution of the Riemann problem in relativistic hydrodynamics. *Journal of Fluid Mechanics*, *258*, 317-333. Retrieved from <https://ui.adsabs.harvard.edu/abs/1994JFM...258..317M> doi: 10.1017/S0022112094003344
- Martí, J. M., Müller, E., Font, J. A., Ibáñez, J. M. Z., & Marquina, A. (1997, April). Morphology and Dynamics of Relativistic Jets. *Astrophysical Journal*, *479*(1), 151-163. Retrieved from <https://ui.adsabs.harvard.edu/abs/1997ApJ...479..151M> doi: 10.1086/303842
- McKinney, J. C., Tchekhovskoy, A., Sadowski, A., & Narayan, R. (2014, July). Three-dimensional general relativistic radiation magnetohydrodynamical simulation of super-Eddington accretion, using a new code HARMRAD with M1 closure. *Monthly Notices of the Royal Astronomical Society*, *441*(4), 3177-3208. Retrieved from <https://ui.adsabs.harvard.edu/abs/2014MNRAS.441.3177M> doi: 10.1093/mnras/stu762
- Mendoza, S., Hidalgo, J. C., Olvera, D., & Cabrera, J. I. (2009, May). Internal shocks in relativistic jets with time-dependent sources. *Monthly Notices of the Royal Astronomical Society*, *395*, 1403-1408. Retrieved from <http://adsabs.harvard.edu/abs/2009MNRAS.395.1403M> doi: 10.1111/j.1365-2966.2009.14483.x
- Michel, F. C. (1972, January). Accretion of Matter by Condensed Objects. *Astrophysics and Space Science*, *15*(1), 153-160. Retrieved from <https://ui.adsabs.harvard.edu/abs/1972Ap&SS...15..153M> doi: 10.1007/BF00649949
- Mignone, A., & Bodo, G. (2005, November). An HLLC Riemann solver for relativistic flows - I. Hydrodynamics. *Monthly Notices of the Royal Astronomical Society*, *364*, 126-136. Retrieved from <https://ui.adsabs.harvard.edu/#abs/2005MNRAS.364..126M> doi: 10.1111/j.1365-2966.2005.09546.x

- Mignone, A., Bodo, G., Massaglia, S., Matsakos, T., Tesileanu, O., Zanni, C., & Ferrari, A. (2007, May). PLUTO: A Numerical Code for Computational Astrophysics. *Astrophysical Journal Supplements*, 170(1), 228-242. doi: 10.1086/513316
- Mizuno, Y. (2022, January). GRMHD Simulations and Modeling for Jet Formation and Acceleration Region in AGNs. *Universe*, 8(2), 85. Retrieved from <https://ui.adsabs.harvard.edu/abs/2022Univ...8...85M> doi: 10.3390/universe8020085
- Moffat, J. W. (2020, November). Supermassive Black Hole Accretion and Growth. *arXiv e-prints*, arXiv:2011.13440. Retrieved from <https://ui.adsabs.harvard.edu/abs/2020arXiv201113440M>
- Moreno Méndez, E., López-Cámara, D., & De Colle, F. (2017, September). Dynamics of jets during the common-envelope phase. *Monthly Notices of the Royal Astronomical Society*, 470(3), 2929-2937. Retrieved from <https://ui.adsabs.harvard.edu/abs/2017MNRAS.470.2929M> doi: 10.1093/mnras/stx1385
- Moschetta, J.-M., Gressier, J., Robinet, J.-C., & Casalis, G. (2001). The carbuncle phenomenon: A genuine euler instability ? In *Godunov methods: Theory and applications* (pp. 639–645). Boston, MA: Springer US. Retrieved from https://doi.org/10.1007/978-1-4615-0663-8_63 doi: 10.1007/978-1-4615-0663-8_63
- Most, E. R., Papenfort, L. J., Tootle, S. D., & Rezzolla, L. (2021, September). On accretion discs formed in MHD simulations of black hole-neutron star mergers with accurate microphysics. *Monthly Notices of the Royal Astronomical Society*, 506(3), 3511-3526. Retrieved from <https://ui.adsabs.harvard.edu/abs/2021MNRAS.506.3511M> doi: 10.1093/mnras/stab1824
- Muxlow, T., & Garrington, S. (1991). Observations of large scale extragalactic jets. In P. A. Hughes (Ed.), *Beams and jets in astrophysics* (p. 52–99). Cambridge University Press. Retrieved from <https://doi.org/10.1017/CBO9780511564703> doi: 10.1017/CBO9780511564703.003
- Nagar, N. M., Vogel, S. N., Stone, J. M., & Ostriker, E. C. (1997, Jun). Kinematics of the Molecular Sheath of the HH 111 Optical Jet. *Astrophysical Journal*, 482, L195-L198. Retrieved from <https://ui.adsabs.harvard.edu/#abs/1997ApJ...482L.195N> doi: 10.1086/310703
- Narayan, R., & McClintock, J. E. (2012, January). Observational evidence for a correlation between jet power and black hole spin. *Monthly Notices of the Royal Astronomical Society*, 419(1), L69-L73. Retrieved from <https://ui.adsabs.harvard.edu/abs/2012MNRAS.419L..69N> doi: 10.1111/j.1745-3933.2011.01181.x
- Narayan, R., & Yi, I. (1994, June). Advection-dominated Accretion: A Self-similar Solution. *Astrophysical Journal Letters*, 428, L13. Retrieved from <https://ui.adsabs.harvard.edu/abs/1994ApJ...428L..13N> doi: 10.1086/187381

- Narayan, R., & Yi, I. (1995, October). Advection-dominated Accretion: Underfed Black Holes and Neutron Stars. *Astrophysical Journal*, *452*, 710. Retrieved from <https://ui.adsabs.harvard.edu/abs/1995ApJ...452..710N> doi: 10.1086/176343
- Novikov, I. D., & Thorne, K. S. (1973, January). Astrophysics of black holes. In *Black holes (les astres occlus)* (p. 343-450). Retrieved from <https://ui.adsabs.harvard.edu/abs/1973blho.conf..343N>
- Paczynski, B., & Abramowicz, M. A. (1982, Feb). A model of a thick disk with equatorial accretion. *Astrophysical Journal*, *253*, 897-907. Retrieved from <https://ui.adsabs.harvard.edu/abs/1982ApJ...253..897P> doi: 10.1086/159689
- Pandey, B. P., & Vladimirov, S. V. (2019, Feb). Charged Grains and Kelvin-Helmholtz Instability in Molecular Clouds. *Astronomical Journal*, *157*, 83. Retrieved from <https://ui.adsabs.harvard.edu/#abs/2019AJ...157...83P> doi: 10.3847/1538-3881/aafc32
- Panotopoulos, G., Rincón, Á., & Lopes, I. (2021, October). Accretion of matter and spectra of binary X-ray sources in massive gravity. *Annals of Physics*, *433*, 168596. Retrieved from <https://ui.adsabs.harvard.edu/abs/2021AnPhy..43368596P> doi: 10.1016/j.aop.2021.168596
- Pariev, V. I., Blackman, E. G., & Boldyrev, S. A. (2003, August). Extending the Shakura-Sunyaev approach to a strongly magnetized accretion disc model. *Astronomy and Astrophysics*, *407*, 403-421. Retrieved from <https://ui.adsabs.harvard.edu/abs/2003A&A...407..403P> doi: 10.1051/0004-6361:20030868
- Pavan, A., Ciolfi, R., Kalinani, J. V., & Mignone, A. (2021, September). Short gamma-ray burst jet propagation in binary neutron star merger environments. *Monthly Notices of the Royal Astronomical Society*, *506*(3), 3483-3498. Retrieved from <https://ui.adsabs.harvard.edu/abs/2021MNRAS.506.3483P> doi: 10.1093/mnras/stab1810
- Penna, R. F., Narayan, R., & Sądowski, A. (2013, December). General relativistic magnetohydrodynamic simulations of Blandford-Znajek jets and the membrane paradigm. *Monthly Notices of the Royal Astronomical Society*, *436*(4), 3741-3758. Retrieved from <https://ui.adsabs.harvard.edu/abs/2013MNRAS..436.3741P> doi: 10.1093/mnras/stt1860
- Perucho, M., Lobanov, A. P., Martí, J. M., & Hardee, P. E. (2006, Sep). The role of Kelvin-Helmholtz instability in the internal structure of relativistic outflows. The case of the jet in 3C 273. *Astronomy and Astrophysics*, *456*, 493-504. Retrieved from <https://ui.adsabs.harvard.edu/#abs/2006A&A...456..493P> doi: 10.1051/0004-6361:20065310

- Petrich, L. I., Shapiro, S. L., & Teukolsky, S. A. (1988, May). Accretion onto a moving black hole: An exact solution. *Phys. Rev. Lett.*, *60*, 1781–1784. Retrieved from <https://link.aps.org/doi/10.1103/PhysRevLett.60.1781> doi: 10.1103/PhysRevLett.60.1781
- Porth, O., Chatterjee, K., Narayan, R., Gammie, C. F., Mizuno, Y., Anninos, P., ... Event Horizon Telescope Collaboration (2019, August). The Event Horizon General Relativistic Magnetohydrodynamic Code Comparison Project. *Astrophysical Journal Supplements*, *243*(2), 26. Retrieved from <https://ui.adsabs.harvard.edu/abs/2019ApJS..243...26P> doi: 10.3847/1538-4365/ab29fd
- Porth, O., Olivares, H., Mizuno, Y., Younsi, Z., Rezzolla, L., Moscibrodzka, M., ... Kramer, M. (2017, May). The black hole accretion code. *Computational Astrophysics and Cosmology*, *4*(1), 1. Retrieved from <https://ui.adsabs.harvard.edu/abs/2017ComAC...4....1P> doi: 10.1186/s40668-017-0020-2
- Prendergast, K. H., & Burbidge, G. R. (1968, February). On the Nature of Some Galactic X-Ray Sources. *Astrophysical Journal Letters*, *151*, L83. Retrieved from <https://ui.adsabs.harvard.edu/abs/1968ApJ...151L..83P> doi: 10.1086/180148
- Price, D. J., Wurster, J., Tricco, T. S., Nixon, C., Toupin, S., Pettitt, A., ... Lodato, G. (2018, September). Phantom: A Smoothed Particle Hydrodynamics and Magnetohydrodynamics Code for Astrophysics. *Publications of the Astronomical Society of Australia*, *35*, e031. Retrieved from <https://ui.adsabs.harvard.edu/abs/2018PASA...35...31P> doi: 10.1017/pasa.2018.25
- Proga, D., & Begelman, M. C. (2003, January). Accretion of Low Angular Momentum Material onto Black Holes: Two-dimensional Hydrodynamical Inviscid Case. *Astrophysical Journal*, *582*(1), 69-81. Retrieved from <https://ui.adsabs.harvard.edu/abs/2003ApJ...582...69P> doi: 10.1086/344537
- Radice, D., & Rezzolla, L. (2012, Nov). THC: a new high-order finite-difference high-resolution shock-capturing code for special-relativistic hydrodynamics. *Astronomy and Astrophysics*, *547*, A26. Retrieved from <https://ui.adsabs.harvard.edu/#abs/2012A&A...547A..26R> doi: 10.1051/0004-6361/201219735
- Raga, A. C., Navarro-González, R., & Villagrán-Muniz, M. (2000, April). A New, 3D Adaptive Grid Code for Astrophysical and Geophysical Gasdynamics. *Revista Mexicana de Astronomía y Astrofísica*, *36*, 67.
- Rezzolla, L., & Zanotti, O. (2013). *Relativistic Hydrodynamics*. Retrieved from <https://ui.adsabs.harvard.edu/abs/2013rehy.book.....R>

- Riccardi, G., & Durante, D. (2008). Primitive Variable Recovering in Special Relativistic Hydrodynamics Allowing Ultra-Relativistic Flows. *International Mathematical Forum*, *42*, 2081 - 2111. Retrieved from <http://www.m-hikari.com/imf-password2008/41-44-2008/riccardiIMF41-44-2008-2.pdf>
- Richards, C. B., Baumgarte, T. W., & Shapiro, S. L. (2021, February). Accretion onto a small black hole at the center of a neutron star. *arXiv e-prints*, arXiv:2102.09574. Retrieved from <https://ui.adsabs.harvard.edu/abs/2021arXiv210209574R>
- Rodionov, A. V. (2018, May). Artificial viscosity to cure the carbuncle phenomenon: The three-dimensional case. *Journal of Computational Physics*, *361*, 50-55. Retrieved from <https://ui.adsabs.harvard.edu/#abs/2018JCoPh.361...50R> doi: 10.1016/j.jcp.2018.02.001
- Roe, P. L. (1981, October). Approximate Riemann Solvers, Parameter Vectors, and Difference Schemes. *Journal of Computational Physics*, *43*, 357-372. Retrieved from <http://adsabs.harvard.edu/abs/1981JCoPh..43..357R> doi: 10.1016/0021-9991(81)90128-5
- Roe, P. L. (1986). Characteristic-based schemes for the Euler equations. *Annual Review of Fluid Mechanics*, *18*, 337-365. Retrieved from <http://adsabs.harvard.edu/abs/1986AnRFM..18..337R> doi: 10.1146/annurev.fl.18.010186.002005
- Romero, G. E., Boettcher, M., Markoff, S., & Tavecchio, F. (2017, July). Relativistic Jets in Active Galactic Nuclei and Microquasars. *Space Science Reviews*, *207*, 5-61. Retrieved from <http://adsabs.harvard.edu/abs/2017SSRv..207...5R> doi: 10.1007/s11214-016-0328-2
- Ruan, W., Xia, C., & Keppens, R. (2018, Nov). Solar flares and Kelvin-Helmholtz instabilities: A parameter survey. *Astronomy and Astrophysics*, *618*, A135. Retrieved from <https://ui.adsabs.harvard.edu/#abs/2018A&A...618A.135R> doi: 10.1051/0004-6361/201833362
- Russell, H. R., Fabian, A. C., McNamara, B. R., & Broderick, A. E. (2015, July). Inside the Bondi radius of M87. *Monthly Notices of the Royal Astronomical Society*, *451*(1), 588-600. Retrieved from <https://ui.adsabs.harvard.edu/abs/2015MNRAS.451..588R> doi: 10.1093/mnras/stv954
- Ryu, D., Chattopadhyay, I., & Choi, E. (2006, sep). Equation of state in numerical relativistic hydrodynamics. *The Astrophysical Journal Supplement Series*, *166*(1), 410-420. Retrieved from <https://doi.org/10.1086%2F505937> doi: 10.1086/505937
- Sarbach, O., & Zannias, T. (2013, July). Relativistic kinetic theory: An introduction. In *Ix mexican school on gravitation and mathematical physics: Cosmology for the xxist century: Gravitation and mathematical physics division of the mexican physical society dgfm-smf* (Vol. 1548, p. 134-155). doi: 10.1063/1.4817035

- Sedov, L. I. (1959). *Similarity and Dimensional Methods in Mechanics*. Retrieved from <https://ui.adsabs.harvard.edu/abs/1959sdmm.book.....S>
- Semenov, V., Dyadechkin, S., & Punsly, B. (2004, August). Simulations of Jets Driven by Black Hole Rotation. *Science*, *305*(5686), 978-980. Retrieved from <https://ui.adsabs.harvard.edu/abs/2004Sci...305..978S> doi: 10.1126/science.1100638
- Shakura, N. I., & Sunyaev, R. A. (1973, Jun). Reprint of 1973A&A....24..337S. Black holes in binary systems. Observational appearance. *Astronomy and Astrophysics*, *500*, 33-51. Retrieved from <https://ui.adsabs.harvard.edu/abs/1973A&A....24..337S>
- She-Ming Lau-Chapdelaine, S., & Radulescu, M. I. (2016, May). Viscous solution of the triple shock reflection problem. *arXiv e-prints*, arXiv:1605.05943. Retrieved from <https://ui.adsabs.harvard.edu/#abs/2016arXiv160505943S>
- Shrestha, M., Steele, I. A., Kobayashi, S., Jordana-Mitjans, N., Smith, R. J., Jermak, H., ... Guidorzi, C. (2022, February). GRB 191016A: a highly collimated gamma-ray burst jet with magnetized energy injection. *Monthly Notices of the Royal Astronomical Society*, *509*(4), 5964-5973. Retrieved from <https://ui.adsabs.harvard.edu/abs/2022MNRAS.509.5964S> doi: 10.1093/mnras/stab3368
- Shu, C.-W., & Osher, S. (1988). Efficient implementation of essentially non-oscillatory shock-capturing schemes. *Journal of Computational Physics*, *77*(2), 439 - 471. Retrieved from <http://www.sciencedirect.com/science/article/pii/0021999188901775> doi: [https://doi.org/10.1016/0021-9991\(88\)90177-5](https://doi.org/10.1016/0021-9991(88)90177-5)
- Siegel, D. M., & Metzger, B. D. (2017, December). Three-Dimensional General-Relativistic Magnetohydrodynamic Simulations of Remnant Accretion Disks from Neutron Star Mergers: Outflows and r -Process Nucleosynthesis. *Physical Review Letters*, *119*(23), 231102. Retrieved from <https://ui.adsabs.harvard.edu/abs/2017PhRvL.119w1102S> doi: 10.1103/PhysRevLett.119.231102
- Siegel, D. M., & Metzger, B. D. (2018, May). Three-dimensional GRMHD Simulations of Neutrino-cooled Accretion Disks from Neutron Star Mergers. *Astrophysical Journal*, *858*(1), 52. Retrieved from <https://ui.adsabs.harvard.edu/abs/2018ApJ...858...52S> doi: 10.3847/1538-4357/aabaec
- Sod, G. A. (1978). A Survey of Several Finite Difference Methods for Systems of Non-linear Hyperbolic Conservation Laws. *Journal of Computational Physics*, *27*(1), 1-31. Retrieved from <https://hal.archives-ouvertes.fr/hal-01635155> doi: 10.1016/0021-9991(78)90023-2
- Spilker, J. S., Phadke, K. A., Aravena, M., Béthermin, M., Chapman, S. C., Dong, C., ... Weiss, A. (2020, December). Ubiquitous Molecular Outflows in $z > 4$ Massive,

- Dusty Galaxies. I. Sample Overview and Clumpy Structure in Molecular Outflows on 500 pc Scales. *Astrophysical Journal*, 905(2), 85. Retrieved from <https://ui.adsabs.harvard.edu/abs/2020ApJ...905...85S> doi: 10.3847/1538-4357/abc47f
- Stone, J. M., Gardiner, T. A., Teuben, P., Hawley, J. F., & Simon, J. B. (2008, Sep). Athena: A New Code for Astrophysical MHD. *The Astrophysical Journal Supplement Series*, 178, 137-177. Retrieved from <https://ui.adsabs.harvard.edu/abs/2008ApJS..178..137S> doi: 10.1086/588755
- Stone, J. M., & Hardee, P. E. (2000, Sep). Magnetohydrodynamic Models of Axisymmetric Protostellar Jets. *Astrophysical Journal*, 540, 192-210. Retrieved from <https://ui.adsabs.harvard.edu/abs/2000ApJ...540..192S> doi: 10.1086/309289
- Stone, J. M., & Norman, M. L. (1992, Jun). ZEUS-2D: A Radiation Magnetohydrodynamics Code for Astrophysical Flows in Two Space Dimensions. I. The Hydrodynamic Algorithms and Tests. *The Astrophysical Journal Supplement Series*, 80, 753. Retrieved from <https://ui.adsabs.harvard.edu/abs/1992ApJS...80..753S> doi: 10.1086/191680
- Stone, J. M., Tomida, K., White, C. J., & Felker, K. G. (2020, July). The Athena++ Adaptive Mesh Refinement Framework: Design and Magnetohydrodynamic Solvers. *Astrophysical Journal Supplements*, 249(1), 4. Retrieved from <https://ui.adsabs.harvard.edu/abs/2020ApJS..249...4S> doi: 10.3847/1538-4365/ab929b
- Synge, J. (1957). *The relativistic gas*. Amsterdam: North-Holland. doi: <https://doi.org/10.1063/1.3062345>
- Tasker, E. J., Brunino, R., Mitchell, N. L., Michielsen, D., Hopton, S., Pearce, F. R., ... Theuns, T. (2008, Nov). A test suite for quantitative comparison of hydrodynamic codes in astrophysics. *Monthly Notices of the Royal Astronomical Society*, 390, 1267-1281. Retrieved from <https://ui.adsabs.harvard.edu/abs/2008MNRAS.390.1267T> doi: 10.1111/j.1365-2966.2008.13836.x
- Taylor, G. (1950, March). The Formation of a Blast Wave by a Very Intense Explosion. I. Theoretical Discussion. *Proceedings of the Royal Society of London Series A*, 201(1065), 159-174. Retrieved from <https://ui.adsabs.harvard.edu/abs/1950RSPSA.201..159T> doi: 10.1098/rspa.1950.0049
- Tchekhovskoy, A. (2015). Launching of Active Galactic Nuclei Jets. In I. Contopoulos, D. Gabuzda, & N. Kylafis (Eds.), *The formation and disruption of black hole jets* (Vol. 414, p. 45). Retrieved from <https://ui.adsabs.harvard.edu/abs/2015ASSL..414...45T> doi: 10.1007/978-3-319-10356-3_3

- Tejeda, E., & Aguayo-Ortiz, A. (2019, August). Relativistic wind accretion on to a Schwarzschild black hole. *Monthly Notices of the Royal Astronomical Society*, *487*(3), 3607-3617. Retrieved from <https://ui.adsabs.harvard.edu/abs/2019MNRAS.487.3607T> doi: 10.1093/mnras/stz1513
- Tejeda, E., Mendoza, S., & Miller, J. C. (2012, Jan). Analytic solutions to the accretion of a rotating finite cloud towards a central object - II. Schwarzschild space-time. *Monthly Notices of the Royal Astronomical Society*, *419*(2), 1431-1441. Retrieved from <https://ui.adsabs.harvard.edu/abs/2012MNRAS.419.1431T> doi: 10.1111/j.1365-2966.2011.19800.x
- Thorne, K. S. (1974, July). Disk-Accretion onto a Black Hole. II. Evolution of the Hole. *Astrophysical Journal*, *191*, 507-520. Retrieved from <https://ui.adsabs.harvard.edu/abs/1974ApJ...191..507T> doi: 10.1086/152991
- Titarev, V., & Toro, E. (2004). Finite-volume weno schemes for three-dimensional conservation laws. *Journal of Computational Physics*, *201*(1), 238 - 260. Retrieved from <http://www.sciencedirect.com/science/article/pii/S0021999104002281> doi: <https://doi.org/10.1016/j.jcp.2004.05.015>
- Toro, E. F. (2009). *Riemann Solvers and Numerical Methods for Fluid Dynamics*. Springer. Retrieved from <https://link.springer.com/book/10.1007/b79761>
- Toro, E. F., Spruce, M., & Speares, W. (1994, July). Restoration of the contact surface in the HLL-Riemann solver. *Shock Waves*, *4*(1), 25-34. Retrieved from <https://ui.adsabs.harvard.edu/abs/1994ShWav...4...25T> doi: 10.1007/BF01414629
- van Leer, B. (1977, March). Towards the ultimate conservative difference scheme. III - Upstream-centered finite-difference schemes for ideal compressible flow. IV - A new approach to numerical convection. *Journal of Computational Physics*, *23*, 263-299. Retrieved from <http://adsabs.harvard.edu/abs/1977JCoPh..23..263V> doi: 10.1016/0021-9991(77)90094-8
- Vink, J. S. (2011, November). The theory of stellar winds. *Astrophysics and Space Science*, *336*(1), 163-167. Retrieved from <https://ui.adsabs.harvard.edu/abs/2011Ap&SS.336..163V> doi: 10.1007/s10509-011-0636-7
- Weis, K., & Bomans, D. J. (2020, February). Luminous Blue Variables. *Galaxies*, *8*(1), 20. Retrieved from <https://ui.adsabs.harvard.edu/abs/2020Galax...8...20W> doi: 10.3390/galaxies8010020
- Wheeler, J. A. (1964). Geometrodynamics and the issue of final state. In *Les Houches Summer School of Theoretical Physics: Relativity, Groups and Topology* (pp. 317-522). Retrieved from <https://inspirehep.net/literature/1353706>

- Wienkers, A. F., & Ogilvie, G. I. (2018, Jul). Non-linear hydrodynamic instability and turbulence in eccentric astrophysical discs with vertical structure. *Monthly Notices of the Royal Astronomical Society*, *477*, 4838-4855. Retrieved from <https://ui.adsabs.harvard.edu/#abs/2018MNRAS.477.4838W> doi: 10.1093/mnras/sty899
- Woodward, P., & Colella, P. (1984, Apr). The Numerical Stimulation of Two-Dimensional Fluid Flow with Strong Shocks. *Journal of Computational Physics*, *54*, 115-173. Retrieved from <https://ui.adsabs.harvard.edu/#abs/1984JCoPh..54..115W> doi: 10.1016/0021-9991(84)90142-6
- Xu, W., & Stone, J. M. (2019, October). Bondi-Hoyle-Lyttleton accretion in supergiant X-ray binaries: stability and disc formation. *Monthly Notices of the Royal Astronomical Society*, *488*(4), 5162-5184. Retrieved from <https://ui.adsabs.harvard.edu/abs/2019MNRAS.488.5162X> doi: 10.1093/mnras/stz2002
- Yao, P. Z., Dexter, J., Chen, A. Y., Ryan, B. R., & Wong, G. N. (2021, November). Radiation GRMHD simulations of M87: funnel properties and prospects for gap acceleration. *Monthly Notices of the Royal Astronomical Society*, *507*(4), 4864-4878. Retrieved from <https://ui.adsabs.harvard.edu/abs/2021MNRAS..507.4864Y> doi: 10.1093/mnras/stab2462
- Yen, H.-W., Takakuwa, S., Gu, P.-G., Hirano, N., Lee, C.-F., Liu, H. B., ... Wu, C.-J. (2019, March). Signs of outflow feedback from a nearby young stellar object on the protostellar envelope around HL Tauri. *Astronomy and Astrophysics*, *623*, A96. Retrieved from <https://ui.adsabs.harvard.edu/abs/2019A&A...623A..96Y> doi: 10.1051/0004-6361/201834209
- Yuan, F., & Narayan, R. (2014, August). Hot Accretion Flows Around Black Holes. *Ann. Rev. Ast. & Ast.*, *52*, 529-588. Retrieved from <https://ui.adsabs.harvard.edu/abs/2014ARA&A..52..529Y> doi: 10.1146/annurev-astro-082812-141003
- Zhu, Z.-Y., Zhou, E.-P., & Li, A. (2018, August). Neutron Star Equation of State from the Quark Level in Light of GW170817. *Astrophysical Journal*, *862*, 98. Retrieved from <https://ui.adsabs.harvard.edu/#abs/2018ApJ...862...98Z> doi: 10.3847/1538-4357/aacc28

